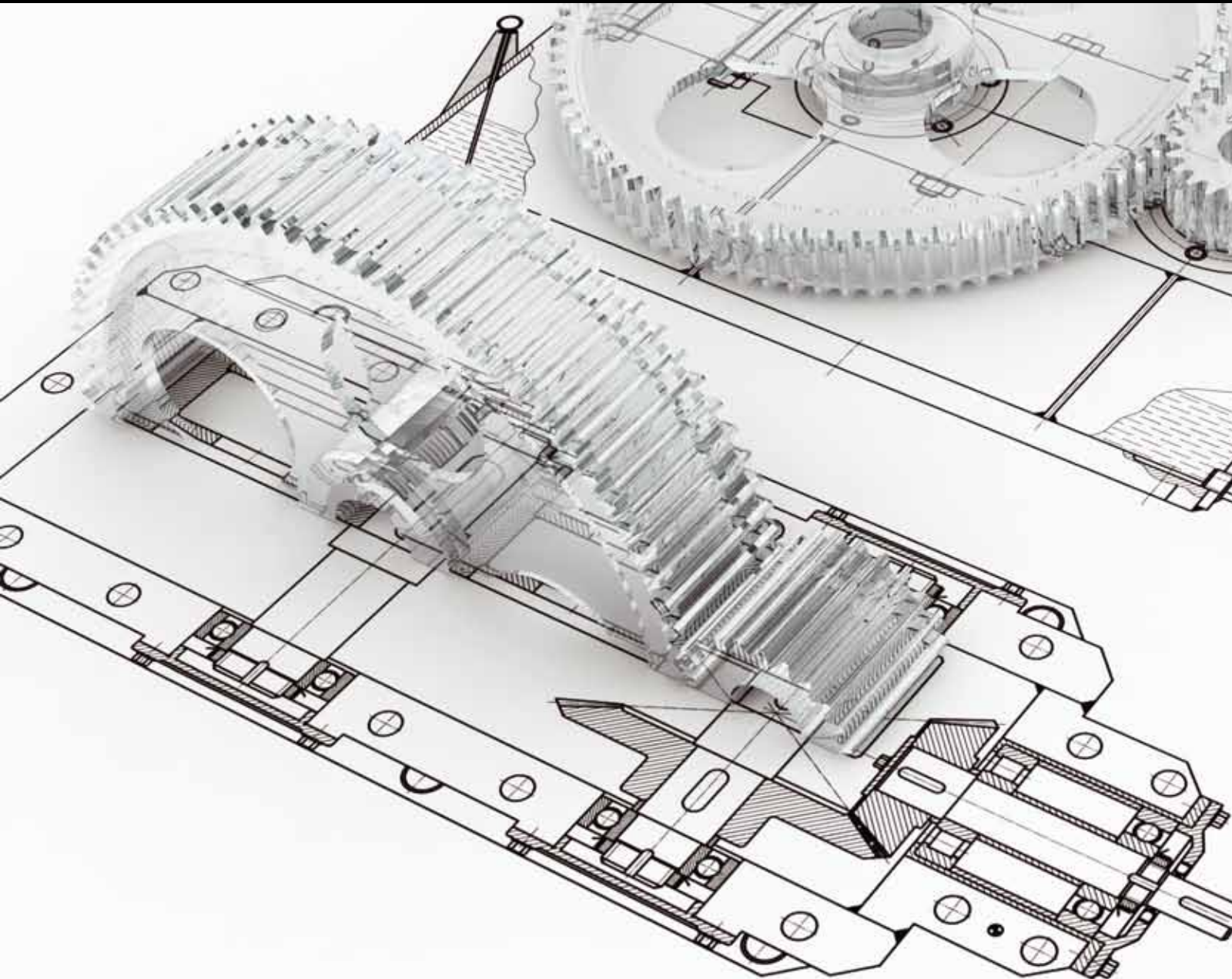


# Mechanical Behavior and Microstructure Evolution in Manufacturing Processes

Guest Editors: Gang Wang, Feng Jiang, and Lei Zhang





---

# **Mechanical Behavior and Microstructure Evolution in Manufacturing Processes**

Advances in Mechanical Engineering

---

**Mechanical Behavior and Microstructure  
Evolution in Manufacturing Processes**

Guest Editors: Gang Wang, Feng Jiang, and Lei Zhang



---

Copyright © 2013 Hindawi Publishing Corporation. All rights reserved.

This is a special issue published in “Advances in Mechanical Engineering.” All articles are open access articles distributed under the Creative Commons Attribution License, which permits unrestricted use, distribution, and reproduction in any medium, provided the original work is properly cited.

## Editorial Board

Koshi Adachi, Japan  
Mehdi Ahmadian, USA  
Rehan Ahmed, UK  
Muhammad Tahir Akhtar, Japan  
Nacim Alilat, France  
M. Affan Badar, USA  
Luis Baeza, Spain  
R. Balachandran, UK  
Claude Bathias, France  
Adib Becker, UK  
Leonardo Bertini, Italy  
L. A. Blunt, UK  
Noël Brunetière, France  
Marco Ceccarelli, Italy  
Fakher Chaari, Tunisia  
Chin-Lung Chin, Taiwan  
Hyung H. Cho, Republic of Korea  
S.B. Choi, Republic of Korea  
Kangyao Deng, China  
Francisco D. Denia, Spain  
T.S. Dhanasekaran, USA  
Nihad Dukhan, USA  
Farzad Ebrahimi, Iran  
Ali El Wahed, UK  
Bogdan I. Epureanu, USA  
M. R. Eslami, Iran  
Ali Fatemi, USA  
Mario L. Ferrari, Italy  
Siegfried Fouvry, France  
Ian Frigaard, Canada  
Mergen H. Ghayesh, Canada  
Luís Godinho, Portugal

Tian Han, China  
Woo-Suck Han, France  
Francisco J. Huera-Huarte, Spain  
D. Jalali-Vahid, Iran  
Jiin Yuh Jang, Taiwan  
Zhongmin Jin, UK  
Xiaodong Jing, China  
S.-W. Kang, Republic of Korea  
Xianwen Kong, UK  
Michal Kuciej, Poland  
Yaguo Lei, China  
Zili Li, The Netherlands  
Cheng-Xian Lin, USA  
Jaw-Ren Lin, Taiwan  
S. Nima Mahmoodi, USA  
Oronzio Manca, Italy  
Ramiro Martins, Portugal  
Aristide Fausto Massardo, Italy  
Francesco Massi, Italy  
T. H. New, Singapore  
Kim Choon Ng, Singapore  
C. T. Nguyen, Canada  
Hiroshi Noguchi, Japan  
Hakan F. Oztog, Turkey  
Duc Truong Pham, UK  
Jurij Prezelj, Slovenia  
Xiaotun Qiu, USA  
Pascal Ray, France  
Robert L. Reuben, UK  
Pedro A.R. Rosa, Portugal  
Elsa de Sá Caetano, Portugal  
D.R. Salgado, Spain

Mohammad Reza Salimpour, Iran  
Sunetra Sarkar, India  
Pietro Scandura, Italy  
A. Seshadri Sekhar, India  
Ahmet Selim Dalkılıç, Turkey  
Liyuan Sheng, China  
Xi Shi, China  
Seiichi Shiga, Japan  
C. S. Shin, Taiwan  
Ray W. Snidle, UK  
Margaret M. Stack, UK  
Neil Stephen, UK  
Kumar K. Tamma, USA  
Yaya Tan, China  
Anand Thite, UK  
Cho W. Solomon To, USA  
Yoshihiro Tomita, Japan  
Shan-Tung Tu, China  
Sandra Velarde-Suárez, Spain  
Moran Wang, China  
Junwu Wang, China  
Jia-Jang Wu, Taiwan  
Fengfeng Xi, Canada  
Gongnan Xie, China  
Hiroshi Yabuno, Japan  
Wei Mon Yan, Taiwan  
Jianqiao Ye, UK  
Byeng D. Youn, USA  
Bo Yu, China  
Jianbo Yu, China  
Zhongrong Zhou, China

# Contents

**Mechanical Behavior and Microstructure Evolution in Manufacturing Processes**, Gang Wang, Feng Jiang, and Lei Zhang  
Volume 2013, Article ID 431032, 3 pages

**The Experimental Analysis of Forming and Strength of Clinch Riveting Sheet Metal Joint Made of Different Materials**, Jacek Mucha, Ľuboš Kaščák, and Emil Spišák  
Volume 2013, Article ID 848973, 11 pages

**Effect of Detail Design on Fatigue Performance of Aircraft Door Frame**, Kang Jianxiong, Gao Hangshan, Wang Fusheng, and Yue Zhufeng  
Volume 2013, Article ID 329613, 7 pages

**Mathematical and Simulation Modelling of Moisture Diffusion Mechanism during Plastic IC Packages Disassembly**, Peng Mou, Dong Xiang, and Guanghong Duan  
Volume 2013, Article ID 928671, 9 pages

**Performance Evolution of Phytic Acid Conversion Film in the Forming Process**, Xiufang Cui, Lili Lin, Erbao Liu, Guo Jin, and Jie Jin  
Volume 2013, Article ID 740303, 7 pages

**Dynamic Mechanical Behaviors of 6082-T6 Aluminum Alloy**, Peng Yibo, Wang Gang, Zhu Tianxing, Pan Shangfeng, and Rong Yiming  
Volume 2013, Article ID 878016, 8 pages

**Vertical Spindle Grinding of Si and Granite with a New Abrasive Disk**, Yiqing Yu, Juan Liu, Bin Kuang, Jianyun Shen, and Xipeng Xu  
Volume 2013, Article ID 768104, 7 pages

**Analysis of Grinding Force and Elastic Deformation in Thread Grinding Process**, Wei Wang and Xianying Feng  
Volume 2013, Article ID 827831, 6 pages

**Numerical Simulation of the Moving Induction Heating Process with Magnetic Flux Concentrator**, Feng Li, Xuekun Li, Tianxing Zhu, and Yiming (Kevin) Rong  
Volume 2013, Article ID 907295, 9 pages

**Affecting the Ageing Behaviour of Injection-Moulded Microparts Using Variothermal Mould Tempering**, Steve Meister and Dietmar Drummer  
Volume 2013, Article ID 407964, 7 pages

**Effect of the Codeposition Ions on Structural and Tribological Properties of Electro-Brush Plated Coating**, Xiufang Cui, Jinggao Zhong, Dingding Hou, Erbao Liu, Guo Jin, and Qingfen Li  
Volume 2013, Article ID 852091, 6 pages

**Modeling and Optimizing Energy Utilization of Steel Production Process: A Hybrid Petri Net Approach**, Peng Wang, Zeyi Jiang, Zhitao Liu, and Shanghong Fu  
Volume 2013, Article ID 191963, 11 pages

**Numerical Simulation of Force Enhancement by Cellular Material under Blast Load**, Chang Qi, Shu Yang, and Renjing Gao  
Volume 2013, Article ID 328651, 10 pages

**Austenite Grain Growth Behavior of AISI 4140 Alloy Steel**, Lin Wang, Dongsheng Qian, Jun Guo, and Yan Pan  
Volume 2013, Article ID 762890, 7 pages

**Gas-Assisted Heating Technology for High Aspect Ratio Microstructure Injection Molding**, Shia-Chung Chen, Chen-Yang Lin, Jen-An Chang, and Pham Son Minh  
Volume 2013, Article ID 282906, 10 pages

**An Experimental Investigation of Residual Stresses in High-Speed End Milling 7050-T7451 Aluminum Alloy**, Xiaoming Huang, Jie Sun, Jianfeng Li, Xiong Han, and Qingchun Xiong  
Volume 2013, Article ID 592659, 7 pages

**Mesh Regeneration Method for Jig-Shape Optimization Design of the High-Aspect-Ratio Wing**, S. H. Huo, F. S. Wang, Z. Yuan, and Z. F. Yue  
Volume 2013, Article ID 513637, 8 pages

**Melt Pressure Signature Tracking Using an Adaptive Kalman Filter in Microinjection Molding**, Hang Liu, Hong Hu, Kai Leung Yung, Yan Xu, and Xing Wei Zhang  
Volume 2013, Article ID 801964, 10 pages

## Editorial

# Mechanical Behavior and Microstructure Evolution in Manufacturing Processes

Gang Wang,<sup>1</sup> Feng Jiang,<sup>2</sup> and Lei Zhang<sup>3</sup>

<sup>1</sup> Department of Mechanical Engineering, Tsinghua University, Beijing 100084, China

<sup>2</sup> College of Mechanical Engineering and Automation, Huaqiao University, Fujian, Xiamen 361021, China

<sup>3</sup> Scientific Forming Technologies Corporation (SFTC), 2545 Farmers Drive, Suite 200, Columbus, OH 43235, USA

Correspondence should be addressed to Gang Wang; gwang@tsinghua.edu.cn

Received 25 November 2013; Accepted 25 November 2013

Copyright © 2013 Gang Wang et al. This is an open access article distributed under the Creative Commons Attribution License, which permits unrestricted use, distribution, and reproduction in any medium, provided the original work is properly cited.

The high requests for modern manufacturing processes have been proposed on high precision, low cost, short cycle time, and environment friendliness in the past decade. The intensive research on material behavior and evolution has become the foundation of processes with abundant achievements. Recent advances in material and manufacturing have introduced new technologies and fundamental investigation to study dynamic mechanical properties, history of microstructure variation, mechanisms for manufacturing, and overall effect of process parameters. Knowledge and understanding of material fundamentals have led to the development of new materials, new processes, new measurement methodology, and accurate physics-based models.

The papers selected for this special issue present the effort and achievement in this area. Although the selected topics and papers only focus on some specific issues and may not be comprehensive as representation of the area, they represent the versatile attempts and advances, that we have the pleasure of sharing with the readers.

This special issue contains seventeen papers. Three papers are related to microstructure evolution and other three papers focus on the mechanical performance of certain metal materials. Eight papers are regarding the effect of process parameters on final quality for precision machining and other manufacturing processes. Finally, three papers concentrate on the theoretical algorithm research on mechanical design, manufacturing, and industrial engineering.

In the first paper, titled “*Effect of the co-depositionions on structural and tribological properties of electro-brush plated*

*coating*,” X. Cui et al. have investigated the effects of the codeposition ions on structural and tribological properties of electro-brush plated coatings. The microstructure and phase structure were also studied with SEM, XPS, and XRD. It was concluded that the hardness and tribological property of the coatings are improved obviously when proper chemical ion W or Cu codeposited with iron ion is added. The interface bond strength between the coating and the substrate is improved obviously for the Fe-W-Cu coatings.

In the second paper, titled “*Austenite grain growth behavior of AISI 4140 alloy steel*,” L. Wang et al. presents an algorithm to model the austenite grain growth in isothermal condition and elevated temperature. The experiments have been conducted to provide the data support and validate the model. Meanwhile, the standard error analysis has been done to assess and optimize the coefficients in the function of grain growth.

In the third paper, titled “*Performance evolution of phytic acid conversion film in the forming process*,” X. Cui et al. investigated the evolution of the microstructure, composition, roughness, corrosion resistance, nanomechanical property, and residual stress in the film formation process. It was concluded that, in the forming process, the changes of microstructure, mechanical property and corrosion property, are closely related to the variation of elements and residual stress. The determination of residual stress and cracking time is the key factor to optimize preparation techniques and control film quality.

In the fourth paper, titled “*Dynamic mechanical behaviors of 6082-T6 aluminum alloy*,” P. Yibo et al. have investigated the dynamic mechanical behaviors of aluminum alloy and a Johnson-Cook constitutive relationship has been regressed based on the designed tensile tests with a strain rate from quasistatic ( $10^{-3} \text{ s}^{-1}$ ) to moderate ( $100 \text{ s}^{-1}$ ), which has a good agreement with experimental data. The effect of strain rate and strain on the flow stress was discussed. It can be seen that more precipitates appear with an increasing strain rate through BSE graphic analysis, which may enhance the pinning effect on grain boundaries.

In the fifth paper, titled “*Effect of detail design on fatigue performance of aircraft door frame*,” K. Jianxiong et al. assess the fatigue performance of two designs, single-side and double-side door frames, by conducting the fatigue test. The finite element method was taken to examine the stress distribution. It was concluded that double-side design can reduce stress concentration around the bevel of specimen effectively, which resulted in a fatigue life of 18–21 times longer than that of single-side one. The fracture has been observed to analyze the generation and propagation of cracks.

In the sixth paper, titled “*Numerical simulation of force enhancement by cellular material under blast load*,” C. Qi et al. have developed finite element (FE) models of cellular material under blast load to analyze the force evolution. The comparison between the FE methods and one-dimensional analytical model has been conducted to verify the capability of FE methods. The relationship between blast load intensity and the length of the foam bar was analyzed. It was found that the time of momentum transfer between the compacted foam bar and the protected structure was very short compared with the total time of the blast event, which caused force enhancement.

In the seventh paper, titled “*An experimental investigation of residual stresses in high-speed end milling 7050-T7451 aluminum alloy*,” X. Huang et al. have studied the regularity of residual stress in high-speed end milling process of 7050-T7451 aluminum alloy. The effect of machining parameters on residual stress has been investigated by designing orthogonal cutting experiments and the significance of four parameters is ranked. It was concluded that the residual stresses in feed direction were higher than that in cutting direction, and that decrease of the cutting speed and increase of the feed rate led to significant increase significantly in compressive residual stresses on finished surface.

In the eighth paper, titled “*Analysis of grinding force and elastic deformation in thread grinding process*,” W. Wang and X. Feng present a dynamic numerical thread grinding model to analyze grinding force and dynamic contact arc length. The elastic deformation of workpiece was drawn by using force analysis. The effect of some parameters, for example, grinding speed and angle of helix, has been investigated. However, more experimental work needs to be done to validate the model.

In the ninth paper, titled “*Vertical spindle grinding of Si and granite with a new abrasive disk*,” Y. Yu et al. have presented a fabricating process of an ultrafine abrasive tool

for vertical spindle grinding on Si wafer and granite. Sol-gel was applied to granulate ultrafine abrasives in order to reduce the aggregation of ultrafine abrasives and disks were dressed to expected flatness by using a brazed diamond pad. Based on the experiments on a high precision vertical spindle grinding machine, it was found that the brazed diamond abrasives could dress the grinding disks with high efficiency and satisfactory flatness and the new ultrafine abrasive disks had the ability to process silicon wafers and granite slabs with an acceptable performance.

In the tenth paper, titled “*The experimental analysis of forming and strength of clinch riveting sheet metal joint made of different materials*,” J. Mucha et al. have presented the design of the pressed joint processes using forming process. The design of rivets has a significant influence on the forming quality. The joint performance was characterized with a comprehensive examination of the morphology of joint cross section, shear force, failure mode of joints, microhardness, and metallurgy.

In the eleventh paper, titled “*Affecting the ageing behaviour of injection-moulded micro parts using variothermal mould tempering*,” S. Meister and D. Drummer have investigated the ageing behavior of injection-molded micro parts in dependence on the process conditions by using a variothermal injection mold. The results have confirmed that the mold temperature affects the inner properties and the resulting mechanical behavior. The effect of morphology on physical and chemical ageing has been compared and it is concluded that a more intense physical ageing happens with unpropitious morphology. Furthermore, a process induced favored morphology can attenuate the ageing effects and enhance mechanical properties.

In the twelfth paper, titled “*Gas-assisted heating technology for high aspect ratio micro-structure injection molding*,” S.-C. Chen et al. have designed a gas-assisted mold preheating process for injection of plastic material. The effect of preheating temperature and mold gas size on filling efficiency has been investigated. It was concluded that hot gas heating could enhance the filling capability with a filling percent of 91% for high aspect ratio small grooves because the temperature uniformity was improved with the hot gas.

In the thirteenth paper, titled “*Mathematical and simulation modelling of moisture diffusion mechanism during plastic IC packages disassembly*,” P. Mou et al. have researched the moisture diffusion behavior during PCB disassembling process with a diffusion model. The effect of parameters, for example, baking temperature and time, on result of moisture removal has been investigated by using experiments and simulations. It is found that the resistance to moisture diffusion mainly came from the internal part of the IC packages.

In the fourteenth paper, titled “*Numerical simulation of the moving induction heating process with magnetic flux concentrator*,” F. Li et al. have developed FE model to investigate the mechanism of the moving induction heating with metal powder bonded magnetic flux concentrator. Effect of process factors on temperature field of workpiece has been analyzed with the proposed model that has been validated with experimental results on AISI 1045 steel.

In the fifteenth paper, titled “*Melt pressure signature tracking using an adaptive Kalman filter in microinjection molding*,” H. Liu et al. have proposed an adaptive Kalman filter algorithm based on F-distribution for real-time tracking of the melt pressure in microinjection process. The proposed method can improve the convergence of the filtered signal during the tracking process and track the moments that sudden changes occur in the pressure signature. The experimental work provided the evidence for use in the mass production of microinjection moldings.

In the sixteenth paper, titled “*Modeling and optimizing energy utilization of steel production process: a hybrid petri net approach*,” P. Wang et al. have presented a new method for the process based on hybrid petri nets (HPN) to model energy flow within the real steel production process. A real steel production process from one typical integrated steel plant has been analyzed as a case in which the steel production, energy efficiency, and self-made gas surplus were set as the main optimized goals. A fuzzy linear programming method was carried out to obtain the multiobjective optimization results. Based on the analysis, some suggestions were given to improve the low efficiency and high cost.

In the seventeenth paper, titled “*Mesh regeneration method for jig-shape optimization design of the high-aspect-ratio wing*,” S. H. Huo et al. have proposed a mesh regeneration method for the jig-shape optimization design of a high-aspect-ratio wing. Three different cases on jig-shape optimizations based on the method were carried out and the designed jig-shapes have a good agreement with the expectation under the impact of static aeroelasticity. Lift coefficients of all the three jig shape optimization were proven to be larger than that of the original design.

## **Acknowledgment**

We would like to thank the authors for their excellent contributions and patience in assisting us. Finally, the fundamental work of all reviewers on these papers is also very warmly acknowledged.

Gang Wang  
Feng Jiang  
Lei Zhang

## Research Article

# The Experimental Analysis of Forming and Strength of Clinch Riveting Sheet Metal Joint Made of Different Materials

Jacek Mucha,<sup>1</sup> L'uboš Kaščák,<sup>2</sup> and Emil Spišák<sup>2</sup>

<sup>1</sup> Faculty of Mechanical Engineering and Aeronautics, Rzeszow University of Technology, al. Powstańców Warszawy 8, 35-959 Rzeszów, Poland

<sup>2</sup> Faculty of Mechanical Engineering, Technical University of Košice, Mäsiarska 74, 040 01 Košice, Slovakia

Correspondence should be addressed to Jacek Mucha; [j\\_mucha@prz.edu.pl](mailto:j_mucha@prz.edu.pl)

Received 19 June 2013; Revised 18 September 2013; Accepted 3 October 2013

Academic Editor: Gang Wang

Copyright © 2013 Jacek Mucha et al. This is an open access article distributed under the Creative Commons Attribution License, which permits unrestricted use, distribution, and reproduction in any medium, provided the original work is properly cited.

The paper presents the pressed joint technology using forming process with or without additional fastener. The capabilities for increasing the load-carrying ability of mechanical joints by applying special rivets and dies were presented. The experimental research focused on joining steel sheet metal made of different materials. The joint forming was performed with the solid round die and rectangular split die for riveted joint forming. The load-carrying ability of joints was evaluated by measuring the maximum load force in the shearing test in the tensile testing machine. The effect of joint forming process on joined material strain was compared by measuring the microhardness of the joints.

## 1. Introduction

The assembly process development is driven by the automotive industry, especially by companies manufacturing car body elements. These companies are involved in developing and implementing new solutions which are more environmentally friendly.

The processes of plastic joining of sheet metal constructions are even more successful. These processes belong among “white manufacturing processes” [1]. Unlike spot welding and welding, they do not emit dangerous vapors [2]. Mechanical joining of sheet metals is commonly used to manufacture the controlled crush zones elements in cars [3, 4].

In most clinching joint cases, the static strength is lower than that for spot weld joints. The clinching joint strength can be increased by using higher forming force in order to achieve decreased bottom thickness “X” of the cap part of the joint [5]. Another method is using the modified forming with the rivet [6].

The mechanical joints are competitive comparing to conventional joints and can be used successfully while joining thin-walled sheet metal profiles in the framework construction houses [7–10].

The tool geometry must be selected properly in order to provide optimum joint forming conditions while joining materials. The selection of optimal values is a problem mentioned in papers developed among the others by Oudjene et al. [11], Coppieters et al. [12], Roux and Bouchard [13].

First works on experimental researches of forming joints using round segmented die were presented by Lambiase in two papers [14, 15]. This is quite a new look on clinching joint forming capability.

The mechanical joint forming using the nonround split die with rivet is not a well-known problem.

The most up-to-date papers and the only ones on such joints forming capability are papers presented by Mucha, Kaščák, and Spišák [6]. Another paper presenting the effectiveness of this joining method is the paper published by Mucha and Witkowski [10].

Thus the authors decided to present results of joint researches conducted by Technical University of Košice and Rzeszów University of Technology.

## 2. Clinch Riveting Process

The joining process in the ClinchRivet (CR) technology is similar to the self-pierce riveting (SPR) and clinching (CL).

The lock consisting of joined sheet metals is created by the plastic deformation of a solid rivet [16]. For CL technology, the lock is formed by the rigid punch along with relevant die. The upper sheet metal is perforated while pressing the rivet with the self-pierce riveting (SPR) technology. The sheet metals are locked by anchoring the rivet in the lower sheet metal.

Whereas, CR technology entails pressing the solid rivet and anchoring this rivet in the upper sheet metal. The upper sheet metal is anchored in the lower sheet material (Figure 1). In this way, the joint is created.

No fastener is required in the CL joint. SPR and CR require specially selected rivets: the tubular and solid one.

The material lock is created in CR joint, as this is also the case for CL joint. The measurable lock parameters are  $t_n$  and  $t_u$  (Figure 1(b)). The strength and the destruction mechanism of CR joint, similarly to CL joint, depend mainly on created lock size and the  $t_n$  and  $t_u$  ratio. The CR joint bottom thickness is a critical area for joint tightness. Figure 1(b) shows how to measure the joint bottom thickness.

### 3. Materials and Methods

The research experiments were conducted in order to determine the joining capability of different material by ClinchRivet riveting technology developed by Tox Pressotechnik [17].

The maximum joint load-carrying ability increase range and the joint structure hardness were observed. The joint quality evaluation was performed visually (externally) and internally by preparing metallographic microsections. For various joints, the lock parameters  $t_s$  and  $t_n$  were also measured. For selected variants of CR and CL joints the above mentioned lock parameters were compared.

The maximum strength of clinching joint was compared with ClinchRivet joint.

**3.1. Sheets Material.** The examined sheet metals were made of steel and aluminum alloy. The steel sheet plates of 0.8 mm thickness are used in car body elements in Volkswagen Group car assembly plant, Skoda Mlada Boleslav in Bratislava. For comparison purposes, the aluminum alloy 5754 sheet metal of the same thickness in H111 state, material number 3.3535, was used. Different mechanical properties enabled examining the joint forming capability by straining the rivet being pressed. The chemical composition and mechanical properties were presented in Tables 1 and 2.

**3.2. The Rivet and Joint Forming Tools.** Single rivet type of specified geometry (Figure 2) was used in joint forming; an average hardness of the steel rivet in five measurements was 357 HV<sub>0.1</sub>. The used rivet was made of material designated by the catalog number A5x5-2Al by TOX Pressotechnik. Main alloy additives in the chemical composition, besides carbon, are 0.35% Al and 1.5% Mn. The microstructure of the rivet material (zoom x500) is presented in Figure 3.

For all ClinchRivet rivet joining cases, we used the same die (Figure 4(a)). In the joining experiment, the Tox

TABLE 1: Basic mechanical properties of materials sheets.

Materials		Rp <sub>0.2</sub> (MPa)	Rm (MPa)	A <sub>80</sub> (%)
Grade	Number			
RA-K 40/70	standard	450	766	36
	1.0947			
H220PD	1.0358	238	382	36
DC06	1.0873	185	310	41
DX51D + Z	1.0226	160	390	23
5754 H111	3.3535	80	215	14

Pressotechnik die, catalog number TOX SKB 14.180.246182, was used.

The clinching joint (CL) was created with punch and die (Figure 4(b)) manufactured especially for thin sheet metal joining. These tools are used in the laboratory of Department of Technologies and Materials at the Technical University of Košice. The basic tool geometry was presented in Figure 4(c). The CR rivet diameter was close to the diameter of die forming the CL joint.

Smaller die and punch diameters are dedicated in CL process for thin sheet metals. They result in a better lock in the overpress (cap part of the joint which is formed by the punch pressing the joined materials into the die) [18]. Forming joints of sheet metal of different thickness are often accompanied by the material fracture. The tool geometry selection is especially important for thin sheet metals [19].

The die with CR rivet is more universal and forms high quality joints. The punch head with automatic rivet feeder was used while forming CR joints.

Joint forming was performed on the CMB frame press with an electric EMPK drive made by Tox Pressotechnik, maximum loading force of 100 kN. EMPK servo drive enables positioning the punch with 0.01 mm accuracy and measuring the joint forming force versus travel at maximum error of 0.5% force value. In all joining the rivet (CR) was pressed in order to achieve the flat surface of the upper sheet metal. The final punch position was set in order to achieve the distance between the die face and the punch face that equals the sum of sheet metal thicknesses. The distance value was defined in the control software of the press drive. This value was identical for all material combinations. Thus for different sheet materials different forming force was achieved.

CL joints were created for identical  $X$  value of the bottom thickness. The value recommended by the tool manufacturers equals 25% of sum of joined sheet thicknesses. The same value was used in the experiment.

**3.3. Joint Specimens and Combinations.** The overlap joint specimens (Figure 5) were prepared for shearing test; 7 pieces for all arrangement. The force versus punch movement while forming was recorded.

The correct joint structure depends on many factors, including tool geometry, the strain hardening characteristics and material of sheet metal being joined, and rivet. The material flow while clinching process is limited to a small region around tools [20]. The optimization of tool geometry

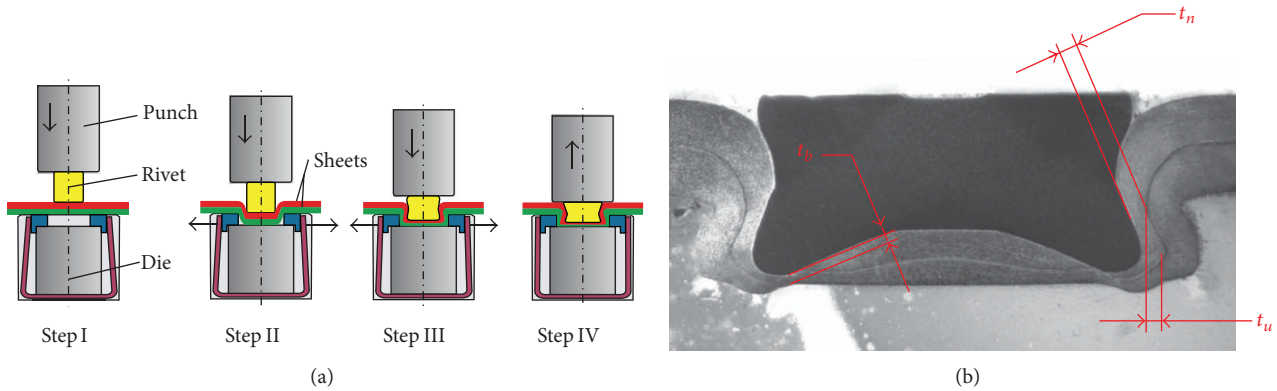


FIGURE 1: Clinch riveting process: (a) joint forming and (b) general section of a clinched joint.

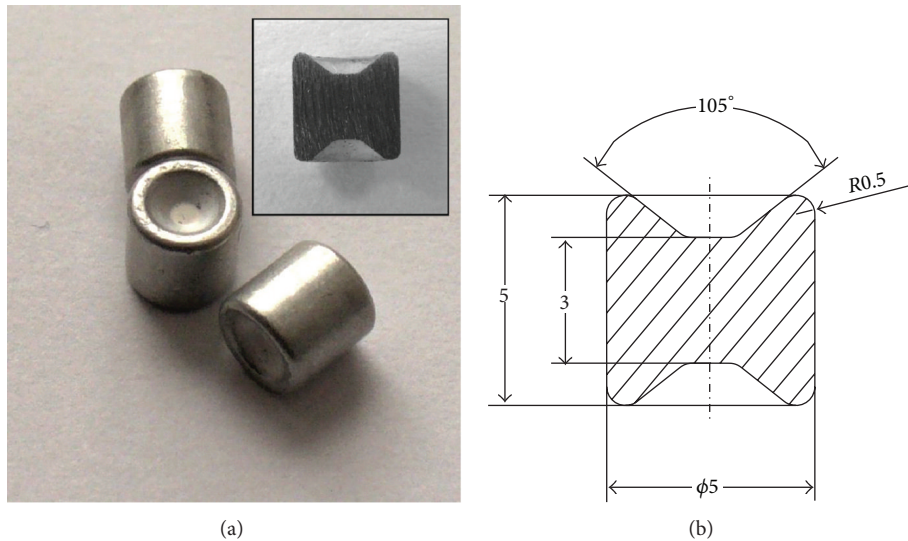


FIGURE 2: Rivets used in CR joint forming (a) and basic geometry (b).

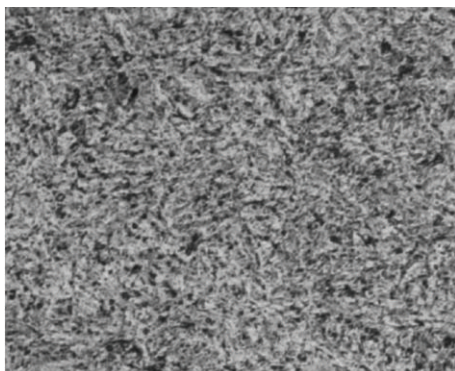


FIGURE 3: Rivet material microstructure ( $\times 500$ ).

for clinching process requires detailed knowledge on the material strain hardening characteristics. This issue was comprehensively presented by Coppieters et al. [21].

This paper focuses on effect of material type change on internal joint structure forming. Examined sheet plate arrangements are presented in Table 3.

CR joints were performed for all material variants from A to F and CL joints for variants A, C, and F.

**3.4. Shear Tests and Microhardness.** The shearing tests were performed on a universal tensile testing machine equipped with extensometer system and the sensor head for force measurements. The results were recorded by recording the joint shearing curve course in the static tension test of an overlap joint at 10 mm/min.

Sometimes the internal sheet metal defects cause the higher or lower joint strength. Higher differences of maximum joint shearing force were recorded in some cases during the experiment. Two most distinctive results were rejected, and subsequently the average value of 5 tests was calculated. To achieve the same test amount for each joining combination, the average of five results was accounted for.

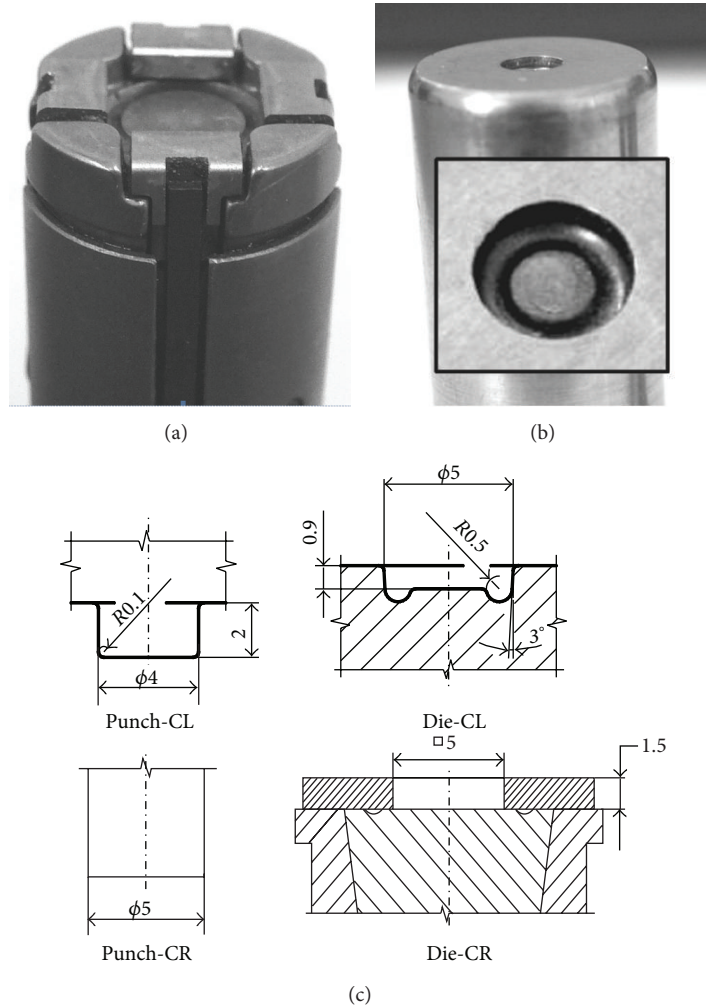


FIGURE 4: Dies for joint forming: (a) CR, (b) CL, and (c) geometry tools.

TABLE 2: Chemical composition (in (%) of wt) of materials.

Materials	C	Mn	Si	P	S	Al	Cu	Ni	Cr	Ti	V	Nb	Mo	Co	Fe	Mg
RA-K 40/70	0.204	1.683	0.198	0.018	0.003	1.731	0.028	0.018	0.055	0.009	0.004	0.004	0.008	—	Remainder	—
H220PD	0.012	0.435	0.119	0.057	0.002	0.041	0.040	0.013	0.046	0.033	0.012	0.052	0.009	0.047	Remainder	—
DC06	0.020	0.071	0.010	0.017	0.002	0.055	0.038	0.011	0.022	0.062	0.008	0.023	0.009	0.035	Remainder	—
DX51D + Z	0.064	0.178	0.007	0.016	0.002	0.120	0.041	0.002	0.023	0.002	0.005	0.015	0.004	0.019	Remainder	—
5754 H111	—	0.50	0.40	—	—	Remainder	0.10	—	0.30	0.15	—	—	—	—	0.40	3.0

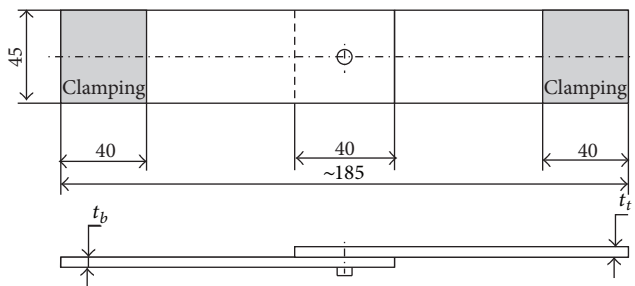


FIGURE 5: Overlap joint for shearing strength tests.

The quality evaluation of clinching joints included metallographic and microhardness analyses. The 1N load was applied in measurements for about 15 s. The measurements were performed for specified locations on the joint cross-section (Figures 6(a) and 6(b)). Then the microsections were repolished and other measurements were performed. Three measurements were performed in each location. For tested materials, the starting material's microhardness was measured.

In order to compare the rivet and sheet material strain hardening change, the microhardness measurement

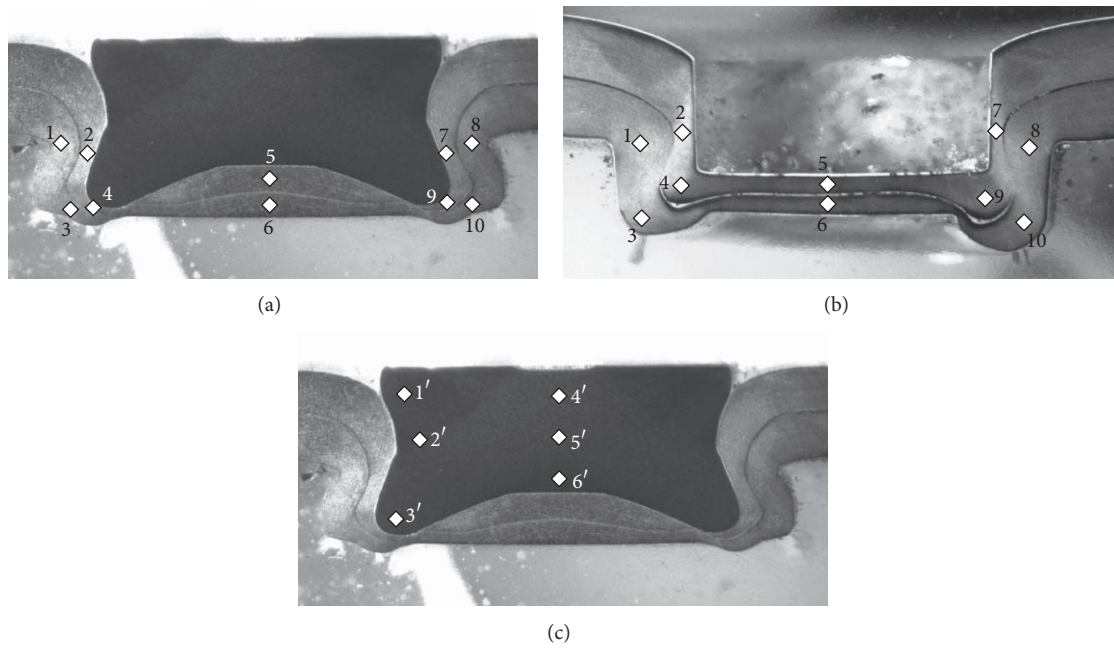


FIGURE 6: Microhardness measurement locations in joined sheet metals for (a) CR, (b) CL, and (c) rivet—CR.

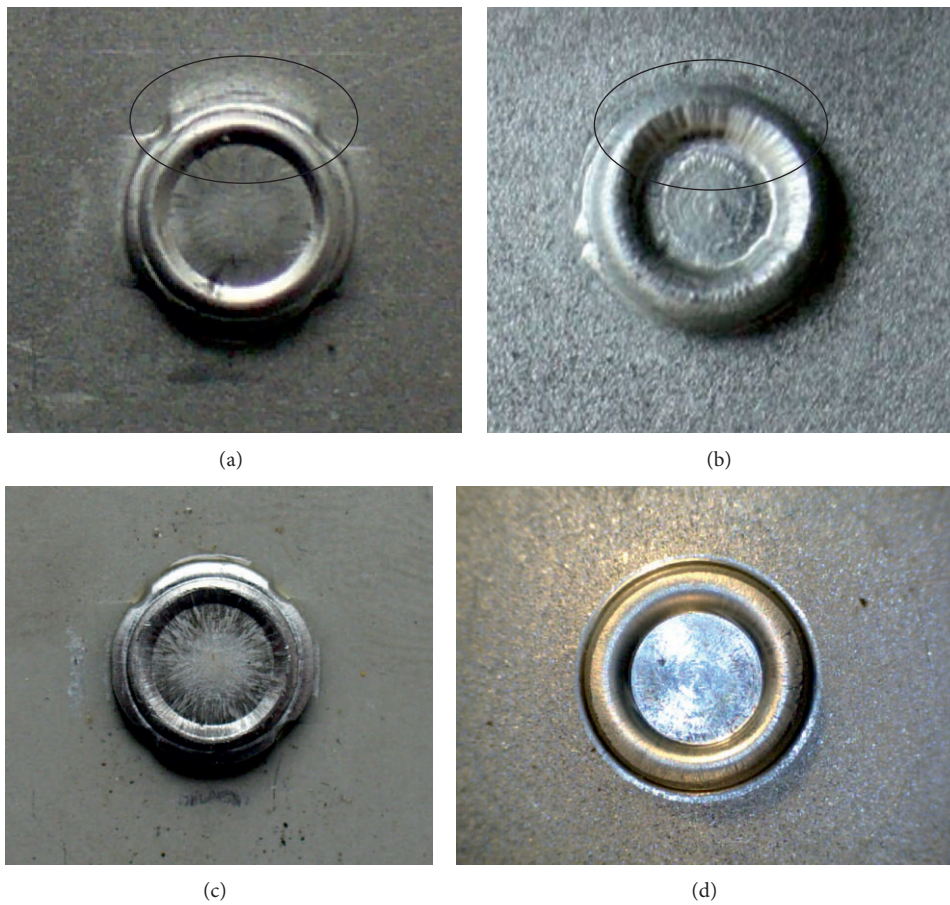


FIGURE 7: The bulge of a joint formed in CR process for H220PD material (a) and DC06 (c) and CL process for H220PD material (b) and DC06 (d).

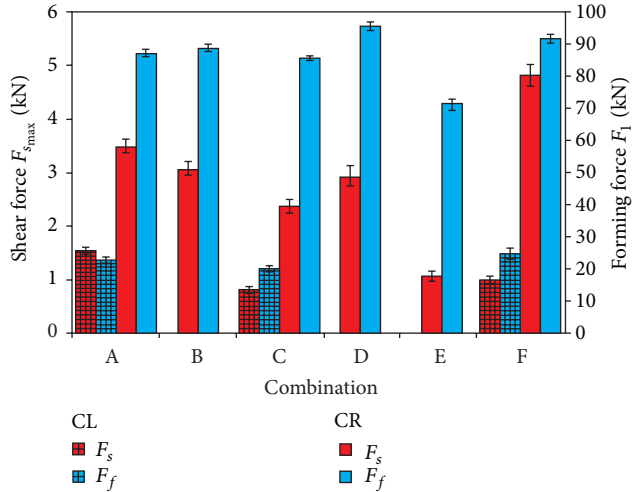


FIGURE 8: The forming force ( $F_f$ ) and maximum joint shearing strength CR ( $F_s$ ) for various materials and their combinations—average values.

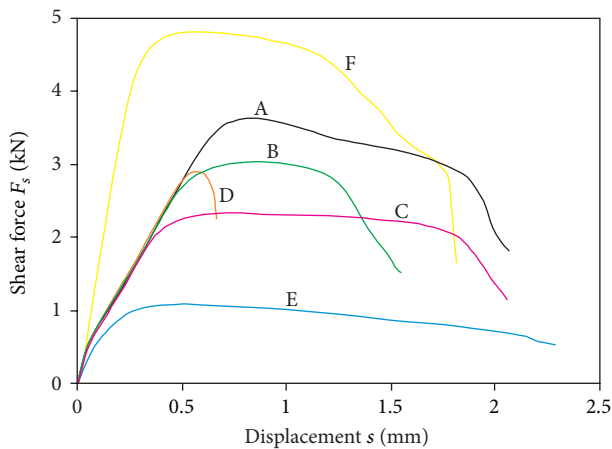


FIGURE 9: The example shearing curves of the ClinchRivet (CR) joint for sheet metal combination.

(Figure 6(c)) of the rivet in the sheet joint made of H220PD was performed.

#### 4. Results and Discussion

The die with movable segments is required for CR joining (Figure 4(a)). Joining without a rivet requires no such a solution and the solid rigid die may be used (Figure 4(b)). Thus, the bulge of various shapes on the die contact side is achieved (Figure 7).

H220PD steel features the highest yield stress among all examined sheet materials. Large radial sheet metal plane transition into the bulge is visible right at the joint base (Figure 7(a)). On the other hand, in CL joint, the huge material breakdown may be observed on the bulge circumference (Figure 7(b)). Visible grooves show the difficult plastic material flow while pressing it into the die impression.

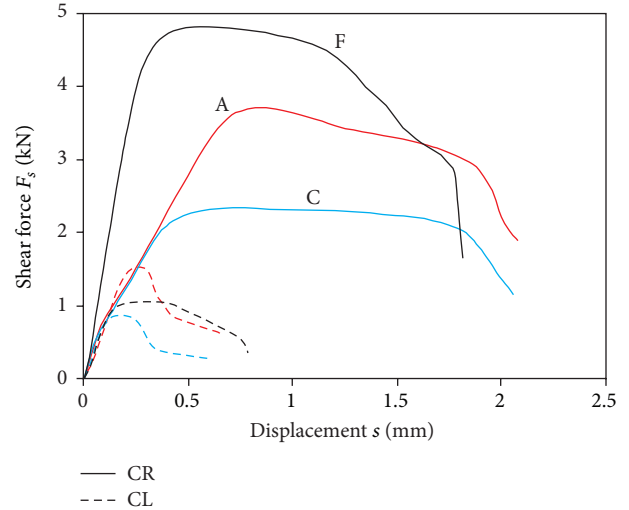


FIGURE 10: Comparison of an example shearing curve for joints made of DX51D (A-red), DC06 (C-blue), and H220PD (F-black).

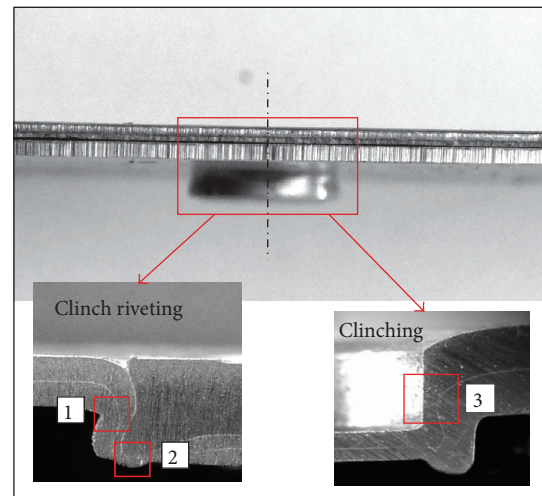


FIGURE 11: The matter of CL and CR joint.

The bulge size in the die groove depends on the material type and tool geometry. This problem was clarified in several papers developed among the others by Mucha [5], Oudjene et al. [11], Jayasekara et al. [18], Lebaal et al. [19], Lee et al. [22], and Coppieters et al. [23]. On the other hand, the ClinchRivet joint forming problem is rarely known.

For a material of lower yield stress and better formability, more correct joint forming is achieved both for CR (Figure 7(c)) and CL (Figure 7(d)).

Forming CR joints using DX51D + Z/RA-K 40/70 required the highest pressing force, whereas the highest joint shearing force was achieved for H220PD/H220PD (Figure 8).

The forming force generated by the riveting machine drive significantly deforms the riveting press frame [24]. High strain of the joining device's frame may lead to asymmetric joint forming.

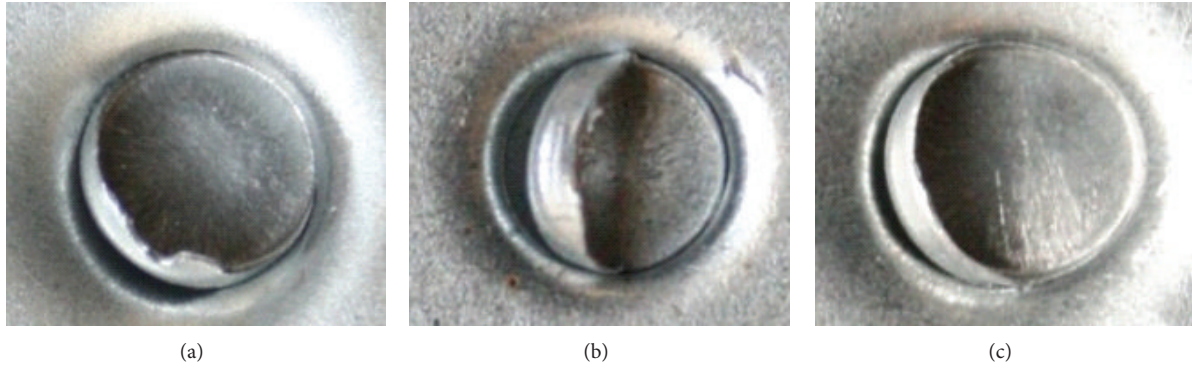


FIGURE 12: Failures of CL joints: (a) samples with H220PD materials, (b) samples with DC06 materials, and (c) samples with DX51D materials.

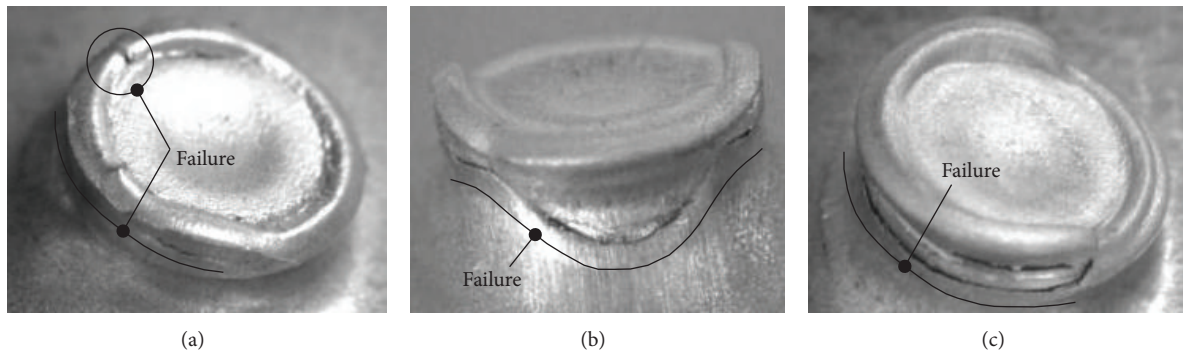


FIGURE 13: Failures of CR joints: (a) samples with H220PD materials, (b) samples with DC06 materials, and (c) samples with DX51D materials (the defect is indicated by the line).

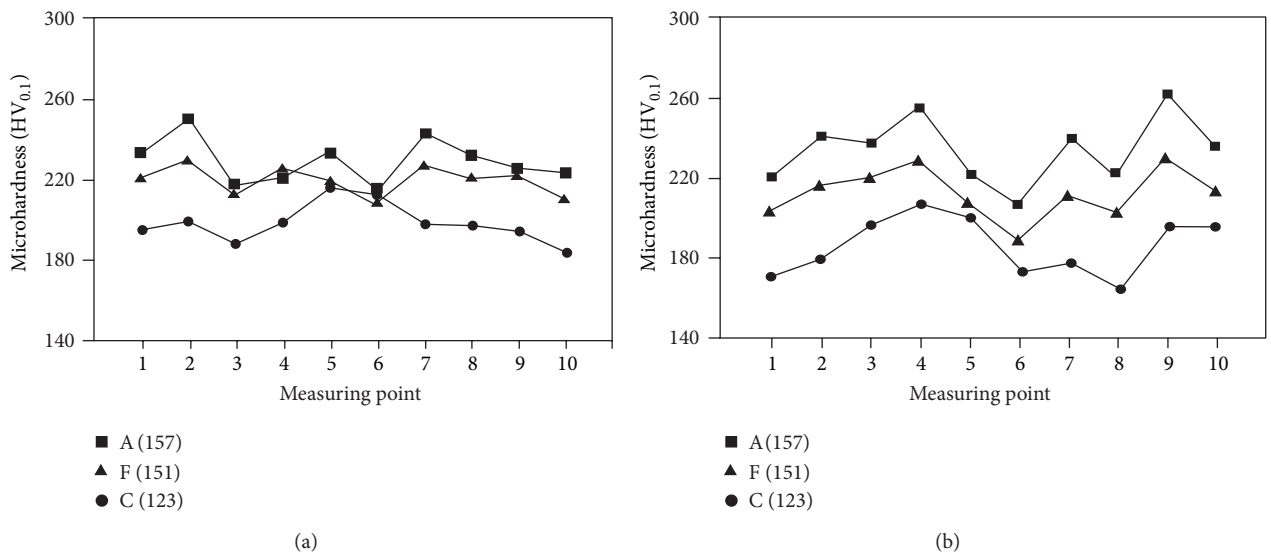


FIGURE 14: The microhardness in cross-section points for joints (a) CL and (b) CR.

TABLE 3: Combination of materials.

$t_t = t_b = 0.8 \text{ mm}$	Combination					
	A	B	C	D	E	F
Sheet						
Top ( $t_t$ )	DX51D + Z	DX51D + Z	DC 06	DX51D + Z	5754 H111	H220PD
Bottom ( $t_b$ )	DX51D + Z	H220PD	DC 06	RA-K 40/70	5754 H111	H220PD

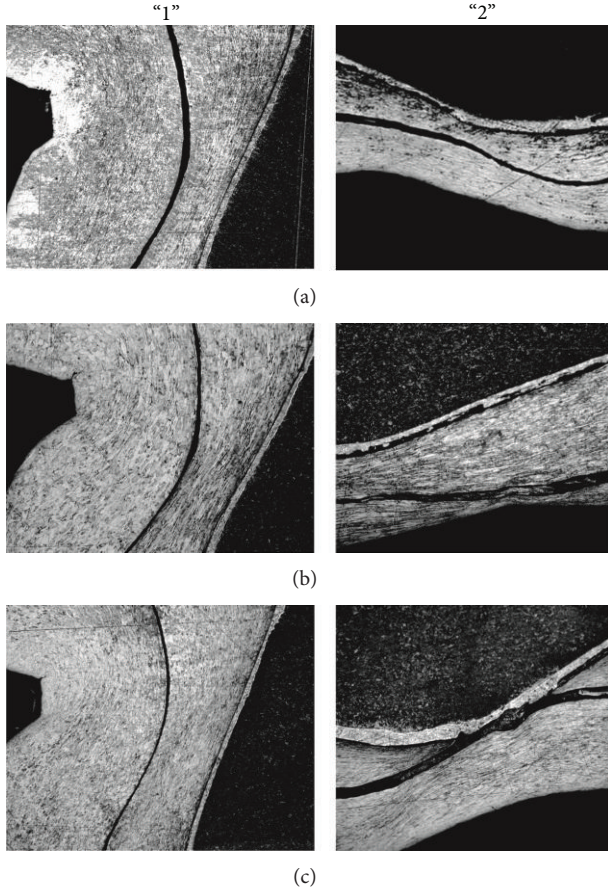


FIGURE 15: The metallographic images of joint area: (a) DX51D, (b) DC06, and (c) H220PD.

TABLE 4: The measured neck thickness and undercut value (in mm).

Parameter	Combination					
	A*	B	C*	D	E	F*
Undercut $t_u$	0.16/0.28	0.32	0.13/0.29	0.12	0.35	0.08/0.25
Neck thickness $t_n$	0.07/0.26	0.29	0.10/0.31	0.22	0.17	0.12/0.19

\*CL/CR.

Depending on sheet metal material type, for the same rivet different maximum shearing force and the shearing curve are achieved (Figure 9).

The maximum load-carrying ability of joints prepared with CR technology is several times higher comparing to joints prepared with CL technology (Figure 10) making the joint with rivet (CR) features a better forming, thus resulting in higher strength. Note the very high energy consumption of CR forming process comparing to CL technology without rivet. For sheet metal material layout "A," the forming force was 22 kN, for layout "C"  $F_f = 20$  kN, and for layout "F"  $F_f = 24$  kN.

The typical feature of CR joint is that the overpress is stiffened by the pressed rivet, and for CL joint the inner part is empty (Figure 11). Thus a bit different joint destruction mechanism appears in shearing tests.

While shearing, the CL joint overpress separates by the necking material ductile failure (Figure 11, area "3"). The rest of sheet metal remains in the lower sheet material (Figure 12). This is one of the clinching joint's destruction mechanisms [15].

The destruction mechanism of CR joint overpress is different comparing to CL joint. The separation is due to material ductile failure in area "1" (Figure 11) and due to complete pulling the rivet out of the lower sheet metal. The rivet remains in the upper sheet metal.

The upper sheet metal formed as a bulge by the rivet tears on its circumference (Figure 13). For H220PD, the fracture is visible in the bottom and on the circumference (Figure 13(a)). For remaining analyzed joints (made of DC06 and DX51D), the fracture occurred on the overpress circumference (Figures 13(b) and 13(c)).

Knowing the microhardness change, it is possible to forecast fracture sensitive areas. In the mechanical processes, the stress state, grain size, and material properties determined allowable deformations [25].

The values presented in Figure 14 were achieved by measuring the microhardness in specified locations on the metallographic microsections. The starting microhardness for corresponding sheet materials was indicated in brackets.

Different microhardness values were achieved both for CL and CR joints depending on the material type. The highest values were achieved for DX51D, and the lowest for DC06. This was related to mechanical properties and material's strain hardening curve. Such a microhardness arrangement was observed for both CL and CR joints. For CR joint (Figure 14(b)), the microhardness differences between materials were higher than those for joints produced with CL technology (Figure 14(a)).

For CR joint, the microhardness values in measurement points "4" and "9" are higher than values for CL joint. Similar situation occurs in points "3" and "10." As the segmented die has moving elements, it enables more intensive plastic material flow. While the material flows, the die segments move, and the material hardens more due to a plastic strain in previously mentioned areas of joint.

Whereas in the necking area of the upper sheet material for CR joint (in points "2" and "7") the microhardness increase is lower than that for CL joint. For CR joint, the upper and lower sheets are slightly bent by the plastically flowing material of the joint bottom, while forming with the rigid die results in significant material extension, thus significantly increasing the material hardening and material hardness itself.

An inappropriate material selection for SPR joint may result in joint fracture [26]. The rivet's state of stress, especially in very small ones, is of very high importance [27].

The initial structure of the rivet for CR technology was uniform and free of strain (Figure 3). No defects due to the rivet pressing were observed for each CR joint forming. The overpress bottom's joined material thickness reduction occurred (Figure 15). The necking occurred on the side surface, in a similar way to clinching joints [2]. The largest gap between sheet metals occurred for DX51D (Figure 15(a)), and for remaining cases gaps were smaller (Figures 15(b) and

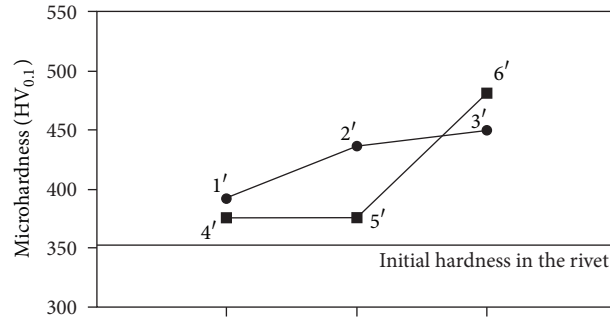


FIGURE 16: The hardness change in specified rivet locations for joint made of H220PD.

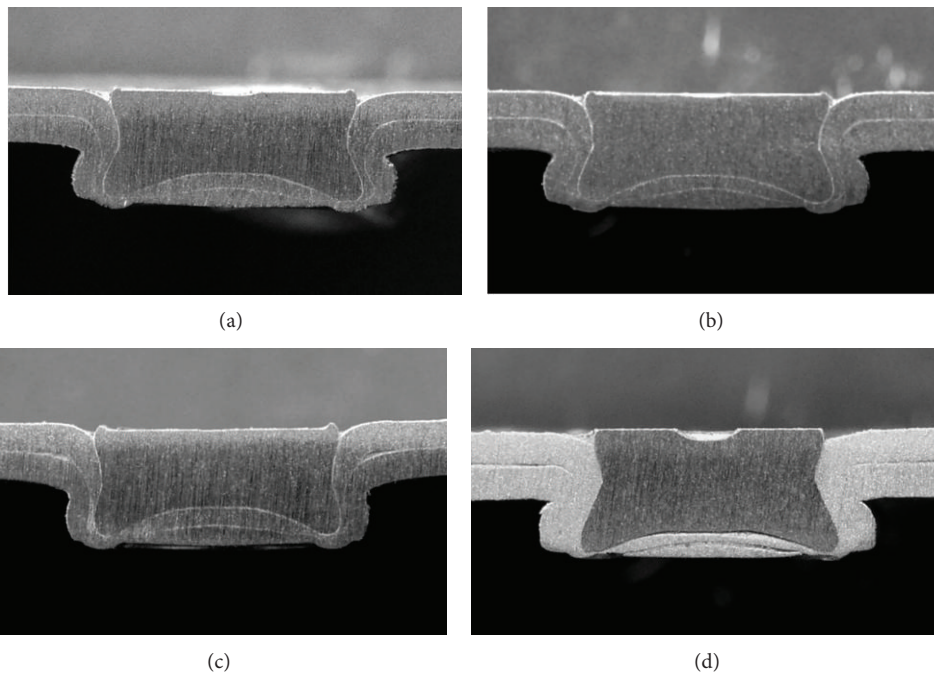


FIGURE 17: CR joint cross-section for material combinations: (a) DX51D/DX51D (A), (b) DX51D/H220PD (B), (c) DX51D/RA-K 40/70, (d) 5754/5754.

15(c)). The cylindrical surface thickness values were similar. The relevant differences were observed in the joint bottom, namely, at the deformed rivet edge.

The thicknesses of thinned upper and lower sheet DX51D were identical. Changing the material to DC06 resulted in excessive lower sheet thickness reduction, and the material continuity was maintained. While changing the sheet material to H220PD, the upper sheet metal thickness reduced and then the upper sheet fractured. This was due a different formability limit of joined materials.

For H220PD sheet material, the formability limit was achieved closely to the points. The microhardness values in points “4” and “9” (Figure 14(b)) and the sheet material continuity curve in the joint (Figure 15(c)) show that the formability limit for H220PD was achieved.

One of the highest CR joint forming forces was achieved for H220PD. For this material combination, the upper sheet metal fracture also occurred (Figure 15(c)-2). In this joint, the

highest rivet’s microhardness increase occurred in its lower part locking the sheet material (Figures 6(c) and 16).

The material on the top of the rivet in its axis has no contact with the tool (tapered hole in the rivet). While pressing the rivet, firstly the rivet edges are upset, and then the material starts flowing in the lateral directions to the rivet axis. The microhardness increase was the highest in point “6” of this area.

The material on the rivet edges in the lower rivet part has a limited capability of plastic flow. The rivet edge is pressed into joined sheets. The lower part of the edge is bent outwards while pressing. The microhardness in point “4” of this area is lower than the value in point “6”.

Around the external rivet’s surface (points “1,” “2,” and “3”), the microhardness increase is not as high as an axial one, as a result of the initial shape. Around the external side and edge the rivet has to strain in extent that enables forming the lock without rivet fracture.

Depending on joined material arrangement, different lock forming occurs and the rivet deforms in different way (Figure 17). The lowest material lock was achieved for DX51D/RA-K 40/70 material arrangement (Figure 17(c) and Table 4). Changing the lower sheet from DX51D + Z to RA-K 40/70 (variants A and D) decreased  $t_u$  by 57% and  $t_n$  by 15% (Table 4). The rivet did not strain enough to deform the sheet metals. The rivet edges were upset, thus resulting in sheet metal thickness reduction in the lower part of the joint. The largest interlocking was achieved for material 5754, but both sheets material were thinned (Figure 17(d)). For sheets made of alloy 5754 parameter  $t_u$  increased by 25%, and  $t_n$  decreased by 34% comparing to joint made of DX51D + Z. For alloy 5754, the forming force was high, and the maximum load-carrying ability while shearing was quite low (Figure 8).

While comparing CL with CR for H220PD (both sheets), significant increase in  $t_u$  parameter by 212% and  $t_n$  parameter by 58% was observed (Table 4). For sheet metal arrangement according to variants "A" and "C", the increased material locking was also observed. The highest improvement was achieved for variant "F".

All the materials studied could be joined by clinching. With a few exceptions, this result was not expected at the outset of the study. The maximum shearing load depends heavily on the type of clinching method used (CL or CR) and varies significantly. For some material type arrangements, joining with rivet (CR) resulted in joint material separation.

## 5. Conclusions

The experimental CR joint forming analysis allowed researching the forming force depending on the sheet material type.

Depending on the joined material type, the rivet formed the joint, for which the maximum shearing force of joint overlapping was achieved.

For tested materials, the highest force was achieved for DX51D + Z/RA-K 40/70, and the lowest one was achieved for alloy 5754. For 5754, the highest difference between the forming force and the maximum shearing force was achieved. The high force value is due to a rivet material strain demand.

Applying the rivet for joint forming increases the lock size in sheet material ( $t_u$ ) for DX51D + Z by 75% comparing to CL joint. However, forming the joint in this combination requires increasing the forming force by 290%.

Changing the joining method from CL to CR for material DC 06 increased the  $t_u$  value by 123%. The force increased for this sheet material layout was 280%.

The best effect of lock increase in the joint was achieved while changing the joining method for H220PD material. The  $t_u$  parameter increased by 150%. Increasing the lock size in this case of CR joint forming requires increasing the forming force by 283% compared to CL joint.

Clinching joints of 5 mm diameter feature much lower maximum joint strength compared to joint with an additional rivet. For DX51D + Z and DC06, the maximum joint shearing force increase was 150%. While for H220PD, the maximum joint shearing force increase was 316%.

CR joint forming pushes the unsafe material thinning area to the joint bottom. In CL joints, the necking locates in the center of the overpress height.

While joining different sheet metals, the critical thinning may occur, thus resulting in material layer fracture. The material discontinuities lower such a joint tightness. This may result in faster inner corrosion due to external factors.

Using the rivet in joint also changes the separation method. While shearing the CL joint, some part of the upper sheet metal remains in the lower sheet material. While shearing the CR joint, whole upper sheet metal remains on the rivet. The separation itself occurs by separating the sheet metals.

## Acknowledgment

The paper was elaborated within the project "Application of progressive tool coatings for increasing the effectiveness and productivity of forming sheets made of modern materials" (APVV-0682-11).

## References

- [1] L. M. Alves, E. J. Dias, and P. A. F. Martins, "Joining sheet panels to thin-walled tubular profiles by tube end forming," *Journal of Cleaner Production*, vol. 19, no. 6-7, pp. 712-719, 2011.
- [2] J. Mucha, L. Kaščák, and E. Spišák, "Joining the car-body sheets using clinching process with various thickness and mechanical property arrangements," *Archives of Civil and Mechanical Engineering*, vol. 11, no. 1, pp. 135-148, 2011.
- [3] B. Bartczak, D. Gierczycka-Zbrożek, Z. Gronostajski, S. Polak, and A. Tobota, "The use of thin-walled sections for energy absorbing components: a review," *Archives of Civil and Mechanical Engineering*, vol. 10, no. 4, pp. 5-19, 2010.
- [4] Z. Gronostajski and S. Polak, "Quasi-static and dynamic deformation of double-hat thin-walled elements of vehicle controlled body crushing zones joined by clinching," *Archives of Civil and Mechanical Engineering*, vol. 8, no. 2, pp. 57-65, 2008.
- [5] J. Mucha, "The analysis of lock forming mechanism in the clinching joint," *Materials and Design*, vol. 32, no. 10, pp. 4943-4954, 2011.
- [6] L. Kaščák, E. Spišák, and J. Mucha, "Evaluation of properties of joints made by clinching and self-piercing riveting methods," *Acta Metallurgica Slovaca*, vol. 18, no. 4, pp. 172-180, 2012.
- [7] R. Davies, R. Pedreschi, and B. P. Sinha, "The shear behaviour of press-joining in cold-formed steel structures," *Thin-Walled Structures*, vol. 25, no. 3, pp. 153-170, 1996.
- [8] R. F. Pedreschi, B. P. Sinha, and R. Davies, "Advanced connection techniques for cold-formed steel structures," *Journal of Structural Engineering*, vol. 123, no. 2, pp. 138-144, 1997.
- [9] R. F. Pedreschi and B. P. Sinha, "An experimental study of cold formed steel trusses using mechanical clinching," *Construction and Building Materials*, vol. 22, no. 5, pp. 921-931, 2008.
- [10] J. Mucha and W. Witkowski, "The experimental analysis of the double joint type change effect on the joint destruction process in uniaxial shearing test," *Thin-Walled Structures*, vol. 66, pp. 39-49, 2013.
- [11] M. Oudjene, L. Ben-Ayed, A. Delamézière, and J.-L. Batoz, "Shape optimization of clinching tools using the response surface methodology with Moving least-square approximation,"

- Journal of Materials Processing Technology*, vol. 209, no. 1, pp. 289–296, 2009.
- [12] S. Coppieters, P. Lava, S. Baes, H. Sol, P. Van Houtte, and D. Debruyne, “Analytical method to predict the pull-out strength of clinched connections,” *Thin-Walled Structures*, vol. 52, pp. 42–52, 2012.
- [13] E. Roux and P. O. Bouchard, “Kriging metamodel global optimization of clinching joining processes accounting for ductile damage,” *Journal of Materials Processing Technology*, vol. 213, no. 7, pp. 1038–1047, 2013.
- [14] F. Lambiase, “Influence of process parameters in mechanical clinching with extensible dies,” *The International Journal of Advanced Manufacturing Technology*, vol. 66, no. 9–12, pp. 2123–2131, 2013.
- [15] F. Lambiase and A. Di Ilio, “Finite element analysis of material flow in mechanical clinching with extensible dies,” *Journal of Materials Engineering and Performance*, vol. 22, no. 6, pp. 1629–1636, 2013.
- [16] S. Gao and L. Budde, “Mechanism of mechanical press joining,” *International Journal of Machine Tools and Manufacture*, vol. 34, no. 5, pp. 641–657, 1994.
- [17] <http://www.tox-de.com/>.
- [18] V. Jayasekara, K. H. Min, J. H. Noh et al., “Rigid-plastic and elastic-plastic finite element analysis on the clinching joint process of thin metal sheets,” *Metals and Materials International*, vol. 16, no. 2, pp. 339–347, 2010.
- [19] N. Lebaal, M. Oudjene, and S. Roth, “The optimal design of sheet metal forming processes: application to the clinching of thin sheets,” *International Journal of Computer Applications in Technology*, vol. 43, no. 2, pp. 110–116, 2012.
- [20] A. A. de Paula, M. T. P. Aguilar, A. E. M. Pertence, and P. R. Cetlin, “Finite element simulations of the clinch joining of metallic sheets,” *Journal of Materials Processing Technology*, vol. 182, no. 1–3, pp. 352–357, 2007.
- [21] S. Coppieters, P. Lava, H. Sol, A. van Bael, P. van Houtte, and D. Debruyne, “Determination of the flow stress and contact friction of sheet metal in a multi-layered upsetting test,” *Journal of Materials Processing Technology*, vol. 210, no. 10, pp. 1290–1296, 2010.
- [22] C.-J. Lee, J.-Y. Kim, S.-K. Lee, D.-C. Ko, and B.-M. Kim, “Design of mechanical clinching tools for joining of aluminium alloy sheets,” *Materials and Design*, vol. 31, no. 4, pp. 1854–1861, 2010.
- [23] S. Coppieters, S. Cooreman, P. Lava, H. Sol, P. van Houtte, and D. Debruyne, “Reproducing the experimental pull-out and shear strength of clinched sheet metal connections using FEA,” *International Journal of Material Forming*, vol. 4, no. 4, pp. 429–440, 2011.
- [24] T. Markowski, J. Mucha, and W. Witkowski, “FEM analysis of clinching joint machine’s c-frame rigidity,” *Maintenance and Reliability*, vol. 15, no. 1, pp. 51–57, 2013.
- [25] F. Stachowicz, “Effects of microstructure on the mechanical properties and limit strains in uniaxial and biaxial stretching,” *Journal of Mechanical Working Technology*, vol. 19, no. 3, pp. 305–317, 1989.
- [26] N. H. Hoang, O. S. Hopperstad, M. Langseth, and I. Westermann, “Failure of aluminium self-piercing rivets: an experimental and numerical study,” *Materials and Design*, vol. 49, pp. 323–335, 2013.
- [27] W. Presz and R. Cacko, “Analysis of the influence of a rivet yield stress distribution on the micro-SPR joint—initial approach,” *Archives of Civil and Mechanical Engineering*, vol. 10, no. 4, pp. 69–75, 2010.

## Research Article

# Effect of Detail Design on Fatigue Performance of Aircraft Door Frame

Kang Jianxiong, Gao Hangshan, Wang Fusheng, and Yue Zhufeng

Department of Engineering Mechanics, Northwestern Polytechnical University, Xi'an 710129, China

Correspondence should be addressed to Kang Jianxiong; pihoul210@163.com

Received 28 June 2013; Revised 26 October 2013; Accepted 27 October 2013

Academic Editor: Gang Wang

Copyright © 2013 Kang Jianxiong et al. This is an open access article distributed under the Creative Commons Attribution License, which permits unrestricted use, distribution, and reproduction in any medium, provided the original work is properly cited.

The fatigue tests were carried out on door frame containing single-side design and double-side design to assess the effect of different designs on fatigue life. By contrast, the finite element method (FEM) was also used to analyze the stress distribution of the two frames. At last, the fracture morphologies of the specimens after fatigue test were examined by scanning electron microscopy. The results revealed that the double-side design could elevate about 18~21 times of fatigue life. The direction of crack propagation is transverse in single-side frame, while it is longitudinal in double-side frame.

## 1. Introduction

The door is an important part of the airplane, and the reliability of opening the door has a great effect on flight safety. The inadvertent opening could lead to terrible consequence during flight. The inadvertent opening probability is  $10^{-9}$  per flying hour, which is provided in civil airworthy literatures [1, 2].

The design of aircraft door has been studied by a number of researchers, using mainly two methods. In the first method, the reliability analysis model was applied into the door designing, based on the principle of structure reliability, containing structural motion function [3, 4], motion accuracy [5], and abrasion [6, 7], and so forth. In the second method, a mechanism considering the value and dispersion of wear volume of sealing belts was set up for the door design [8].

Another way to make the door more reliable is to improve its fatigue performance. The fatigue lives of key components are mainly determined by the geometrical design details. In the structural design of commercial aircraft, the sketches of doors and door frames are important.

However, these studies on structural design were all based on experiments, which are very expensive. Hence, the finite element method (FEM) was employed to analyze the distribution of stress and strain of doorframes' sketch with different metrics.

In this paper, a series of fatigue tests were conducted on Aluminum alloy 2024 door frames with two different designs to investigate their fatigue behaviors. The stress distributions of the door frames with different designs were shown by referring to the finite element results, and the Mises stresses were also compared. Then the basic test data were processed based on the principle of statistics. Finally, the optical microscope was used to analyze the fracture surface of the specimen.

## 2. Material Property

The material used in this study was Aluminum alloy 2024, with chemical composition, 92.49% Al, 4.77% Cu, 1.52% Mg, 0.59% Mn, 0.18% Si, 0.3% Fe, and 0.03% Ti. The stress-strain curve of the aluminum alloy 2024 was plotted in Figure 1, generating Young's modulus  $E = 73$  GPa and yield stress  $y = 322$  MPa, respectively. Poisson's ratio was measured to be  $\nu = 0.33$ . According to [9], fatigue strength coefficient  $\sigma'_f = 103$  MPa, fatigue ductility factor  $\epsilon'_f = 0.22$ , and fatigue strength index  $b = -0.124$ , fatigue ductility index  $c = -0.59$ .

## 3. Tests

*3.1. Dimensions of Specimen.* The geometry and the final dimensions of specimens were shown in Figure 2.

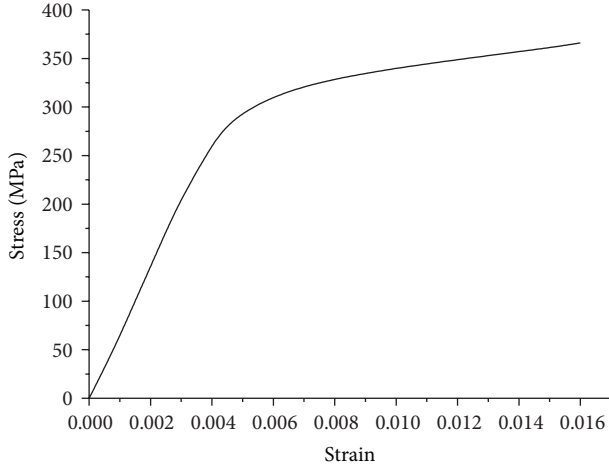


FIGURE 1: Stress-strain curve of Aluminum alloy 2024.

The two-type specimens had the same top views, but the double-side one had one more symmetrical side.

**3.2. Fixture and Load.** The experiment setup was shown in Figure 3(a). The specimen was fixed by two bolted plates, and the uniform load was applied on the surface of the specimen by gusset. The coordinate system in Figure 3(a) was used in this paper.

**3.3. Fatigue Test.** Two specimens were statically tested with single-side and double-side design, respectively. Twelve specimens were fatigue tested and divided into two groups named S and D according to different designs. Each group has 6 specimens. At room temperature, all the specimens were tested on a servohydraulic fatigue testing machine (Instron 8802, as shown in Figure 3(b)). The stress ratio  $R$  ( $\sigma_{\min}/\sigma_{\max}$ ) was 0.06 and the frequency was 5 Hz.

## 4. Finite Element (FE) Model

**4.1. Description of the FE Model.** In this study, 3D FE models were developed. The ABAQUS/standard finite element package was used to carry out the analysis [10]. In the ABAQUS element library, ABAQUS linear hexahedron reduced integration elements; C3D8R (three-dimensional eight noded continuum elements) was used to mesh the model. Both of the two models contain three parts, the specimen, the clamping fixture, and the bolts (as shown in Figure 4).

The type of attachment used on the surface of clamping fixture was “TIE,” and it was also used among specimen, clamping fixture, and bolt. The normal contact between specimen and clamping fixture was defined as “Hard contact.” The coefficient of coulomb friction in tangential direction is 0.2.

**4.2. Constraint and Load.** According to the test, the lower surface of the clamping fixture was fully constrained, while the side and upper surfaces are free. The uniform load applied

TABLE 1: Failure load of static test.

Type of specimen	Failure load (KN)
Single-side	69.57
Double-side	90.24

TABLE 2: Basic data of single-side specimen.

Specimen number	Experiment condition	Fatigue life (cycles)
S-1	$F_{\max} = 15 \text{ KN}, R = 0.1$	7217
S-2	$F_{\max} = 6 \text{ KN}, R = 0.1$	170912
S-3	$F_{\max} = 10 \text{ KN}, R = 0.1$	19726
S-4	$F_{\max} = 10 \text{ KN}, R = 0.1$	30738
S-5	$F_{\max} = 10 \text{ KN}, R = 0.1$	34257
S-6	$F_{\max} = 10 \text{ KN}, R = 0.1$	36944

TABLE 3: Basic data of double-side specimen.

Specimen number	Experiment condition	Fatigue life (cycles)
D-1	$F_{\max} = 45 \text{ KN}, R = 0.1$	4499
D-2	$F_{\max} = 30 \text{ KN}, R = 0.1$	8726
D-3	$F_{\max} = 6 \text{ KN}, R = 0.1$	1046763
D-4	$F_{\max} = 10 \text{ KN}, R = 0.1$	584134
D-5	$F_{\max} = 10 \text{ KN}, R = 0.1$	743559
D-6	$F_{\max} = 10 \text{ KN}, R = 0.1$	469031

on the surface of the specimen is 1 MPa. The conditions of constrain and load are shown in Figure 5.

## 5. Result and Discussion

**5.1. FEM Results.** The FEM results are shown in Figures 6 and 7. Figure 6 shows that the stress concentration of the double-side specimen occurred in the bevel of specimen under the first hole and the second hole, with the Mises stress of 178.5 MPa and 162.2 MPa, respectively. Figure 7 shows that stress concentration of the double-side specimen occurred in the bevel under the second hole and the third hole, with the Mises stress of 232.6 and 213.2 MPa, respectively. For the single-side specimen, the maximum Mises stress around the hole occurred in the left side of the third hole, with the Mises stress of 85.2 MPa and the normal stress  $\sigma_{33} = 85.0 \text{ MPa}$ . For the stress of hole edge of double-side specimen, the maximum Mises stress occurred in the left side of the first hole, with the Mises stress of 80.8 MPa and the normal stress  $\sigma_{33} = 79.6 \text{ MPa}$ . It is shown that the door frame using double-side design can reduce the stress concentration around the bevel of specimen effectively. For the stress around the hole edge, the stress concentration was reduced obviously with the design of double side.

**5.2. Text Result.** Only one specimen was provided for each type for static test, and the failure loads were shown in Table 1.

**5.2.1. Fatigue Result.** The number of each group of specimen for fatigue test is 6, and the basic data of each group were shown in Tables 2 and 3.

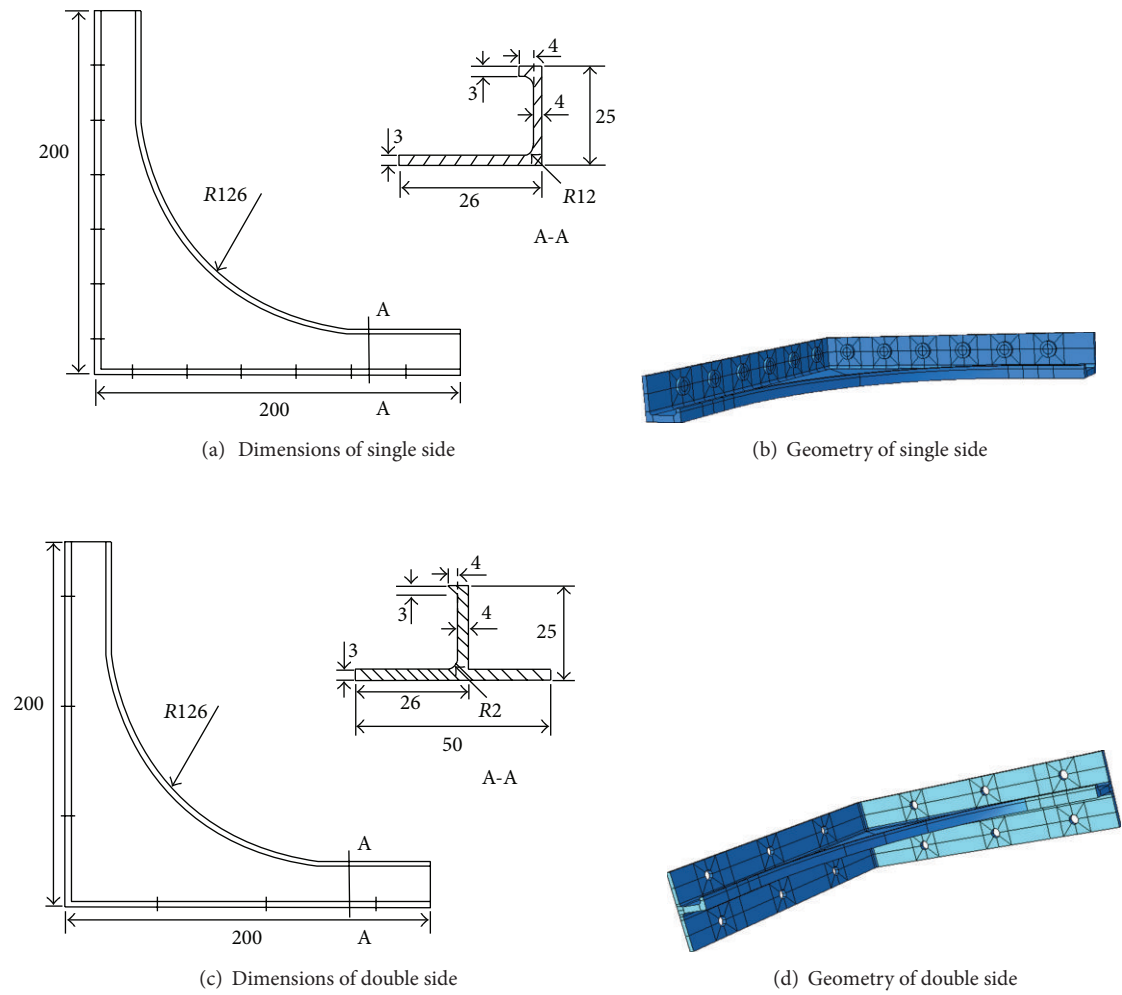


FIGURE 2: Geometries of the door frames with different designs.

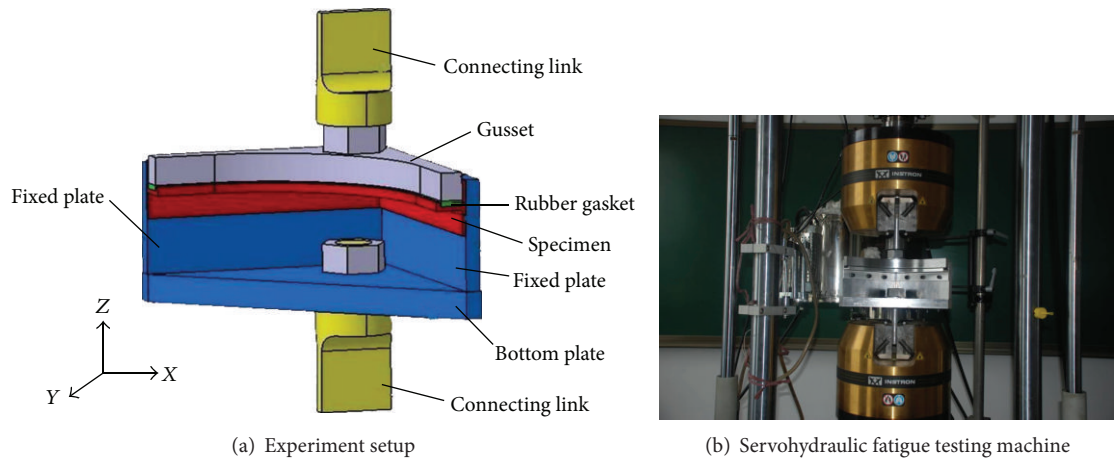


FIGURE 3: Experiment setup and testing machine.

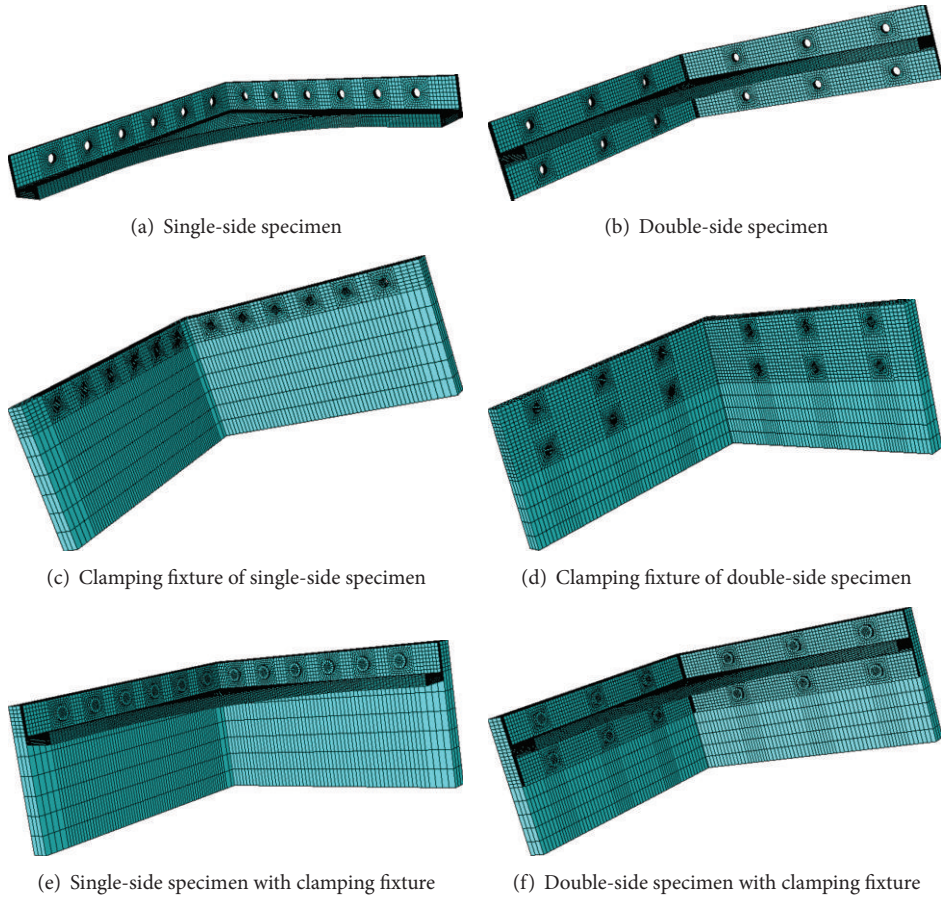


FIGURE 4: FE models of door frames.

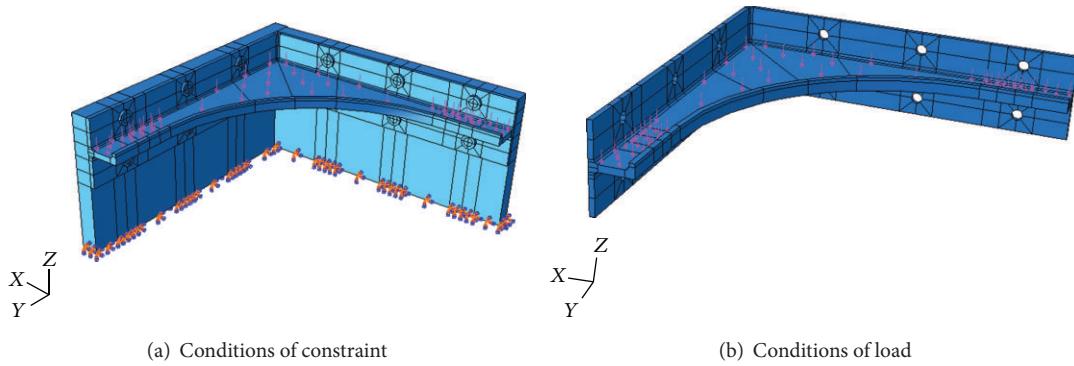


FIGURE 5: Conditions of constraint and load.

5.2.2. *Fatigue Contrast Analysis.* Calculation of the basic data and the analysis result of the fatigue lives in the same stress level (10 kN) were shown in Table 4 and Figure 8.

Table 4 and Figure 8 showed that the average life of double-side specimens is increased by 20 times.

TABLE 4: Analysis result of fatigue lives.

	Average life (cycles)	Standard deviation	Coefficient of variation
Single-side specimen	30416.25	7566.32559	0.24876
Double-side specimen	598908	137859.01858	0.23018

TABLE 5: Logarithm fatigue lives.

Single-side specimen			Double-side specimen		
Specimen number	$x_{1i} = \log N_{1i}$	$x_{1i}^2$	Specimen number	$x_{2i} = \log N_{2i}$	$x_{2i}^2$
S-3	4.295039	18.44736	D-4	5.766512	33.25266
S-4	4.487676	20.13924	D-5	5.871315	34.47233
S-5	4.534749	20.56395	D-6	5.671202	32.16253
S-6	4.567544	20.86246			
$\Sigma$	17.885008	80.01301	$\Sigma$	17.309029	99.88752

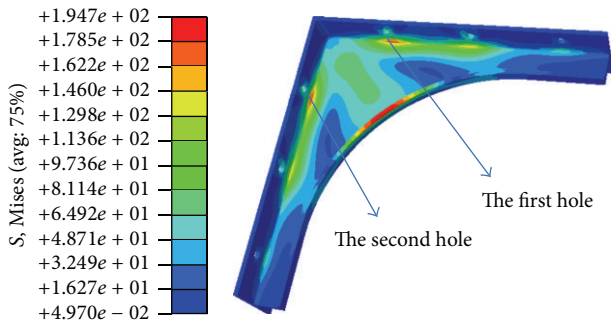


FIGURE 6: FEM results of double-side specimen.

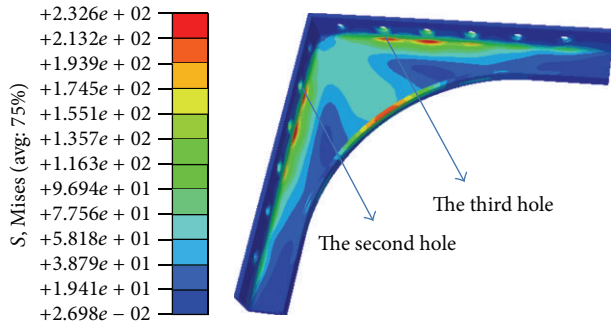


FIGURE 7: FEM results of single-side specimen.

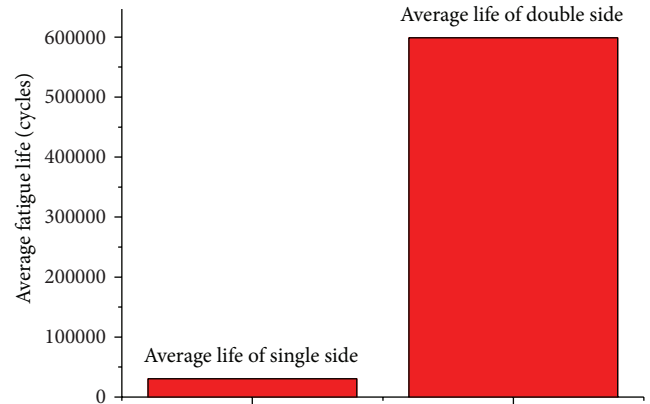


FIGURE 8: Analysis result of fatigue lives.

For double-side specimen,

$$\begin{aligned} \bar{x}_2 &= \frac{1}{n_2} \sum_{i=1}^{n_2} x_{2i} = \frac{1}{3} \times 17.309029 = 5.769676, \\ s_2^2 &= \frac{1}{n_2 - 1} \sum_{i=1}^{n_2} (x_{2i} - \bar{x}_2)^2 = \frac{1}{n_2 - 1} (\sum x_{2i}^2 - n\bar{x}_2^2) \\ &= \frac{99.88752 - 3 \times 5.769676^2}{3 - 1} = 0.010018. \end{aligned} \tag{2}$$

### 5.2.3. Fatigue Numerical Analysis

(a) *Logarithm Fatigue Life.* All the fatigue lives in the same stress level were shown in Table 5.

(b) *The Mean Value  $\bar{x}$  & Variance  $s^2$*

For single-side specimen,

$$\begin{aligned} s_1^2 &= \frac{1}{n_1 - 1} \sum_{i=1}^{n_1} (x_{1i} - \bar{x}_1)^2 = \frac{1}{n_1 - 1} (\sum x_{1i}^2 - n\bar{x}_1^2) \\ &= \frac{80.01301 - 4 \times 4.471252^2}{4 - 1} = 0.014877. \end{aligned} \tag{1}$$

(c) *F Check.* The  $F$  check should be done before the  $t$  check. The value of  $F$  can be obtained by using  $s_1^2$  and  $s_2^2$  as follows [11]:

$$F = \frac{0.014877}{0.010018} = 1.485027. \tag{3}$$

The degree of freedom of molecule is  $4 - 1 = 3$  and the degree of freedom of denominator is  $3 - 1 = 2$ . Take  $\alpha = 5\%$ ; then  $F_\alpha = 16$  [11]. As  $F < F_\alpha$ , it can be known that the standard deviation is equality.

(d) *t* Check. Calculation the value of *t* is by reference [11] as follows:

$$\begin{aligned}
 t &= (\bar{x}_1 - \bar{x}_2) \times \left( \sqrt{\frac{(n_1 - 1)s_1^2 + (n_2 - 1)s_2^2}{n_1 + n_2 - 2}} \sqrt{\frac{1}{n_1} + \frac{1}{n_2}} \right)^{-1} \\
 &= (4.471252 - 5.769676) \\
 &\quad \times \left( \sqrt{\frac{(4 - 1) \times 0.014877 + (3 - 1) \times 0.010018}{4 + 3 - 2}} \sqrt{\frac{1}{4} + \frac{1}{3}} \right)^{-1} \\
 &= -2.587.
 \end{aligned} \tag{4}$$

The degree of freedom is  $\nu = n_1 + n_2 - 2 = 4 + 3 - 2 = 5$ ; take  $\alpha = 5\%$ ,  $t_\alpha = 2.571$  [11]. As  $|t| > t_\alpha$ , the conclusion can be that the contrast of fatigue life of the two different specimen is obvious, and, as  $\bar{x}_2 > \bar{x}_1$ , the double-side specimen has a much higher fatigue life.

(e) *Interval Estimation*. Take  $\gamma = 95\%$ ; then  $t_\gamma = 2.571$  by reference [11]. As  $\bar{x}_2 > \bar{x}_1$ , the equation of interval estimation can be written as follow:

$$\begin{aligned}
 (\bar{x}_2 - \bar{x}_1) - t_\gamma s_{12} \sqrt{\frac{1}{n_1} + \frac{1}{n_2}} \\
 < \mu_2 - \mu_1 < (\bar{x}_2 - \bar{x}_1) + t_\gamma s_{12} \sqrt{\frac{1}{n_1} + \frac{1}{n_2}}.
 \end{aligned} \tag{5}$$

The upper limit and lower limit of confidence is

$$\begin{aligned}
 (\bar{x}_2 - \bar{x}_1) + t_\gamma s_{12} \sqrt{\frac{1}{n_1} + \frac{1}{n_2}} &= 1.323796, \\
 (\bar{x}_2 - \bar{x}_1) - t_\gamma s_{12} \sqrt{\frac{1}{n_1} + \frac{1}{n_2}} &= 1.273052.
 \end{aligned} \tag{6}$$

The interval estimation under 95% degree of confidence is

$$1.273052 < \mu_2 - \mu_1 < 1.323796. \tag{7}$$

The equation can be as follow:

$$1.273052 < \lg \frac{[N_{50}]_2}{[N_{50}]_1} < 1.323796. \tag{8}$$

Make each item of the above equation antilogarithm as follows:

$$18.7522 < \frac{[N_{50}]_2}{[N_{50}]_1} < 21.0764. \tag{9}$$

The above equation shows that the fatigue life of double-side frame is 18–21 times that of the single-side frame with 95% degree of confidence.

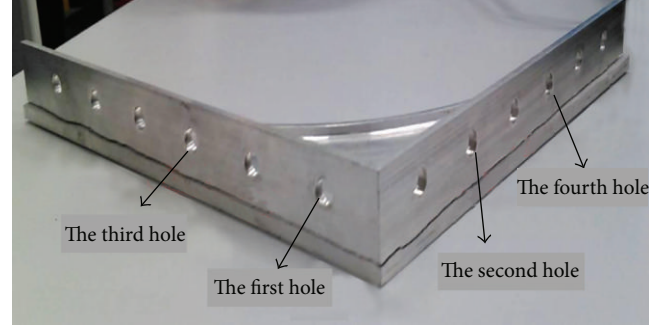


FIGURE 9: Cracks of single-side specimen.

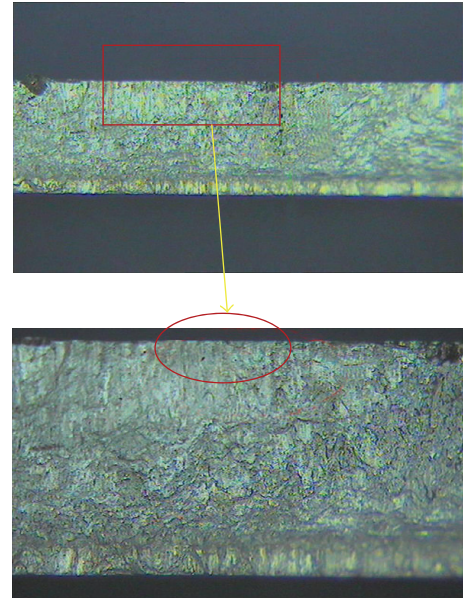


FIGURE 10: Typical fracture surface of single-side specimen.

**5.3. Fracture Analysis.** After the fatigue test, the optical microscope was used to analyze the fracture of the specimen. Cracks of single-side specimen (Figure 9) were found in the lower parts of the second hole and the third hole, which agreed well with the FEM result. Besides, the propagation direction of crack was cross as shown in Figure 10.

Cracks of double-side specimen (Figure 11) were found in the lower parts of the first hole and the second hole, which agreed well with the FEM result. Besides, the propagation direction of crack was lengthwise as shown in Figure 12.

## 6. Conclusions

A series of experiments were conducted on Aluminum alloy 2024 door frame with different designs to investigate their fatigue behaviors. The conclusions can be drawn as follows.

- (1) The static strength of the double-side structure is obviously higher than that of the single-side structure.
- (2) The FEM results show that the door frame in double-side design can reduce the stress concentration

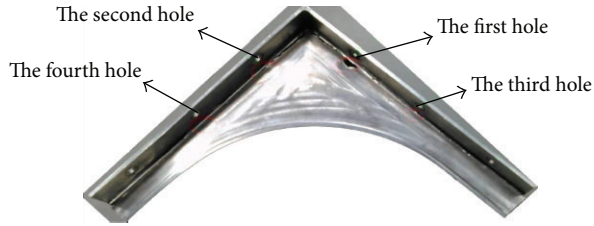


FIGURE 11: Cracks of double-side specimen.

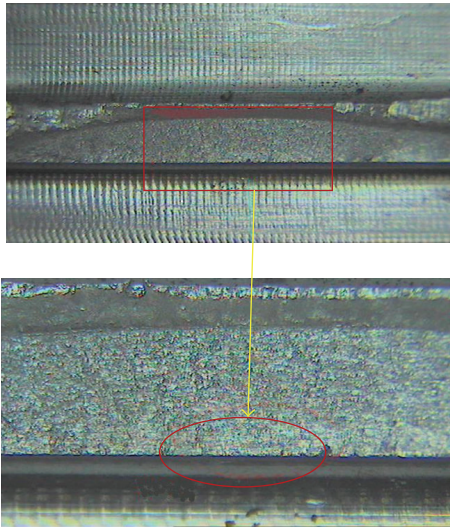


FIGURE 12: Typical fracture surface of double-side specimen.

around the bevel of specimen effectively. The stress concentration around the hole was reduced obviously by adopting the double-side design.

- (3) It is verified by  $F$  check and  $t$  check that the fatigue life of the double-side design is obviously longer than that of the single-side design.
- (4) The interval estimation shows that fatigue life of double-side frame is 18–21 times that of the single-side frame with 95% degree of confidence.
- (5) After the fatigue test, the optical microscope was used to analyze the fracture of the specimen, and the results agreed well with the FEM results. The crack propagation directions were also obtained for the two types of specimens.

## Acknowledgments

This study is supported by the National Natural Science Foundation (no.: 51175424), the 111 Project (no.: B07050), and the Basic Research Foundation of Northwestern Polytechnical University (no.: JC20110257).

## References

- [1] *Guidelines and Methods for Conducting the Safety Assessment Process on Civil Airborne Systems and Equipment*, SAE, 1996.

- [2] CCAR-25-R3, Civil Aviation Administration of China, 2001.
- [3] R. Z. Shmerling and F. N. Catbas, “Load rating and reliability analysis of an aerial guideway structure for condition assessment,” *Journal of Bridge Engineering*, vol. 14, no. 4, pp. 247–256, 2009.
- [4] T. Hu, “Movement reliability of rotation joint of umbrella antenna,” *Chinese Journal of Space Science*, vol. 25, no. 6, pp. 552–5557, 2005.
- [5] J. Zhang, “The composition kinematic reliability of path mechanism,” *Applied Mechanics and Materials*, vol. 34–35, pp. 1070–1075, 2010.
- [6] Z. Guo, Y. Feng, and Y. Feng, “Wear reliability of linkage under periodic loading,” *Journal of Northwestern Polytechnical University*, vol. 24, no. 5, pp. 644–648, 2006.
- [7] B.-M. Hsu and M.-H. Shu, “Reliability assessment and replacement for machine tools under wear deterioration,” *International Journal of Advanced Manufacturing Technology*, vol. 48, no. 1–4, pp. 355–365, 2010.
- [8] J.-G. Zhang, Y.-W. Liu, and D. Su, “Analysis techniques for aircraft mechanism reliability and application,” *Acta Aeronautica et Astronautica Sinica*, vol. 27, no. 5, pp. 827–829, 2006.
- [9] S. Suresh, *Fatigue of Materials*, Cambridge University Press, Cambridge, Mass, USA, 1999.
- [10] *ABAQUS/Standard User's Manual. Version 6.1*, HKS Inc., 2000.
- [11] Y. Shi, W. Xu, and C. Qin, *Mathematical Statistics*, Science Press, Beijing, China, 2009.

## Research Article

# Mathematical and Simulation Modelling of Moisture Diffusion Mechanism during Plastic IC Packages Disassembly

**Peng Mou, Dong Xiang, and Guanghong Duan**

*Department of Mechanical Engineering, Tsinghua University, Beijing 100084, China*

Correspondence should be addressed to Peng Mou; [moupeng@mail.tsinghua.edu.cn](mailto:moupeng@mail.tsinghua.edu.cn)

Received 31 May 2013; Revised 27 September 2013; Accepted 27 September 2013

Academic Editor: Feng Jiang

Copyright © 2013 Peng Mou et al. This is an open access article distributed under the Creative Commons Attribution License, which permits unrestricted use, distribution, and reproduction in any medium, provided the original work is properly cited.

Reuse of plastic IC packages disassembled from printed circuit boards (PCBs) has significant environmental benefits and economic value. The interface delamination caused by moisture diffusion is the main failure mode of IC packages during the disassembling process, which greatly reduces the reusability and reliability of disassembled IC packages. Exploring moisture diffusion mechanism is a prerequisite to optimize prebaking processes before disassembling that is an effective way to avoid the interface delamination. To this end, a computational model with variable boundary conditions is developed based on the different combination state of water in IC packages. The distribution characteristics and mechanism of moisture diffusion behavior are analyzed including the humidity distribution field and the relation among baking temperature, water loss rate, and baking time during baking process, and then the results are validated by FEA simulation based on the improved definition of relative moisture concentration. Baking under variable temperature is proposed and compared with the baking process and baking efficiency under constant temperature to find out the optimized baking parameters. Finally, a set of curves which indicate the relation between baking energy consumption and temperature are determined under actual industrial baking experiments, which could be used as references to develop industrial standards for PCB disassembling process.

## 1. Introduction

Printed circuit board is the typical and fundamental component for almost all electronic products. With the rapid development and updating of electrical and electronic products, the amount of waste PCBs is increasing sharply and has caused severe environmental problems. Recycling and reusing waste PCBs have become a significant challenge in many countries. According to the statistical data, the average designed lifespan of plastic IC packages mounted on PCBs is about 500,000 hours, but their average service life is just around 20,000 hours, only 5% of their designed lifespan. Reuse of these plastic IC packages disassembled from PCBs will bring great environmental benefits and economic value.

Currently, polymer materials have been widely used in microelectronic IC packaging. Since the polymer materials are a kind of high porous material, the IC packaging is susceptible to moisture absorption and the moisture will condense in free volumes or nanopores in polymer materials and along interfaces [1]. The moisture concentration will

reach to saturated state after serving for a long time under ambient environment. The condensed moisture will vaporize and diffuse during the traditional heating disassembling process, which makes the interfacial adhesion strength drops substantially, and delamination may occur at weak interfaces. Figure 1 shows the comparison of delaminated IC packages with normal IC packages by using ultrasound scanned pictures of a type of PQFP package.

When delamination occurs, the cracks caused by the interface delamination provided convenient intrusive channel for humidity and contaminative ions, which may accelerate the IC packages' corrosion rate and reduce its lifespan and reliability. Moisture diffusion has great influence on the reliability of IC packages and is the main reason to induce interface delamination. In order to improve the reliability of IC package, it is necessary to study the mechanism of moisture diffusion induced interface delamination. In the past 10 years, many researches have been made on moisture diffusion mechanism and behavior for packaging reflow process.

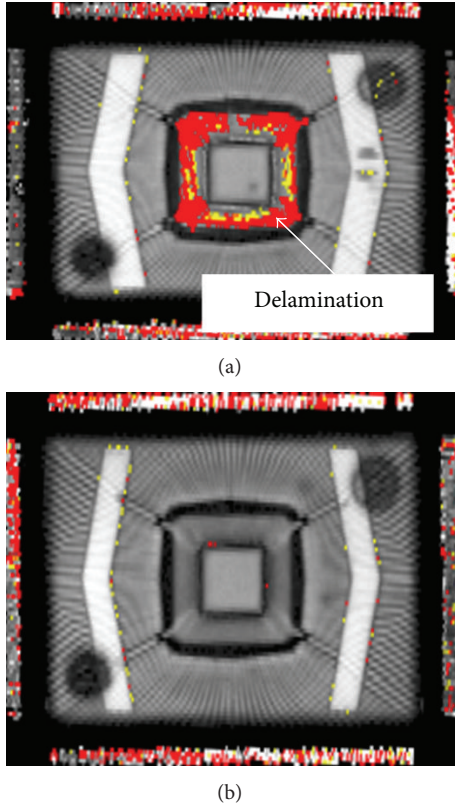


FIGURE 1: Ultrasound scanned pictures of IC packages. (a) IC packages with delamination. (b) Normal IC packages.

Zhang et al. [1] integrated the thermomechanical and hygromechanical stress together to consider the non-uniform moisture distribution during reflow. The shear stress was found to be dominated along all the interfaces, and the molding compound/lead-frame interface around the junction of die attach fillet would be the initiation of delamination. Xie et al. [2, 3] developed direct concentration approach (DCA) to solve moisture diffusion problems under varying ambient temperature and humidity loading conditions. In DCA, the moisture concentration was used as a basic field variable, and constraint equations were applied at interfaces to satisfy the interface continuity requirement. DCA was then applied to 3D ultrathin stacked-die chip scale packages, and the results showed that a small reduction in substrate thickness could result in a significant decrease in moisture concentration. Zhao et al. [4] analyzed the effects of temperature and humidity on the failure of QFN by using moisture sensitivity analysis and wet-thermal simulation method. Mei and Yao [5] presented a combined numerical methodology to predict the thermal-humidity behavior of the Chip on Glass packaging process. Among these researchers, the research team coming from Lamar University has conducted many fruitful research works on moisture diffusion and interfacial delamination [6–8]. Fan et al. presented a micromechanics-based vapor pressure model to study the moisture impacts on package reliability. The model could describe the evolution of vapor pressure in voids. Effective stress concept was introduced to consider the effect of vapor pressure in the development

of a continuum mechanics framework. Vapor pressure was considered as internal field variable, which is related to moisture evaporation. The latest research of FAN concentrated on the effects of temperature gradient on moisture diffusion in high power devices. Results showed that devices at ON condition operate at less humid ambient condition than at OFF condition because of the created local hot spots.

Although current researches on moisture diffusion are of high reference value, most of them focused on the surface mount reflowing process, which is different from actual disassembling process. As for the used IC packages, since the moisture concentration has reached to the saturated state and the long time working will cause some microcracks to gather inside IC packages, which make used IC packages more sensitive to moisture diffusion when compared with new IC packages. In order to improve the reusability and reliability of disassembled IC packages, it is very important to reduce the interface delamination during the disassembling process. Our previous experiments indicated that prebaking process before disassembling could effectively reduce the interface delamination failure [9–11].

In this paper, a computational model with variable boundary conditions is developed based on the different combination state of water in IC packages, which is used to study the distribution characteristics and mechanism of moisture diffusion behavior during prebaking process. Furthermore, the humidity distribution field and the relation among baking temperature, water loss rate, and baking time during baking process are analyzed based on the computational model, and the results are validated by FEA simulation and field experiments under variable temperature baking process. The optimized baking parameters are suggested based on FEA analysis and baking experiments.

## 2. Theoretical Model of Moisture Diffusion

**2.1. Microscopic Mechanism of Moisture Diffusion.** The packaging materials of the most IC packages are porous polymeric compound material. It is estimated that the density of water vapor absorbed in the polymer is  $0.0802 \text{ mg/mm}^3$ , which is about 8% of the liquid water and 100 times of the standard water vapor [12], and the water molecules or moisture inside the polymeric compound is condensed into the mixed liquid/vapor two-phase state. When absorbed, the moisture is stored in micropores or free volumes in the polymer material. Some water molecules stayed freely inside the micropores of the compound materials which are called as *unbounded state*, and some other water molecules had connected with the hydrogen bond of  $\text{NH}_4$  and  $\text{OH}$  of the polymer compound which is called *bounded state*. When combined with the hydrogen bond of the compound, the absorbed water molecules will weaken the combination of compound macromolecule with  $\text{SiO}_4$  layer on the chip surface and then induce the interface delamination.

The main microfactors which affect the moisture absorption are polarity of the polymer material and the volume of the micropores. The diffusion coefficient of the nonamines compound materials is much larger than

the amine-containing compound materials around 5°C. The reason for their difference on diffusion coefficient is that amine-containing compound materials provided more capture points which hindered the movement of the water molecules.

In fact, the moisture diffusion is not sensitive to the overall molecular thermal motion but restricted to the partial intense molecule thermal motion. The density and distribution of the gathered moisture stayed in the micropores of different material interface play a significant influence on the compound properties [12].

**2.2. Mathematical Definition of Moisture Diffusion.** The moisture diffusion is the mass transfer process of water molecules, and it met *FICK's Second Theorem* shown in

$$\frac{\partial C}{\partial t} = D \left( \frac{\partial^2 C}{\partial x^2} + \frac{\partial^2 C}{\partial y^2} + \frac{\partial^2 C}{\partial z^2} \right), \quad (1)$$

where  $D$  is the diffusion coefficient ( $\text{mm}^2/\text{s}$ ) and  $C$  is humidity ( $\text{mg}/\text{mm}^3$ ).  $D$  changes with temperatures, and it is decided by the properties of the chip material and meets *Arrhenius Equation* shown in

$$D = D_0 \exp\left(-\frac{E_D}{RT}\right), \quad (2)$$

where  $R$  is the gas constant ( $8.31441 \text{ J}/\text{K}\cdot\text{mol}$ ),  $T$  is the Kelvin degree, and  $E_D$  is the activation energy of diffusion coefficient.

From (2),  $D$  is a function of  $T$ . Usually, used IC packages are baked under constant temperature and  $D$  is a constant value. For most IC packages, the length is about 25–30 mm and the width is about 14–16 mm, which is much larger than the thickness, about 2–3 mm, so the heterogeneity on length and width direction could be ignored and the diffusion process could be simplified only along the thickness direction. Then, the equation could be simplified as

$$\frac{\partial C}{\partial t} = D \left( \frac{\partial^2 C}{\partial x^2} \right). \quad (3)$$

The upper and lower surfaces of the IC chips are exposed to the same humidity environment and the moisture diffusion on both sides has symmetrical features, so using half of the chip is enough to calculate and analyze the diffusion process. The driving force of moisture diffusion at the boundary is the difference between real-time concentration and the final equilibrium concentration.

The distribution function of moisture humidity along the thickness direction could be described as  $C = f(x)$  at the initial state, and the boundary conditions and initial conditions of moisture diffusion in IC packages are shown in

$$\begin{aligned} C &= f(x), \quad t = 0, \\ D \frac{\partial C}{\partial n} + H(C|_{x=\pm 1} - C_\infty) &= 0, \quad t > 0, \\ \frac{\partial C}{\partial x} &= 0, \quad t \geq 0, \quad x = 0, \end{aligned} \quad (4)$$

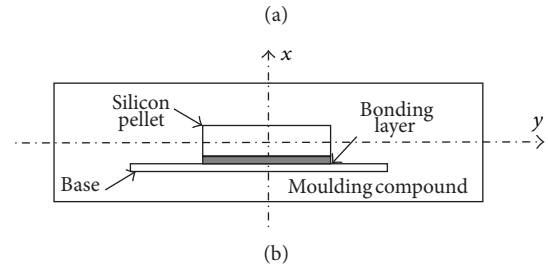


FIGURE 2: Appearance and sectional view of ITE8705. (a) Appearance of ITE8705. (b) Sectional view of ITE8705.

where  $H$  is the diffusion speed ( $\text{mm}/\text{s}$ ). Equations (3)-(4) are general description of moisture diffusion and could be used to solve distribution of moisture and humidity at specific time.

**2.3. Mathematical Solving of Moisture Diffusion.** The commonly used PQFP IC packages ITE8705 is selected as the studying object, whose appearance and structural sectional view are shown in Figure 2.

According to the actual baking experiments, the moisture content curve has great differences under different baking process and IC packages. The differences may be caused by the variable boundary condition. It is not possible for the moisture content at the boundary to mutate when external conditions change. There should be continuous changing transitional boundary layer around the IC packages. The properties of boundary layer, including press, ambient humidity, temperature, and air flow rate during the baking process, have great impact on diffusion speed ( $H$ ). At the initial moment, the humidity has an initial value  $C_0$  and then would diffuse continuously until reaching to an equilibrium concentration  $C_\infty$ .

As for moisture diffusion, moisture concentration ( $C$ ) is the driving forces of transmission process, which are decided by the difference of concentration inside IC packages. Since larger difference will induce greater driving force, the moisture diffuses at very high speed at the initial stage. The diffusing speed will slow down since the concentration is reaching to an equilibrium state gradually. So, the moisture concentration decreased very fast at the initial stage and the speed of decreasing will slow down gradually, which is monotonically decreasing function.

The vapor pressure is directly affected by the moisture concentration and disassembling temperature. Moisture concentration will affect the vapor pressure during the disassembling process at higher temperature and then decides whether the interface delamination would arise inside

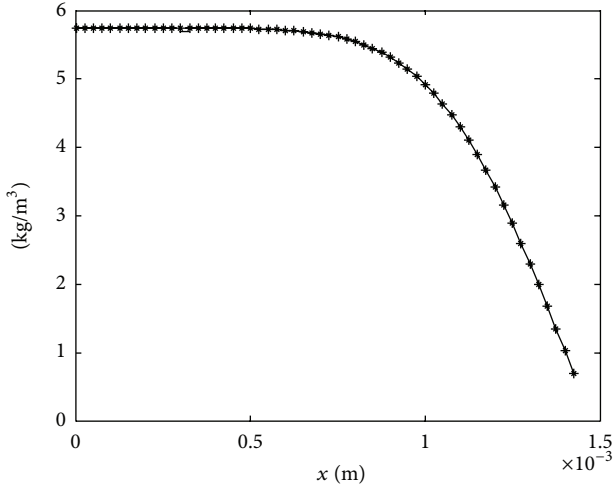


FIGURE 3: Distribution of moisture concentration.

the IC packages. The moisture concentration gradient from the middle to surface of IC packages after baking for 0.5 h at 125°C is shown in Figure 3.

Figure 3 shows that moisture concentration is very high at the inside middle layer, and it decreased very quickly from internal to external surface. Since bonding layer is in the central part of the IC packages, it has small connection with the plastic module, which causes very large diffusion resistance. So, moisture concentration is very high at the inside middle layer and it may form greater local vapor pressure, which may cause potential microcracks or even interface delamination. Since the used IC packages are more sensitive to the vapor pressure, it is better to reduce the baking temperature to ensure its reliability.

In fact, it is very difficult to make real-time measuring of the moisture concentration, but the moisture content could be obtained directly by weighing during the baking process. It is a long time to bake the IC packages to totally dried state. Even if the IC packages are baked under 125°C, it still needs about 120 hours to dry it and the time and economic costs are too high to be acceptable.

The relation among baking temperature, baking time, and baking effect is shown in Figure 4.

Figure 4 shows that baking time is very sensitive with baking temperature below 100°C. The reducing rate of baking time has very little difference when baking temperature is higher than 150°C. So, it is not advisable to reduce baking time by increasing baking temperature above 150°C.

### 3. FEA of Moisture Diffusion

**3.1. Basis of FEA Simulation.** The moisture diffusion process has similar control equation with heat transfer process according to (1), and it is possible to use the thermal analysis module of FEA software to analyze the moisture diffusion process.

The comparison of the heat transfer and moisture diffusion is listed in Table 1.

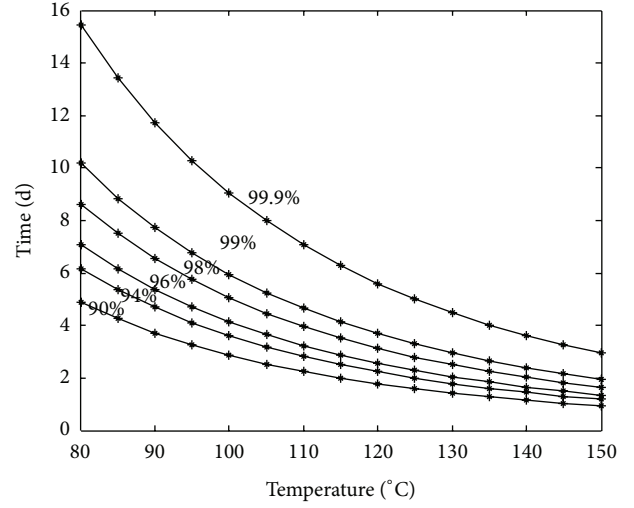


FIGURE 4: Baking temperature and time curve clusters.

TABLE 1: Comparison of heat transfer and moisture diffusion [13].

Feature	Heat transfer	Moisture diffusion
Field variables	Temperature, $T$	Moisture concentration, $C$
Density	$\rho$ (kg/m <sup>3</sup> )	1
Conductivity	$K$ (W/m °C)	$D \cdot C_{sat}$ (kg/sec m)
Specific heat	$c$ (J/kg °C)	$C_{sat}$ (kg/m <sup>3</sup> )
Thermal expansion coefficient	$\alpha$	$\beta \cdot C_{sat}$

**3.2. Improved Definition of Relative Concentration.** For IC packages, the moulding compound and bonding layer are the main moisture absorber. The moisture concentration at their boundary is not continuous because of the differences of their physical properties.

The significant difference between heat transfer and moisture diffusion process is the continuity of the field variables,  $T$  and  $C$ . The temperature  $T$  is continuous during the heat transfer process, but the moisture concentration  $C$  is discontinuous at the interface of different materials, as shown in Figure 5, and made it inadmissible to FEA treatment.

In order to solve this problem, Wong proposed the definition of relative concentration (wetness) as follows [15]:

$$w = \frac{C}{C_{\infty}}. \quad (5)$$

If  $w$  is continuous in different medium ( $a$  and  $b$ ), then the hypothesis could be described as

$$\frac{C_a}{C_{\infty a}} = \frac{C_b}{C_{\infty b}} \iff \frac{C_a}{C_b} = \frac{C_{\infty a}}{C_{\infty b}} = \text{const.} \quad (6)$$

The above hypothesis could be proved by *Henry Partial Pressure Theorem*. According to the actual disassembling and baking process, when moved into the drying cabinet, the saturated moisture concentration of IC packages is equal to

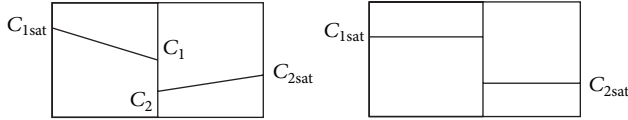


FIGURE 5: Discontinuous moisture concentration at different material interface [14].

the outside water vapor concentration  $C_{ext}$ . The improved definition of the initial relative concentration is shown in

$$w = \frac{C_0}{C_{\infty}} = \frac{C_0}{C_{ext}} \geq 1, \quad (7)$$

and the relative concentration on the boundary is

$$w = \frac{C_{ext}}{C_{\infty}} = \frac{C_{ext}}{C_{ext}} = 1. \quad (8)$$

As shown in Figure 6, the moisture concentration of the IC packages would equal the vapor concentration in the external environment during a long time of diffusion, and the final relative concentration would be  $w = 1$ , instead of  $w = 0$ .

When substituting relative concentration ( $w$ ) for absolute humidity ( $C$ ), (1) could be converted into a relative concentration diffusion differential equations, which is identical with heat transfer process, and the thermal analysis module could be used to analyze the moisture diffusion process.

**3.3. Simulation of Moisture Diffusion at Constant Temperature.** The studying object, IC packages ITE8705 (shown in Figure 1), has symmetrical shape, and the gradient direction of moisture diffusion mainly concentrates on the thickness direction. When building the FEA model, half of the IC package section is enough for calculation and analysis.

Currently, there are no available baking standards for PCB disassembly process, but the industry standard (IPC/JEDEC J-STD-033A) for baking new IC packages could be used for reference. Since the disassembled IC packages are very sensitive to the moisture due to the potential existence of internal microcracks, the baking temperature should be carefully selected when considering the efficiency and reliability. In this study,  $90^{\circ}\text{C}$  and  $125^{\circ}\text{C}$  are selected for moisture diffusion analysis from the four temperature levels defined in IPC/JEDEC J-STD-033A ( $40^{\circ}\text{C}$ ,  $90^{\circ}\text{C}$ ,  $125^{\circ}\text{C}$ , and  $150^{\circ}\text{C}$ ). The assumptions and experimental conditions are as follows.

- (i) Assuming that disassembled IC packages have worked or have been stored at  $25^{\circ}\text{C}/60\% \text{ RH}$  for a long time, they have reached saturated moisture concentration.
- (ii) The temperature of baking ovens is set to  $90^{\circ}\text{C}/1.5\% \text{ RH}$  and  $125^{\circ}\text{C}/1.5\% \text{ RH}$  separately.

Humidity distribution field of IC packages after baking at  $90^{\circ}\text{C}$  for 120 hours is shown in Figure 7.

Bonding layer is in the central part of the IC packages and it has small connection with the plastic module, which caused very large diffusion resistance. Though the moisture diffusion coefficient of the bonding layer is greater than the plastic

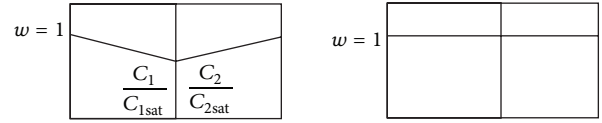


FIGURE 6: Continuous relative concentration at different medium inside IC packages.

TABLE 2: Time and temperature setting of variable baking.

Temperature	Baking time (h)							
$90^{\circ}\text{C}$	72	48	36	24	18	12	6	0
$125^{\circ}\text{C}$	0	24	36	48	54	60	66	72

module, the speed of its moisture diffusion is the slowest due to the restriction of its geometry and location. So, the bonding layer area has the highest moisture concentration. It needs about 288 hours to bake the IC packages to dry state at  $90^{\circ}\text{C}$ . Humidity distribution field of IC packages after baking at  $125^{\circ}\text{C}$  for 120 hours is shown in Figure 8.

Generally, higher baking temperature will cause greater temperature gradient along the thickness direction of IC packages, which will increase the driving force of moisture diffusion and then accelerate the diffusion speed. Figure 8 indicates that the diffusion speed increased quickly with the temperature, and the balance time for baking has been shortened greatly.

**3.4. Simulation of Moisture Diffusion at Variable Temperature.** According to the relation among baking temperature, time, and moisture concentration, the baking process at constant temperature has very complicated impact on the efficiency, energy, and baking time. The optimization of these indicators is contradictory. In order to resolve these contradictions, baking at variable temperature could achieve the integrated optimization.

The variable baking parameters are determined according to the following two rules.

- (i) Reduce the moisture changing rate at the initial stage to ensure the chip's security and integrity.
- (ii) Accelerate the moisture changing rate at the second stage to reduce the balancing time for moisture diffusion.

Based on the above two rules, a group of parameters listed in Table 2 are selected for variable baking simulation.

Similarly, the assumptions and experimental conditions are the same as baking at constant temperature. Because the balancing humidity is different under  $90^{\circ}\text{C}$  and  $125^{\circ}\text{C}$  and the change of relative concentration is not continuous, the final results are expressed by absolute humidity. Taking the 7th parameter as the example, Figure 9 indicates the baking simulation process under  $90^{\circ}\text{C}$  (6 h) and  $125^{\circ}\text{C}$  (66 h).

In the first 6 hours, moisture diffusion process is consistent with the baking process at constant temperature. When baking temperature rises from  $90^{\circ}\text{C}$  to  $125^{\circ}\text{C}$  at the second stage, higher baking temperature will cause greater

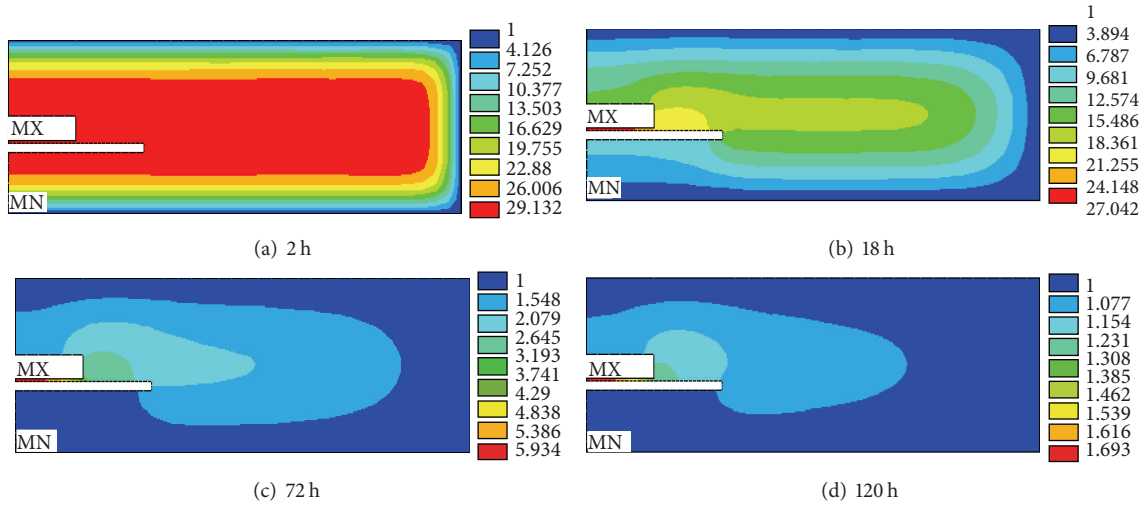


FIGURE 7: Humidity distribution field of IC packages after baking at 90°C for 120 hours.

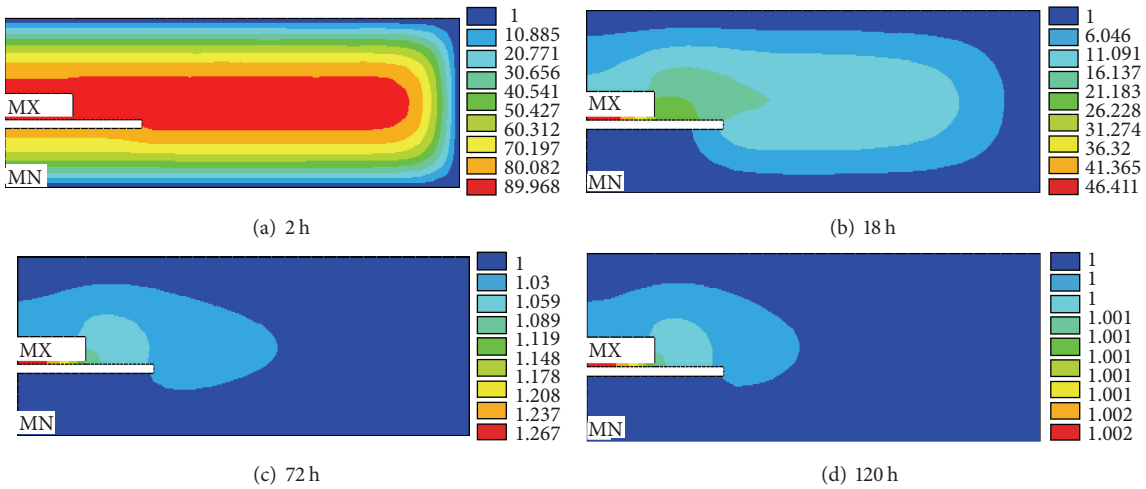


FIGURE 8: Humidity distribution field of IC packages after baking at 125°C for 120 hours.

temperature gradient along the thickness direction of IC packages, which will increase the driving force of moisture diffusion. So, the increase of the temperature accelerates the moisture diffusion speed and moisture changing rate sharply. After baking for 36 hours, the humidity is at very low level and the increasing of temperature has very limited impact on the diffusion speed of moisture.

In order to secure the reusability and reliability of the IC packages, it is rational to bake them under 90°C for 7 to 10 hours. In the second baking stage, baking temperature could be increased around 125°C to accelerate the moisture diffusion speed and shorten the baking time for economic and cost reasons.

#### 4. Results and Discussion

According to the above FEA simulation, baking at variable temperature has greater advantage than baking at constant temperature when considering the baking time and the IC package's integrity and reliability. Economic and cost

aspects should be carefully evaluated before actual industrial application. Baking process consumed a lot of energy which should be optimized to make it affordable.

The baking power increases with baking temperature during the baking process and then decreases the baking time. The relation between total baking energy and baking temperature is complicated, which is decided by the function relation among baking power, baking time, and baking temperature. In order to evaluate the energy consumption and baking cost, a commonly used industrial blast electric oven (DHG-9053A), shown in Figure 10, is selected for building energy consumption model.

The energy consumption of the blast electric oven is mainly used to drive the blower and heating to maintain the temperature. The energy consumption model could be described in

$$P = K_1 \times \frac{\lambda \times (T_b - T_a) \times F}{d} + C_a \times m_a \times (T_b - T_a) + P_c, \quad (9)$$

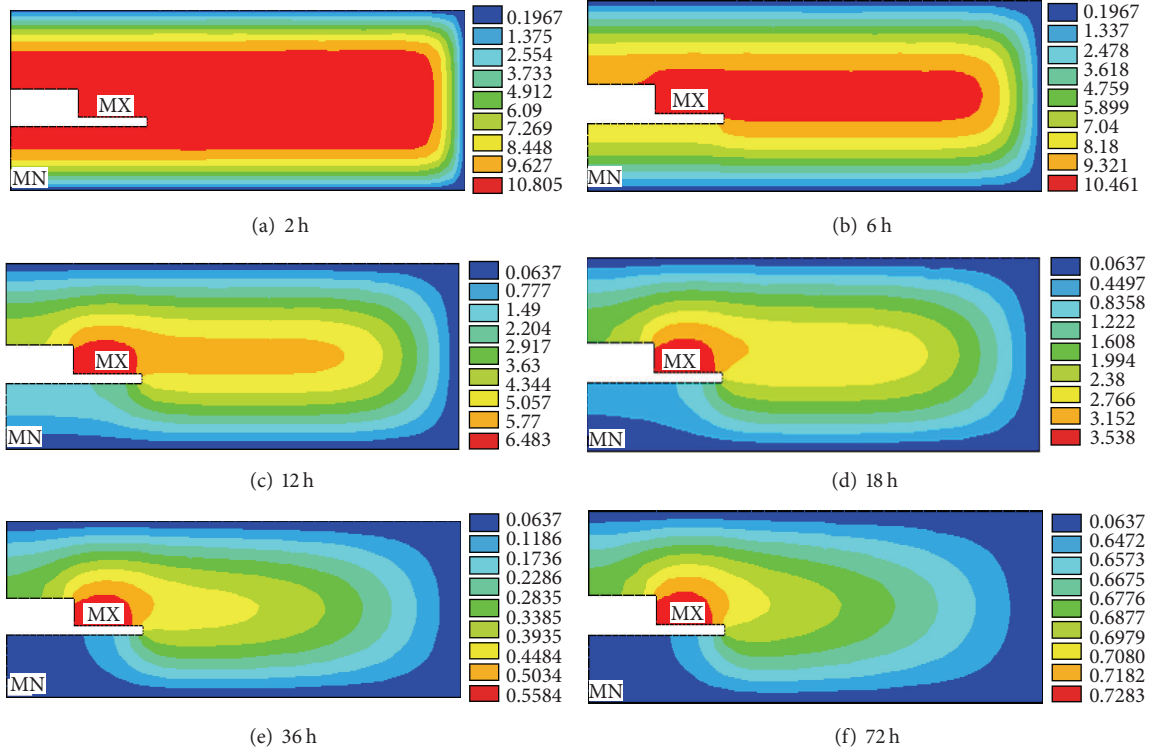


FIGURE 9: Humidity distribution field of IC packages after baking at variable temperature under 90°C (6h)–125°C (66h).

where  $K_1$  is the thermal conductivity coefficient of the oven,  $F$  is the conductivity area,  $d$  is the thickness,  $C_a$  is the air specific heat capacity,  $m_a$  is the air mass exchanged within unit time,  $T_b$  is the internal oven temperature and  $T_a$  is the outside air temperature, and  $P_c$  is the other energy consumed during the baking process.

According to (9), the energy consumption has a direct proportion with the temperature difference between internal oven and external environment. For a given oven, the characteristic parameters are determined and could be measured by baking experiment.

The baking time is decided by the baking results (usually expressed as water loss rate). For the selected IC package (ITE8705), the relation between water loss rate and baking time has been tested and listed in Table 3.

In fact, the difference of absolute water loss is not very significant at different water loss rate. Since the baking time varies greatly from 90% to 99.9999%, it is necessary to define reasonable baking parameters to make it acceptable for industrial application.

In the premise of reducing interface delamination and improving the reliability of the IC packages, the relation among baking temperature, water loss rate, and baking time during baking process is confirmed by experiments. The temperature and power parameters are listed in Table 4.

The relation between baking energy consumption and temperature under different water loss rate is tested and shown in Figure 11.

Figure 11 indicates that baking energy at different baking temperature has not been much different at the beginning

TABLE 3: Relation between water loss rate and baking time.

Time (H)	18	24	38	57	115
Water loss rate (%)	90	96	99	99.9	99.9999

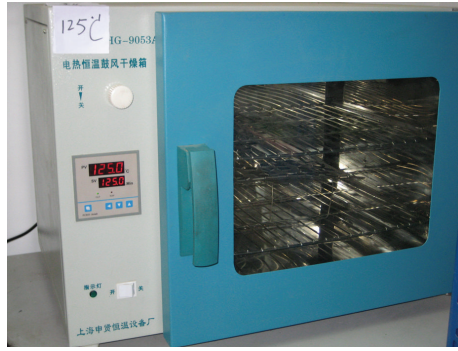
TABLE 4: Temperature and average power baking process.

Temperature (°C)	60	80	100	120	140	160
Average power (W)	385	474	536	612	677	750

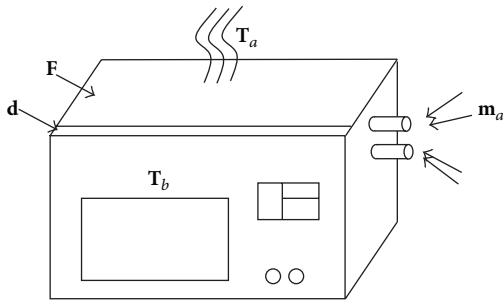
stage, so it is not advisable to increase the temperature of the previous baking stage, and higher temperature will not reduce the energy consumption and may increase the possibility of interface delamination. The baking standards which are defined by the final moisture content had significant influence on the heating time as well as the consumed baking energy. The tested curve clusters could be used as references to develop industrial standards for PCB disassembling process when high IC packages reliability and reusability are required.

### 5. Conclusions

This paper studies the moisture diffusion behavior during PCB disassembling process by building computational model with variable boundary conditions. The distribution of moisture concentration and relation among baking temperature, baking time, and baking effect have been confirmed based on the combination of the model and baking experiments. It is found that the resistance for moisture diffusion mainly came from the internal part of the IC packages. Then, improved



(a)



(b)

FIGURE 10: Blast electric oven.

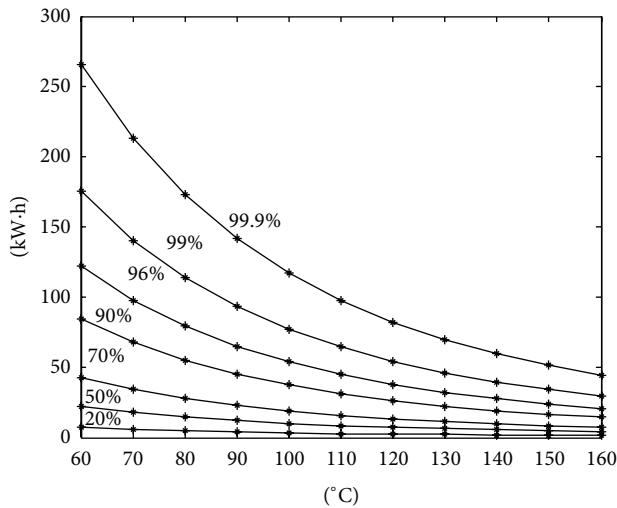


FIGURE 11: Relation between baking energy consumption and temperature under different water loss rate.

definition of the relative concentration is defined and the model is validated and applied by FEA simulation. When compared with constant temperature, baking at variable temperature could achieve optimized efficiency and energy consumption. In order to secure the reusability and reliability of the IC packages, it is rational to bake them under 90°C for 7 to 10 hours, and then the baking temperature could be increased around 125°C to accelerate the moisture diffusion speed and shorten the baking time for economic and cost reasons. Finally, a set of curves which indicates the relation between baking energy consumption and temperature

is determined under actual industrial baking experiments, which could be used as references to develop industrial standards for PCB disassembling process.

The impact of moisture humidity on crack propagation is still uncertain and the microscopic mechanism of their relation should be a research focus in the near future.

## Nomenclature

- D:** Diffusion coefficient ( $\text{mm}^2/\text{s}$ )  
**C:** Moisture concentration ( $\text{mg}/\text{mm}^3$ )  
**R:** Gas constant ( $8.31441 \text{ J}/\text{K}\cdot\text{mol}$ )  
**H:** Diffusion speed ( $\text{mm}/\text{s}$ ).

## Acknowledgments

The research is supported by the NSFC project (Grant no. 51075233) and National Key Technology R&D Program (Grant no. 2011BAF11B06).

## References

- [1] M. Zhang, S. W. R. Lee, and X. Fan, "Stress analysis of hygrothermal delamination of Quad Flat No-lead (QFN) packages," in *Proceedings of the ASME International Mechanical Engineering Congress and Exposition (IMECE '08)*, pp. 339–347, Boston, Mass, USA, October–November 2008.
- [2] B. Xie, X. J. Fan, X. Q. Shi, and H. Ding, "Direct concentration approach of moisture diffusion and whole-field vapor pressure modeling for reflow process—part I: theory and numerical implementation," *Journal of Electronic Packaging*, vol. 131, no. 3, Article ID 031010, 7 pages, 2009.
- [3] B. Xie, X. J. Fan, X. Q. Shi, and H. Ding, "Direct concentration approach of moisture diffusion and whole-field vapor pressure modeling for reflow process—part II: application to 3D ultrathin stacked-die chip scale packages," *Journal of Electronic Packaging*, vol. 131, no. 3, Article ID 031011, 6 pages, 2009.
- [4] Y. Zhao, C. Chang, H. Chen, and G. Gao, "Simulation analysis of delamination failure and thermal-moisture," *Semiconductor Technology*, vol. 35, no. 6, pp. 550–554, 2010.
- [5] Y. Mei and X. Yao, "A numerical method on thermal-humidity behavior of electronic packaging," in *Proceedings of the 12th International Conference on Electronic Packaging Technology and High Density Packaging (ICEPT-HDP '11)*, pp. 1044–1048, August 2011.
- [6] X. J. Fan, J. Zhou, G. Q. Zhang, and L. J. Ernst, "A micromechanics-based vapor pressure model in electronic packages," *Journal of Electronic Packaging*, vol. 127, no. 3, pp. 262–267, 2005.
- [7] X. Fan and J.-H. Zhao, "Moisture diffusion and integrated stress analysis in encapsulated microelectronics devices," in *Proceedings of the 12th International Conference on Thermal, Mechanical and Multi-Physics Simulation and Experiments in Microelectronics and Microsystems (EuroSimE '11)*, April 2011.
- [8] X. Fan and C. Yuan, "Effect of temperature gradient on moisture diffusion in high power devices and the applications in LED packages," in *Proceedings of the Electronic Components & Technology Conference*, pp. 1466–1470, Las Vegas, Nev, USA, May 2013.
- [9] X. Ding, X. Liu, D. Xiang, J. Yang, and G. Duan, "Research on delamination failure of plastic IC packages in components

- reuse processes,” in *Proceedings of the 4th World Congress on Maintenance*, Haikou, China, November 2008.
- [10] X. Ding, *Research on delamination problem in plastic IC packages during PCB disassembly [M.S. thesis]*, Tsinghua University, 2009.
- [11] Z. Z. Liu, *Moisture diffusion modeling and optimization of the baking process for disassembled IC packages [Bachelor thesis]*, Tsinghua University, 2011.
- [12] X. Cai, W. Huang, B. Xu, and Z. Cheng, “Morphology of the water in plastic electronic packaging materials,” *Chinese Journal of Materials Research*, vol. 16, no. 5, pp. 507–511, 2002.
- [13] E. H. Wong, S. W. Koh, K. H. Lee, and R. Rajoo, “Advanced moisture diffusion modeling & characterisation for electronic packaging,” in *Proceedings of the 52nd Electronic Components and Technology Conference*, pp. 1297–1303, May 2002.
- [14] J. Bie, X. Sun, and S. Jia, “Recent advances in the study of moisture absorption in plastic electronic packaging,” *Advances in Mechanics*, vol. 37, no. 1, pp. 35–47, 2007.
- [15] E. H. Wong, S. W. Koh, K. H. Lee, K.-M. Lim, T. B. Lim, and Y.-W. Mai, “Advances in vapor pressure modeling for electronic packaging,” *IEEE Transactions on Advanced Packaging*, vol. 29, no. 4, pp. 751–759, 2006.

## Research Article

# Performance Evolution of Phytic Acid Conversion Film in the Forming Process

Xiufang Cui,<sup>1</sup> Lili Lin,<sup>1</sup> Erbao Liu,<sup>1</sup> Guo Jin,<sup>1</sup> and Jie Jin<sup>2</sup>

<sup>1</sup> Institute of Surface/Interface Science and Technology, School of Materials Science and Chemical Engineering, Harbin Engineering University, Harbin 150001, China

<sup>2</sup> Engineering Research Center for Electrophysical Apparatus and Application Technology, Beijing Research Institute of Automation for Machinery Industry, Beijing 100120, China

Correspondence should be addressed to Guo Jin; [jinguo@hrbeu.edu.cn](mailto:jinguo@hrbeu.edu.cn)

Received 28 May 2013; Accepted 22 September 2013

Academic Editor: Gang Wang

Copyright © 2013 Xiufang Cui et al. This is an open access article distributed under the Creative Commons Attribution License, which permits unrestricted use, distribution, and reproduction in any medium, provided the original work is properly cited.

To improve conversion film techniques, control film properties and improve quality of following techniques, in this study, the environment-friendly phytic conversion films were deposited on AZ91D magnesium alloy. The performance evolution of the film during the forming process such as mechanical property, residual stress, corrosion resistance, micromorphology, composition, and roughness was investigated by nanomechanical testing system, electrochemical workstation, scanning electron microscope, Auger electron spectroscopy, and atomic force microscope. The results indicate that, in the forming process, the changes of micromorphology, roughness, mechanical property, and corrosion property are closely related to the variation of elements and residual stress. With the prolonging of film formation time, the difference between film elements and substrate elements gradually increases, and the residual stress first increases then decreases. When the film formation time is about 30 min, the film begins to crack and the residual stress is released, which leads to the decrease of mechanical property and corrosion resistance of the film.

## 1. Introduction

Chemical conversion film is widely applied to various fields of surface modification and protection due to its low cost, convenient preparation, uniform thickness, and special physicochemical property [1–4]. Usually as middle protective coating, stability and reliability of conversion film has significance to the safety and protective effect of following coating [5–7]. Microstructure, elements, mechanical property, and residual stress of conversion film are the major factors that contribute to failures such as cracking, stripping, falling off, and corrosion in direct and indirect application process, which can severely influence the range of application and service life of film [8–11]. In the forming process, changes of elements or thickness and dry shrinkage may lead to some residual stress within conversion film [12, 13]. Determination of this kind of stress has not been reported at present. Conversion film is important yet special in protection field, and residual stress may lead to deformation, cracking [14]. Therefore, accurate determination of micromechanical property and residual

stress has great engineering significance and scientific value for the control and design of conversion film with good properties.

Because of the particularity of conversion film preparation techniques, its mechanical property is affected by many factors and changes with chemical reactions [14, 15]. Therefore, it is significant to study the microstructure, composition, roughness, and evolution law of residual stress in film forming process to improve conversion film techniques, control film properties and improve quality of following techniques. In this study, the evolution of the microstructure, composition, roughness, corrosion resistance, nanomechanical property, and residual stress in the film formation process was investigated.

## 2. Experimental

Die-cast AZ91D magnesium alloy samples were used as the substrate. Test coupons were polished by waterproof abrasive

paper, from 360 grits down to 2500 grits, and after that fine-polished by using diamond paste of  $3.5\ \mu\text{m}$ ; then they were degreased with absolute ethanol in ultrasonic bath for 15 min and subsequently dried by cold air at room temperature. The conversion treatment parameters were as follows: phytic acid concentration of 5 g/L and temperature of  $20^\circ\text{C}$ .

The morphologies of conversion coatings were observed using atomic force microscopes (AFM) and scanning electron microscopy (SEM). The characterization of the composition and depth distribution of elements in the conversion coatings was detected by Auger electron spectroscopy (AES) depth profiling with a base pressure below  $1 \times 10^{-7}$  Pa. For electron excitation a primary electron beam of 10 keV was used. During depth profiling the samples were sputtered by two symmetrically inclined Ar ion beams of 2 keV. The sputtering rate was about 6 nm/min. The atomic concentrations were calculated by means of relative sensitivity factors of 0.3 for P transition at 120 eV, 0.085 for C transition at 272 eV, 0.35 for O transition at 506 eV, 0.13 for Mg transition at 1178 eV, and 0.075 for Al transition at 1390 eV.

All the electrochemical experiments were carried out in 3.5% NaCl solution at room temperature with the electrochemical system (Parstat 2273). The surface area of the working electrodes was  $1\ \text{cm}^2$ . Ag/AgCl electrode was used as the reference electrode, and platinum plate with a surface area of about  $1\ \text{cm}^2$  was used as the auxiliary electrode. Potentiodynamic polarization experiments were performed at a scan rate of 0.3 mV/s.

Nanomechanical properties were conducted by employing a TriboIndenter (Hysitron Corporation) with the displacement and load resolutions being 0.1 nm and  $0.1\ \mu\text{N}$ , respectively. Indentation was made using a Berkovich indenter calibrated with a standard fused silica specimen. The indenter was also used as an AFM tip, and the indented surface was imaged after indentation. An average indentation load-depth curve and the corresponding real contact area were used to calculate the residual stress in the conversion coatings.

### 3. Results and Discussions

**3.1. Microstructure and Composition of Conversion Coating.** The dissolution of substrate and the formation of films are relatively fast at the initial stage. In order to deeply analyze this process, the film morphology is observed by using AFM at the initial stage of film formation (0–15 min), and the results are shown in Figure 1. The morphology of untreated sample is shown in Figure 1(a). The surface is relatively smooth with some slight protuberances and pits. Figure 1(b) shows the morphology of sample immersed in phytic acid solution for 1 s. The pits are deeper than the untreated sample, which may be due to the dissolution of substrate. Some compounds appear in the pits which are used as the nucleation points of the films beginning to form. Figure 1(c) shows the morphology of sample immersed in phytic acid solution for 5 s. Pits in Figure 1(b) have been filled on the whole, and the film was deposited on the surface. After 15 s, the deposition of chelate continues on the

formed film as shown in Figure 1(d). Many growing points uniformly spread on the surface, and the protuberances and pits turn slight. When time continues to increase, particulates continuously grow, and the film becomes thicker and thicker as shown in Figures 1(e) and 1(f). After 15 min, the film grows nodular without obvious protuberances and pits, and the consistent film comes into being on the surface of AZ91D.

Figure 2 shows the further analysis of conversion surface morphology at different forming times by using SEM. In Figure 2(a), the surface morphology of AZ91D shows that the surface is mainly composed of dark  $\alpha$  phase and bright  $\beta$  phase. After 5 min (Figure 2(b)) and 15 min (Figure 2(c)), the surface is smooth without cracks. After the film has been formed, the second phase still exists, which shows that the film formed in this stage is relatively thin. After 1 hour, microcracks begin to appear on the surface, and with the increase of time the crack density and width increase. The film formed on  $\beta$  phase is more compact than that on  $\alpha$  phase, as is shown in Figures 2(d), 2(e), and 2(f).

Figure 3 shows the elements depth analysis results of film after 3 hours. The results indicate that the major elements of the film are C, O, Mg, Al, and P. According to the element analysis of AZ91D and phytic acid, the phytic acid conversion film on AZ91D is the product of the reaction between phytic acid and Mg, Al in AZ91D. From Figure 3, it can be seen that O content in surface is the most, up to 40%, and the second is Mg and then is Al and P. Meanwhile, the major element contents of film display grading changes with depth. Mg and Al increase along with depth, while C, O, and P decrease with the increase of depth. It can be concluded that the number of metal ion chelating phytic acid on magnesium alloy decreases with the increase of film formation time. When sputtering depth reaches 2400 nm, element contents have matched those of AZ91D magnesium alloy, which indicates that the depth of film for immersion 3 h is about 2400 nm.

Figure 4 shows the atomic percentages of film elements on AZ91D surface at different formation times. The P, C, and O come from phytic acid, whose contents roughly increase with time prolonging; Mg and Al come from magnesium alloy substrate, roughly decreasing with the increase of time.

Table 1 shows the results of surface roughness of conversion film at different formation times. With the prolonging of formation time, roughness of film first decreases and then increases. Initially, between 1 min and 30 min, film surface roughness remains steady with low value. This phenomenon matches the results achieved by scanning electron microscope in formation process. In the initial formation stage, the hydrogen evolution reaction happens on magnesium alloy surface by the action of aqueous solution, which leads to the dissolution of substrate and the increase of surface roughness. With the increase of formation time, covering area of film on substrate surface becomes larger and larger, the hydrogen evolution reaction reduces, and protuberances and pits caused by substrate dissolution are gradually filled. After substrate surface is totally covered by film, surface roughness remains in a stable range. About 1 hour later, with time prolonging, film thickness increases and begins to crack, and

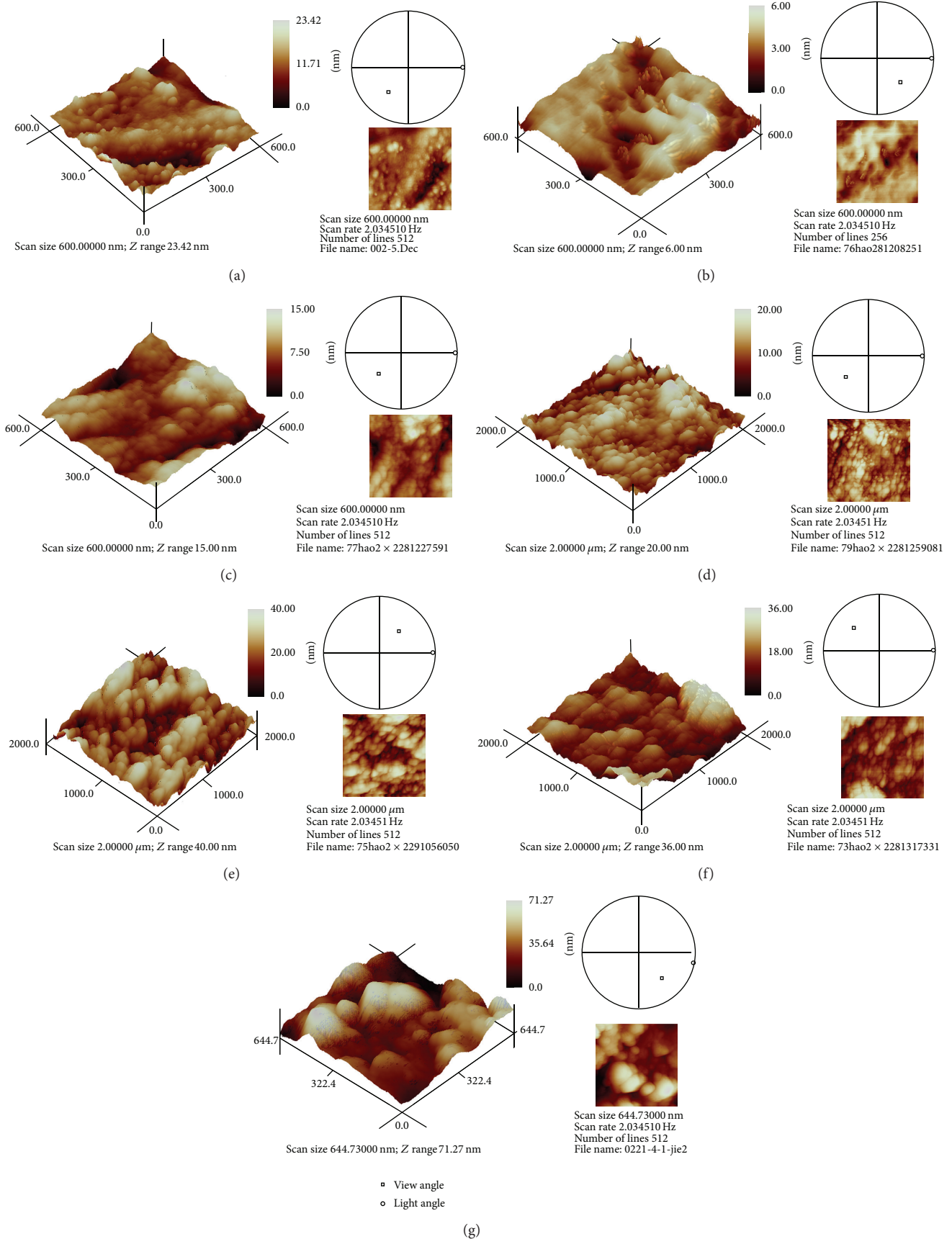


FIGURE 1: AFM pictures of conversion film at different forming times: (a) 0 min, (b) 1 s, (c) 5 s, (d) 15 s, (e) 1 min, (f) 5 min, and (g) 15 min.

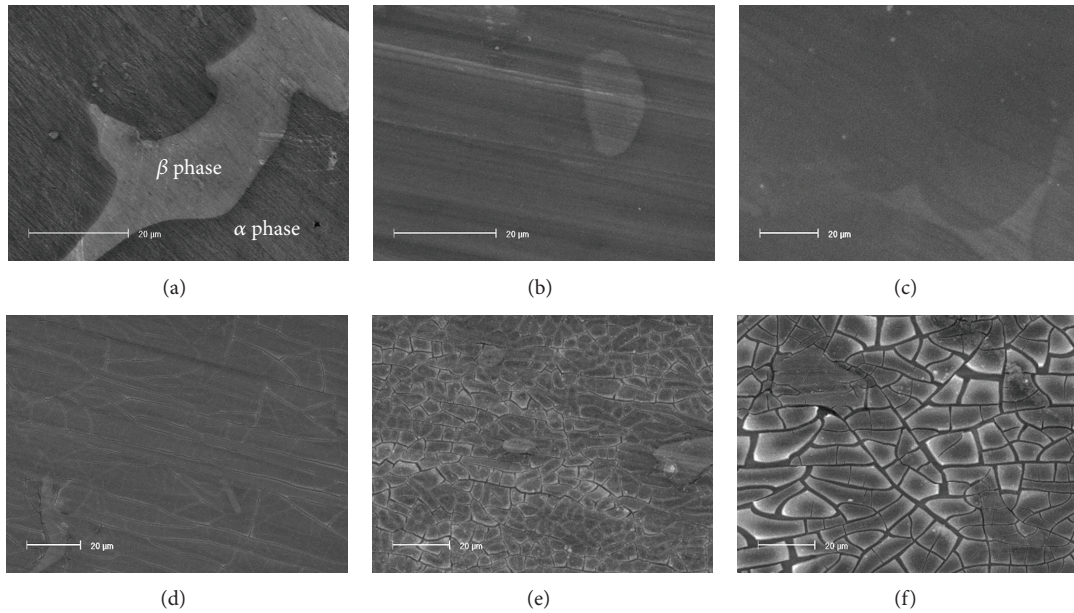


FIGURE 2: SEM pictures of conversion film at different formation times: (a) 0 min, (b) 5 min, (c) 15 min, (d) 1 h, (e) 3 h, and (f) 8 h.

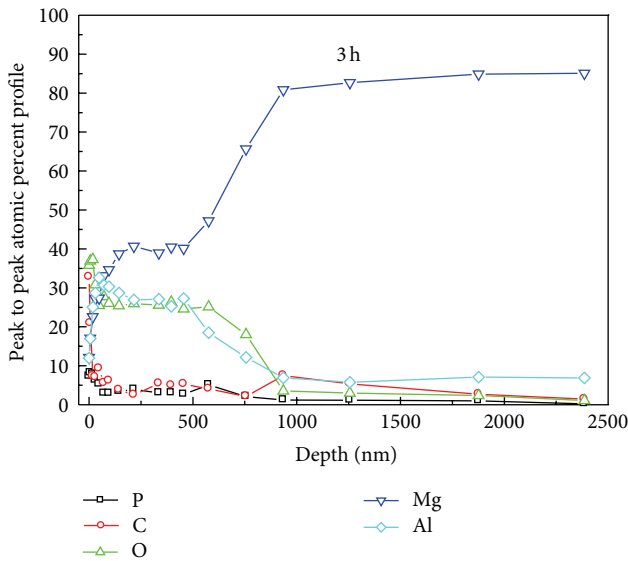


FIGURE 3: Depth profile of elements in the phytic acid conversion coatings for immersion 3 h on AZ91D magnesium alloy.

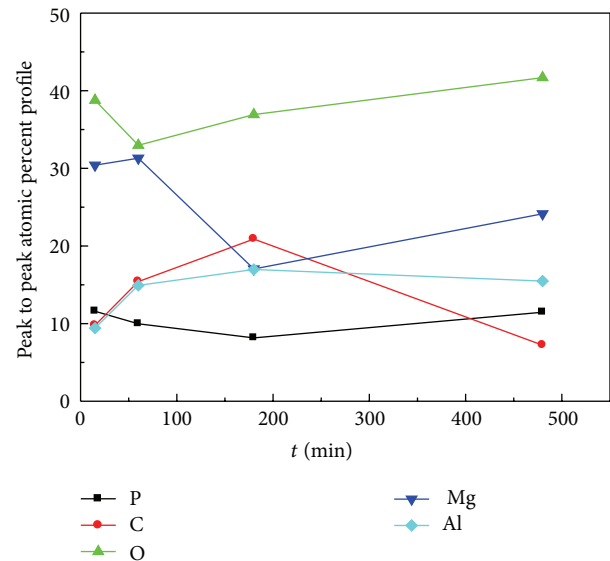


FIGURE 4: AES elements surface analysis of conversion film at different formation times.

the surface quality slowly decreases and roughness increases again.

**3.2. Corrosion Resistance of Conversion Coating.** Figure 5 shows the dynamic potential polarization curves of film at different formation times. With the time prolonging, the corrosion resistance first increases and then decreases. At 15 min, the self-corrosion current density is the smallest. At other formation time, film displays passivation of different degrees. From 1 hour to 8 hours, both self-corrosion potential and self-corrosion current density increase along with time

increasing. This indicates that the film thickness increases along with time, but crack reduces the resistance in corrosion medium; therefore, corrosion resistance declines when time increases.

**3.3. Mechanical Property and Residual Stress of Conversion Coating.** Figure 6 shows the load-displacement curve at different formation times. From 1 s to 1 min, the film just begins to deposit, so the load curve is greatly influenced by grinded magnesium alloy substrate surface; the law of curve is not obvious. From 1 min to 15 min, in loading process, with

TABLE 1: Roughness conversion film at different film formation times.

Time	1 s	1 min	5 min	15 min	30 min	1 h	3 h	8 h
Ra (nm)	2.99	2.49	2.48	2.46	2.50	2.66	3.15	4.23

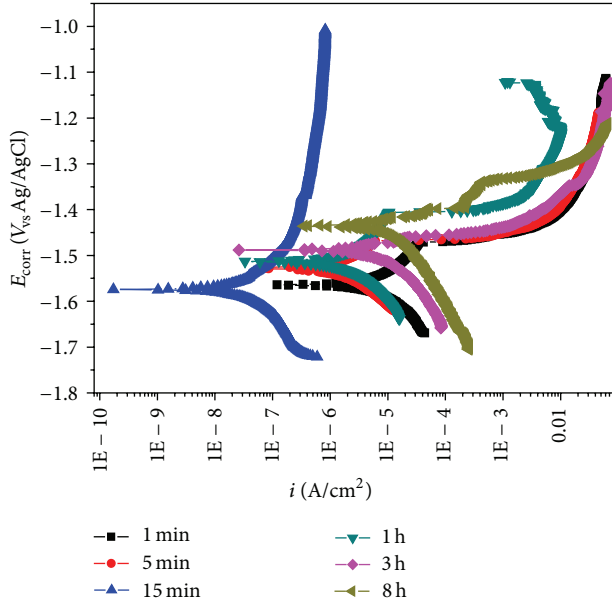


FIGURE 5: Dynamic potential polarization curve of film at different formation times.

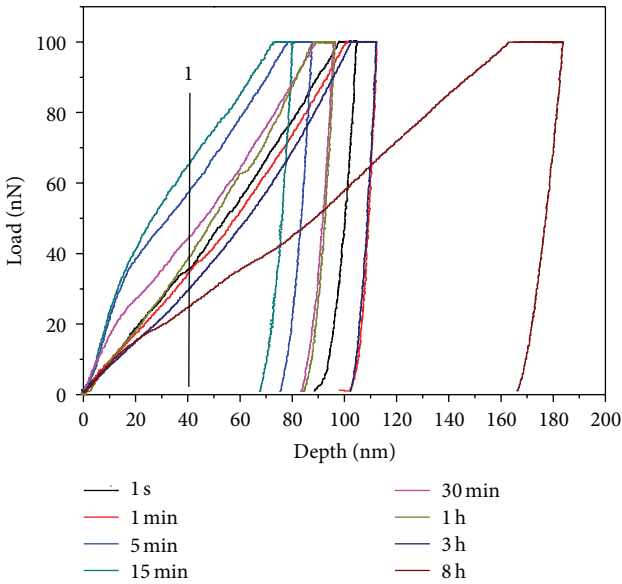


FIGURE 6: Load-displacement curves of conversion film at different film formation times.

same indentation depth, indentation load increases with the increase of formation time. When formation time prolongs to 30 min, indentation load decreases.

Figure 7 shows the nanomechanical performance analysis results of film at different formation times. Hardness and

modulus elasticity are the average of three measurements. With the increase of formation time, modulus elasticity and hardness present similar variation trend. At initial state (1 s–1 min), thickness is small, and mechanical performance is greatly influenced by substrate surface, so modulus elasticity and hardness display downtrend. With the increase of thickness, influence of substrate becomes smaller and smaller; at the time of 15 min, film displays the optimum mechanical performance. When time prolongs to more than 30 min, mechanical performance presents a slow downtrend. Along with the increase of time, lowering speed increases. Combined with morphology analysis results, the reasons for this phenomenon are that with the increase of formation time, thickness increases, compositional difference between film and substrate gradually increases, and thus residual stress increases after film being dried. When stress becomes bigger than bond of film surface, cracks appear, and along with the increase of formation time, crack density and width increase, so mechanical performance of film gradually weakens.

According to morphology and mechanical property in film formation process, this paper chooses the following formula put forward by Suresh and Giannakopoulos to calculate the value of residual stress [16]:

$$\sigma = H \left( \frac{A_0}{A} - 1 \right). \tag{1}$$

In the formula,  $H$  is material hardness and  $A_0$  and  $A$  are, respectively, indentation projection areas without and with residual stress.  $A$  and  $H$  can be acquired by analyzing the nanoindentation results. Figure 8 shows the indentation AFM profile of conversion film after 1 hour. Processing the original data at different formation times, the values of  $A$  are shown in Table 2 and the values of  $H$  are shown in Figure 7(a).

Figure 9 shows the calculated values of residual stress. It can be seen that with the increase of film formation time, the residual tensile stress first increases and then decreases, and it can achieve the maximum about 15 min later. Combined with morphology analysis, it can be known that, before cracking, with the increase of thickness, residual stress also increases. When cracks gradually appear, residual stress is released and begins to decrease with the increase of crack width and density.

#### 4. Conclusions

The initial formation process of conversion films is mainly the dissolution process of magnesium alloy substrate and the chelate reaction process of phytic acid and magnesium alloy. With the increase of film formation time, conversion films on magnesium alloy gradually become dense, roughness reduces, and substrate gradually decreases. The residual stress

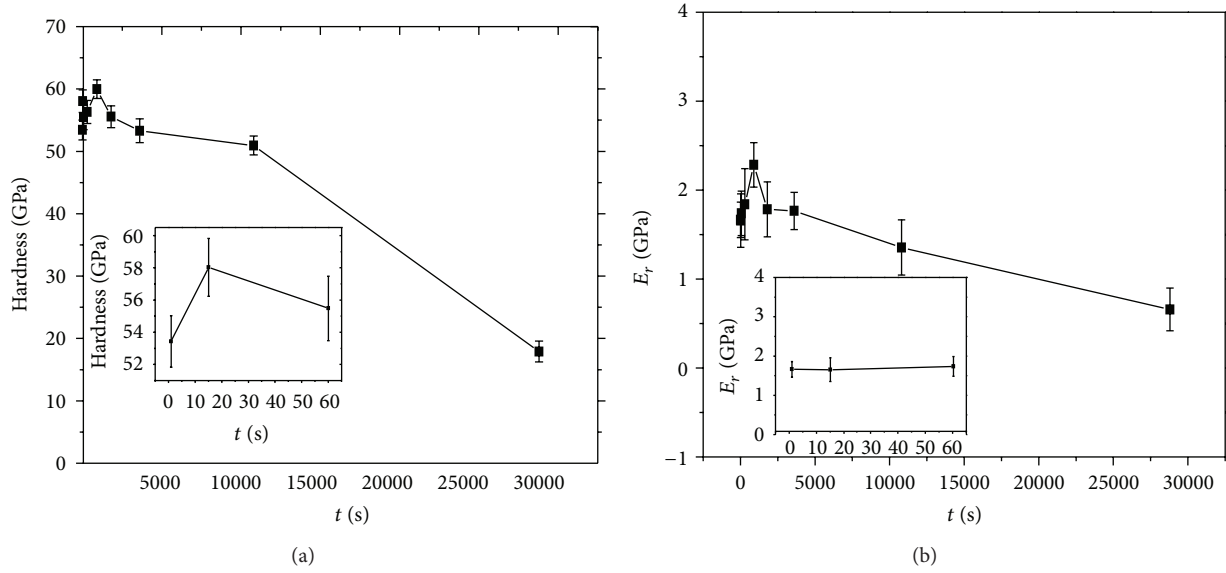


FIGURE 7: Mechanical performance variation of film at different formation times: (a) hardness, (b) elastic modulus.

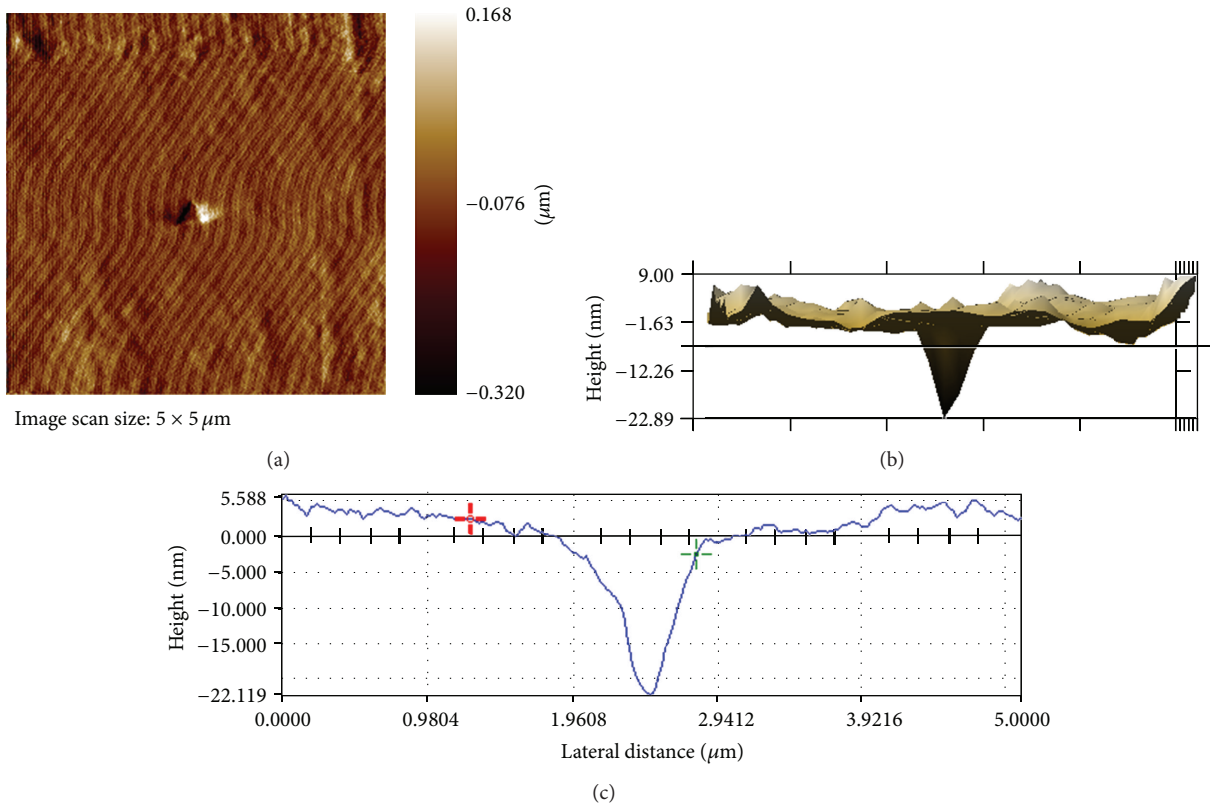


FIGURE 8: Indentation AFM profile of conversion film after 1 hour: (a) 2D, (b) 3D, and (c) cross-section.

TABLE 2: Nanoindentation areas at different film formation times.

Time	1 s	1 min	5 min	15 min	30 min	1 h	3 h	8 h
A1 ( $\text{nm}^2$ )	30027.6	57471.2	50991.5	43761.0	55972.8	56556.7	63698.0	76112.8
A2 ( $\text{nm}^2$ )	36023.2	59354.2	51352.4	44215.1	56547.2	57358.9	65324.1	79865.7

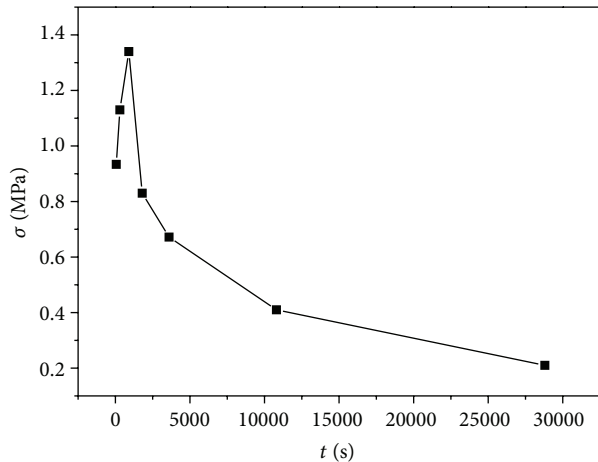


FIGURE 9: Residual stress variation of conversion film at different formation times.

leads to gradual cracking in film surface, and the residual stress is released, the surface roughness increases, and mechanical property decreases. In film formation process, the corrosion property of film also changes with the quality of film, first increases and then decreases. Therefore, the determination of residual stress and cracking time is the key factor to optimize preparation techniques and control film quality.

## Acknowledgments

This work is financially supported by National Basic Research Program of China (973 Program) (no. 2011CB013404), National Natural Science Foundation of China (nos. 51275105 and 51375106), Fundamental Research Funds for the Central Universities (no. HEUCF20130910003), and Foundation of Heilongjiang (nos. QC2010108 and E201026).

## References

- [1] T. Ishizaki, R. Kudo, T. Omi et al., "Corrosion resistance of multilayered magnesium phosphate/magnesium hydroxide film formed on magnesium alloy using steam-curing assisted chemical conversion method," *Electrochimica Acta*, vol. 62, no. 15, pp. 19–29, 2012.
- [2] D. K. Heller, W. G. Fahrenholtz, and M. J. O'Keefe, "Chemical and structural analyses of subsurface crevices formed during spontaneous deposition of cerium-based conversion coatings," *Materials Characterization*, vol. 62, no. 11, pp. 1071–1075, 2011.
- [3] D. P. Dubal, D. S. Dhawale, R. R. Salunkhe, and C. D. Lokhande, "A novel chemical synthesis of  $Mn_3O_4$  thin film and its stepwise conversion into birnessite  $MnO_2$  during super capacitive studies," *Journal of Electroanalytical Chemistry*, vol. 647, no. 1, pp. 60–65, 2010.
- [4] X. B. Chen, X. Zhou, T. B. Abbott, M. A. Easton, and N. Birbilis, "Double-layered manganese phosphate conversion coating on magnesium alloy AZ91D: insights into coating formation, growth and corrosion resistance," *Surface and Coatings Technology*, vol. 217, pp. 147–155, 2013.
- [5] X. F. Cui, G. Jin, Q. F. Li, Y. Y. Yang, Y. Li, and F. H. Wang, "Electroless Ni–P plating with a phytic acid pretreatment on AZ91D magnesium alloy," *Materials Chemistry and Physics*, vol. 121, no. 1–2, pp. 308–313, 2010.
- [6] Y. Liu, D. Beckett, and D. Hawthorne, "Effect of heat treatment, top coatings and conversion coatings on the corrosion properties of black electroless Ni–P films," *Applied Surface Science*, vol. 257, no. 9, pp. 4486–4494, 2011.
- [7] W. C. Say, C. C. Chen, and S. J. Hsieh, "Electrochemical characterization of non-chromate surface treatments on AZ80 magnesium," *Materials Characterization*, vol. 59, no. 10, pp. 1400–1406, 2008.
- [8] A. A. Zuleta, E. Correa, M. Sepúlveda et al., "Effect of  $NH_4HF_2$  on deposition of alkaline electroless Ni–P coatings as a chromium-free pre-treatment for magnesium," *Corrosion Science*, vol. 55, pp. 194–200, 2012.
- [9] E. M. Qureshi, A. M. Malik, and N. U. Dar, "Residual stress fields due to varying tack welds orientation in circumferentially welded thin-walled cylinders," *Advances in Mechanical Engineering*, vol. 2009, Article ID 351369, 9 pages, 2009.
- [10] R. Yahata and H. Kozuka, "Stress evolution of sol-gel-derived silica coatings during heating: the effects of the chain length of alcohols as solvents," *Thin Solid Films*, vol. 517, no. 6, pp. 1983–1988, 2009.
- [11] J. G. Wang, Y. Wang, and Z. Q. Huo, "Finite element residual stress analysis of planetary gear tooth," *Advances in Mechanical Engineering*, vol. 2013, Article ID 761957, 12 pages, 2013.
- [12] E. Ferchaud, F. Christien, V. Barnier, and P. Paillard, "Characterisation of Ga-coated and Ga-brazed aluminium," *Materials Characterization*, vol. 67, no. 1, pp. 17–26, 2012.
- [13] N. Bay, M. Eriksen, X. Tan, and O. Wibom, "A friction model for cold forging of aluminum, steel and stainless steel provided with conversion coating and solid film lubricant," *CIRP Annals*, vol. 60, no. 1, pp. 303–306, 2011.
- [14] R. Asthana, A. Kumar, and N. B. Dahotre, "Coatings and surface engineering," *Journal of Materials Processing and Manufacturing Science*, no. 5, pp. 313–395, 2006.
- [15] S. M. Wong, "Residual stress measurements on chromium films by X-ray diffraction using the  $\sin^2\psi$  method," *Thin Solid Films*, vol. 53, no. 1, pp. 65–71, 1978.
- [16] S. Suresh and A. E. Giannakopoulos, "A new method for estimating residual stresses by instrumented sharp indentation," *Acta Materialia*, vol. 46, no. 16, pp. 5755–5767, 1998.

## Research Article

# Dynamic Mechanical Behaviors of 6082-T6 Aluminum Alloy

Peng Yibo,<sup>1</sup> Wang Gang,<sup>1</sup> Zhu Tianxing,<sup>1</sup> Pan Shangfeng,<sup>1</sup> and Rong Yiming<sup>1,2</sup>

<sup>1</sup> Department of Mechanical Engineering, Tsinghua University, Beijing 100084, China

<sup>2</sup> Department of Mechanical Engineering, Worcester Polytechnic Institute, Worcester, MA 01609, USA

Correspondence should be addressed to Wang Gang; gwang@mail.tsinghua.edu.cn

Received 10 July 2013; Revised 8 October 2013; Accepted 8 October 2013

Academic Editor: Feng Jiang

Copyright © 2013 Peng Yibo et al. This is an open access article distributed under the Creative Commons Attribution License, which permits unrestricted use, distribution, and reproduction in any medium, provided the original work is properly cited.

The structural components of high speed trains are usually made of aluminum alloys, for example, 6082. The dynamic mechanical behavior of the material is one of key factors considered in structural design and safety assessment. In this paper, dynamic mechanical experiments were conducted with strain rate ranging from  $0.001\text{ s}^{-1}$  to  $100\text{ s}^{-1}$  using Instron tensile testing machine. The true stress-strain curves were fitted based on experimental data. Johnson-Cook model of 6082-T6 aluminum alloy was built to investigate the effect of strain and strain rate on flow stress. It has shown that the flow stress was sensitive to the strain rate. Yield strength and tensile strength increased with a high strain rate, which showed strain rate effect to some extent. Fracture analysis was carried out by using Backscattered Electron imaging (BSE). As strain rate increased, more precipitates were generated in fracture.

## 1. Introduction

The type 6 aluminum alloys belong to the moderate intensity alloy. Due to their excellent extrusion resistance, weld ability, and corrosion resistance, they were widely used in the railway train, automobile, aviation, and other transport means [1]. As the technology of high-speed rail continues to develop, 6082-T6 aluminum alloy was widely used as high-speed rail body material due to its light weight and excellent mechanical properties. The survey has found that the strain rate of 6082-T6 aluminum alloy is about  $70\text{ s}^{-1}$  during the service; therefore, studying the mechanical properties under different strain rate and building a high-precision material constitutive model are of great importance to the safety of the trains. Currently, studies of 6082-T6 aluminum alloy mainly focused on its weld ability, failure, and heat treatment [2–5], but few studies have been focused on its constitutive model, especially for secondary strain rate constitutive model.

In this paper, five repeated tensile tests were carried out using Instron tensile testing machine under each strain rate, and complete stress-strain curves were obtained from quasistatic to moderate strain rates ( $0.001\text{ s}^{-1}$ – $100\text{ s}^{-1}$ ). Johnson-Cook model of 6082-T6 aluminum alloy was built to investigate the effect of strain and strain rate on flow stress. Fracture analysis was carried out by using Back-scattered Electron imaging (BSE).

## 2. Experimental Design

Experimental materials were 6082 aluminum plate specimens with T6 aging treatment (insulated for 8 hours at  $175^\circ\text{C}$  after solution treatment at  $500\text{--}540^\circ\text{C}$ ). Its chemical composition was shown in Table 1 and its mechanical properties were shown in Table 2 [6].

The experiment used two types of samples showed in Figure 1. The typical rectangular cross-section sample was used under low strain rate ( $0.001\text{ s}^{-1}$ – $1\text{ s}^{-1}$ ), with the gauge length of 30 mm, thickness of 4 mm, and width of 10 mm; the clamping segment length on both ends is 35 mm. Under moderate strain rate ( $10\text{ s}^{-1}$ – $100\text{ s}^{-1}$ ), samples with extended gripping end were used. Other parameters stay the same as the specimen under low strain rate. The samples used under different strain rate were showed in Table 3.

For the low strain rate ( $0.001\text{ s}^{-1}$ – $1\text{ s}^{-1}$ ) experiments, Instron 8874 tensile testing machine was used. And VHS 160-100-20 type tensile testing machine was used for medium strain rate ( $10\text{ s}^{-1}$ – $100\text{ s}^{-1}$ ) experiments. The maximum tensile speed of this tensile testing machine is 20 m/s, and the maximum load is 160 t. The noncontact digital speckle method [7] was used to measure the stress and strain. To eliminate the impact of the initial acceleration process of the testing machine on strain rate, an air-way area of the samples was designed. At this stage, the testing machine accelerated

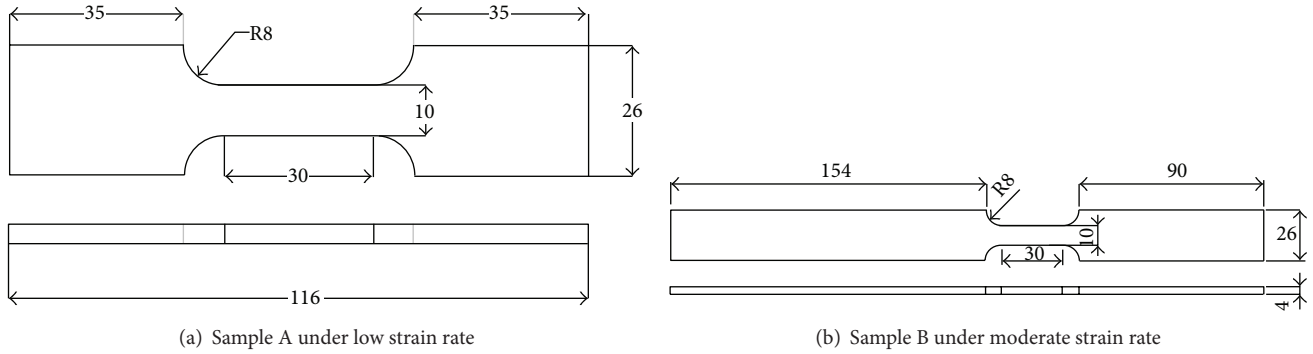


FIGURE 1: 6082-T6 aluminum alloy specimens.

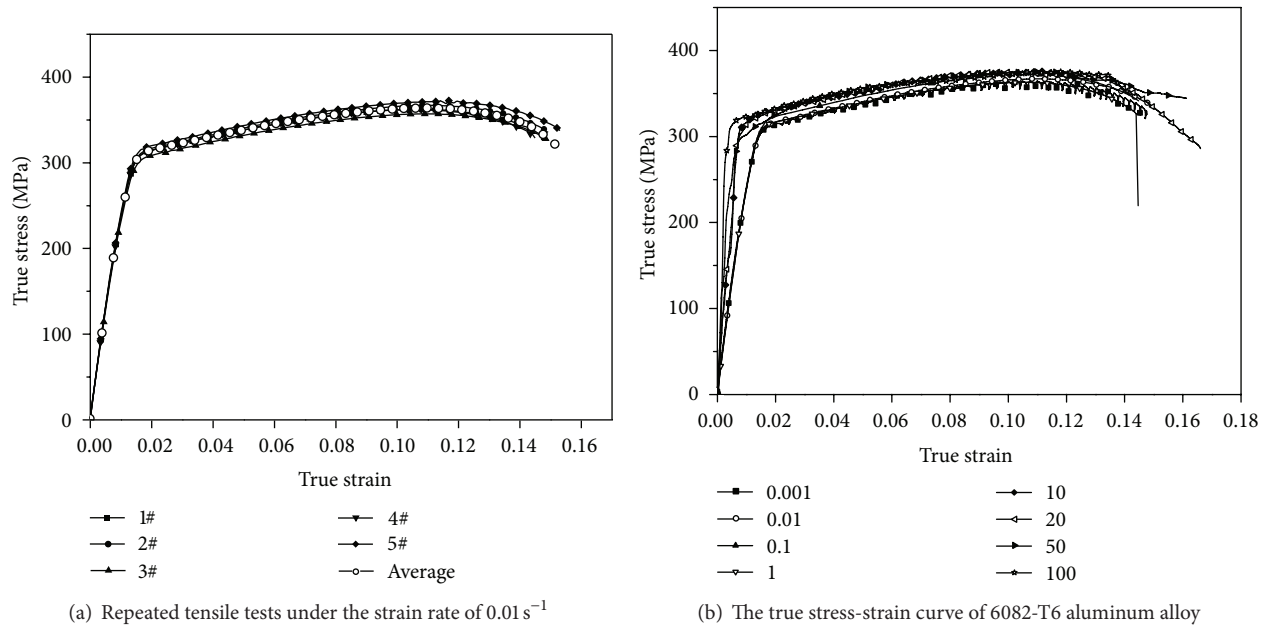


FIGURE 2: The true stress-strain curve.

when the speed reached a predetermined rate and then the load was added.

### 3. Results and Analysis

**3.1. Stress-Strain Curve.** Figure 2 showed the true stress-strain curves of 6082-T6 aluminum alloy, and the overall shapes of the curves were on the elastic stage; the flow stress increased rapidly as the strain increased. When the stress reached a certain point, the material began to yield. After entering the plastic stage, under the effects of work-hardening and dynamic recovery, flow stress increased much slower than the beginning part. When the stress reached a certain value, the material began necking and local stress increased sharply [8, 9].

Since the material showed no significant yield point, therefore the strain of 0.2% was used as the yield point; the yield strength and tensile strength were shown in Table 4. As the strain rate increased from  $0.001 \text{ s}^{-1}$  to  $100 \text{ s}^{-1}$ , the yield

TABLE 1: 6082-T6 aluminum alloy chemical composition.

Si	Mg	Fe	Cu	Mn	Cr	Zn	Ti	Others	Al
0.7-1.3	0.6-1.2	$\leq 0.5$	$\leq 0.1$	0.4-1	$\leq 0.25$	0.2	$\leq 0.1$	0.15	Balance

TABLE 2: 6082-T6 aluminum alloy mechanical properties.

Alloy	$\delta_h$	$\delta_{p0.2}$	$\delta$
6082-T6	310	260	8%

TABLE 3: Tensile test condition setting.

Sample	A	A	A	A	B	B	B	B
Strain rate/ $\text{s}^{-1}$	0.001	0.01	0.1	1	10	20	50	100

stress increased from 306.1 MPa to 322.63 MPa, increased by 5.4%, and the tensile strength increased from 364 MPa to 384 MPa, increased by 5.49%. Yield strength and tensile

TABLE 4: Yield and tensile strength of 6082-T6 alloy under different strain rate.

Strain rate/s <sup>-1</sup>	0.001	0.01	0.1	1	10	20	50	100
$\sigma_s$ /MPa	306.10	309.61	309.19	311.74	313.79	317.04	321.67	322.63
$\sigma_p$ /MPa	364	367	372.55	367.83	373.35	374.81	375.54	384

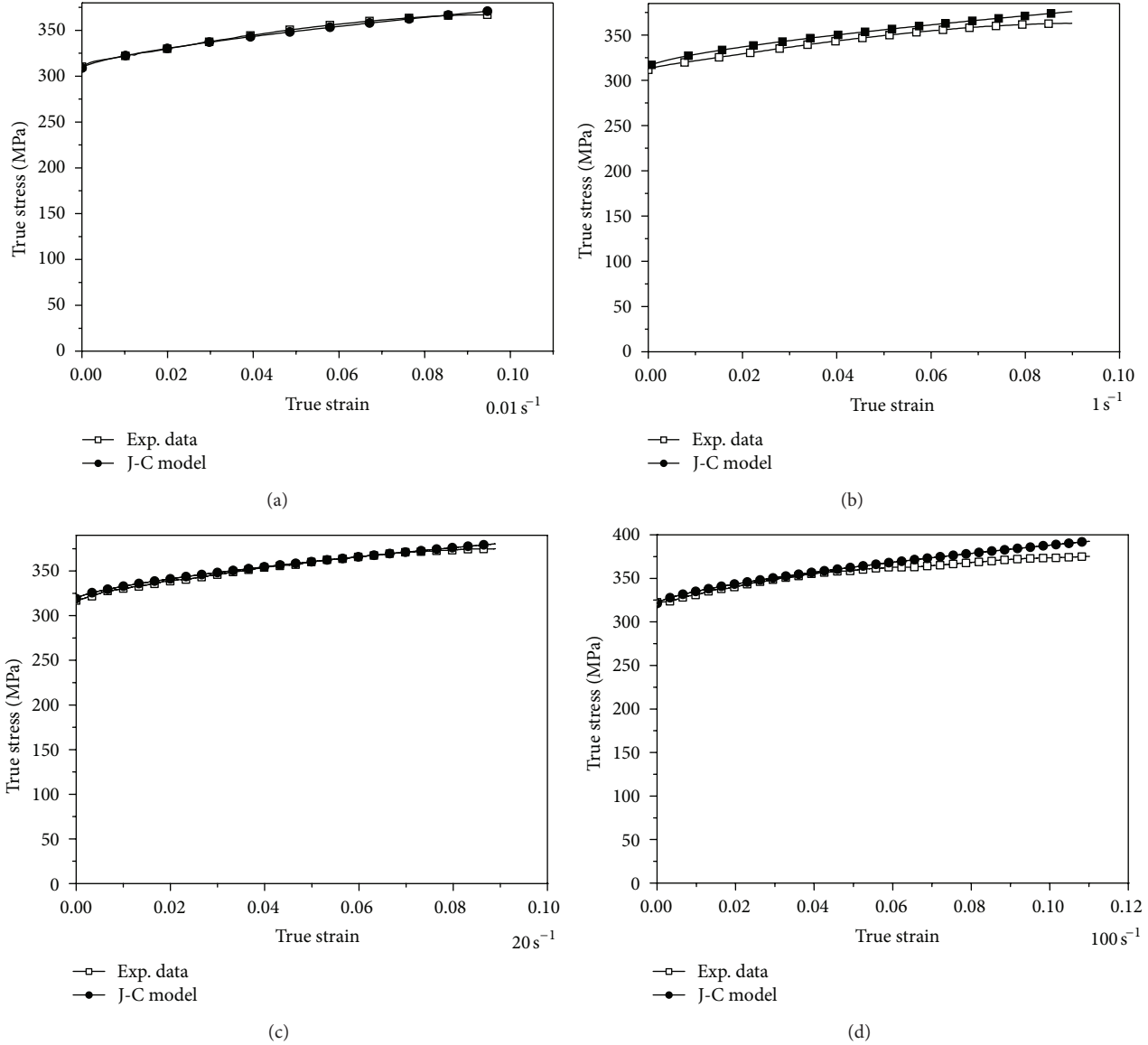


FIGURE 3: Constitutive model and experimental curves.

strength increased with a high strain rate, which showed strain rate hardening effect to some extent.

Generally, in the plastic stage, flow stress increased due to dislocation motion and the result of the interaction of dislocations. At the beginning of the plastic stage, a large number of dislocations formed and began to expand at the action of stress. When the dislocations crossed the grain boundary and other dislocations or precipitates, they stopped and induced stress. Meanwhile, the second phase particles on the grain boundary had pinning effect, which hindered

the grain boundary sliding and grain growth to improve the strength of the material [10]. Therefore, the alloy could withstand a larger force.

3.2. *Constitutive Model.* The most commonly used thermal-viscoelastic constitutive models were Johnson-Cook model, Zerilli-Armstrong model, Follansbee-Kocks model, and Bodner-Paton model [11]. As Johnson-Cook model clearly expressed hardening, strain rate hardening, and temperature softening effects, this paper would adopt Johnson-Cook

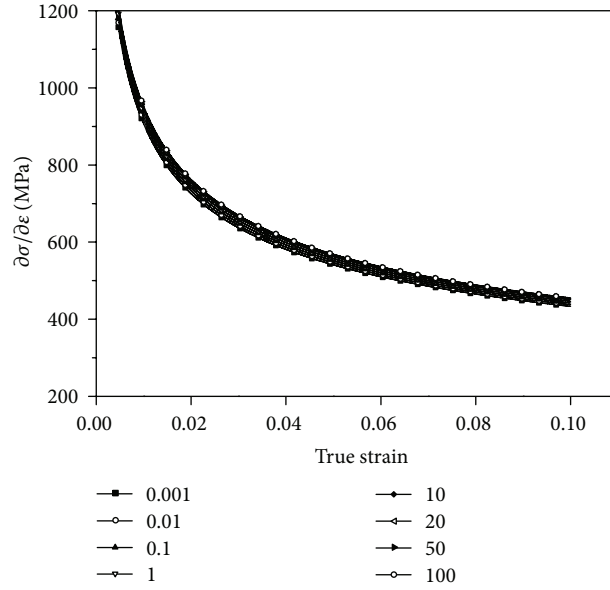


FIGURE 4: Strain on flow stress.

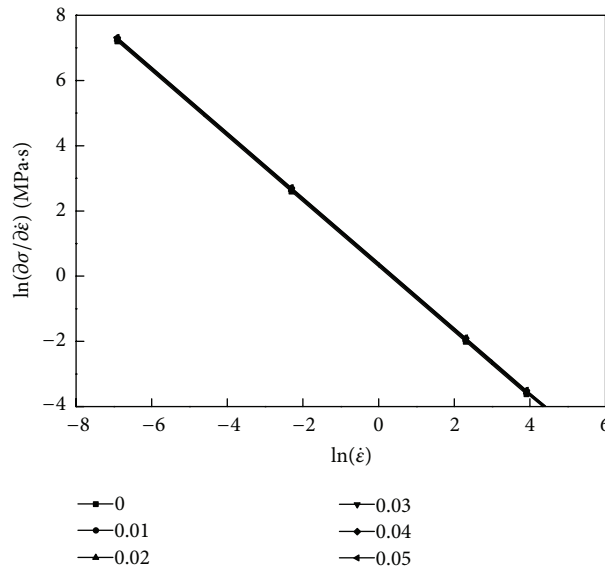


FIGURE 5: Strain rate on flow stress.

model building the constitutive model of 6082-T6 aluminum alloy. The expression of Johnson-Cook model was

$$\sigma = (A + B\varepsilon_p^n)(1 + C \ln \dot{\varepsilon}^*)(1 - T^{*m}). \quad (1)$$

And  $(A + B\varepsilon_p^n)$ ,  $(1 + C \ln \dot{\varepsilon}^*)$ ,  $(1 - T^{*m})$  described the effect of hardening, strain rate hardening, and temperature softening effects, respectively.  $\sigma$  was the von-Mises flow stress,  $A$  was yield strength,  $B$  and  $n$  were strain hardening parameters,  $C$  was the strain rate sensitivity coefficient, and  $m$  was the temperature softening effect coefficient.  $\varepsilon_p$  was the equivalent plastic strain, and  $\dot{\varepsilon}^*$  was the dimensionless equivalent strain rate.  $T^*$  was the dimensionless temperature item.

Since the experiments were carried out at room temperature, the constitutive equation could be simplified as

$$\sigma = (A + B\varepsilon_p^n)(1 + C \ln \dot{\varepsilon}^*). \quad (2)$$

By fitting the experimental data, the Johnson-Cook model of 6082-T6 aluminum alloy was achieved as follows:

$$\sigma = (305.72 + 304.9\varepsilon_p^{0.6796})(1 + 0.00437 \ln \dot{\varepsilon}^*). \quad (3)$$

Figure 3 showed the experimental data and Johnson-Cook model under different strain rate. As can be seen, the Johnson-Cook model and experiment data met good agreement. The dynamic properties of 6082-T6 aluminum

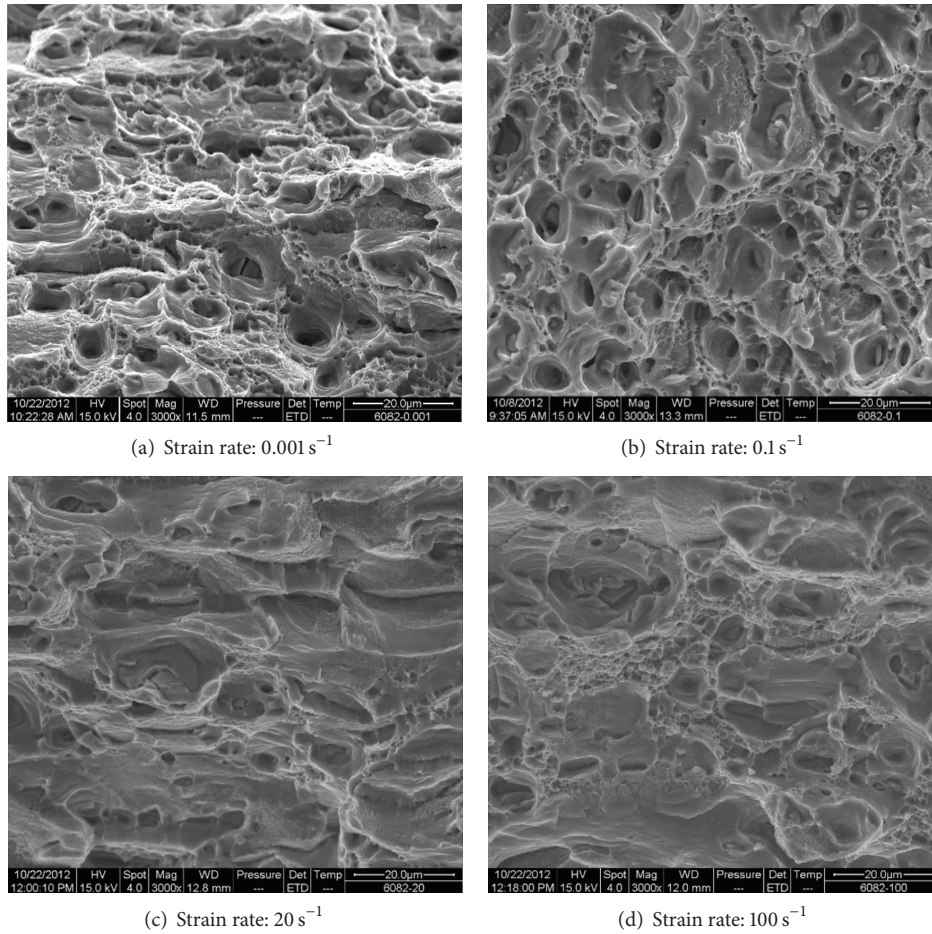


FIGURE 6: SEM photographs of fracture under strain rates of  $0.001 \text{ s}^{-1}$  and  $100 \text{ s}^{-1}$ .

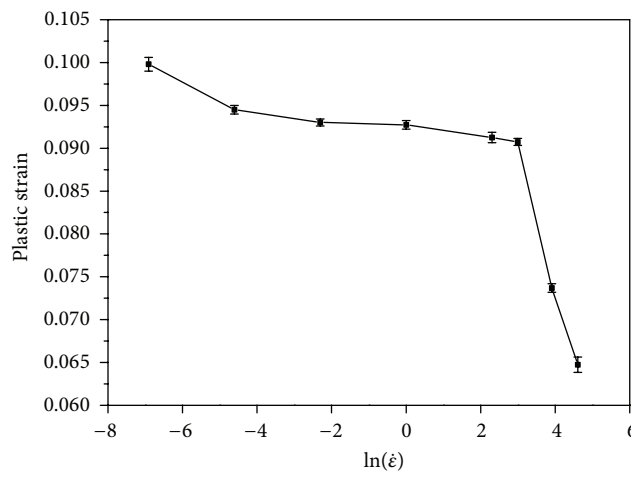


FIGURE 7: Plastic strain under different strain rate.

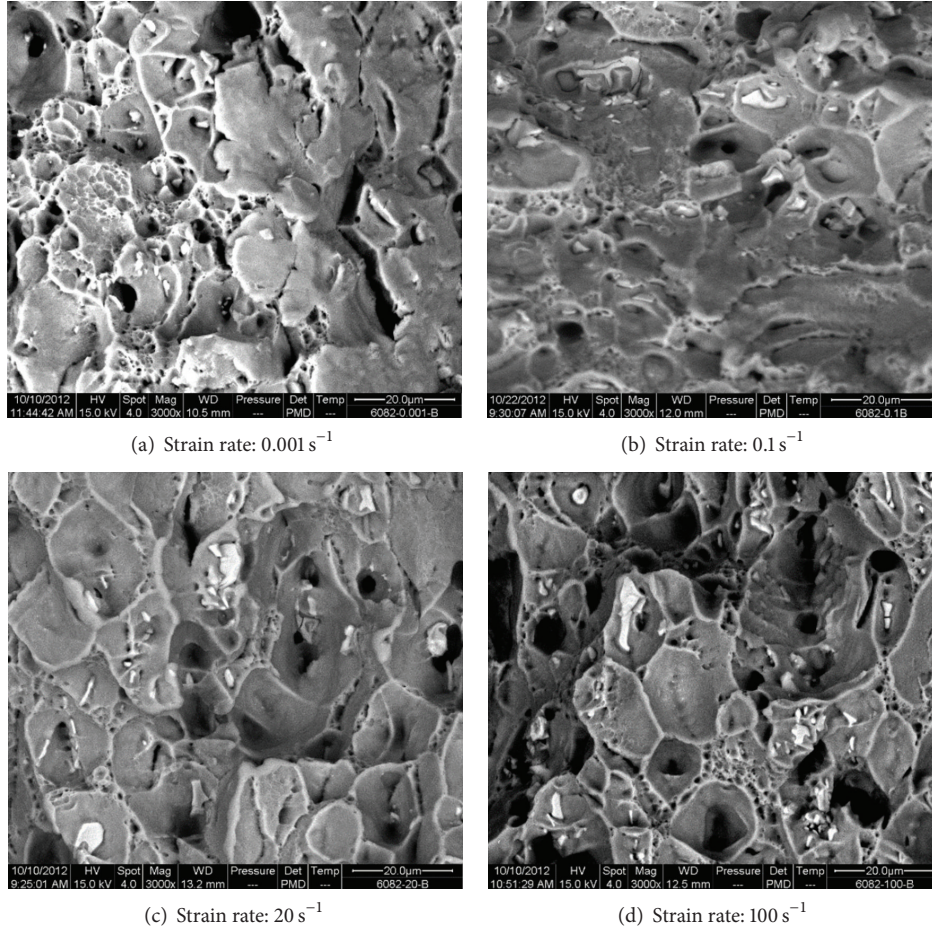


FIGURE 8: Backscattered photo of 6082-T6 aluminum alloy fracture.

alloy fit very well using Johnson-Cook model with the strain rate ranging from  $0.001 \text{ s}^{-1}$  to  $100 \text{ s}^{-1}$ .

**3.3. Strain and Strain Rate on the Flow Stress.** The constitutive equations of 6082-T6 aluminum alloy could be described as:

$$\sigma = (305.72 + 304.9\epsilon_p^{0.6796}) (1 + 0.00437 \ln \dot{\epsilon}^*). \quad (4)$$

The effect of strain and strain rate on flow stress could be described as follows:

$$\begin{aligned} \frac{\partial \sigma}{\partial \epsilon} &= 0.6796 \cdot 304.9\epsilon_p^{-0.3204} \cdot (1 + 0.00437 \ln \dot{\epsilon}^*) \\ &= 207.2\epsilon_p^{-0.3204} \cdot (1 + 0.00437 \ln \dot{\epsilon}^*) \end{aligned} \quad (5)$$

$$\frac{\partial \sigma}{\partial \dot{\epsilon}} = (305.72 + 304.9\epsilon_p^{0.6796}) \cdot 0.00437 \cdot \frac{1}{\dot{\epsilon}^*}.$$

Figure 4 showed the effect of strain on the flow stress. As can be seen, at a determined strain rate, the flow stress increased rapidly as the strain increased in the initial stage, then, the growth rate decreased; and remained at a low level above zero, which meant that without other factors, the stress would get bigger and bigger as the strain increased, and

this was because that, under the influence of stress, new dislocations developed, and even secondary slipping system started moving; thus, the material could bear a higher force.

Generally, strain rate sensitivity was related to microstructure of the material. Referring to the research of Humphrey and Jankowski [13], the effect of strain rate for the yield strength could be divided into three stages. The first stage is called nonthermal activation zone, and in this stage, the stress was not sensitive to strain rate. The second stage was more sensitive to strain rate due to dislocation motion controlled thermal activation mechanism. As the strain rate increased, phonon drag phenomenon occurred at this time, and the flow stress was more sensitive to strain rate [12–16].

In this study, the nonthermal activation mechanism was the main mechanism for controlling the flow stress. Figure 5 showed that in the nonthermal activation zone, as the strain rate increases, changing rate of stress over strain decreases, the stress increment caused by nonthermal activation mechanism is limited.

**3.4. Fracture Analysis.** Basically, ductile damage was described by void nucleation, growth, coalescence, and final fracture. Figure 6 showed the SEM photographs of fracture under strain rates of  $0.001 \text{ s}^{-1}$ ,  $0.1 \text{ s}^{-1}$ ,  $20 \text{ s}^{-1}$ , and  $100 \text{ s}^{-1}$ . Dimples

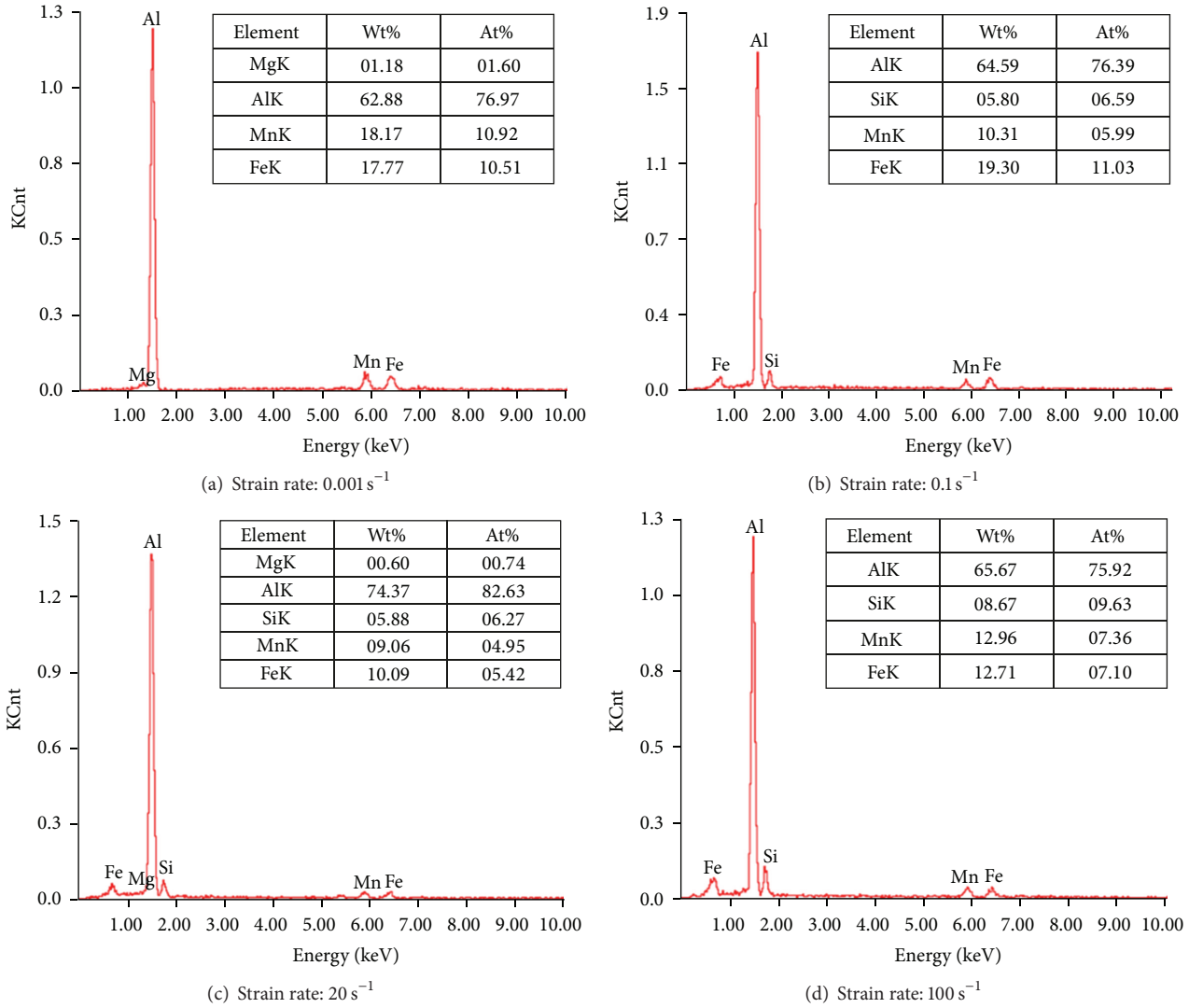


FIGURE 9: Precipitates composition analysis.

observed in SEM micrographs represented microvoids created during the tensile test. The parabolic shaped impressions shown in micrograph at failure may be representing shear failure as expected in ductile materials. As can be seen in Figure 8, the dimples in lower strain rate were smaller and well centered in shape. However a combination of small and large dimples was observed in high strain rate. As the strain rate increased, the percentage of dimples decreased, which meant that the material showed more brittleness. Besides, the dimples under lower strain rate were deeper than those under higher strain rate [17, 18].

Figure 7 showed the plastic strain under different strain rate. As can be seen, with the strain rate increasing, the plastic strain decreased and showed more brittleness. Usually, dimples were on behalf of toughness, and cleavage fracture represented brittleness. Dimples were the result of empty aggregation. At first, spaces formed inside the material and gradually grew together with other spaces under the action of the slip and then the dimples were formed. Cleavage fracture

surface occurred along a certain crystal plane, when two cleavage crack intersected, cleavage steps formed. Because there existed the situation that when positive cleavage come across negative cleavage, they will offset one another, the cleavage tends to expand to plane. As more cleavage appeared at a higher strain rate, the plastic strain got smaller than that at a lower strain rate.

Figure 8 showed the backscatter photos of 6082-T6 aluminum alloy. The light particles were in second phase, and it showed that the second phase particles were rich in Mn, Mg, Si, Fe, and other elements (Figure 9). There were mainly two kinds of precipitates: precipitates with Mg element and precipitates without Mg element. Among all the 32 randomly selected precipitates (4 under each strain rate), only 31.2% percent had element of Mg. Usually, aluminum and magnesium formed compound of  $\text{Al}_8\text{Mg}_5$ , but it is hard to nucleate and the size was small, playing a limited role in strengthening the material [19]. The average mass fraction of Si element, Fe element, Mn element, and Al element in

the other precipitates was about 6.96%, 15.89%, 9.67%, and 67.4% and showed strain rate that is independent. This meant that the precipitates were nearly all of the same kind. And the precipitation strengthening was mainly determined by the number of precipitates.

Figure 8 showed the precipitates under the strain rate of  $0.001\text{ s}^{-1}$ ,  $0.1\text{ s}^{-1}$ ,  $20\text{ s}^{-1}$ , and  $100\text{ s}^{-1}$ ; as strain rate increased, more precipitates were generated in fracture. The size of the precipitates is usually small in a low strain rate; as the strain rate increased, a combination of small and big precipitates appeared. This meant that as the stretching rate increased, precipitates grew with greater speed. The bigger precipitates precipitated before the smaller ones.

Generally, the second phase particles on the grain boundary had pinning effect, which hindered the grain boundary sliding and grain growth to improve the strength of the material. With more precipitates generated in fracture, the dislocation would encounter more obstacles when moving, thus reducing the amount of plastic deformation. Meanwhile, particles crossed by the dislocation loop will have a repulsive force, which will create resistance against the dislocation loop propagation, the existence of more dislocation loops will face more resistance by the particles generating higher resistance forces. In order to maintain deformation compatibility, more dislocations would start to move, so the material could bear higher stress.

#### 4. Conclusions

In this paper, complete stress-strain curves of 6082-T6 aluminum alloy were obtained with strain rate varying from quasistatic ( $10^{-3}\text{ s}^{-1}$ ) to moderate strain rate ( $100\text{ s}^{-1}$ ). The Johnson-Cook constitutive model was built based on experimental data. The effect of strain rate and strain on the flow stress was discussed. Finally, the fracture was analyzed on morphology and precipitates.

6082-T6 aluminum alloy has low strain rate sensitivity. The established Johnson-Cook constitutive equation of 6082-T6 aluminum alloy has good agreement with experiment data with a strain rate from  $10^{-3}\text{ s}^{-1}$  to  $100\text{ s}^{-1}$  at room temperature. As the strain rate increases, changing rate of stress over strain decreases. It can be seen that more precipitates appear with an increasing strain rate through BSE graphic analysis, which may enhance the pinning effect on grain boundaries.

#### Acknowledgments

The research has been financially supported by the National Basic Research Program of China (2011CB013404) and the National Science and Technology Major Project of the Ministry of Science and Technology of China under Project (2012ZX04012011).

#### References

- [1] G. Wang and Z. Yin, "6005 aluminum alloy isothermal transformation curve drawing and its application," *Journal of Materials Engineering*, vol. 32, no. 2, 2012.
- [2] K. L. Nielsen, T. Pardoën, V. Tvergaard, B. de Meester, and A. Simar, "Modelling of plastic flow localisation and damage development in friction stir welded 6005A aluminium alloy using physics based strain hardening law," *International Journal of Solids and Structures*, vol. 47, no. 18-19, pp. 2359–2370, 2010.
- [3] T. Pardoën, F. Scheyvaerts, A. Simar, C. Tekoğlu, and P. R. Onck, "Multiscale modeling of ductile failure in metallic alloys," *Comptes Rendus Physique*, vol. 11, no. 3-4, pp. 326–345, 2010.
- [4] W. Yang, L. Huang, R. Zhang et al., "Electron microscopy studies of the age-hardening behaviors in 6005A alloy and microstructural characterizations of precipitates," *Journal of Alloys and Compounds*, vol. 514, pp. 220–233, 2012.
- [5] G. Mrówka-Nowotnik and J. Sieniawski, "Influence of heat treatment on the microstructure and mechanical properties of 6005 and 6082 aluminium alloys," *Journal of Materials Processing Technology*, vol. 162-163, pp. 367–372, 2005.
- [6] Online Materials Information Resource, <http://www.matweb.com/>.
- [7] F. Labbé, "Strain-rate measurements by electronic speckle-pattern interferometry (ESPI)," *Optics and Lasers in Engineering*, vol. 45, no. 8, pp. 827–833, 2007.
- [8] H.-Z. Li, X.-M. Zhang, M.-A. Chen, and Z.-P. Zhou, "Hot deformation behavior of 2519 aluminum alloy," *The Chinese Journal of Nonferrous Metals*, vol. 15, no. 4, pp. 621–625, 2005.
- [9] W.-G. Guo and H.-W. Tian, "Strain rate sensitivity and constitutive models of several typical aluminum alloys," *The Chinese Journal of Nonferrous Metals*, vol. 19, no. 1, pp. 56–61, 2009.
- [10] Y. Huang, Y. Wang, and Z. Chen, "Phase-field simulation of second phase particles precipitated along the grain and pinning effect," *Rare Metal Materials and Engineering*, no. 10, 2012.
- [11] R. Liang and A. S. Khan, "A critical review of experimental results and constitutive models for BCC and FCC metals over a wide range of strain rates and temperatures," *International Journal of Plasticity*, vol. 15, no. 9, pp. 963–980, 1999.
- [12] M. L. Wilkins, R. D. Streit, and J. E. Reaugh, "Cumulative strain-damage model of ductile fracture: simulation and prediction of engineering fracture tests," Tech. Rep. UCRL-53058, Lawrence Livermore Laboratory, Livermore, Calif, USA, 1980.
- [13] R. T. Humphrey and A. F. Jankowski, "Strain-rate sensitivity of strength in macro-to-micro-to-nano crystalline nickel," *Surface and Coatings Technology*, vol. 206, no. 7, pp. 1845–1849, 2011.
- [14] Y. Bao, "Dependence of ductile crack formation in tensile tests on stress triaxiality, stress and strain ratios," *Engineering Fracture Mechanics*, vol. 72, no. 4, pp. 505–522, 2005.
- [15] M. L. Wilkins, R. D. Streit, and J. E. Reaugh, "Cumulative strain-damage model of ductile fracture: simulation and prediction of engineering fracture tests," Tech. Rep. UCRL-53058, Lawrence Livermore Laboratory, Livermore, Calif, USA, 1980.
- [16] S. E. Clift, P. Hartley, C. E. N. Sturgess, and G. W. Rowe, "Fracture prediction in plastic deformation processes," *International Journal of Mechanical Sciences*, vol. 32, no. 1, pp. 1–17, 1990.
- [17] B. M. Darras, F. H. Abed, S. Pervaiz, and A. Abdul-Latif, "Analysis of damage in 5083 aluminum alloy deformed at different strain rates," *Materials Science & Engineering A*, vol. 568, pp. 143–149, 2013.
- [18] Y. Chen, S. Zheng, J. Tu et al., "Fracture characteristics of notched investment cast TiAl alloy through in situ SEM observation," *Transactions of Nonferrous Metals Society of China*, vol. 22, no. 10, pp. 2389–2394, 2012.
- [19] R. Tian, *Cast Aluminum*, Central South University Press, 2006.

## Research Article

# Vertical Spindle Grinding of Si and Granite with a New Abrasive Disk

Yiqing Yu, Juan Liu, Bin Kuang, Jianyun Shen, and Xipeng Xu

*The Ministry of Education Research Center for Machining of Brittle Materials, Huaqiao University, Xiamen 361021, China*

Correspondence should be addressed to Yiqing Yu; yyqing@hqu.edu.cn

Received 27 July 2013; Accepted 17 October 2013

Academic Editor: Gang Wang

Copyright © 2013 Yiqing Yu et al. This is an open access article distributed under the Creative Commons Attribution License, which permits unrestricted use, distribution, and reproduction in any medium, provided the original work is properly cited.

An investigation was reported of a new attempt in the fabrication of an ultrafine abrasive tool for vertical spindle grinding. The principle of sol-gel was applied to granulate ultra-fine abrasives in order to reduce their aggregation. The granulated abrasives were then added to resin bonds, thereby forming ultra-fine abrasive grinding disks. Before grinding, the disks were dressed to expected flatness using a brazed diamond pad. The dressed grinding disks were then used to grind silicon wafers and natural granite. Both dressing and grinding were conducted on a high precision vertical spindle grinding machine. After grinding, the morphologies of the workpiece materials were examined. With regard to the different concerns for silicon wafers and granite, surface roughness was measured for the silicon wafers and gloss readings were measured for the granite surfaces. It was found that the brazed diamond abrasives could dress the grinding disks with high efficiency and satisfactory flatness. The new ultra-fine abrasive disks were found to be able to process silicon wafers and granite slabs to acceptable results.

## 1. Introduction

Grinding with ultrafine abrasive tools is one of the most widely used processes for precision machining of many materials such as ceramics, glass, natural stone materials, and novel materials used in the semiconductor industry [1–4]. In the production of ultrafine abrasive tools for grinding, resin and copper are two common bonds, in which case ultrafine abrasives are supposed to distribute uniformly in either resin or copper. However, ultrafine abrasives tend to agglomerate with the decrease of grit sizes due to the increase of abrasive surface energies [5]. Accordingly, it is almost impossible to let ultrafine abrasives distribute uniformly in the bonds only by traditional powder metallurgical techniques. As a result of random distribution of ultrafine abrasives in the bonds, it is quite difficult to control the precision and surface quality of components during grinding with ultrafine abrasives.

Therefore, tremendous studies have been done during the past decades in order to improve the dispersing of ultrafine abrasives in resin or metal bonds. Nakamura et al. proposed a new method to fabricate ultrafine abrasive tools using the principle of sol-gel [6]. Ikeno et al. developed an ultrafine silica abrasive tool by applying an electrophoretic deposition

technology [7]. In our previous study, the sol-gel technique was found to be effective in granulating ultrafine abrasives of diameter greater than  $5\ \mu\text{m}$  [8].

As an attempt to fabricate ultrafine abrasive tools for grinding, the present work was undertaken to combine the granulating ability of sol-gel with the bonding ability of resin. The main purpose of this work is to elucidate the possibility of combining the dispersing of sol-gel granulation and advantages of resin as a bonding matrix. It is hoped that the results obtained in this work will be of benefit to the development of high-performance ultrafine abrasive tools for high precision and cost-effective grinding.

## 2. Fabrication of a New Grinding Disk

In order to reduce the aggregation of ultrafine abrasives in the fabrication of resin-bonded grinding disks, the first step in the present work was to granulate ultrafine abrasives based on the principle of sol-gel. The setup for producing gel spheres containing ultrafine abrasives is illustrated in Figure 1. According to the principle of chemistry, the sodium salt solution of alginate can react with the metallic ion of  $\text{Ca}^{2+}$  and form gels. In the present work, ultrafine abrasives

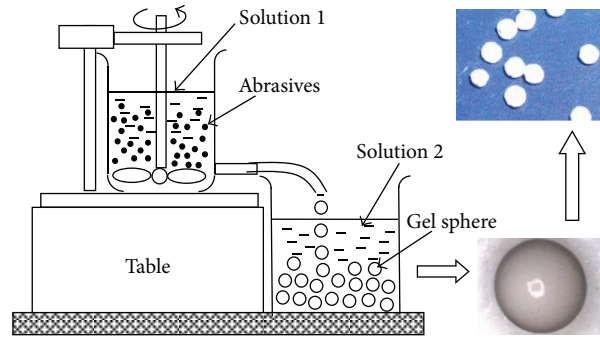


FIGURE 1: The setup for producing gel spheres containing ultrafine abrasives.

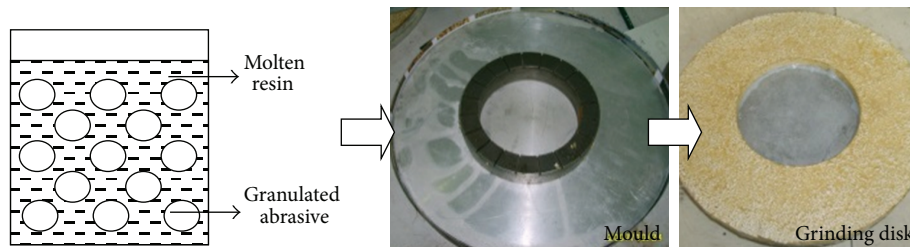


FIGURE 2: The procedure to fabricate the grinding disk.

were added to the sodium alginate solution, indicated as solution 1 in Figure 1. It is well known that it is much easier to make ultrafine abrasives disperse uniformly in a liquid than in such powder bonds as resin and metal. Then, the sodium alginate solutions containing uniformly dispersed abrasives were dropped into the calcium solution, indicated as solution 2 in Figure 1, to produce gel spheres. The nozzle was carefully chosen to make gel spheres with average diameter of 3.5 mm. The concentration of calcium solution was determined through many tests and finally fixed at 2.0 wt%, whereas the sodium salt solution of alginate was 3.0 wt%.

After granulation, the spheres containing ultrafine abrasives were dried to small balls, as shown in Figure 1. These gel-bonded (granulated) ultrafine abrasives were then combined together by resin to form a grinding disk of 320 mm in diameter. To make the grinding disk, the resin was heated up to 80°C and the gel-bonded abrasives were stirred uniformly in the molten resin. Figure 2 shows the procedure to make the grinding disk in the present work.

### 3. Dressing of the Grinding Disk

In order to make the grinding disk flat enough to carry out grinding, an experimental setup (see Figure 3) was proposed to dress the grinding disk fabricated above. Based on our previous study [9], in which case dressing with loose abrasives, bonded  $\text{Al}_2\text{O}_3$  wheel and brazed diamonds were compared and the brazed diamonds were found to be most effective; a brazed diamond pad was used here and the diamond abrasives of 70/80 US mesh were applied (see Figure 4). The grinding disk and dressing pad were installed on a vertical spindle grinding machine to facilitate dressing.

The rotating speeds for the grinding disk and the dressing pad were 250 rpm and 50 rpm, respectively.

A micrometer was used to detect the unevenness of the grinding disk, whereas a Hirox KH-1000 optical microscope attached to a digital video system was used to observe the morphologies of the dressed grinding disk.

The unevenness values of the grinding disk before and after dressing are compared in Figure 5. It should be noted that “outer,” “middle,” and “inner” here are corresponding to three different positions in diameter 277.5 mm, 235 mm, and 192.5 mm, respectively. For the position at a specified diameter, measurements were carried out for 20 times at an equal interval of 18 degrees along the circumference, thereby leading to 20 numbers for each curve in Figure 5. The morphologies of the grinding disk before and after dressing are shown in Figure 6. Both Figures 5 and 6 indicate that the dressing is effective in obviously reducing the unevenness of the grinding disk.

### 4. Grinding of Silicon Wafer and Granite with the Dressed Disk

In order to evaluate the grinding performance of the grinding disk, silicon wafer and granite were chosen as the workpiece materials. The diameter of the silicon wafer was 76 mm with its original surface roughness of  $0.54 \mu\text{m}$  (Ra). Two typical granites, red one and black one, were used, in which case the red one is much harder than the black according to the factory records. The values of shore hardness for the red and black granites are 95 and 76, respectively.

Ultrafine  $\text{Al}_2\text{O}_3$  abrasives of  $5 \mu\text{m}$  were used for fabricating the grinding disks. For grinding of silicon wafers,

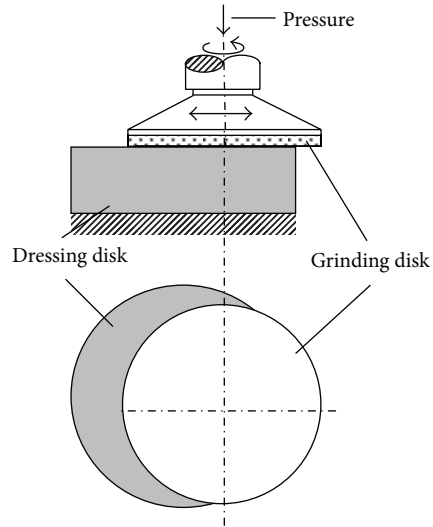
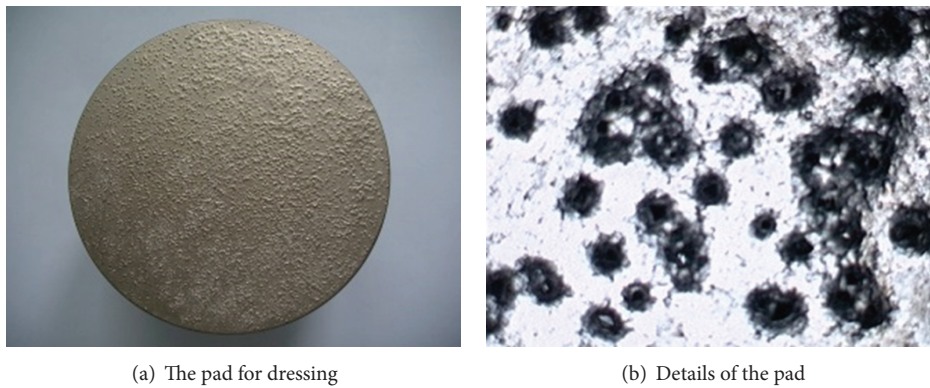


FIGURE 3: The setup to dress the grinding disk.



(a) The pad for dressing

(b) Details of the pad

FIGURE 4: The brazed diamond pad for dressing.

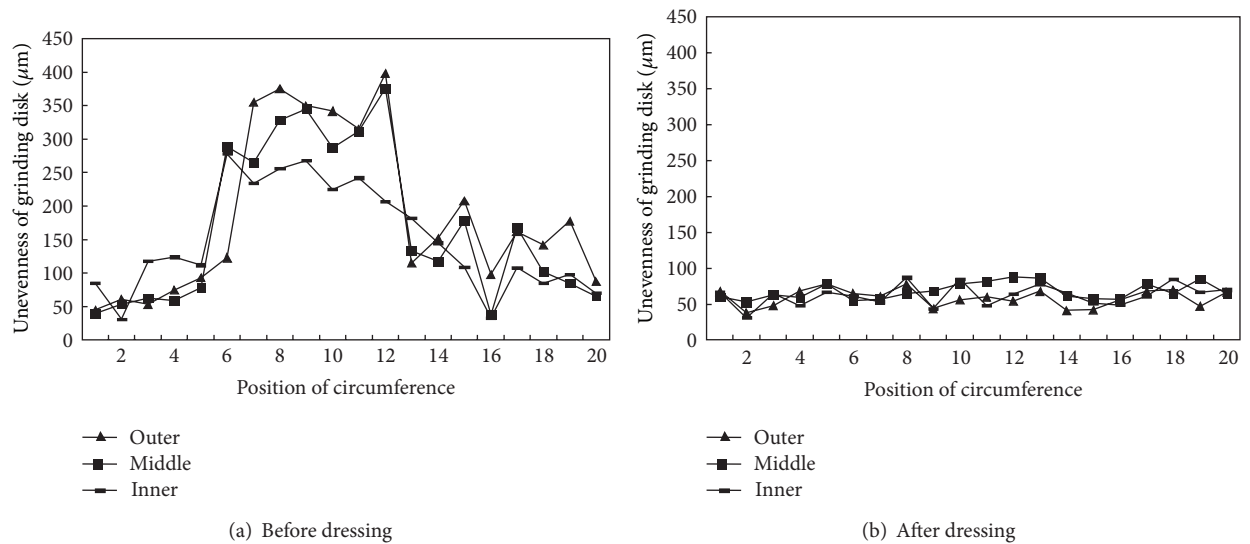


FIGURE 5: Unevenness of grinding disk before/after dressing.

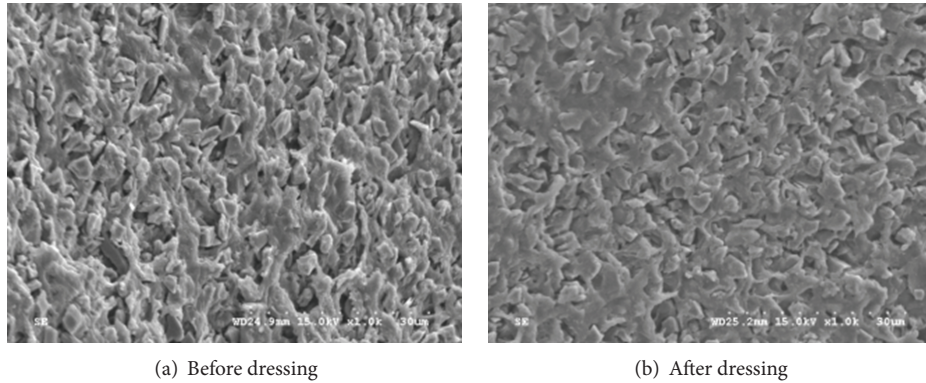


FIGURE 6: Morphologies of the grinding disk (1000x).

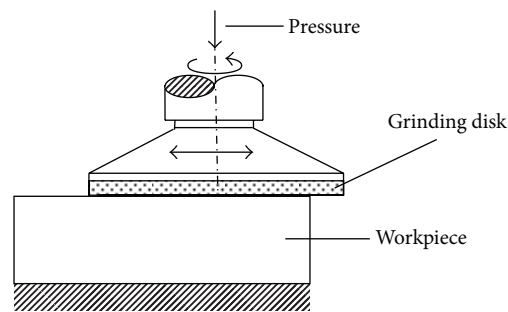


FIGURE 7: The test rig for grinding of silicon wafer/granite.

$\text{Al}_2\text{O}_3$  abrasives of  $20\ \mu\text{m}$  and  $10\ \mu\text{m}$  were also used to make a comparison.

The experimental setup for the grinding of both silicon wafer and granite is shown in Figure 7. The rotating speed of the silicon wafer in grinding was 250 rpm and the grinding disk rotated at 200 rpm with a pressure of  $13.7 \times 10^4$  Pa. The grinding time was set to 30 min.

For the grinding of granite, the speed of workpiece was 250 rpm and the grinding disk rotated at 100 rpm with a pressure of  $13.7 \times 10^4$  Pa.

The morphologies of ground silicon and granite were checked by the Hirox KH-1000 optical microscope. In addition to microobservations, the morphological features of the ground silicon wafer were quantitatively evaluated in terms of surface roughness using a Mahr Perthometer M1 profiler. For roughness values ( $R_a$ ), a traverse length of 4 mm, with the standard 0.8 mm cut-off, was chosen. During measuring, 20 points were taken randomly on the ground surface of the workpiece in order to reduce the influence of individual abnormal data, and then, the mean values were calculated.

Since the glossiness is one of the most important quality criteria to evaluate the grinding of granite, a WGG60-S digital gloss meter was used to measure the gloss readings of ground granite surfaces.

The morphologies of silicon wafer after grinding were compared with three abrasive sizes in Figure 8. It can be seen that the silicon wafer becomes smoother as the size of abrasives decrease and the surface scratches (see Figure 8(a)) were basically removed after grinding with ultrafine abrasive

of  $5\ \mu\text{m}$  (see Figure 8(c)). This was also supported by the results of surface roughness, as shown in Figure 9. It needs to note that the  $R_a$  is as low as 15 nm for the grinding with  $5\ \mu\text{m}$  abrasives, which might be comparable to the results reported by some published studies on the grinding of silicon wafers with fixed abrasives.

The morphologies of the red granite after grinding are shown in Figure 10 and the changes of gloss readings at different grinding stages are plotted in Figure 11. The gloss readings for the black granite are also given in Figure 11, which will be addressed later on. It can be seen that the granite surface becomes smoother with the increasing of grinding time, and accordingly, the gloss readings increase with the grinding time. In our previous studies [10], gloss readings were found to increase with the increasing surface roughness in an exponential curve for the grinding of granite. This can be used to account for the relationship between Figures 10 and 11.

Similar results can also be seen for the grinding of the black granite (see Figures 11 and 12). However, only half of the time was used to reach same gloss readings on the black granite as compared to the red one, indicating that the cutting of black granite by  $\text{Al}_2\text{O}_3$  is easier than the cutting of the red one. Moreover, higher gloss readings were achieved on the black granite, which is in agreement with factory records. By the way, the gloss readings for both granites mentioned here are comparable to those by traditional processing methods, which deserves further comparison in future studies.

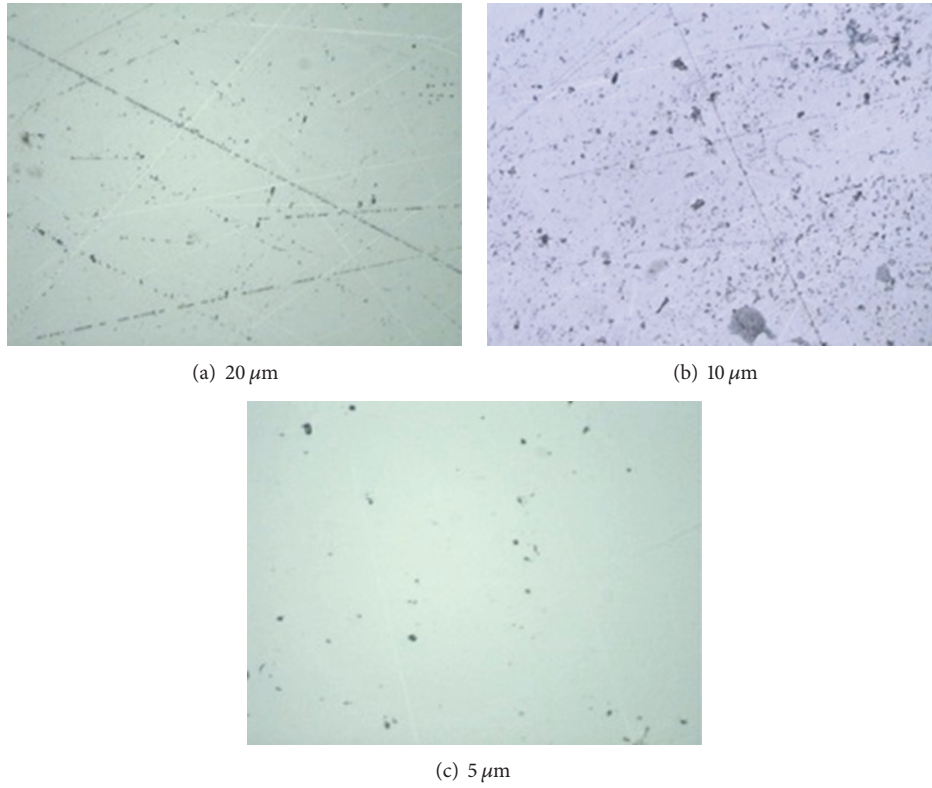


FIGURE 8: Morphologies of Si wafer ground with abrasives of different sizes (500x).

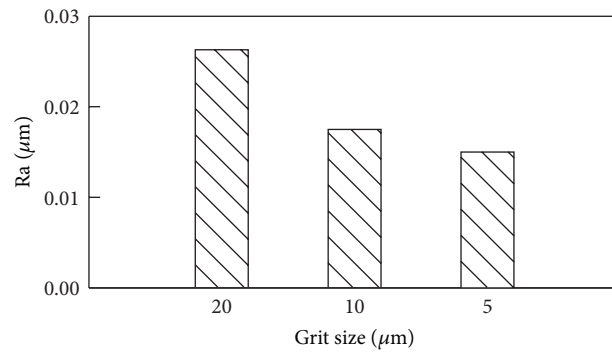


FIGURE 9: Surface roughness of Si wafers versus abrasive size.

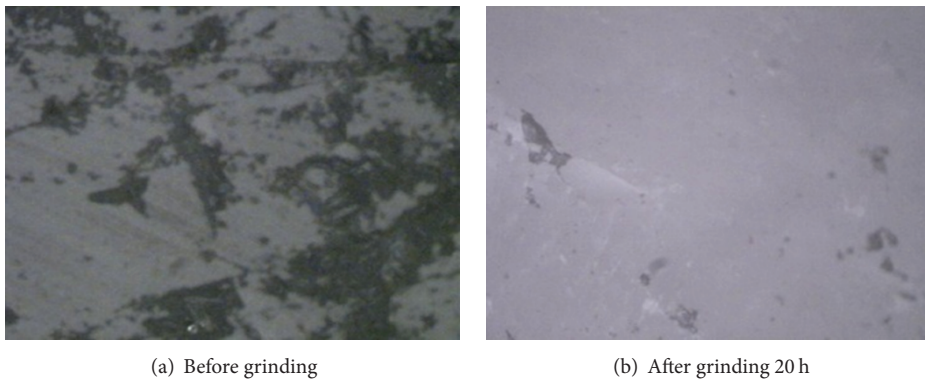


FIGURE 10: Surfaces of the red granite (500x).

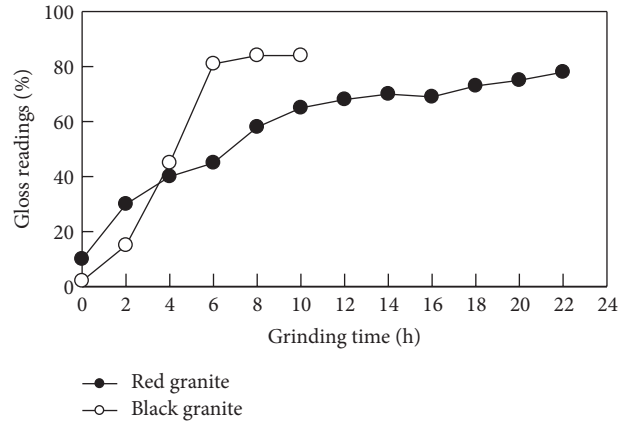


FIGURE 11: Gloss readings of the two granites versus time.

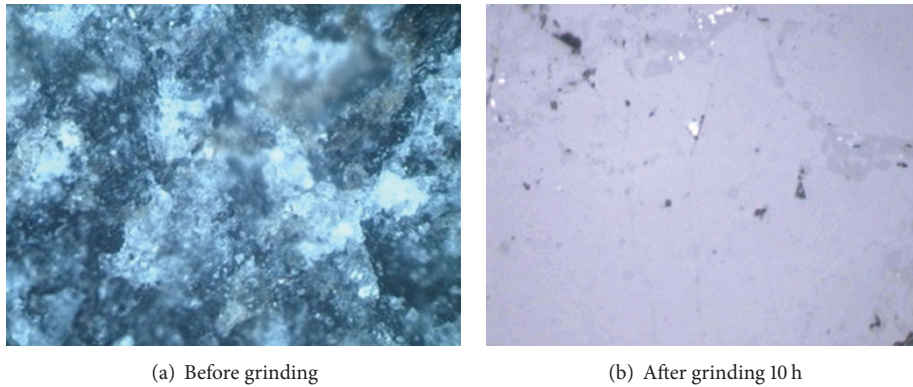


FIGURE 12: Surfaces of the black granite (500x).

## 5. Conclusions

The combination of sol-gel granulation and resin bonding was found to be possible in manufacturing ultrafine abrasive tools for fine grinding of silicon wafer and granite. In order to facilitate effective grinding, the grinding disks need to be dressed before grinding and brazed diamond disks can be used to dress the grinding disks to expected flatness. The grinding with abrasives of  $5\ \mu\text{m}$  can obviously remove the scratches on silicon wafer, thereby leading to a smooth surface of  $15\ \text{nm}$  (Ra).

For granite grinding, the rapid increase of gloss readings with the grinding time indicated the effectiveness of grinding process in surface smoothing. But the long time to achieve acceptable gloss readings on the granite surfaces indicates the low efficiency of the grinding disk in material removal, which might be due to the weak ability of  $\text{Al}_2\text{O}_3$  in cutting hard brittle materials such as granite.

Future work might be planned with the incorporation of ultrafine diamond abrasives in the manufacture of the grinding disks in order to enhance the grinding efficiency. Other efforts will focus on the application of the gel-resin coupled disks in the grinding of more kinds of materials.

## Conflict of Interests

All authors declare that there is no conflict of interests regarding the publication of this paper.

## Acknowledgments

This research was supported by Grant nos. 51075159 and U1034006 from the National Natural Science Foundation of China. Thanks are also given to the financial support (IRT1063) from the Changjiang Scholars and Innovative Research Team in University, The Ministry of Education, China. The research was also supported by Program for Innovative Research Team in Science and Technology in Fujian Province University (Program IRTSTFJ), China.

## References

- [1] H. Huang, B. L. Wang, Y. Wang, J. Zou, and L. Zhou, "Characteristics of silicon substrates fabricated using nanogrinding and chemo-mechanical-grinding," *Materials Science and Engineering A*, vol. 479, no. 1-2, pp. 373–379, 2008.
- [2] G. Z. Xie and H. Huang, "An experimental investigation of temperature in high speed deep grinding of partially stabilized

- zirconia,” *International Journal of Machine Tools and Manufacture*, vol. 48, no. 14, pp. 1562–1568, 2008.
- [3] H. Huang and T. Kuriyagawa, “Nanometric grinding of axisymmetric aspherical mould inserts for optic/photonics applications,” *International Journal of Machining and Machinability of Materials*, vol. 2, no. 1, pp. 71–84, 2007.
- [4] R. Komanduri, D. A. Lucca, and Y. Tani, “Technological advances in fine abrasive processes,” *CIRP Annals*, vol. 46, no. 2, pp. 545–596, 1997.
- [5] J. Liu, H. Huang, and X. P. Xu, “Abrasive dispersing in ultra-fine diamond tools,” *Key Engineering Materials*, vol. 381-382, pp. 521–524, 2008.
- [6] H. Nakamura, J. Yan, K. Syoji, and Y. Wakamatsu, “Development of a polishing disc containing granulated fine abrasives,” *Key Engineering Materials*, vol. 238-239, pp. 257–262, 2003.
- [7] J. Ikeno, Y. Tani, and H. Sato, “Development of highly homogeneous pellets applying electrophoretic deposition of ultrafine abrasives for nanometer grinding,” *CIRP Annals*, vol. 43, no. 1, pp. 319–322, 1994.
- [8] J. Liu and X. P. Xu, “Fabrication of ultra-fine diamond abrasive tools by sol-gel,” *Materials Science Forum*, vol. 471-472, pp. 426–430, 2004.
- [9] B. Kuang and X. Xu, “Study on the dressing methods for gel-based ultra-fine abrasive pads,” *Diamond and Abrasives Engineering*, no. 2, pp. 5–8, 2008.
- [10] H. Huang and X. P. Xu, “Interfacial interactions between diamond disk and granite during vertical spindle grinding,” *Wear*, vol. 256, no. 6, pp. 623–629, 2004.

## Research Article

# Analysis of Grinding Force and Elastic Deformation in Thread Grinding Process

Wei Wang and Xianying Feng

School of Mechanical Engineering, Shandong University, Jinan, Shandong 250061, China

Correspondence should be addressed to Wei Wang; [mingshan3@126.com](mailto:mingshan3@126.com)

Received 8 May 2013; Revised 16 September 2013; Accepted 16 September 2013

Academic Editor: Feng Jiang

Copyright © 2013 W. Wang and X. Feng. This is an open access article distributed under the Creative Commons Attribution License, which permits unrestricted use, distribution, and reproduction in any medium, provided the original work is properly cited.

Considering the grinding geometry of the thread grinding dynamic contact arc length, a dynamic numerical thread grinding model has been set up on the basis of study of a single grit grinding model. The properties of grinding force and dynamic contact arc-length have been studied by means of the developed numerical model. The results have shown that the angle of helix has little effect on the dynamic contact arc-length than the wheel speed on the dynamic contact arc-length. And the wheel speed also produced a large effect on grinding force.

## 1. Introduction

Grinding is one of the main methods of precision manufacturing and the process quality depends to a large extent on the experience of the operator. The grinding force comes from the elastic deformation, the plastic deformation, and the grinding swarf from the contact surface of the wheel and the workpiece. Meanwhile, the friction among the grinding grits, bond, and workpiece can also contribute to the grinding force [1]. Among these factors, the workpiece elastic deformation is one of the key influence factors of processing precision for high precision machining. The main challenge in designing ultraprecise grinding machine is developing the accurate grinding force models [2, 3]. In the recent years a number of researchers throughout the world have developed some grinding force models and calculated the formula for different kinds of workpieces. For example, as for the cylindrical grinding, some researchers set up the cylindrical traverse grinding force model on the basis of the analysis principle of the status of a single grinding grit. And some researchers analyzed grinding force by using the stress concentration theory and the mathematical statistics theory [4, 5]. Some studies have been conducted to investigate the grinding theory, analyze the friction force, plow friction, and cutting force in the surface grinding process, and discuss the effect of parameters on the properties of grinding force by analyzing

the numerical number [6, 7]. On the other hand, Liu et al. addressed an empirical model of the grinding force in the study of multivariables in the grinding process [8]. With regard to the grinding force model, researchers presented some analytical results about the workpiece elastic deformation caused by grinding force [9–11]. However little research has been conducted for the thread grinding process. In this paper a numerical thread grinding model will be developed on the basis of the single grinding grit model. The thread grinding dynamic contact arc is analyzed in the viewpoint of the grinding geometry.

## 2. Mathematical Model

*2.1. Arc Length of Contact between the Wheel and the Workpiece.* There is an angle between the wheel axis and the workpiece axis for the thread grinding, which is different from the normal cylindrical grindings. It is necessary that the effective equivalent wheel diameter  $d_e$  must be given between the finished surface and the projection plane of the wheel circumferential speed in grinding zone:

$$d_e = \frac{d_s}{1 + d_s \cos \Phi / d_w}, \quad (1)$$

as shown in Figure 1.

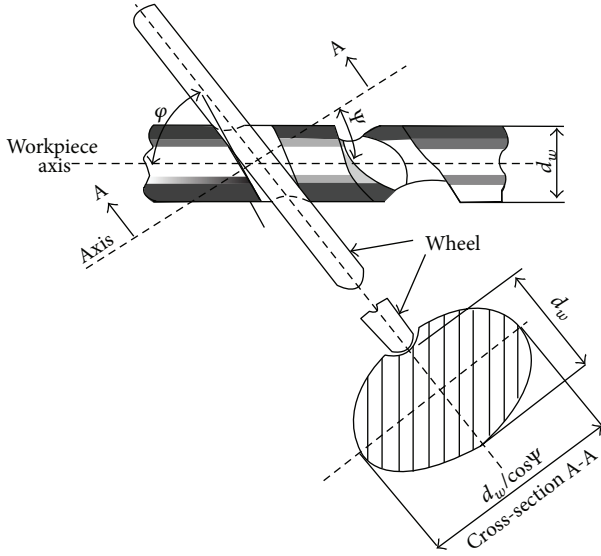


FIGURE 1: Thread grinding sketch map.

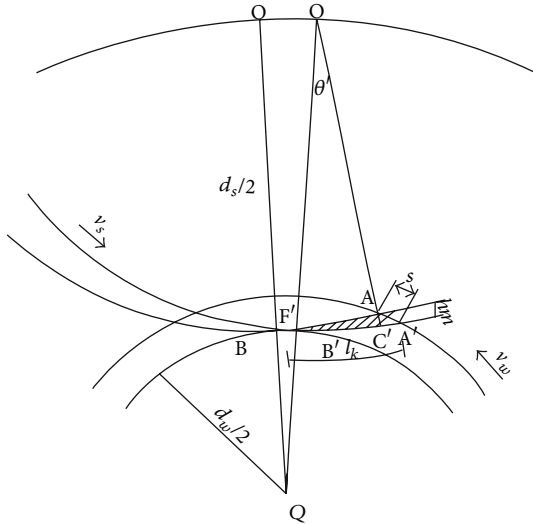


FIGURE 2: The grinding path in the grinding process.

In the thread grinding process, the angle between the wheel axis and the workpiece axis is defined as  $\Psi$  and the thread helical angle is  $\phi$ . Certainly  $\Psi = 90^\circ - \phi$ . For the grinding wheel, the relationships of the workpiece circumferential speed along the helix  $v_w'$  and axial velocity  $v_t$  are given as follows:

$$\tan \phi = \frac{v_w'}{v_t}, \quad \sin \phi = \frac{v_w'}{v_w}. \quad (2)$$

The arc length of contact surface between the wheel and the workpiece is one of the important parameters in grinding process, which produces a significant effect on the grinding force. The analysis of grinding path is the premise of modeling grinding force. The grinding path is shown in Figure 2.

As shown in Figure 2, the active cutting point on the workpiece moves from  $F'$  along the curve path to  $A'$  in the

inverse mill. For the workpiece, the grinding path  $F'B'C'A'$  is a cycloid curve synthesized by the grinding wheel speed  $v_s$  and the workpiece speed  $v_w$ . The cycloid curve can be expressed in the following equations in the radial direction and tangential direction:

radial direction:

$$x = \frac{d_s}{2} \sin \theta' + \frac{d_s v_w}{2 v_s} \theta' \quad (3)$$

tangential direction:

$$y = \frac{d_s}{2} (1 - \cos \theta'), \quad (4)$$

where  $v_s$  is the grinding wheel speed,  $v_w$  is the workpiece speed,  $\theta'$  is the turning angle of the wheel, and  $d_s$  is the diameter of the wheel. The total length of grinding path can be obtained through the grinding path equation:

$$dl_k = \sqrt{\left(\frac{dx}{d\theta'}\right)^2 + \left(\frac{dy}{d\theta'}\right)^2} d\theta'. \quad (5)$$

Hence the kinematic contact arc length is obtained,

$$l_k = \left(1 + \frac{v_w}{v_s}\right) (ad_e)^{1/2}, \quad (6)$$

where  $d_e$  is the effective equivalent wheel diameter and  $a$  is vertically cutting depth.

**2.2. Grinding Force Model.** As the single grinding grit is the basis of the analysis of the grinding force in the grinding process, the stress to a single grit should be studied first, as shown in Figure 3. The single grit grinding force formula is given:

$$dFx = F_p \cos \theta \cos \gamma dA, \quad (7)$$

$$a_g = \rho \cos \theta.$$

The grit has a tip angle because it is the circular cone. The center line points to the wheel radius and the generatrix length is  $\rho$ . Hence the contact area is

$$dA = \frac{1}{2} \rho^2 \sin \theta d\gamma, \quad (8)$$

$$dFx = F_p \cos \theta \cos \gamma \frac{1}{2} \rho^2 \sin \theta d\gamma.$$

Since

$$dFt = dFx \cos \theta \cos \gamma, \quad (9)$$

$$dFn = dFx \sin \theta;$$

therefore, the grinding force on the total grit can be deduced from formulas (8) and (9):

$$F_{tg} = \frac{\pi}{4} F_p a_g^2 \sin \theta, \quad (10)$$

$$F_{tn} = F_p a_g^2 \sin \theta \tan \theta,$$

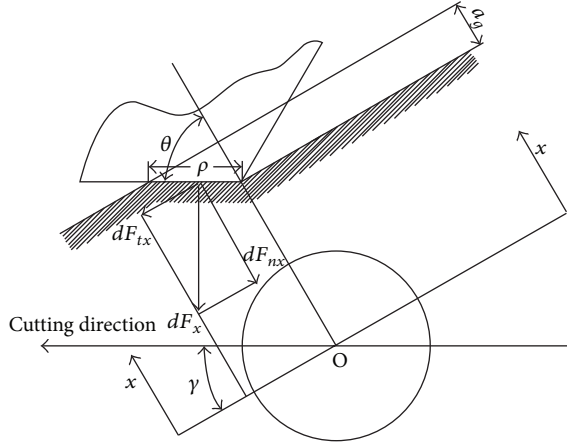


FIGURE 3: Stress on grinding grit.

where  $F_p$  is the grinding force per unit  $N$ ,  $\theta$  is the half tip angle of grit (the half tip angle is changed from  $40^\circ$  to  $72.5^\circ$  in the engineering applications), and  $a_g$  is the grinding depth.

From the kinematic contact length the number of effective kinematic grit  $N_d$  is

$$N_d = N_t l_k b, \quad (11)$$

where  $N_t$  is the number of unit effective static grit on the wheel surface and  $b$  is the grinding width.

Then the grinding force model is obtained:

$$F_t = N_d F_{tg} = \frac{\pi}{4} N_d F_p a_g^2 \sin \theta, \quad (12)$$

$$F_n = N_d F_{tn} = N_d F_p a_g^2 \sin \theta \tan \theta.$$

According to formulas (6) and (9), the thread grinding force can be calculated by the following equations:

$$F_t = N_d F_{tg} = \frac{\pi}{4} N_t \left( 1 + \frac{v_w}{v_s} \right) \times (ad_e)^{1/2} b F_p a_g^2 \sin \theta, \quad (13)$$

$$F_n = N_d F_{tn} = N_t \left( 1 + \frac{v_w}{v_s} \right) \times (ad_e)^{1/2} b F_p a_g^2 \sin \theta \tan \theta. \quad (14)$$

**2.3. Model of Workpiece Elastic Deformation.** The workpiece can be fixed by the two core clampers in front and back surfaces, which forms an elastic system, as shown in Figure 4. When the grinding wheel moves along the workpiece, the workpiece elastic deformation in the normal direction will be caused by the normal grinding force. It produces a large effect on the workpiece processing precision.

The curvature equation caused by  $F_n$  is

$$y'' = -\frac{F_n n x}{6EI} \quad 0 < x < m, \quad (15)$$

$$y'' = -\frac{F_n n x}{6EI} + F_n (x - m) \quad m \leq x < l,$$

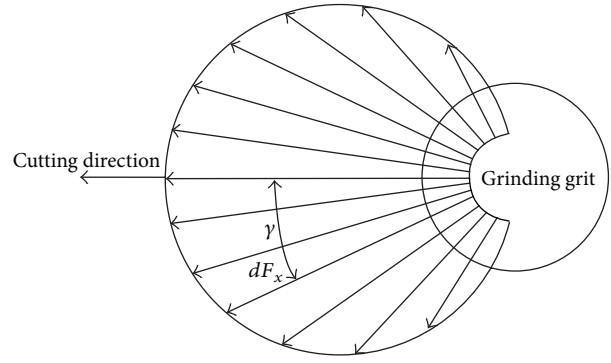


FIGURE 4: Workpiece grinding by the two core clampers in front and back surfaces.

where  $m$  is the distance between the grinding wheel and the front core clamper,  $n$  is the distance between the grinding wheel and the back core clamper,  $y$  is the elastic deformation,  $E$  is the elastic modulus, and  $I$  is the moment of inertia.

The elastic deformation  $y$  can be obtained by integrating (15) twice:

$$y = -\frac{F_n n x^3}{6EI} + A_1 x + B_1 \quad 0 < x < m,$$

$$y = -\frac{F_n n x^3}{6EI} + \frac{F_n (x - m)^3}{6EI} + A_2 x + B_2 \quad m \leq x < l, \quad (16)$$

where  $A_1$ ,  $A_2$ ,  $B_1$ , and  $B_2$  are the integration constants.

The four integration constants can be determined by the following conditions.

- (1) The deformations of  $a$  and  $b$  interfaces are equal.
- (2) Deformation in the core clamper is zero.

So the four integration constants are

$$A_1 = A_2 = \frac{F_n n (l^2 - n^2)}{6EI}, \quad (17)$$

$$B_1 = B_2 = 0.$$

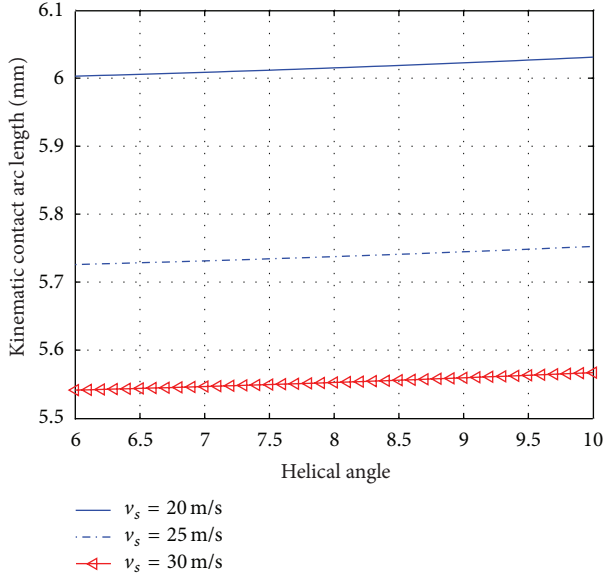


FIGURE 5: The change of kinematic contact arc length.

Substituting (17) and (14) in (16), the elastic deformation can be obtained:

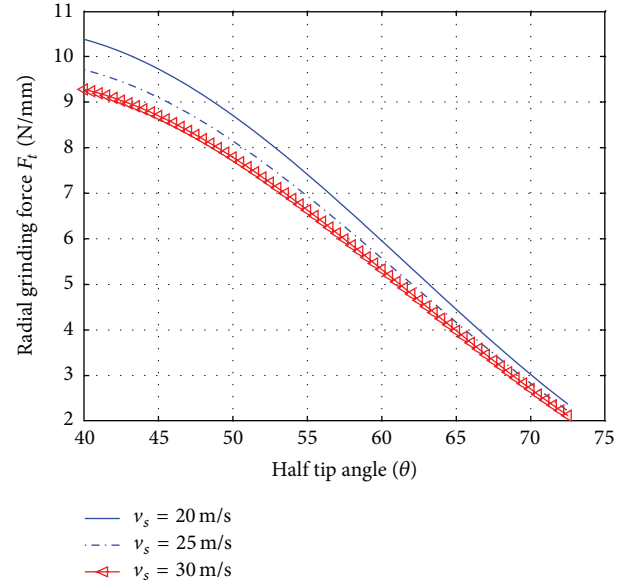
$$\begin{aligned}
 y = & N_t \left( 1 + \frac{v_w}{v_s} \right) (ad_e)^{1/2} b F_p a_g^2 \\
 & \times \sin \theta \tan \theta \frac{[(l^2 - n^2)x - x^3]n}{6lEI} \\
 & + N_t \left( 1 + \frac{v_w}{v_s} \right) (ad_e)^{1/2} b F_p a_g^2 \\
 & \times \sin \theta \tan \theta \frac{(x-m)^3}{6EI}, \quad m \leq x < l.
 \end{aligned} \quad (18)$$

### 3. Calculation and Analysis of Grinding Force Model in the Thread Grinding Process

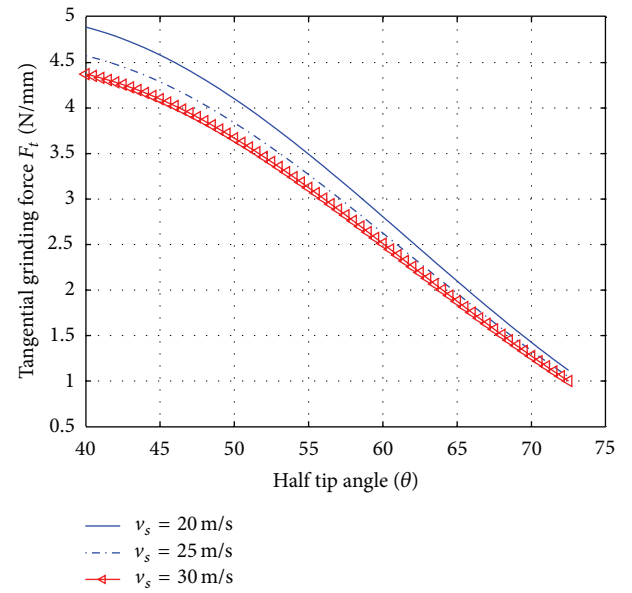
In the case of the thread grinding force study, the working target is ball screw and the grinding wheel is vitrified bonded grinding wheel. The grinding parameters are given as  $v_s = 25\text{--}35$  m/s,  $v_w = 6\text{--}10$  m/min,  $a = 20\text{--}25$   $\mu\text{m}$ ,  $b = 6$  mm,  $l = 5$  m,  $ds = 500$  mm, and  $d_w = 28$  mm and the half tip angle of grit is  $\theta = 40^\circ\text{--}72.5^\circ$ .

**3.1. Effect of the Helical Angle on Kinematic Contact Arc Length.** As shown in Figure 5, the kinematic contact arc length is becoming longer as the helical angle increases with the case of the constant grinding wheel speed. Meanwhile, the kinematic contact arc length is getting shorter with the increase of the grinding wheel speed while keeping the helical angle constant.

**3.2. Effect of the Half Tip Angle on the Grinding Force.** The variations of the grinding force along with the half tip angle



(a) Radial grinding force



(b) Tangential grinding force

FIGURE 6: The variations of the radial and tangential grinding force.

have been analyzed and presented in Figure 6. It can be seen from Figure 6 that both the radial grinding force and the tangential grinding force are reduced with the rise of the half tip angle, while the grinding wheel speed remains constant. The forces get larger when the grinding wheel speed is getting smaller, as shown in Figure 6.

If the grinding wheel speed is constant and the workpiece speed is variable, the radial grinding force and the tangential grinding force are getting smaller with the increase of the half tip angle. If the workpiece speed is constant, the radial grinding force and the tangential grinding force are getting smaller with the increase of the half tip angle. If the half tip

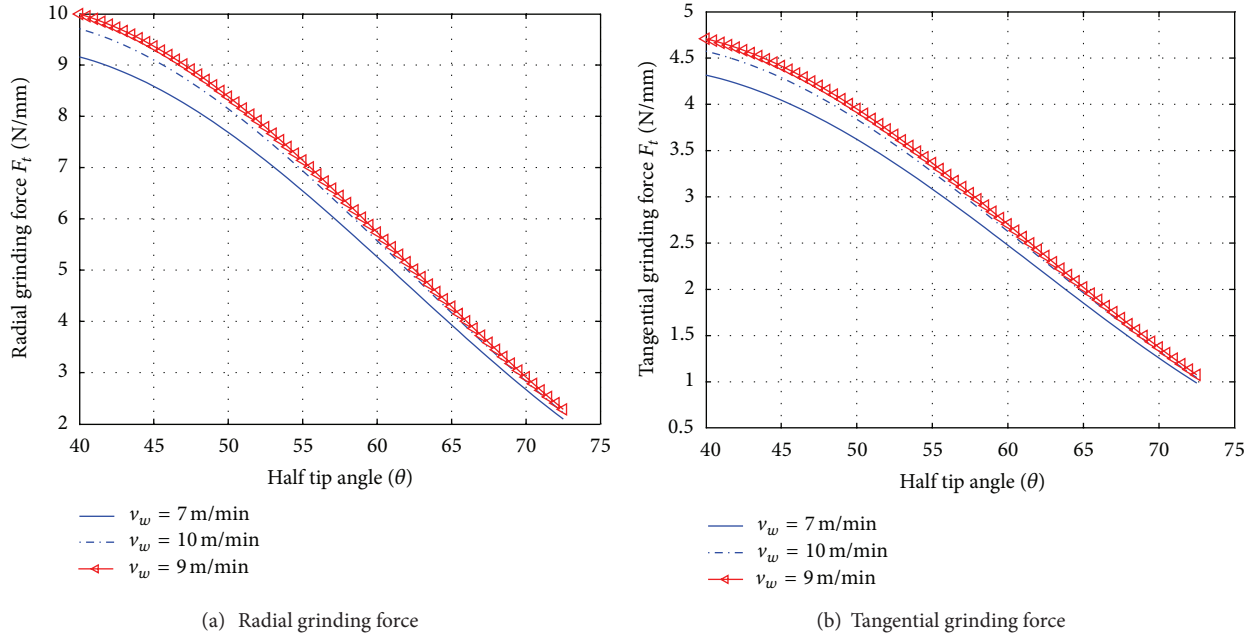


FIGURE 7: The variations of radial and tangential grinding force.

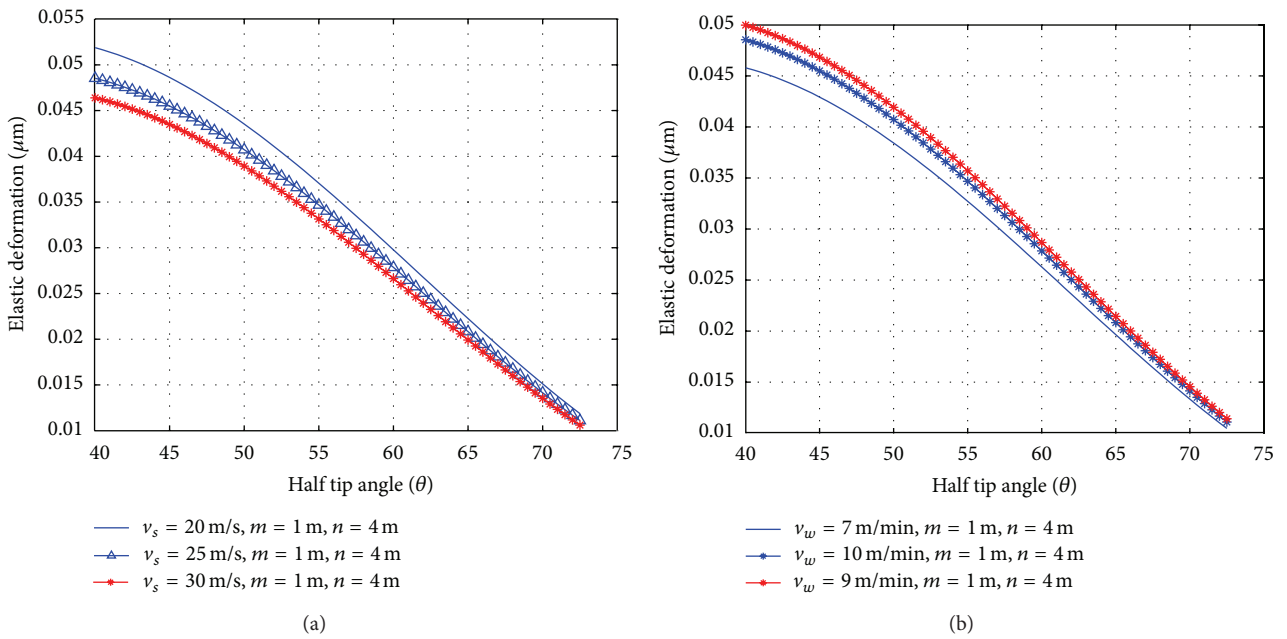


FIGURE 8: Deformation of different speed of grinding wheel and workpiece speed.

angle is constant, the radial grinding force and the tangential grinding force are getting larger with the increase of the workpiece speed, as shown in Figure 7.

The elastic deformation is solved in the condition that the grinding wheel is 1 meter from the front core clamber and 4 meters from the back core clamber. It is shown in Figure 8 that the elastic deformation is affected by many factors like the wheel speed, workpiece speed, and the wheel location. So the adaptive control algorithm must be figured out to compensate the deformation error.

#### 4. Conclusions

The kinematic contact arc length has been analyzed in the thread grinding process by means of the grinding geometry in this paper. The single grit grinding force model has been developed to further obtain the total grinding force model. Thread kinematic contact arc length and thread grinding force are analyzed and calculated on the basis of numerical analysis method. The effect of the grinding wheel speed on thread kinematic contact arc length is significant. The

formula of the elastic deformation in the process is given. It can provide some guidance on the thread processing control algorithm. Future experimental work should be conducted to further verify the developed models in this paper.

## References

- [1] U. S. P. Durgumahanti, V. Singh, and P. V. Rao, "A new model for grinding force prediction and analysis," *International Journal of Machine Tools and Manufacture*, vol. 50, no. 3, pp. 231–240, 2010.
- [2] W. Tao, H. Feng, and H. Zhang, "Development status and key technology of NC screw grinding machine," *Machine Tool & Hydraulics*, no. 10, pp. 252–254, 2009.
- [3] W. Xiong, G. Zhong, and J. I. Zonghui, "Review on the development of high speed precision machine tool dynamics," *Manufacturing Technology and Machine Tool*, no. 9, pp. 35–40, 2009.
- [4] J. Zhang, P. Ge, and L. Zhang, "Research on the grinding force based on the probability statistics," *China Mechanical Engineering*, vol. 18, no. 20, pp. 2399–2402, 2007.
- [5] L. Wang and G. Li, "Modelling and computer simulation for grinding process," *China Mechanical Engineering*, vol. 13, no. 1, pp. 1–4, 2002.
- [6] L. Lichun, F. Jizai, and J. Peklenik, "A study of grinding force mathematical model," *Annals of CIRP*, vol. 29, no. 1, pp. 245–249, 1980.
- [7] M. Younis, M. M. Sadek, and T. El-Wardani, "A new approach to development of a grinding force model," *Journal of Engineering for Industry*, vol. 109, no. 4, pp. 306–313, 1987.
- [8] Q. Liu, X. Chen, Y. Wang, and N. Gindy, "Empirical modelling of grinding force based on multivariate analysis," *Journal of Materials Processing Technology*, vol. 203, pp. 420–430, 2008.
- [9] W. B. Rowe, M. N. Morgan, H. S. Qi, and H. W. Zheng, "The effect of deformation on the contact area in grinding," *Manufacturing Technology*, vol. 42, no. 1, pp. 409–412, 1993.
- [10] D. P. Saini and R. H. Brown, "Elastic deflections in grinding," *Manufacturing Technology*, vol. 29, no. 1, pp. 189–194, 1980.
- [11] D. Y. Gu and J. G. Wager, "New evidence on the contact zone in grinding—contact length, sliding and cutting regions," *Manufacturing Technology*, vol. 37, no. 1, pp. 335–338, 1988.

## Research Article

# Numerical Simulation of the Moving Induction Heating Process with Magnetic Flux Concentrator

Feng Li,<sup>1</sup> Xuekun Li,<sup>1,2</sup> Tianxing Zhu,<sup>1</sup> and Yiming (Kevin) Rong<sup>1,2,3</sup>

<sup>1</sup> Department of Mechanical Engineering, Tsinghua University, Beijing 100084, China

<sup>2</sup> Beijing Key Lab of Precision/Ultra-Precision Manufacturing Equipments and Control, Beijing 100084, China

<sup>3</sup> Department of Mechanical Engineering, Worcester Polytechnic Institute, Worcester, MA 01609, USA

Correspondence should be addressed to Feng Li; [feng-li10@mails.tsinghua.edu.cn](mailto:feng-li10@mails.tsinghua.edu.cn)

Received 31 May 2013; Revised 18 August 2013; Accepted 3 September 2013

Academic Editor: Lei Zhang

Copyright © 2013 Feng Li et al. This is an open access article distributed under the Creative Commons Attribution License, which permits unrestricted use, distribution, and reproduction in any medium, provided the original work is properly cited.

The induction heating with ferromagnetic metal powder bonded magnetic flux concentrator (MPB-MFC) demonstrates more advantages in surface heating treatments of metal. However, the moving heating application is mostly applied in the industrial production. Therefore, the analytical understanding of the mechanism, efficiency, and controllability of the moving induction heating process becomes necessary for process design and optimization. This paper studies the mechanism of the moving induction heating with magnetic flux concentrator. The MPB-MFC assisted moving induction heating for Inconel 718 alloy is studied by establishing the finite element simulation model. The temperature field distribution is analyzed, and the factors influencing the temperature are studied. The conclusion demonstrates that the velocity of the workpiece should be controlled properly and the heat transfer coefficient (HTC) has little impact on the temperature development, compared with other input parameters. In addition, the validity of the static numerical model is verified by comparing the finite element simulation with experimental results on AISI 1045 steel. The numerical model established in this work can provide comprehensive understanding for the process control in production.

## 1. Introduction

Induction heating plays an important role in many industrial manufacturing processes, such as hardening, brazing, tempering, and stress relieving [1]. The emergence of the metal powder bonded magnetic flux concentrator (MPB-MFC) made of ferromagnetic metal powder bonded with organic binder enables the induction heating process to possess higher heating efficiency and improved performance [2]. Due to its special material properties, the MPB-MFC exhibits less heat loss, longer coil life, and better formability into various shapes [3]. Besides, the MPB-MFC assisted induction heating system is studied by establishing the finite element simulation model and experimental verification [4].

However, the moving application occurs in various industrial applications, as shown as in Figure 1, which makes the induction process control more complex. As the magnetic flux field and temperature change in the process, the

corresponding magnetic and thermal physical properties of the workpiece material vary nonlinearly [5, 6]. It will be impossible to achieve an accurate solution when treating all the nonlinear material properties in a coupled manner during the moving induction system. Therefore, it is crucial to analyze the coupled procedure with moving motion for better predictability in the induction process design and optimization.

In this paper, the mechanism of electromagnetic-thermal transformation with moving motion is studied, and the finite element model is established for a plane moving induction heating system with the MPB-MFC on Inconel 718 alloy. In addition, the factors that influence the heating efficiency are studied, and the corresponding results are discussed. The precise modeling and simulation of the moving induction heating process could help better mechanism understanding, which also provides an explicit method for process design and optimization.

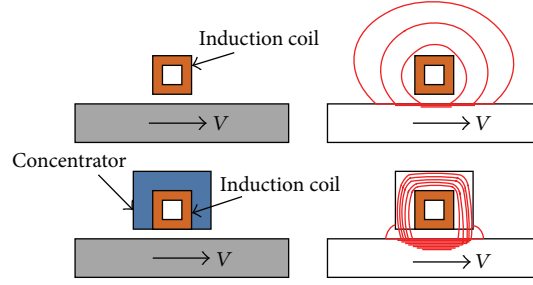


FIGURE 1: The moving induction heating with MPB-MFC.

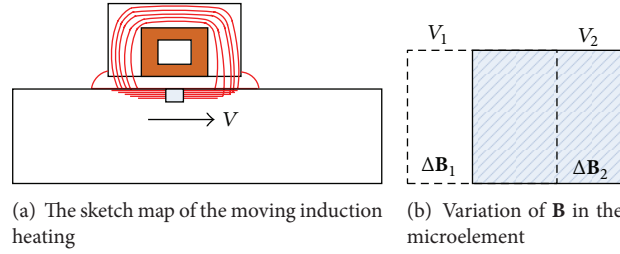


FIGURE 2: The energy transformation in induction heating with MFC.

## 2. Principle of Simulation

**2.1. Mechanism of Moving Induction Heating.** The magneto-dynamic phenomenon in a steady state AC magnetic application is governed by Maxwell's equations (see (1)–(4)), where  $\mathbf{E}$  and  $\mathbf{H}$  are the variables to solve [2]. The relations between the field quantities are specified by (5)–(7) [2].  $\mathbf{H}$  is the magnetic field intensity (A/m), which is generated by current resource. In this paper,  $\mathbf{H}$  is treated as a function of the current intensity  $I$ , frequency  $f$ , and the permeability of the MPB-MFC. Consider the following:

$$\nabla \times \mathbf{H}(I, f, \mu_{\text{MFC}}) = \mathbf{J} + \frac{\partial \mathbf{D}}{\partial t} \quad (\text{from Ampere's law}), \quad (1)$$

$$\nabla \times \mathbf{E} = -\frac{\partial \mathbf{B}}{\partial t} \quad (\text{from Faraday's law}), \quad (2)$$

$$\nabla \cdot \mathbf{D} = \rho \quad (\text{from Gauss's law}), \quad (3)$$

$$\nabla \cdot \mathbf{B} = 0 \quad (\text{from Gauss's law}), \quad (4)$$

$$\mathbf{D} = \epsilon \mathbf{E}, \quad (5)$$

$$\mathbf{B} = \mu(\mathbf{H}, T) \mathbf{H}, \quad (6)$$

$$\mathbf{J} = \sigma \mathbf{E}, \quad (7)$$

where  $\mathbf{J}$  is the conduction current density (A/m<sup>2</sup>),  $\mathbf{D}$  is the electric flux density (C/m<sup>2</sup>),  $t$  is the time (s),  $\mathbf{E}$  is the electric field intensity (V/m or N/C),  $\mathbf{B}$  is the magnetic flux density (T or N/A·m), and  $\rho$  is the electric charge density (C/m<sup>3</sup>).  $\epsilon$  is the relative permittivity.  $\mu$  is the relative magnetic permeability, which is related to  $\mathbf{H}$  and the temperature  $T$ .  $\sigma$  is the electrical conductivity ( $\mu\text{S/cm}$ ).

In order to solve  $\mathbf{E}$  and  $\mathbf{H}$ , it is convenient to bring into a magnetic vector potential  $\mathbf{A}$  and an electric scalar potential  $\varphi$ . Consider the following:

$$\begin{aligned} \mathbf{B} &= \nabla \times \mathbf{A} \\ \mathbf{E} &= -\nabla \varphi - \frac{\partial \mathbf{A}}{\partial t}. \end{aligned} \quad (8)$$

By incorporating the above constitutive relations into Maxwell's equations, the equation solved by the finite elements method is shown as below

$$\nabla \times \left( \frac{1}{\mu} \nabla \times \mathbf{A} \right) = \mathbf{J} = -\sigma \frac{\partial \mathbf{A}}{\partial t} + \mathbf{J}_s, \quad (9)$$

where  $\mathbf{J}_s = -\sigma \nabla \varphi$  is the source current density in the induction coil.

In general, the transient time-dependent heat transfer process in metal materials can be described by the Fourier equation as follows [2]:

$$c\rho \frac{\partial T}{\partial t} + \nabla \cdot (-\lambda \nabla T) = Q_v = \sigma |\mathbf{E}|^2, \quad (10)$$

where  $T$  is the temperature in the metal workpiece,  $c$  is the specific heat,  $\rho$  is the density of the metal material,  $\lambda$  is the thermal conductivity of the metal, and  $Q_v$  is the heat source density induced by eddy currents per unit time in a unit volume, which is obtained by solving the electromagnetic problem and is so-called the heat generation.

The MPB-MFC serves as a magnifier that enhances the magnetic flux's penetration into the workpiece, as indicated in Figure 2(a). A microelement is extracted to be analyzed. In the past increment of time  $\Delta t$ , the microelement will be removed from the dashed box  $V_1$  to the solid one  $V_2$ , as

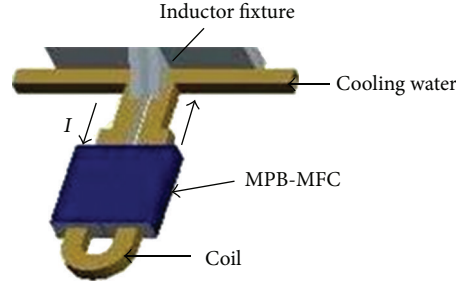


FIGURE 3: The geometry of the inductor.

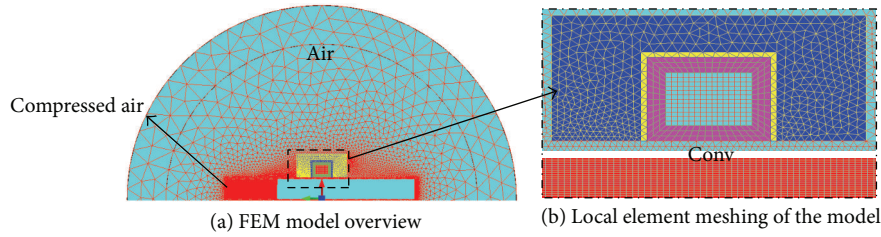


FIGURE 4: Geometric model and the finite element meshing.

shown as Figure 2(b). During this process, the magnetic flux density experiences the variation  $\Delta \mathbf{B} = \Delta \mathbf{B}_1 - \Delta \mathbf{B}_2$ , which will influence the power generation in the workpiece and will be reflected by (2) and (10).

**2.2. Finite Element Modeling.** In this paper, the FEM software FLUX2D is used to calculate the distribution of the electromagnetic field and temperature field for the mobile induction heating process [8]. The geometry dimension for surface induction heating is modeled as indicated in Figure 3. The induction coil is made of a rectangular copper tube with low electrical resistivity. And cooling water flows through it for maintaining the coil at low temperature. The concentrator is machined with a rectangular groove and clamped onto the coil.

The domain of the system is modeled as in Figure 4. The whole system is surrounded by air. The compressed air region means a special region between the workpiece and fixed air surrounding the device, which is the movement route of the workpiece and will be remeshed during every translating calculation step. The compressed air region is meshed into structure elements, and the coil region and subsurface regions of the heated workpiece are meshed with structured element at 0.1 mm, considering the sharp temperature gradient in these zones, as shown as Figure 4(b). There are 49025 nodes and 19450 surface elements in the whole computational domain. The mesh order is the second order, and the time step is set as 0.005 s.

As to the initial conditions, the ambient temperature and the initial temperature of the workpiece are set as 25°C. The region “Conv” is the surface boundary of the workpiece, which in thermal analysis can be expressed as in the below equation (11). The heat transfer coefficient (HTC) of the workpiece surface is equal to 20 W/(m<sup>2</sup>·K), and the radiation

heat loss coefficient here is 0.5 W/(m<sup>2</sup>·K<sup>4</sup>). Consider the following:

$$\lambda \frac{\partial T}{\partial n} = -\alpha (T - T_a) - C_s (T^4 - T_a^4), \quad (11)$$

where  $\partial T / \partial n$  is the temperature gradient in a direction normal to the metal workpiece's surface at the point under consideration,  $T_a$  is the initial temperature of the surrounding air,  $\lambda$  is the thermal conductivity of the workpiece,  $\alpha$  is the convection surface heat transfer coefficient,  $C_s$  is the radiation heat loss coefficient, and  $n$  denotes the normal to the boundary surface of the workpiece.

The finite element model should solve the coupled electromagnetic-thermal computation problem, which involves the consideration of the thermal- and magnetic-dependent material property in the process. The MPB-MFC Ferrotron 559H is selected. Figure 5 illustrates the  $\mathbf{B}$ - $\mathbf{H}$  curve of the concentrator material and the permeability variation with the magnetic field strength. Theoretically, the magnetic permeability of MFC also changes as the temperature rises. However, the permeability of the concentrator does not change too much as it is cooled down continuously by running water through the induction coil.

As for the workpiece material, both the magnetic and thermal properties alter during the induction heating process. The workpiece material is the nickel-based alloy Inconel 718, and its chemical composition is listed in Table 1.

The magnetic permeability  $\mu$  is characterized by the magnetic polarization  $\mathbf{M}$  of the material, which is influenced by both the magnetic field strength and temperature. The quantification of  $\mu$  is carried out through the measurement of the magnetic polarization  $\mathbf{M}$  and the magnetic field strength  $\mathbf{H}$  at various temperature conditions. The measurement is

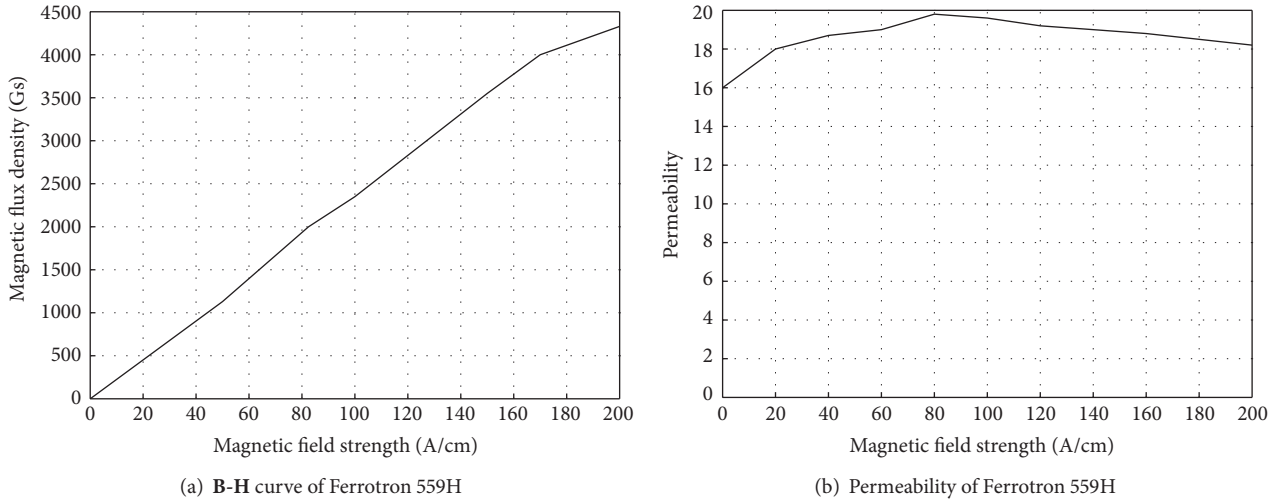


FIGURE 5: B-H curve and permeability of Ferrottron 559H [9].

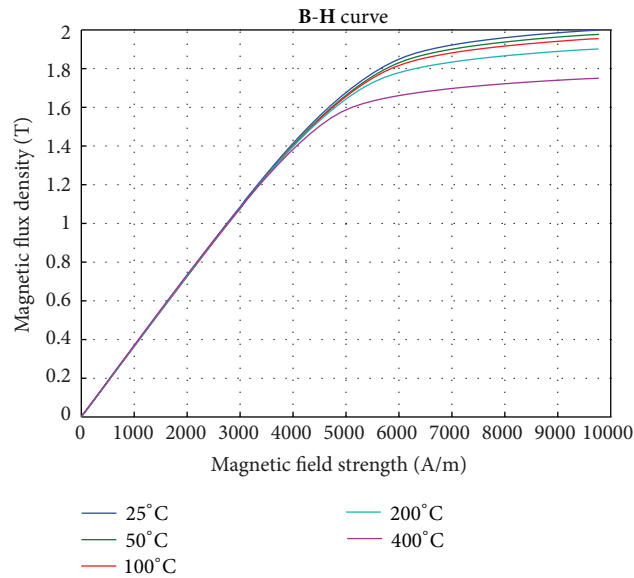


FIGURE 6: The measured B-H curve of AISI 1045.

conducted on the vibrating sample magnetometer Lakeshore-730T (VSM), where a set of **M-H** curves can be generated. Equation (12) indicates the correlation of the permeability  $\mu$  and polarization **M** as follows:

$$\mathbf{B} = \mu_0 \mu_r \mathbf{H} = \mu_0 \mathbf{H} + \mu_0 \mathbf{M}, \quad (12)$$

where  $\mu_0$  is the permeability of vacuum and equals to  $4\pi \times 10^{-7}$  [H/m].

The permeability of the alloy Inconel 718 is treated as constant 1, which is largely different from the plain carbon steel. The B-H curve of AISI 1045 in Figure 6 presents a nonlinearity, which demonstrates that the permeability is related with the magnetic field and the temperature. As the magnetic flux field strength alters below 5000 A/m, the permeability is almost a constant; while the magnetic field strength is higher than  $1 \times 10^5$  A/m, it drops rapidly to 1.

The volumetric heat capacity  $c_p$  and the thermal conductivity  $\lambda$  of the workpiece are dependent on temperature ( $T$ ), while independent on the magnetic field intensity. Figures 7(a) and 7(b) show the  $c_p$ - $T$  and  $\lambda$ - $T$  relationship, respectively, which demonstrates that  $c_p$  and  $\lambda$  of Inconel 718 are nonlinear [7].

### 3. Results and Analysis

Figure 8 shows the cross-section profile of the induction system, and the heating distance is 1 mm. The distance between the points B, C, D, E, and A is, respectively, 10 mm, 12.75 mm, 12.75 mm, and 14.75 mm. The factors influencing the eddy current intensity have not been researched clearly during this novel process. Therefore, in this part, special attention is taken to the power density distribution generated by the eddy current and the temperature field evolution.

TABLE 1: The chemical compositions of Inconel 718, wt% [7].

	Ni	Cr	Fe	C	Mn	Si	Cu	Mo	Co	Al	Ti	Nb	B	P	S
Min	50	17	Rest	0.08	0.35	0.35	0.3	2.8	1.0	0.2	0.7	4.75	0.002	0.015	0.01
Max	55	21						3.3		0.8	1.15	5.5	0.006		

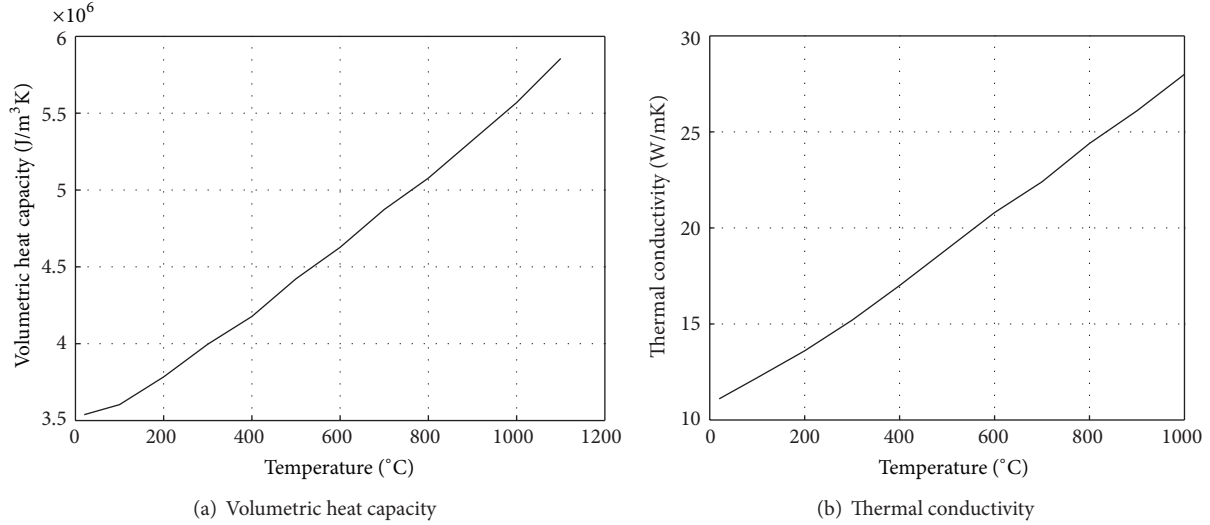


FIGURE 7: Volumetric heat capacity and thermal conductivity of Inconel 718.

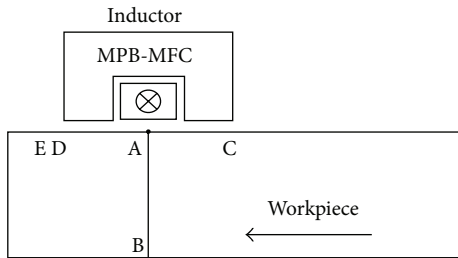


FIGURE 8: Cross-section view of the system.

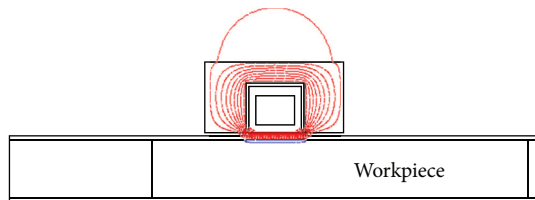


FIGURE 9: Equal flux lines ( $f = 50 \text{ kHz}$ ,  $I = 430 \text{ A}$ ).

Figure 9 shows the equal flux lines distribution on the workpiece surface, and it is obvious that the magnetic flux concentrator plays an essential effect on the magnetic field distribution. The maximum value of the power density at the surface of the workpiece is at point A, which is underneath the magnetic flux concentrator. The power density distribution is shown in Figure 10. The maximum value is higher than  $5 \times 10^8 \text{ W}/(\text{cubic m})$ . When the velocity of the workpiece varies from 0 to 5 mm/s, the power density variation at point A is

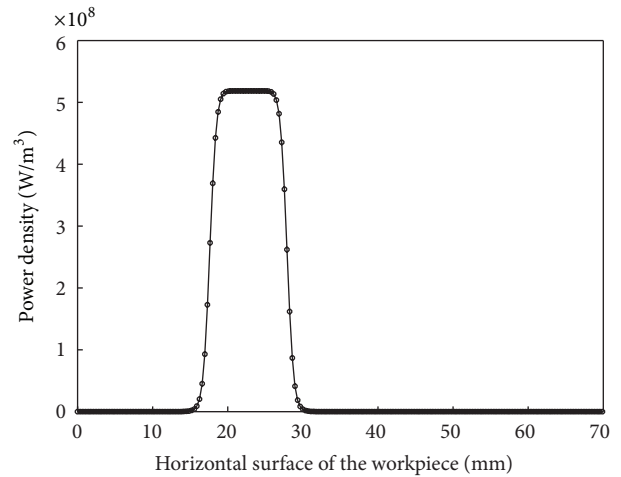


FIGURE 10: Power density distribution along the horizontal surface of the workpiece.

shown in Figure 11. It is indicated that the power induced in the workpiece is related to the velocity. The higher the velocity is, the higher power is in the workpiece. When the velocity is higher than 4 mm/s, the reduce rate of the power is slowed down.

Besides the power density distribution, the temperature field is computed in the following part. Figure 12 shows the temperature field evolution varying with time (while  $v = 5 \text{ mm/s}$ ,  $f = 50 \text{ kHz}$ , and  $I = 430 \text{ A}$ ). It indicates that the

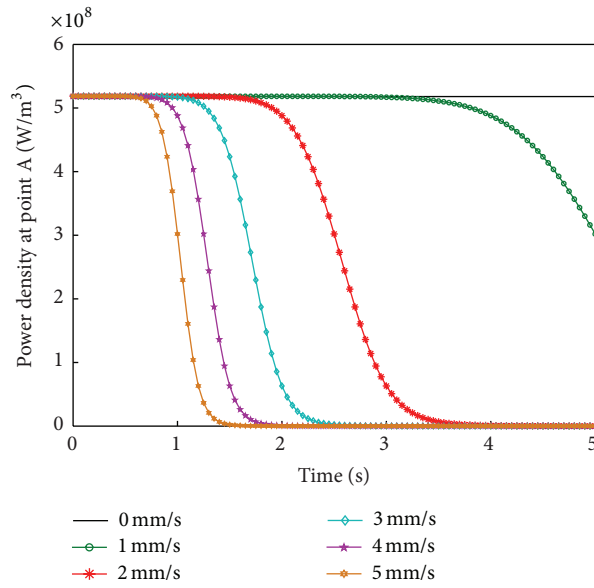


FIGURE 11: Power density variation at point A versus different velocities.

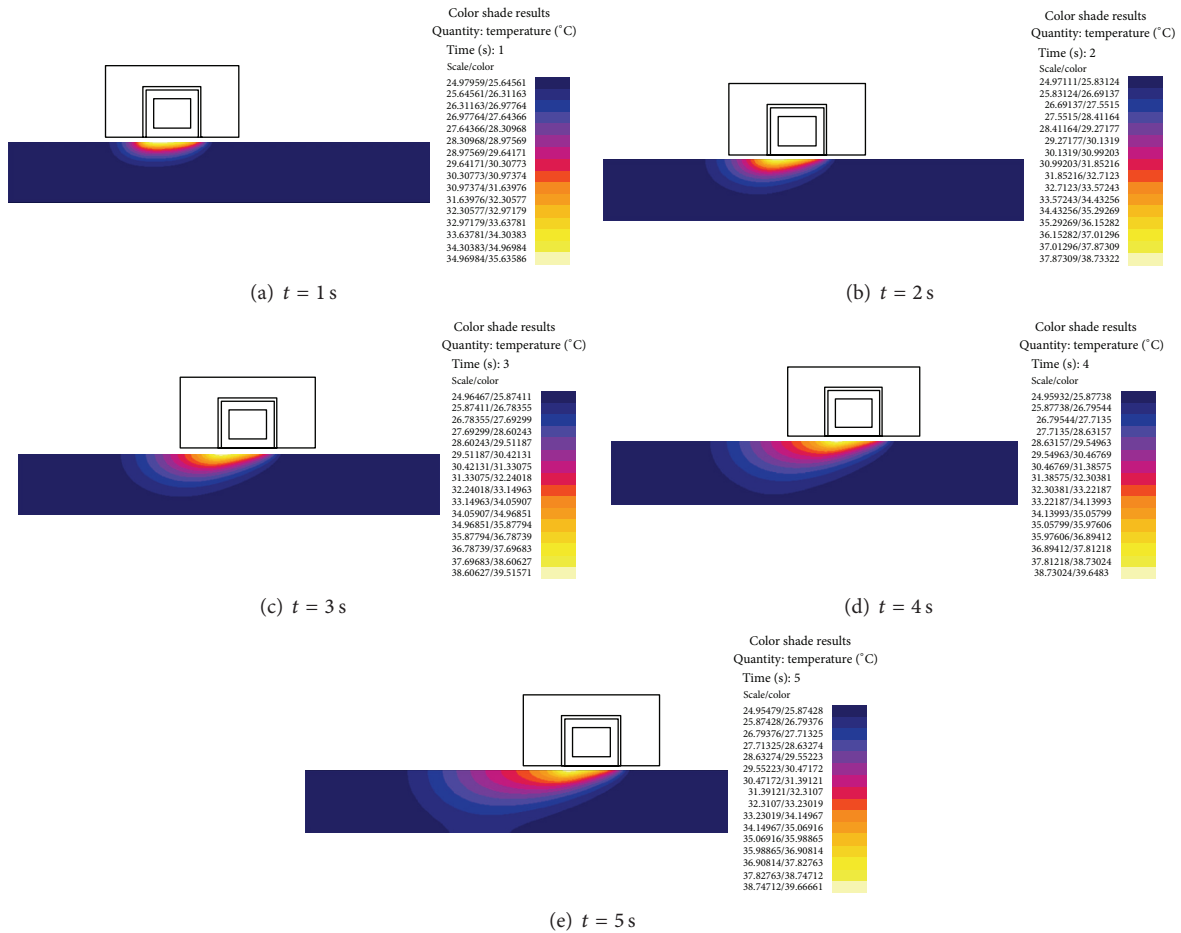


FIGURE 12: Temperature field evolution in the workpiece (while  $v = 5$  mm/s,  $f = 50$  kHz, and  $I = 430$  A).

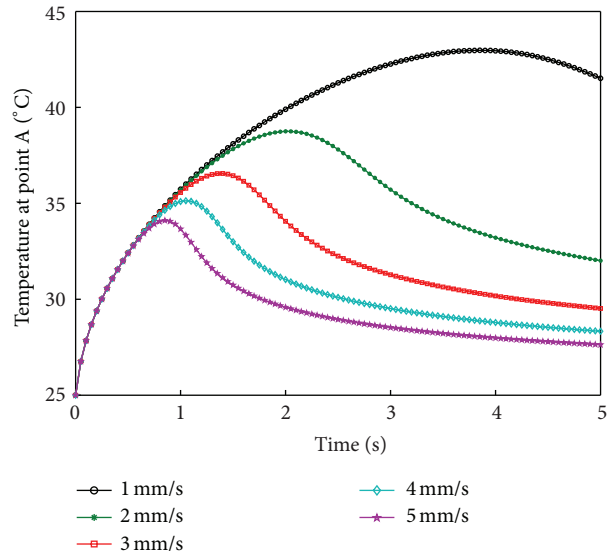


FIGURE 13: Temperature evolution at point A.

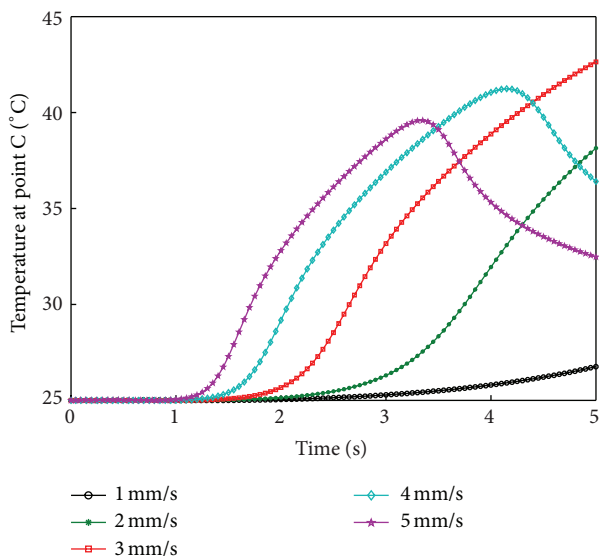


FIGURE 14: Temperature evolution at point C.

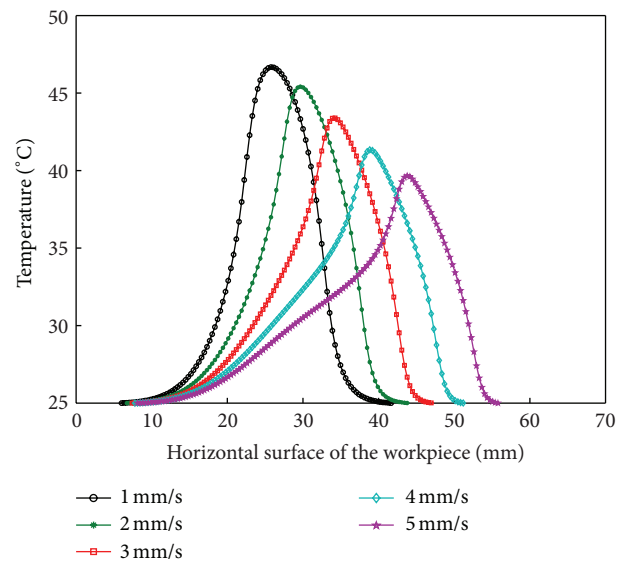


FIGURE 15: Temperature distribution at the surface of the workpiece ( $t = 5$  s).

maximum temperature can achieve up to  $40^{\circ}\text{C}$  in 5 seconds, which also produces a remarkable penetration depth. Figures 13 and 14, respectively, show the temperature evolution at points A and C with the speed of the workpiece varying from 1 mm/s to 5 mm/s. It is demonstrated that the temperature evolution depends largely on the velocity of the workpiece. The tone of temperature growth at points A and C will take great impact on the final temperature field distribution on the surface of the heated workpiece as shown in Figure 15, which describes the distribution of temperature of the workpiece's surface at the end of heating ( $t = 5$  s). The higher the velocity is, the lower the maximum temperature is. But on the contrary, the higher the velocity is, the wilder the temperature

range is. Therefore, in order to acquire the desired uniform temperature distribution, the velocity of the workpiece should be controlled properly.

In order to effectively verify the numerical model and reveal the influence of the boundary cooling condition on the temperature evolution, AISI 1045 steel is heated statically. Figure 16 shows the temperature development history of both simulation and experiment on AISI 1045 steel at points D and E. The result illustrates a good correlation between the simulation and experimental results. The maximum error is approximately 8%, which is within the acceptable range. Figure 17(a) shows the temperature development on the surface point A with the different surface cooling conditions

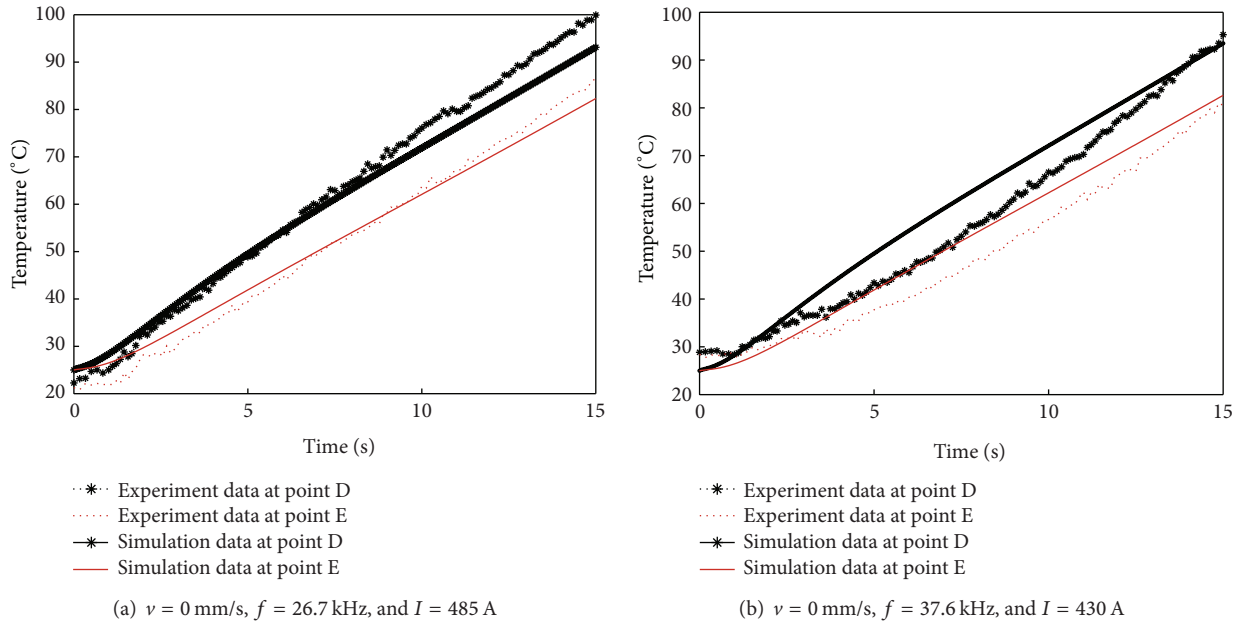


FIGURE 16: Temperature evolution at point D and point E.

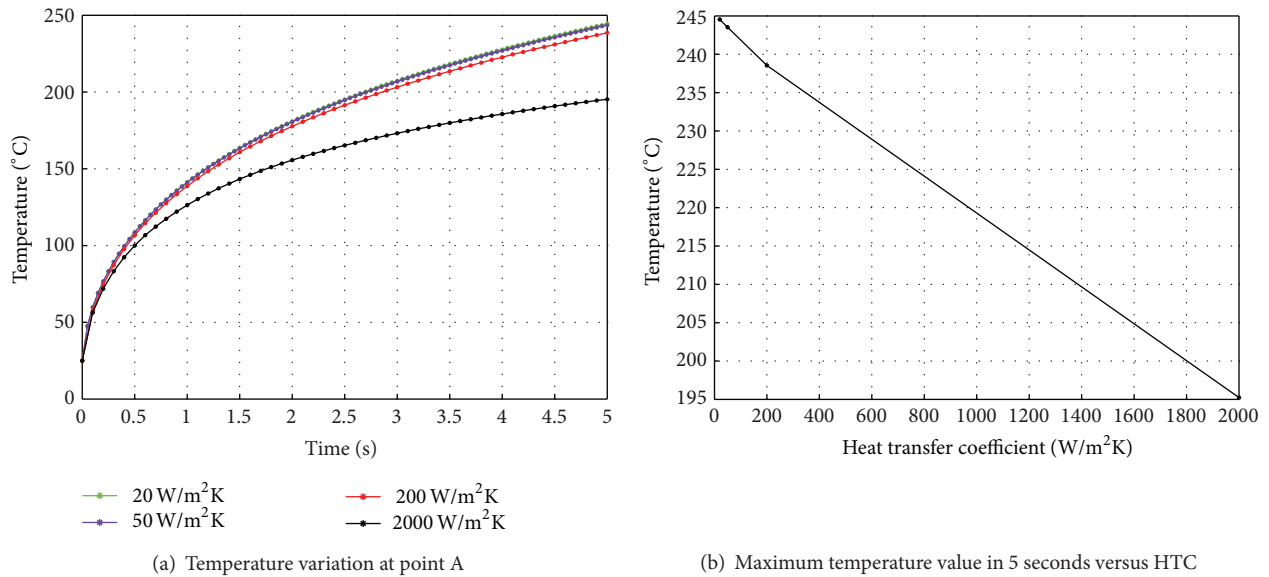


FIGURE 17: Temperature variation at point A.

(while  $v = 0$  mm/s,  $f = 37.6$  kHz, and  $I = 430$  A). The maximum temperature in 5 seconds presents a linear downtrend along with the increasing value of the surface heat transfer coefficient (Figure 17(b)). Figure 18 shows the temperature profiles below the surface point A in 5 seconds with the different surface cooling conditions. It shows an unobvious penetration depth variation with the surface cooling intensity increasing. Therefore, it is clear that the factor influencing the penetration depth of power density and the temperature is not the surface boundary cooling condition, but the input current frequency  $f$ .

#### 4. Conclusions

The moving induction heating possesses wide application in surface hardening for steel. This work studies the moving induction heating progress with MPB-MFC, which establishes the numerical model based on finite element method. The temperature-dependent magnetic and thermal material properties are applied into the simulation, which helps generate accurate prediction results. In addition, the critical factors that influence the heating efficiency are studied, and the following conclusions can be achieved.

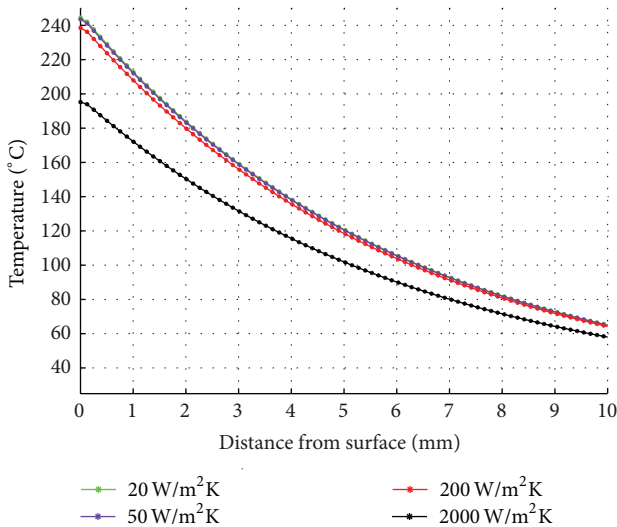


FIGURE 18: Temperature profiles below the surface point A.

- (i) By analyzing the power density and temperature evolution, it is demonstrated that the final temperature field depends largely on the velocity of the workpiece. By rationally matching the velocity, the appropriate power density intensity and anticipated temperature penetration depth can be achieved. Besides, the validity of the static numerical model is verified by comparing the finite element simulation with experimental results on AISI 1045 steel. Therefore, the finite element model proposed in this paper can effectively predict the temperature distribution evolution and can be used for further process analysis and optimization.
- (ii) The cooling condition can effectively alter the surface temperature development during the induction heating process but has little impact on the penetration depth of temperature in the workpiece. The factor influencing the penetration depth of power density and temperature is still magnetic field variation and mainly resulted from the input current frequency  $f$ . This research is useful for the achievement of different desired temperature gradient distribution in the sublayer of the heated workpiece applied in the moving induction heating.
- (iii) Further investigation should be taken to the precisely uniformity control of the temperature distribution.

## Acknowledgments

The research is supported by the National Science Foundation of China (NSFC: 51175294). And special acknowledgement should be given to the Project Z121104002812045 from Beijing Municipal Science & Technology Commission and Project PMEC201201 from the Beijing Key Lab of Precision/Ultra-Precision Manufacturing Equipments and Control.

## References

- [1] V. Rudnev, D. Loveless, R. Cook, and M. Black, *Handbook of Induction Heating*, Inductoheat, Inc., 2003.
- [2] R. S. Ruffini, R. T. Ruffini, V. S. Nemkov, and R. C. Goldstein, "Advanced design of induction processes and work coils for heat treating and assembly in automotive industry," in *Proceedings of the SAE Southern Automotive Manufacturing Conference*, p. 351, 1999.
- [3] V. Nemkov, R. Goldstein, and R. Ruffini, "Magnetic flux controllers for induction heating applications," *Transactions of Materials and Heat Treatment*, vol. 25, no. 5, pp. 567–572, 2004.
- [4] F. Li, X. Li, T. Zhu, Q. Z. Zhao, and Y. M. K. Rong, "Modeling and simulation of induction heating with magnetic flux concentrator," *Applied Mechanics and Materials*, vol. 268–270, pp. 983–991, 2013.
- [5] H. Kagimoto, D. Miyagi, N. Takahashi, N. Uchida, and K. Kawanaka, "Effect of temperature dependence of magnetic properties on heating characteristics of induction heater," *IEEE Transactions on Magnetics*, vol. 46, no. 8, pp. 3018–3021, 2010.
- [6] G. Totten, M. Howes, and T. Inoue, *Handbook of Residual Stress and Deformation of Steel*, ASM International, 2002.
- [7] Z. Tan and W. G. Guo, *Thermal Physical Property of the Engineering Alloy*, Metallurgical Industry Press, Beijing, China, 1991.
- [8] *FLUX 10 User's Guide, Volume 2: Physical Description*, Cedrat Inc., 2009.
- [9] R. Ruffini, *Advanced Induction Heat Treating and Surface Engineering: Technologies and Design Methods (Internal Report)*, FLUXTROL Inc., Beijing, China, 2011.

## Research Article

# Affecting the Ageing Behaviour of Injection-Moulded Microparts Using Variothermal Mould Tempering

**Steve Meister and Dietmar Drummer**

*Friedrich-Alexander-Universität Erlangen-Nürnberg, Institute of Polymer Technology, Am Weichselgarten 9, 91054 Erlangen-Tennenlohe, Germany*

Correspondence should be addressed to Steve Meister; [meister@lkt.uni-erlangen.de](mailto:meister@lkt.uni-erlangen.de)

Received 23 May 2013; Revised 2 September 2013; Accepted 3 September 2013

Academic Editor: Gang Wang

Copyright © 2013 S. Meister and D. Drummer. This is an open access article distributed under the Creative Commons Attribution License, which permits unrestricted use, distribution, and reproduction in any medium, provided the original work is properly cited.

The fast cooling of the melt in an injection moulding process for manufacturing polymer microparts can lead to a modified inner structure, resulting in minor mechanical properties. Furthermore, the ageing can be also dependent on the process-induced properties. The results indicate that especially physical ageing processes occur in parts with unpropitious inner properties. Chemical ageing processes seem to occur independently of the process conditions in microparts. Tensile tests indicate that a process-induced favoured morphology can reduce the ageing-based change of mechanical properties.

## 1. Introduction

Microparts and microsystems technology is reputed as a prospective key technology with an estimated annual growth rate of about 10% [1]. The main fields of application of polymer microparts are seen in the areas of medical technology, as components of optical systems, as microgears in microfluidics, biotechnology, and electronics, or as a microelectromechanical system [2, 3]. The demands on the part quality and reproducibility are also increasing due to the increasing requirements on these microcomponents [4]. Microinjection moulding appears to be one of the most efficient processes for the large-scale production of thermoplastic polymer microparts [5, 6].

Reduced part dimensions cause an increasing cooling affecting the morphological and the resulting mechanical properties of a micropart [7, 8]. In a conventional injection moulding process, the mould surface temperature is far below the melt temperature. This leads to a high cooling velocity and results in a frozen layer close to the mould surface [9] which affects also the filling behaviour due to change in melt viscosity [10]. To counteract this effect, different strategies were developed and investigated to modify and optimize the process parameters. An increasing pressure [11–13] or a high shear rate [14, 15] can favour the crystallization which is

shifted to a higher temperature. Notwithstanding, the most important process parameters that are discussed to influence the part properties are the temperatures of the mould and the melt, whereas the mould temperature appears to be the key parameter [10, 16–18]. In general, with increasing mould or melt temperature the emerging part morphology is favoured, affecting the resulting mechanical properties (e.g., tensile strength) of the part [19–23]. In addition, the usage of thermal low conductive mould materials [20, 24, 25] or a dynamic temperature control of the cavity [26–29] can influence the cooling rate of the melt.

Ageing effects of thermoplastics are differentiated in physical and chemical mechanisms. Physical ageing influences the physical structure (crystallinity, morphology, and orientations) without changing its chemical structure which can lead to cracks and fractures in the part [30, 31]. Chemical ageing affects the chemical structure of the molecular chains and is dependent amongst others on temperature, oxygen concentration, chemical structure, and the structural part properties ageing [31–34]. The effects of degradation on the properties of the aged polymer are versatile. As mentioned by Schnabel [33], the degradation affects the average molecular weight and the molecular weight distribution. Investigations by Valko and Chiklis [35] showed that in the presence of nitrogen the molecular weight of nylon 66 increases due to

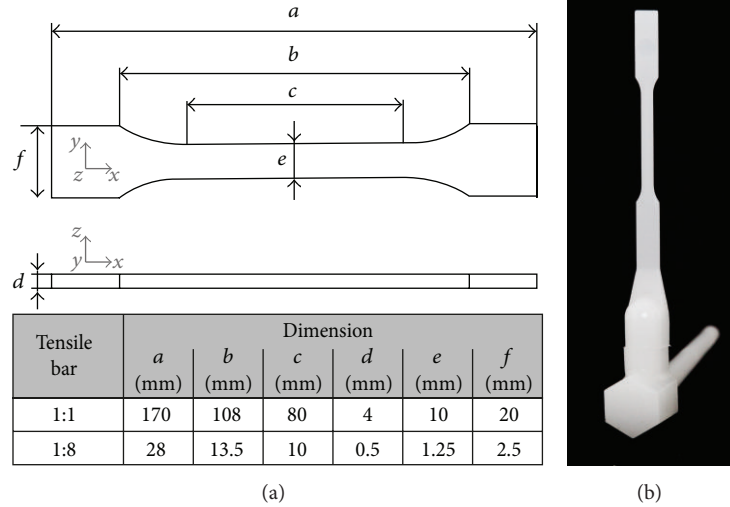


FIGURE 1: Dimensions of the used 1 : 8 scaled tensile bar in comparison to a standardized tensile bar according to EN ISO 3167 type A (a) and picture of an injection-moulded specimen (b).

the cross-linking effect. However, in presence of oxygen it is connected with the simultaneous chain scission due to thermooxidative ageing. The ageing effects can lead to an embrittlement of the polymer part and thus to a reduction in elongation and yield stress [32–34]. Polymer parts with smaller dimensions are particularly more affected by ageing as parts with macroscopic dimensions [36].

## 2. Experimental

The used material was a semicrystalline polyamide 66 (PA66) Ultramid A3 K manufactured by BASF SE. The material was chosen because of its good flow properties and its relevance for the production of common microparts. Characteristic values of the material are shown in Table 1.

For investigations on the influence of process conditions on the long-term properties a scaled tensile bar was used. The dimensions are taken from a normalized tensile bar, according to EN ISO 3167 (type A) and are downscaled up to a ratio of 1 : 8, as shown in Figure 1. Merely the shoulder lengths of the 1 : 8 scaled tensile bar are extended to assure for safe clamping during tensile testing.

The specimen were injection-moulded using an Arburg Allrounder 370U 700–30/30 injection moulding machine, equipped with a position-controlled screw with a diameter of 15 mm. To vary the mould temperature a variothermal process was realized using a variothermal temperature control system (type: SWTS 200, Single Temperierteknik GmbH). The system employs water as the circulating fluid and has a heating and a cooling circuit-switching device. It allows a fluid temperature up to 200°C. The master mould is maintained at a constant temperature (100°C) for the purpose of process stability, and only the temperature of cavity inserts is actively controlled. These cavity inserts were built up layer by layer from a steel powder using a rapid tooling process (LaserCusing, Concept Laser GmbH). This manufacturing process allows for a complex design of cooling channels

TABLE 1: Characteristics of the investigated PA66 (manufacturer's data).

Parameter	PA66
Density ( $\rho$ ) ( $\text{kg}\cdot\text{m}^{-3}$ )	1130
Melting temperature ( $^{\circ}\text{C}$ )	260
Crystallization temperature ( $^{\circ}\text{C}$ )	236
Young's modulus ( $\text{N mm}^{-2}$ )	3100*
Yield strength ( $\text{N mm}^{-2}$ )	85*
Strain at break (%)	30*

\*Dry conditioned.

whereby an optimized tempering of the cavity can be realized. The combination of insulation from the master mould and conformal cooling channels conduces to particularly rapid temperature changes in the cavity. The mould temperature was measured by cavity near temperature sensors.

In the investigations, mould temperatures of 100°C up to 160°C were used. After reaching the defined mould temperature, the melt is injected and the mould is cooled down. The curves of the temperature development for the different mould temperatures during injection are shown in Figure 2.

As a consequence of an increasing mould temperature, the cooling rate of the mould after switching to the cold fluid increases too, due to the higher temperature gradient (the temperature of the cold water stays constant). While for a lower mould temperature the average temperature change is around  $12 \text{ K s}^{-1}$ , it increases with up to  $20 \text{ K s}^{-1}$  for a mould temperature of 160°C.

The samples were artificial aged at a temperature of 140°C under ambient air in a hot air oven (type UT 6050 K, Heraeus Instruments). The specimens were taken out after 21 days.

The crystalline morphology was investigated on  $10 \mu\text{m}$  thick cuts using polarised light microscopy. These cuts were taken out of the middle of the test specimen along

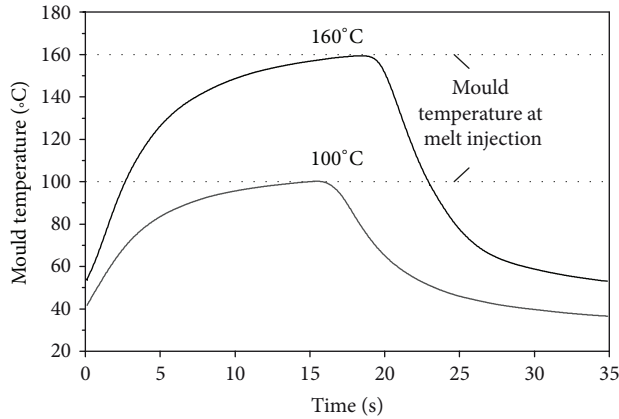


FIGURE 2: Mould temperature development during the variothermal injection moulding process at mould temperature 100 or 160°C.

the injection direction. The cuts of the aged specimen were additionally polished and investigated by incident light microscopy. For the characterization of the crystallinity infrared microscopy (Nicolet 6700 and Nicolet Continuum $\mu$ m, ThermoScientific) was applied. On each part, the crystallinity was measured local resolved across a 10  $\mu$ m thick cut over the cross-section. As Kohan [37] has verified, the ratio  $r$  of extinction of the absorbance bands at 1199  $\text{cm}^{-1}$  for the crystalline part and of 1180  $\text{cm}^{-1}$  for the amorphous part describes the degree of crystallinity. The ratio  $r$  allows an approximate determination of the degree of crystallization by the following equation [38]:

$$f(r) = -1.30591 + 20.0028r - 1.86991r^2. \quad (1)$$

Using the infrared microscopy allows also for investigating the local concentration of carbonyl groups in the part. These functional groups arise by reason of thermo-oxidative reactions in the material and give information about the local ageing. In polyamides the thermooxidative degradation leads to radical generation resulting in carbonyl groups like ketone or aldehyde groups. These groups can react further, for example, to carboxyl acids. These reactions can result in chain scission or in cross-linking of the polymer chains [32]. For this, the solution viscosity number was investigated and performed in accordance with DIN EN ISO 307 with sulfuric acid (98%) as solvent. A cross-linking of the polymer chains leads to an increasing of the molecular weight, observable in a higher viscosity. Chain scission results in a lower molecular weight and a lower viscosity.

To determine the mechanical behaviour of the tensile bars, tensile tests according to ISO 527-1 were performed using the tensile testing machine MicroTester (Instron Deutschland GmbH). Due to the dimension of the 1:8 tensile bar, testing parameters have to be adjusted, as shown in Table 2. For the measurements of the elongations, a glass scale is used. The characterization of process-dependent mechanical properties, due to modified process-induced morphology, using injection-moulded micro tensile bars was validated by Meister et al. [21, 23]. Due to the influence of water on the mechanical behaviour of PA66 samples, these

TABLE 2: Tensile test parameters (1:1 = standard tensile bar, 1:8 = scaled tensile bar).

Tensile bar	1:1	1:8
$l_0$ (mm)	50	11,6
$v_{\text{Young's mod.}}$ ( $\text{mm min}^{-1}$ )	1	0,125
$v$ ( $\text{mm min}^{-1}$ )	50	5

were conditioned in a vacuum oven at 70°C, to measure the properties in dry condition. The moisture of the PA66 parts was verified before testing by Karl Fischer titration and rendered values below 0.2 wt%.

### 3. Results and Discussion

**3.1. Morphological Structure.** The morphological structure of the 1:8 scaled tensile bars of the PA66 parts is shown in Figure 3. The influence of the cooling conditions is visible in the polarized transmitted light microscopy of the thin cuts of the nonaged tensile bars (left). A mould temperature of 100°C during injection moulding and immediate cooling leads to a fine morphological structure due to an increasing nucleation effect as well as a fast cessation of spherulitic growth. A higher mould temperature of 160°C delays the cooling of the melt which results in a clearly observable spherulitic structure. However, with increasing of the mould temperature the size of the spherulites increases too. Because the mould temperature is still below the crystallization temperature a visible surface layer arises. Here the spherulite size remains smaller than in the core layer.

The ageing of the tensile bars can lead to a change in the morphological structure. The specimen without a considerably spherulitic structure (injection moulded at 100°C) shows a significant change. The thermal load enables a postcrystallisation process which, in combination with the sufficient high chain mobility, results in a slight growing of spherulites. In the part with higher process temperatures no change in the spherulitic structure can be observed.

A consideration of the polished cuts of the specimens shows a distinct brown coloration over the whole cross-section of the specimens. The nonaged material appears opaque to white. This discolouration is due to a change in the molecular structure of the material as a result of chemical ageing processes. However, no different extension of the discolouration is evident between the different manufactured parts.

**3.2. Degree of Crystallinity.** The varied cooling conditions affect not only the spherulitic structures in the part but also the degree of crystallinity, Figure 4. As expected, the degree of crystallinity correlates with the observed morphological structures. While the parts injection moulded at a mould temperature of 100°C show a low degree of crystallinity over the complete cross-section, the parts injection moulded at higher mould temperatures reveal an increasing degree of crystallinity. This correlates with the observed surface layer in the morphology structures. The degree of crystallinity in the

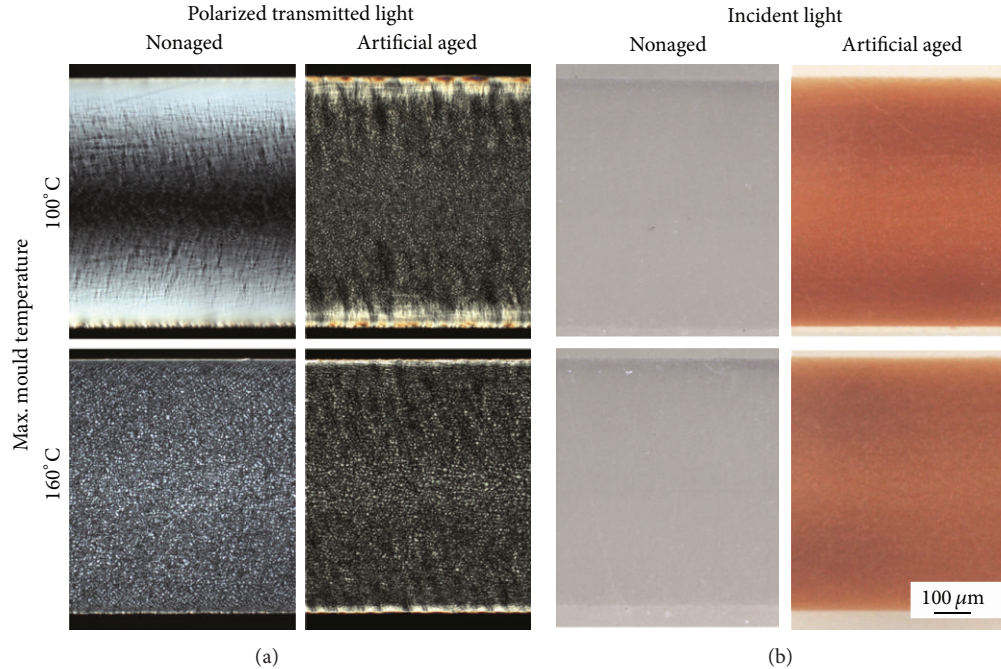


FIGURE 3: Morphology of the different tensile bars in dependence of process and ageing conditions ((a) polarized transmitted light microscopy on 10 μm thin cuts; (b) incident light microscopy of polished midplane cuts).

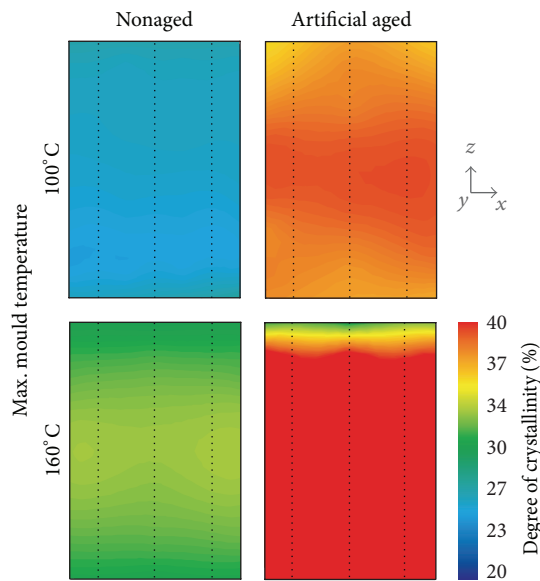


FIGURE 4: Degree of crystallinity of the specimens over the cross-section in dependence of process and ageing conditions.

parts injection moulded at 100°C is about 25%. With higher mould temperature a crystallinity of about 31% is noticeable, where the crystallinity increases also from the surface to the core with a difference of around 4%. Notwithstanding, the degree of crystallinity is for all specimens below a typical value of around 35–45%.

After the artificial ageing, the specimens show an increasing degree of crystallinity resulting from a postcrystallization

process due to the thermal load. Consequently, a physical ageing process occurred in the polymer. The growth of crystallinity takes place all over the part, with an increase of about 13%, whereas with higher mould temperature the change is only 10%, thus, a faster cooling of the mould, and the resulting morphology results in a slightly higher physical ageing.

**3.3. Carbonyl Groups.** The ratio of the carbonyl groups (carbonyl index) enables information about local chemical ageing processes in the part. As a consequence of thermo-oxidative ageing, the concentration of carbonyl groups increases. The measured carbonyl index is shown in Figure 5. The nonaged specimens (left) possess the same low carbonyl index, independent of the process conditions. The low value can be due to a slight load during the processing of the material.

As a consequence of the thermo-oxidative load, a chemical ageing process took place. This is evident in an increasing carbonyl ratio in the specimens. The measurements show that the carbonyl ratio is slightly higher in the surface area as in the core; consequently, the thermo-oxidative ageing occurs initiating from the surface to the core. This is due to the diffusion controlled oxygen concentration which decreases to the core. However, the difference of the carbonyl ratio between surface and core is less significant. So the chemical ageing occurs nearly over the complete cross-section, which is well observable in the part injection moulded at lower temperatures. The higher degree of crystallinity of the parts injection moulded at higher mould temperatures inhibits oxygen diffusion and is additionally more resistant against ageing. However, the difference has a minor significance.

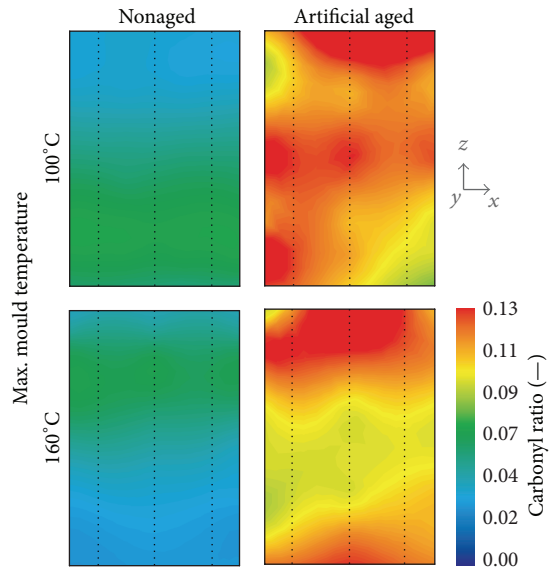


FIGURE 5: Ratio of the carbonyl groups of the specimens over the cross-section in dependence of process and ageing conditions.

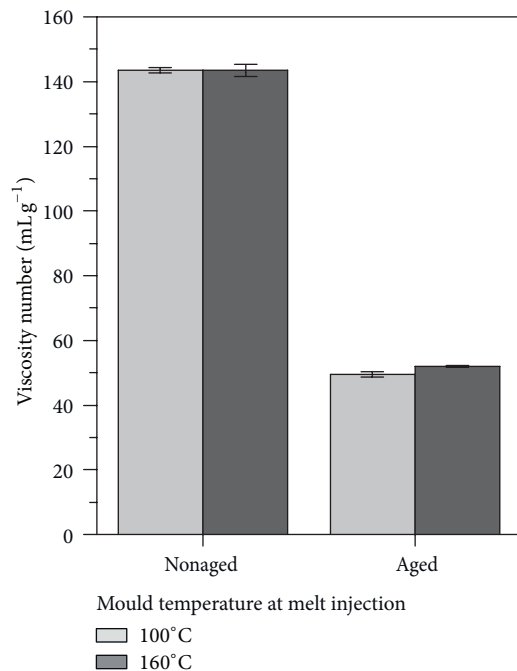


FIGURE 6: Solution viscosity of the nonaged and aged specimens in dependence of process conditions.

**3.4. Solution Viscosity.** The artificial ageing of the micro tensile bars leads to a decrease of viscosity number which is due to a thermo-oxidative degradation and an occurring chain scission in the material, Figure 6. The decrease of the viscosity number shows only a slight dependence from the process conditions. Both a low and a high mould temperature (with a favoured morphology) show a decrease over 60%. Nevertheless, the specimens injection moulded at a higher mould temperature have slight higher solution

viscosity. While the parts injection moulded at the lower mould temperature show an average solution viscosity of  $50 \text{ mL g}^{-1}$ , the parts injection moulded at the higher mould temperature have  $52 \text{ mL g}^{-1}$ . This can be evidence for the influence of the processing on the ageing behaviour of polymers in microparts. In addition, these results go along with the infrared spectroscopic measurements and the analyzed carbonyl ratio.

**3.5. Mechanical Properties.** As a consequence of the different cooling conditions and the affected inner properties, the resulting mechanical properties are affected too. Figure 7 shows the resulting mechanical properties of the different manufactured specimens before and after artificial ageing. The homogeneous morphology and the higher degree of crystallinity support stiffness and strength of the at higher mould temperatures injection-moulded parts. For both, Young's modulus and the tensile strength an increasing value is observed. An effect on the strain at break cannot be found due to the high standard deviation.

The artificial ageing leads to physical and chemical ageing effects, as shown above. As a consequence, the mechanical properties are affected too. Due to the postcrystallization of the specimens Young's modulus increases in all specimens. Because of the higher postcrystallization of the specimens with the process-induced lower degree of crystallinity, they have accordingly the highest increase in Young's modulus. The value increases about 9% while the specimens, injection moulded at  $160^\circ\text{C}$ , show only 4% increase. The chemical ageing effects are reflected in the tensile strength and the strain at break. Because of the influence on the molecular chains and the resulting chain degradation the material embrittles. This effect is typical for polymer ageing and is especially observable in the significant decrease in the strain at break. All the specimens reach after artificial ageing only an elongation of at most 5%. As a consequence, the tensile strength is also influenced. The low elongation at break limits the bearable load of the material and the specimen breaks. This is observable in the decreasing tensile strength of all specimens. However, the specimens injection moulded with a lower mould temperature are more affected by the ageing. These specimens show lower tensile strength in combination with a significant increasing standard deviation. Both are typical results for occurred polymer ageing. The parts with a process-induced favoured morphology exhibit a slight lower influence on the ageing effects as the average tensile strength decreases less and the deviation is also lower.

## 4. Conclusion

The ageing behaviour of injection-moulded microparts in dependence of the process conditions was investigated using a variothermal injection moulding process. The results have confirmed that the mould temperature affects the inner properties and the resulting mechanical behaviour as has already been stated [7, 8, 10, 16–19]. In addition, ageing of polymer microparts is also dependent on the process inducing inner structure. It has been shown that an unpropitious

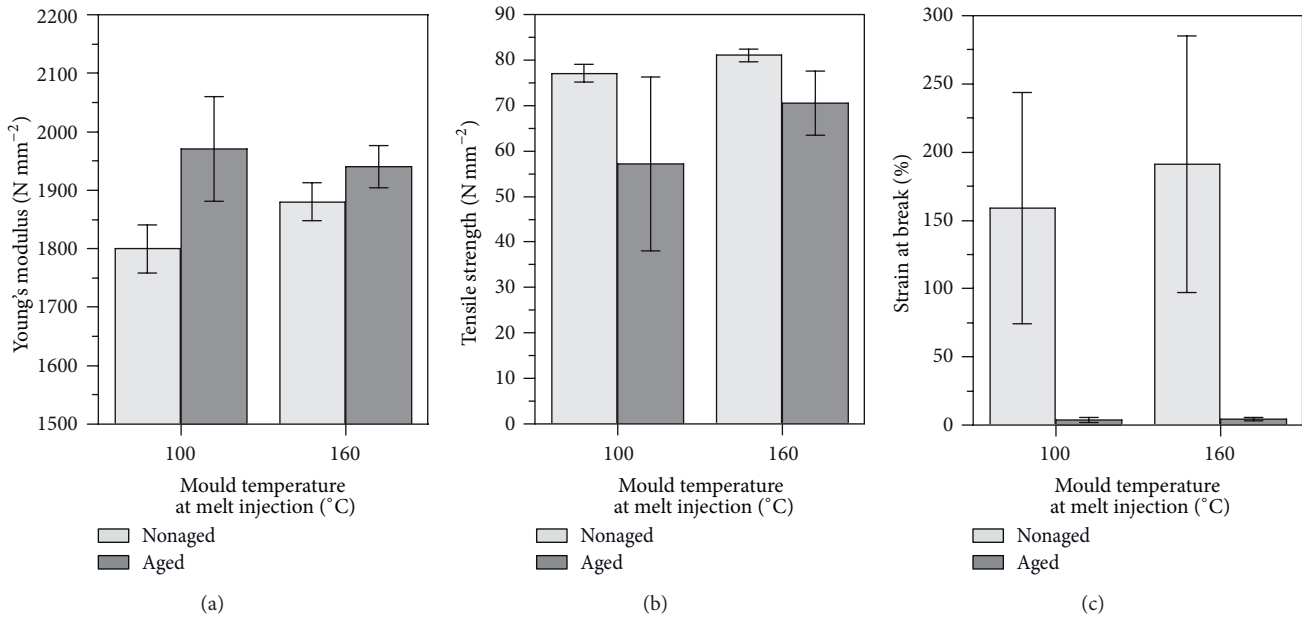


FIGURE 7: Young's modulus (a), tensile strength (b), and strain at break (c) of the nonaged and aged tensile bars in dependence of the mould temperature at melt injection.

morphology leads to a more intense physical ageing, that is, postcrystallization of the material. The chemical ageing effects show that the slight dependence on the morphology as the carbonyl ratio increases or the viscosity decreases in the investigated specimens is the same. However, a process-induced favoured morphology can attenuate the ageing effects.

As a consequence of the affected inner properties, the resulting mechanical properties are influenced too. The stiffness increases due to the increasing degree of crystallinity, whereas the tensile strength and the elongation at break decreases as a result of chemical ageing and molecular chain degradation. The change in mechanical properties by reason of physical and chemical ageing effects is more of intense in a polymer micropart if the inner properties are unpropitious.

Further studies have to investigate the influence of time, especially the question when ageing occurs in microparts and how this is dependent on the process conditions. For example, the local resolved ageing in a part is of interest. It is also open to separate the effects of polymer chain degradation and cross-linking on the long-term part properties. As well, it has to be examined if the found process dependency exists for other polymers or other loads, for example, environmental fluids or energetic radiation.

## Acknowledgments

The authors gratefully acknowledge the Bavarian Research Foundation for funding the work. They also extend their gratitude to their industrial partners Werkzeugbau Hofmann GmbH, Oechsler AG, Single Temperiertechnik GmbH, Hotec GmbH, Arburg GmbH & Co. KG, and BASF SE for providing equipment and material. They further thank Mrs.

Pia Trawiel and Mr. Jürgen König for performing infrared spectroscopy measurements. The authors also acknowledge support by Deutsche Forschungsgemeinschaft and Friedrich-Alexander-Universität Erlangen-Nürnberg within the funding programme Open Access Publishing.

## References

- [1] Leaflet, *Integrierte Intelligenz: Perspektiven der Mikrosystemtechnik*, Federal Ministry of Education and Research, Bonn, Germany, 2010.
- [2] A. K. Angelov and J. P. Coulter, "Micromolding product manufacture: a progress report," in *Proceedings of the Society of Plastics Engineers Annual Technical Conference (ANTEC '04)*, pp. 748–751, Boston, MA, USA, May 2004.
- [3] D. M. Bibber, "Micro molding challenges," in *Proceedings of the Society of Plastics Engineers Annual Technical Conference (ANTEC '04)*, pp. 3703–3711, Chicago, Ill, USA, May 2004.
- [4] O. Pfirrmann and M. Astor, *Trendreport Mikrosystemtechnik—Innovative Ideen Rund Um Die Mikrosystemtechnik*, Prognos AG, Basel, Switzerland, 2006.
- [5] W. Michaeli, A. Spennemann, and R. Gärtner, "New plastication concepts for micro injection moulding," *Microsystem Technologies*, vol. 8, no. 1, pp. 55–57, 2002.
- [6] D. Drummer, G. W. Ehrenstein, C. Hopmann et al., "Innovative process technologies for manufacturing thermoplastic micro parts—analysis and comparative assessment," *Journal of Plastics Technology*, vol. 8, no. 5, p. 439, 2012.
- [7] A. M. Tom, G. S. Layser, and J. P. Coulter, "Mechanical property determination of micro injection molded tensile test specimens," in *Proceedings of the Society of Plastics Engineers Annual Technical Conference (ANTEC '06)*, pp. 2541–2545, Charlotte, Calif, USA, May 2006.
- [8] T. Nguyen-Chung, C. Löser, G. Jüttner, M. Obadal, T. Pham, and M. Gehde, "Morphology analysis of injection molded

- micro-parts," *Journal of Plastics Technology*, vol. 7, no. 3, p. 86, 2011.
- [9] C. Gornik, "Injection moulding of parts with microstructured surfaces for medical applications," *Macromolecular Symposia*, vol. 217, no. 1, p. 365, 2004.
- [10] J. Giboz, T. Copponnex, and P. Mélé, "Microinjection molding of thermoplastic polymers: a review," *Journal of Micromechanics and Microengineering*, vol. 17, no. 6, article R02, p. R96, 2007.
- [11] M. Moneke, *Die Kristallisation von verstärkten Thermoplasten Während der Schnellen Abkühlung und unter Druck [Ph.D. thesis]*, University Darmstadt, Darmstadt, Germany, 2001.
- [12] N. M. Rudolph, T. A. Osswald, and G. W. Ehrenstein, "Influence of pressure on volume, temperature and crystallization of thermoplastics during polymer processing," *International Polymer Processing*, vol. 26, no. 3, p. 239, 2011.
- [13] K. V. Karl, "Über die druckabhängigkeit der viskoelastischen und physikalisch-chemischen eigenschaften von polymeren," *Die Angewandte Makromolekulare Chemie*, vol. 79, no. 1, p. 11, 1979.
- [14] P.-W. Zhu, J. Tung, A. Phillips, and G. Edward, "Morphological development of oriented isotactic polypropylene in the presence of a nucleating agent," *Macromolecules*, vol. 39, no. 5, pp. 1821–1831, 2006.
- [15] C. Stern, A. R. Frick, G. Weickert, G. H. Michler, and S. Henning, "Processing, morphology, and mechanical properties of liquid pool polypropylene with different molecular weights," *Macromolecular Materials and Engineering*, vol. 290, no. 6, pp. 621–635, 2005.
- [16] G. Tosello, A. Gava, H. N. Hansen, and G. Lucchetta, "Study of process parameters effect on the filling phase of micro-injection moulding using weld lines as flow markers," *International Journal of Advanced Manufacturing Technology*, vol. 47, no. 1–4, pp. 81–97, 2010.
- [17] M. T. Martyn, B. Whiteside, P. D. Coates, P. S. Allen, G. Greenway, and P. Hornsby, "Aspects of micromoulding polymers for medical applications," in *Proceedings of the Society of Plastics Engineers Annual Technical Conference (ANTEC '04)*, pp. 3698–3702, Boston, MA, USA, May 2004.
- [18] B. Sha, S. Dimov, C. Griffiths, and M. S. Packianather, "Investigation of micro-injection moulding: factors affecting the replication quality," *Journal of Materials Processing Technology*, vol. 183, no. 2–3, pp. 284–296, 2007.
- [19] E. Haberstroh and M. Brandt, "Determination of mechanical properties of thermoplastics suitable for micro systems," *Macromolecular Materials and Engineering*, vol. 287, no. 12, pp. 881–888, 2002.
- [20] D. Schmiederer and E. Schmachtenberg, "Einflüsse auf die Eigenschaften kleiner und dünnwandiger Spritzgussteile," *Journal of Plastics Technology*, vol. 2, no. 5, p. 1, 2006.
- [21] S. Meister and D. Drummer, "Influence of manufacturing conditions on measurement of mechanical material properties on thermoplastic micro tensile bars," *Polymer Testing*, vol. 32, no. 2, p. 432, 2013.
- [22] H. W. Starkweather, G. E. Moore, J. E. Hansen, T. M. Roder, and R. E. Brooks, "Effect of crystallinity on the properties of nylons," *Journal of Polymer Science*, vol. 21, no. 98, p. 189, 1956.
- [23] S. Meister, K. Vetter, G. W. Ehrenstein, and D. Drummer, "Measurement of mechanical material properties for micro parts on injection moulded micro tensile bars," *Journal of Plastics Technology*, vol. 9, no. 1, p. 74, 2013.
- [24] A. Lurz, I. Kühnert, and E. Schmachtenberg, "Influences on the properties of small and thin-walled injection molded parts—part 2: Importance of the thermal conductivity of the mold material," *Journal of Plastics Technology*, vol. 4, no. 1, p. 1, 2008.
- [25] A. Jungmeier, G. W. Ehrenstein, and D. Drummer, "New aspects of process induced properties of microinjection moulded parts," *Plastics, Rubber and Composites*, vol. 39, no. 7, pp. 308–314, 2010.
- [26] T. Walter, W. Schinköthe, W. Ehrfeld, C. Schaumburg, and L. Weber, "Injection moulding of microstructures with inductive mould heating," in *Proceedings of the 16. Stuttgarter Kunststoff-Kolloquium*, pp. 1–10, Stuttgart, Germany, 1999.
- [27] J. Giessauf, G. Pillwein, and G. Steinbichler, "Varietherm temperature control is fit for production," *Kunststoffe International*, vol. 98, no. 8, pp. 57–62, 2008.
- [28] D. Drummer, K. Gruber, and S. Meister, "Process optimization: alternating temperature technology controls parts properties," *Kunststoffe International*, vol. 101, no. 4, pp. 25–27, 2011.
- [29] S. Meister and D. Drummer, "Investigation on the achievable flow length in injection moulding of polymeric materials with dynamic mould tempering," *The Scientific World Journal*, vol. 2013, Article ID 845916, 7 pages, 2013.
- [30] G. W. Ehrenstein, *Kunststoff-Schadensanalyse: Methoden Und Verfahren*, Hanser, Munich, Germany, 1992.
- [31] G. W. Ehrenstein and S. Pongratz, *Beständigkeit Von Kunststoffen*, Hanser, Munich, Germany, 2007.
- [32] S. Pongratz, *Alterung von Kunststoffen während der Verarbeitung und im Gebrauch [Ph.D. thesis]*, University Erlangen-Nuernberg, Erlangen, Germany, 2000.
- [33] W. Schnabel, *Polymer Degradation: Principles and Practical Applications*, Hanser, Munich, Germany, 1982.
- [34] D. Ferrer-Balas, M. L. MasPOCH, A. B. Martinez, and O. O. Santana, "Influence of annealing on the microstructural, tensile and fracture properties of polypropylene films," *Polymer*, vol. 42, no. 4, pp. 1697–1705, 2001.
- [35] E. I. Valko and C. K. Chiklis, "Effects of thermal exposure on the physicochemical properties of polyamides," *Journal of Applied Polymer Science*, vol. 9, no. 8, p. 2855, 1965.
- [36] S. Meister, A. Jungmeier, and D. Drummer, "Long term properties of injection moulded micro-parts: influence of part dimensions and cooling conditions on ageing behaviour," *Macromolecular Materials and Engineering*, vol. 297, no. 10, p. 994, 2012.
- [37] M. I. Kohan, *Nylon Plastics Handbook*, Hanser, Munich, Germany, 1995.
- [38] A. Jungmeier, *Struktur und Eigenschaften spritzgegossener, thermoplastischer Mikroformteile [Ph.D. thesis]*, University Erlangen-Nuernberg, Erlangen, Germany, 2010.

## Research Article

# Effect of the Codeposition Ions on Structural and Tribological Properties of Electro-Brush Plated Coating

Xiufang Cui, Jinggao Zhong, Dingding Hou, Erbao Liu, Guo Jin, and Qingfen Li

*Institute of Surface/Interface Science and Technology, School of Materials Science and Chemical Engineering, Harbin Engineering University, Harbin 150001, China*

Correspondence should be addressed to Guo Jin; [jinguo@hrbeu.edu.cn](mailto:jinguo@hrbeu.edu.cn)

Received 29 May 2013; Accepted 3 September 2013

Academic Editor: Lei Zhang

Copyright © 2013 Xiufang Cui et al. This is an open access article distributed under the Creative Commons Attribution License, which permits unrestricted use, distribution, and reproduction in any medium, provided the original work is properly cited.

The effects of the codeposition ions on structural and tribological properties of electro-brush plated coatings were investigated. The microstructure and phase structure were studied with scanning electron microscope (SEM), X-ray photoelectron spectroscopy (XPS), and X-ray diffraction (XRD). The hardness and tribological properties of several coatings with different kind of codeposition ions were studied. Results show that among the coatings with different  $\text{FeCl}_2$  contents in electrolyte, the Fe400 coating has the best surface property. When proper chemical ion W codeposited with iron ion is added, the hardness of the coatings is improved obviously and the Fe-W<sub>II</sub> coating has the best properties. When proper element of Cu is added, the hardness and tribological properties of the Fe-W-Cu coatings are also improved. Besides, the interface bond strength between the coating and the substrate is improved obviously, and the Fe-W-Cu<sub>II</sub> coating has the best properties.

## 1. Introduction

Various surface techniques are applied on different alloys to improve the wear resistance of the appearance [1–5]. Among them, the electro-brush plating technology is an important issue of surface engineering [6–11]. However, the application of iron-based brush plating is limited for its disadvantages, such as high residual stress and brittleness of the coatings, which should be further improved [10–13].

In this paper, based upon the iron-based electro-brush plating technology, different kinds of codeposition ions were added in the bath, and the effects of the codeposition ions on structural and tribological properties of electro-brush plated coating on steel GCr15 were investigated.

## 2. Experimental

The chemical composition of steel GCr15 used in the present investigation is shown in Table 1. Test specimen ( $\Phi 18 \times 8$  mm) surfaces were successively polished by using waterproof abrasive paper 80#, 320#, 1000#, 2000#, and then immersed in acetone solution, and cleaned in the SK3300H ultrasonic cleaner for 5 minutes. Electro-brush plating was then carried

out at ambient temperature (about 25°C) and velocity of 6 m/min~12 m/min for 10 min. The electro-brush plating was conducted in the following steps: electrical cleaning → activation → preplating → plating, and the potentials for the above four steps of the electro-brush plating were about +12 V, -12 V, +18 V, and +10 V, respectively. The current density for plating was about 10 A.

Surface micrographs, compositions, and microstructures of the test specimens were observed by scanning electron microscopy (SEM, FEI Quant200), electron energy dispersive spectroscopy (EDS, EDAX), X-ray photoelectron spectroscopy (XPS, K-Alpha), and X-ray diffraction (XRD, X-Pert-Pro). The microhardness of coating was examined by HVS 1000 sclerometer with load fixed at 25 g and load time fixed at 10 s, and the average value of five test data was adopted. Friction and wear tests were measured in a block-on-ring test (M-2000 A) with coated blocks (40×40×10 mm) and SiC cement ring ( $\Phi 50 \times 10$  mm) under the applied loads of 100 N at room temperature. The lubrication oil was liquid paraffin, and the rotate speed was 200 rpm during the test. The wear time was 10 min, and the variation of friction coefficient with sliding time was recorded automatically.

TABLE 1: Chemical composition of steel GCr15 (wt%).

C	Si	Mn	S	P	Cr
0.95–1.05	0.15–0.35	0.2–0.4	≤0.02	≤0.027	1.30–1.65

### 3. Results and Discussions

The SEM photographs of coatings electro-brush plated with different  $\text{FeCl}_2$  contents in electrolyte are given in Figure 1. It can be seen that coatings are all showing the typical cluster crystal with cauliflower shape, where every cluster crystal is composed of many small crystal cells. Figure 1(a) shows that when the content of  $\text{FeCl}_2$  in electrolyte is 250 g/L (namely, the coating is of Fe250), the cluster crystals are uneven and there are some air hole can be seen. Figure 1(b) shows that when the content of  $\text{FeCl}_2$  in electrolyte is 400 g/L (namely, the coating is of Fe400), the cluster crystals are fine and compact; no air hole can be seen. When the content of  $\text{FeCl}_2$  is 550 g/L (namely, the coating is of Fe550), the cluster crystals become very rough (Figure 1(c)). It is concluded that the Fe400 coating has the best surface property. So the content of  $\text{FeCl}_2$  in electrolyte as 400 g/L was chosen in the further studies.

Three Fe-W coatings were made by adding different contents of W ion codeposited with iron ion in the 400 g/L  $\text{FeCl}_2$  electrolyte, where different content of  $\text{Na}_2\text{WO}_4$  was used. The SEM photographs of Fe-W coatings with different W ion contents are given in Figure 2. The EDS results of Fe-W coatings are shown in Table 2. The XRD patterns of specimens with different Fe-W coatings are shown in Figure 3. The microhardness of Fe-W coatings is given in Figure 4.

Figure 2 shows that Fe-W coatings are also showing cluster crystal with cauliflower shape; however, the cluster crystals are small and there is much clearance between the crystals. For Fe-W<sub>III</sub> coating, more clearance between the crystals and the coating is very loose. The EDS tests show that the W contents for the Fe-W<sub>I</sub>, Fe-W<sub>II</sub>, and Fe-W<sub>III</sub> coatings are about 5.85%, 6.98%, and 8.73%, respectively.

From the results of XRD (Figure 3), it can be seen that only the diffract peak of  $\alpha$ -Fe appeared for the four coatings. It suggests that the metallography structure of Fe-W alloy coatings is of  $\alpha$ -Fe.

From Figure 4, it can be seen that the microhardness of Fe-W coatings are all above 600 HV, obviously higher than the one of Fe400 coating which is about 577 HV, and that the best one is the Fe-W<sub>II</sub> coating, which reaches up to 663 HV, indicating that the hardness of the coatings was improved obviously when the chemical ion W codeposited with iron ion was added.

The Fe-W-Cu coatings were made by adding the  $\text{CuCl}_2 \cdot 4\text{H}_2\text{O}$  in the Fe-W electrolyte. The SEM photographs of Fe-W-Cu coatings with different Cu ion contents in electrolyte are given in Figure 5. The EDS results of Fe-W-Cu coatings are shown in Table 3. Results of XRD for the Fe-W-Cu coatings with different contents of Cu ion are shown in Figure 6. To further indicate the existing states of W and Cu in the coatings, the XPS tests were carried out and the results

TABLE 2: W contents for Fe-W coatings (wt%).

Coating	W
Fe-W <sub>I</sub>	5.85
Fe-W <sub>II</sub>	6.98
Fe-W <sub>III</sub>	8.73

TABLE 3: Cu contents for Fe-W-Cu coatings (wt%).

Coating	Cu
Fe-W-Cu <sub>I</sub>	4.20
Fe-W-Cu <sub>II</sub>	5.12
Fe-W-Cu <sub>III</sub>	10.16

are shown in Figure 7. Microhardness and friction coefficient of Fe-W-Cu coatings are given in Figures 8 and 9, respectively.

Figure 5(a) shows that the surface of structural and abrasion properties of Fe-W-Cu<sub>I</sub> coating is uneven, and there are some lacunas that can be found. Figure 5(b) shows that the surface of Fe-W-Cu<sub>II</sub> coating is fine and compact; there are few lacunas that can be seen. From Figure 5(c), it can be seen that the Fe-W-Cu<sub>III</sub> coating is composed of many small granules and the granules are uniform and even. Table 3 shows that the Cu contents for the Fe-W-Cu<sub>I</sub>, Fe-W-Cu<sub>II</sub>, and Fe-W-Cu<sub>III</sub> coatings are about 4.20%, 5.12%, and 10.16%, respectively.

From the results of XRD (Figure 6), it can be seen that only the diffract peak of  $\alpha$ -Fe appeared for the four coatings. It suggests that the metallography structure of Fe-W-Cu coatings is also of  $\alpha$ -Fe.

The XPS results (Figure 7) indicate constituent peaks of the Fe-W-Cu coating. As shown in Figure 7(a), the W 4f peaks are measured elaborately. It is corresponding to  $\text{W}^{4+}$  and W indicating that the coating consisted of  $\text{WO}_2$  and elementary W. In Figure 7(b), it can be seen that the Cu 2p peaks are measured. The binding energy of these peaks is corresponding to  $\text{Cu}^{2+}$ ,  $\text{Cu}^{1+}$ , and Cu indicating that the coating consisted of CuO,  $\text{CuO}_2$ , and elementary Cu.

From Figure 8, it can be seen that the microhardness of Fe-W<sub>II</sub> and all the Fe-W-Cu coatings is above 600 HV. It indicates that the hardness of the Fe-W-Cu coatings was also improved.

In Figure 9, it can be seen that the friction coefficients of Fe-W-Cu coatings are all lower than the one of the Fe-W<sub>II</sub> coating which indicates that the Cu element is helpful to reduce the friction coefficient of the coating and the Fe-W-Cu<sub>II</sub> coating has the lowest friction coefficient. The EDS results show that the Cu content increases on the worn surface. It can be concluded that the antifriction mechanism is the segregation of Cu element at the interface between the friction pair during the friction process.

The SEM photographs of coating sections after corrosion are given in Figure 10. It is seen that the thickness of Fe-W-coating layers is about 120  $\mu\text{m}$  (Figures 10(a)–10(c)). There are some air holes in Fe-W<sub>I</sub> and Fe-W<sub>III</sub> coatings whereas the Fe-W<sub>II</sub> coating is fine and compact, and the border between

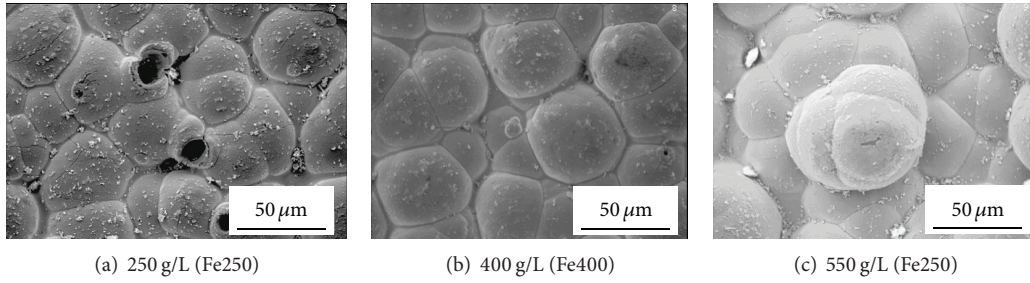


FIGURE 1: SEM photographs of coatings with different FeCl<sub>2</sub> contents in electrolyte.

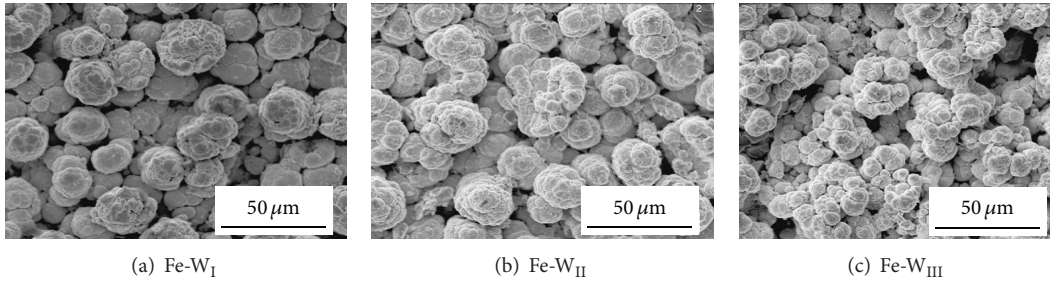


FIGURE 2: SEM photographs of Fe-W coatings with different W ion contents in electrolyte.

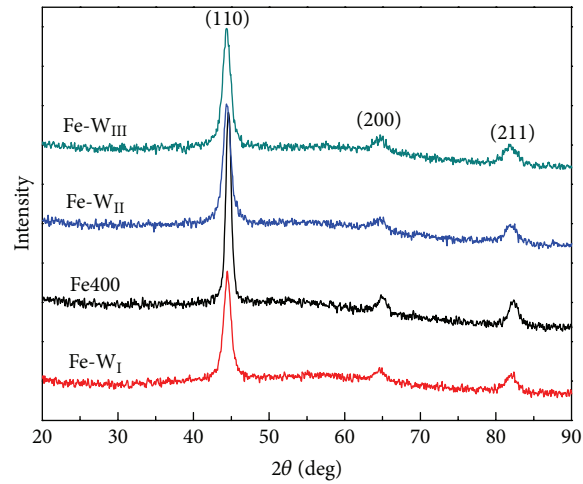


FIGURE 3: XRD of Fe-W coatings.

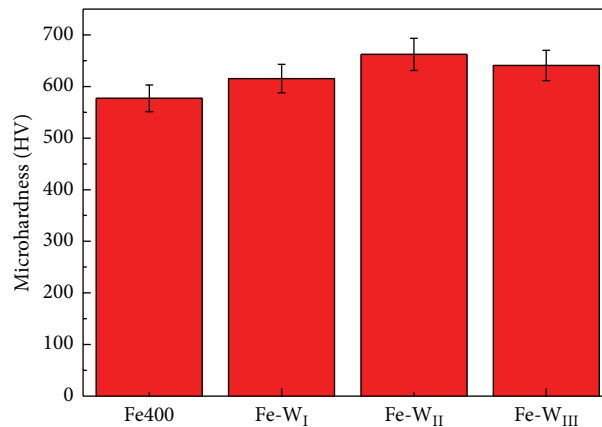


FIGURE 4: Microhardness of Fe-W coatings.

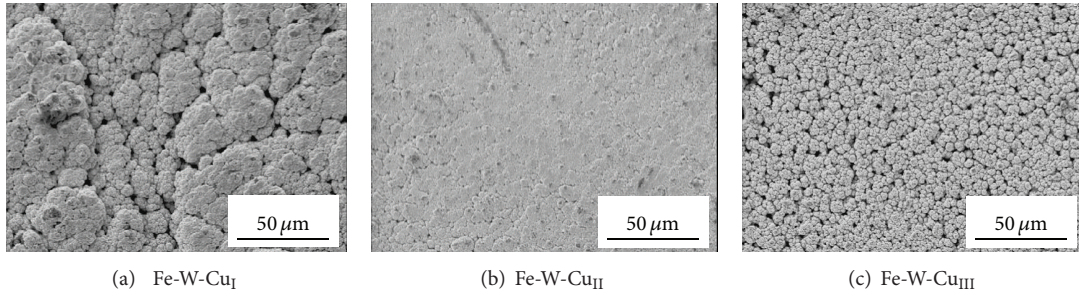


FIGURE 5: SEM photographs of Fe-W-Cu coatings with different Cu ion contents in electrolyte.

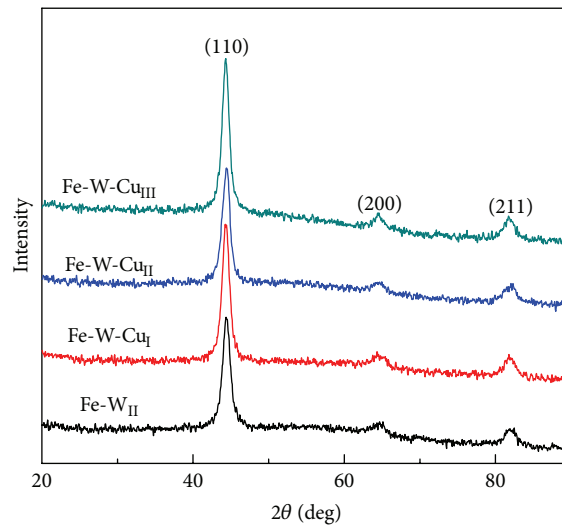


FIGURE 6: XRD of Fe-W-Cu coatings.

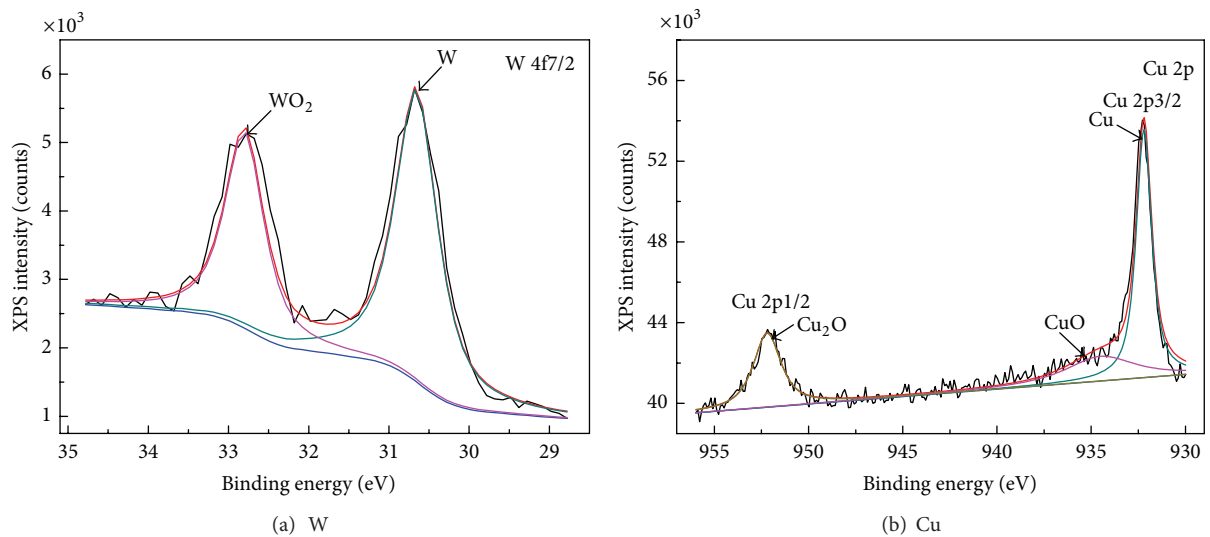


FIGURE 7: XPS high-resolution spectra of W and Cu in Fe-W-Cu coating.

the coating and the substance is good showing a nice link between them. It indicates that the Fe-W<sub>II</sub> coating has the best properties. The thickness of Fe-W-Cu-coating layers is about 100  $\mu\text{m}$  (Figures 10(d)–10(f)), and there are also some lacunas in the Fe-W-Cu<sub>I</sub> and Fe-W-Cu<sub>III</sub> coatings; however, they are

much better than the Fe-W<sub>I</sub> and Fe-W<sub>III</sub> coatings. As for the Fe-W-Cu<sub>II</sub> coating, it is very fine and compact, and the border between the coating and the substance is perfect, showing a very good link of them. From the results, we may conclude that the interface bond strength between the coating and the

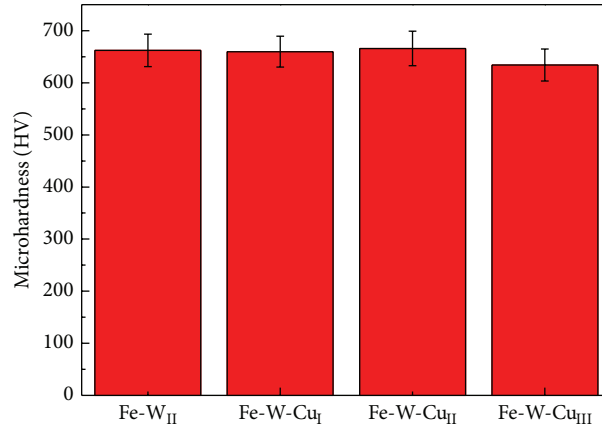


FIGURE 8: Microhardness of Fe-W-Cu coatings.

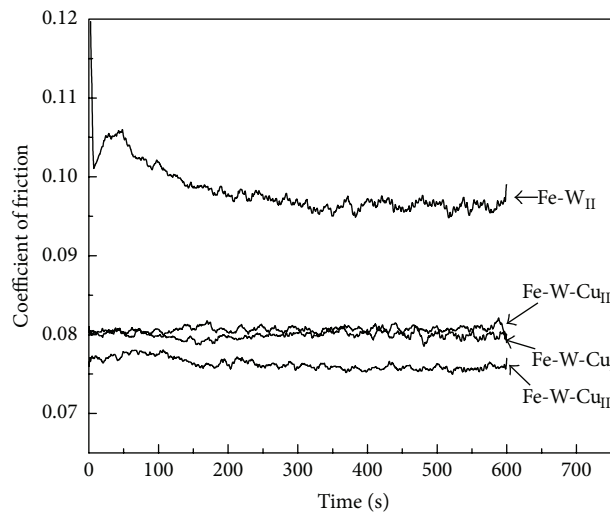


FIGURE 9: Friction coefficient of Fe-W-Cu coatings.

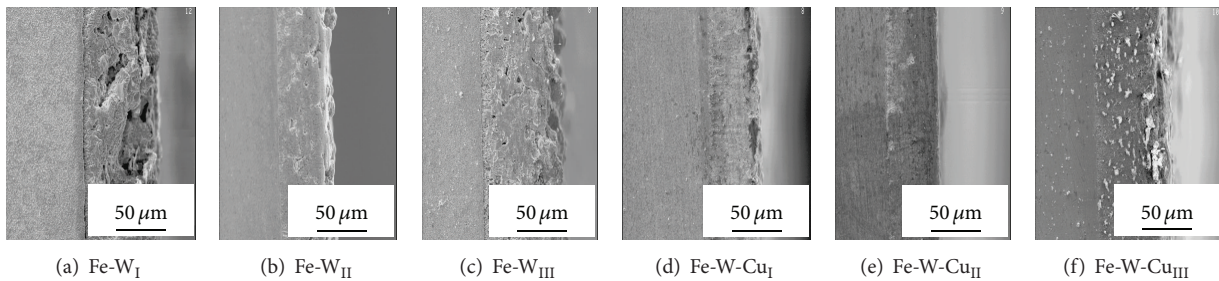


FIGURE 10: SEM photographs of coating sections.

substrate is improved obviously when the element of Cu was added.

**4. Conclusions**

The Fe400 coating has the best surface property among the coatings with different FeCl<sub>2</sub> contents in electrolyte. The hardness of the coatings is improved obviously when proper chemical ion W codeposited with iron ion is added. When

proper element of Cu is added, the hardness and tribological properties of the coatings are also improved, and the interface bond strength between the coating and the substrate is improved obviously for the Fe-W-Cu coatings.

**Acknowledgments**

This work is financially supported by the National Basic Research Program of China (973 Program) (no.

2011CB013404), the National Natural Science Foundation of China (nos. 51275105, 51375106), and the Foundation of Heilongjiang (nos. QC2010108, E201026).

## References

- [1] Q. Y. Hou, "Microstructure and wear resistance of steel matrix composite coating reinforced by multiple ceramic particulates using SHS reaction of Al—TiO<sub>2</sub>—B<sub>2</sub>O<sub>3</sub> system during plasma transferred arc overlay welding," *Surface and Coatings Technology*, vol. 15, pp. 113–122, 2013.
- [2] M. Barletta and D. Bellisario, "Effects of IR pre-curing conditions on wear resistance of metal flake powder coatings," *Progress in Organic Coatings*, vol. 70, no. 4, pp. 273–286, 2011.
- [3] Y. de Hazan, D. Zimmermann, M. Z'graggen et al., "Homogeneous electroless Ni-P/SiO<sub>2</sub> nanocomposite coatings with improved wear resistance and modified wear behavior," *Surface and Coatings Technology*, vol. 204, no. 21-22, pp. 3464–3470, 2010.
- [4] Z. Mao, J. Wang, B. Sun, and R. K. Bordia, "Wear resistance of reactive plasma sprayed and laser remelted TiB<sub>2</sub>—TiC<sub>0.3</sub>N<sub>0.7</sub> based composite coatings against medium carbon steel," *Applied Surface Science*, vol. 257, no. 7, pp. 2610–2616, 2011.
- [5] F. Fernandes, A. Ramalho, A. Loureiro, J. M. Guilemany, M. Torrell, and A. Cavaleiro, *Influence of nanostructured ZrO<sub>2</sub> additions on the wear resistance of Ni-based alloy coatings deposited by APS process*, vol. 303, no. 1-2, pp. 591–601, 2013.
- [6] B. Jiang, B. Xu, S. Dong, Y. Yi, and P. Ding, "Contact fatigue behavior of nano-ZrO<sub>2</sub>/Ni coating prepared by electro-brush plating," *Surface and Coatings Technology*, vol. 202, no. 3, pp. 447–452, 2007.
- [7] R. Gnanamuthu, N. Yong, and C. Lee, "Brush electroplated CoSn<sub>2</sub> alloy film for application in lithium-ion batteries," *Journal of Alloys and Compounds*, vol. 564, no. 5, pp. 95–99, 2013.
- [8] X. Li, X. Wang, R. Gao, and L. Sun, "Study of deposition patterns of plating layers in SiC/Cu composites by electro-brush plating," *Applied Surface Science*, vol. 257, no. 23, pp. 10294–10299, 2011.
- [9] G. Z. Ma, B. S. Xu, H. D. Wang, X. H. Wang, G. L. Li, and S. Zhang, "Research on the microstructure and space tribology properties of electric-brush plated Ni/MoS<sub>2</sub>—C composite coating," *Surface and Coatings Technology*, vol. 221, pp. 142–149, 2013.
- [10] N. Tsyntsar, J. Bobanova, X. Ye et al., "Iron-tungsten alloys electrodeposited under direct current from citrate-ammonia plating baths," *Surface and Coatings Technology*, vol. 203, no. 20-21, pp. 3136–3141, 2009.
- [11] J. Sudagar, J. Lian, and W. Sha, "Electroless nickel, alloy, composite and nano coatings—a critical review," *Journal of Alloys and Compounds*, vol. 571, no. 15, pp. 183–204, 2013.
- [12] B. Han and X. Lu, "Tribological and anti-corrosion properties of Ni-W-CeO<sub>2</sub> coatings against molten glass," *Surface and Coatings Technology*, vol. 202, no. 14, pp. 3251–3256, 2008.
- [13] J. Tang, Z. Han, Y. Zuo, and Y. Tang, "A corrosion resistant cerium oxide based coating on aluminum alloy 2024 prepared by brush plating," *Applied Surface Science*, vol. 257, no. 7, pp. 2806–2812, 2011.

## Research Article

# Modeling and Optimizing Energy Utilization of Steel Production Process: A Hybrid Petri Net Approach

Peng Wang,<sup>1</sup> Zeyi Jiang,<sup>1,2</sup> Zhitao Liu,<sup>1</sup> and Shanghong Fu<sup>1</sup>

<sup>1</sup> School of Mechanical Engineering, University of Science and Technology Beijing, Beijing 100083, China

<sup>2</sup> Beijing Engineering Research Center of Energy Saving and Environmental Protection, Beijing 100083, China

Correspondence should be addressed to Zeyi Jiang; [jiangzeyi@gmail.com](mailto:jiangzeyi@gmail.com)

Received 18 May 2013; Accepted 9 September 2013

Academic Editor: Gang Wang

Copyright © 2013 Peng Wang et al. This is an open access article distributed under the Creative Commons Attribution License, which permits unrestricted use, distribution, and reproduction in any medium, provided the original work is properly cited.

The steel industry is responsible for nearly 9% of anthropogenic energy utilization in the world. It is urgent to reduce the total energy utilization of steel industry under the huge pressures on reducing energy consumption and CO<sub>2</sub> emission. Meanwhile, the steel manufacturing is a typical continuous-discrete process with multiprocedures, multiobjects, multiconstraints, and multimachines coupled, which makes energy management rather difficult. In order to study the energy flow within the real steel production process, this paper presents a new modeling and optimization method for the process based on Hybrid Petri Nets (HPN) in consideration of the situation above. Firstly, we introduce the detailed description of HPN. Then the real steel production process from one typical integrated steel plant is transformed into Hybrid Petri Net model as a case. Furthermore, we obtain a series of constraints of our optimization model from this model. In consideration of the real process situation, we pick the steel production, energy efficiency and self-made gas surplus as the main optimized goals in this paper. Afterwards, a fuzzy linear programming method is conducted to obtain the multiobjective optimization results. Finally, some measures are suggested to improve this low efficiency and high whole cost process structure.

## 1. Introduction

China is the world's largest steel producer and consumer, and the production of crude steel and apparent steel consumption are up to 683.88 and 649.85 million tons (Mt) in 2012 respectively [1]. The steel industry has been the most important end-use sector in China. Despite these achievements, its expansion are impossible to achieve without a huge increase in energy input, especially in the form of coal, which resulted in severe environmental problems in the coal mining regions and around the steel plants. The Chinese steel industry was responsible for 16.1% of primary energy consumption and 15% of associated carbon dioxide emissions in 2009. Steel production is an energy-intensive manufacturing process, so it is quite important and necessary to optimize energy system for steel production process. However, we cannot ignore economic and environmental aspects because it is essential for steel enterprises to boost productivity and reduce emissions. These key issues are the main subjects of our study.

Steel production process is extremely diverse, encompassing the extraction of natural resources, conversion into raw materials, and manufacture of finished products [2]. It covers a wide range of multiprocedures, multiobjects, multiconstraints, multimachines, and energy flow, material flow and information flow that are strongly coupled [3]. Processes may be either continuous or discrete due to machine breakdowns and some discrete procedures in the real process. Since process industry has many special features, it is quite difficult to be modeled and optimized. Meanwhile, the requirements are various for steel company when dealing with energy problem. Therefore, we should take multiobjectives optimization in this study, and fuzzy optimization method can be used to solve these difficulties conveniently, which is widely applied to engineering problems [4, 5].

Methodologies and frameworks dealing with these troubles are introduced in some researches and published literatures. Linear programming based on algorithms, such as MILP and cyclic scheduling, has been applied for planning

and scheduling cases. In addition, Petri Net has an inherent attribute in representing sequent, concurrent, and conflicting logic in an intuitive and visual way.

Since the appearance of Timed Continuous Petri Net (TCPN) in 1990, some Hybrid Petri Net (HPN) models have been conducted in studying the industry systems [6, 7]. The most impressive characteristic of HPN model is that dynamic system behaviors, discrete production states, and event-driven system actions are integrated in one model structure. It naturally represents some nonlinear mechanism of the process and provides inherent restrictions of search space of optimization algorithm. Previous studies about Petri Net (PN) are certain method to show elements and their relationship abstractly, whose purpose is to seek the best decisions to achieve manufacturing system analysis, control and optimization [8]. In addition, Petri Net (PN) was widely used in iron and steel production system. Jun et al. proposed a modeling example to realize the efficient operation of the gas flow network in steel plants using Hybrid Petri Net [9–11]. According to the above, HPN is a feasible method to simulate and optimize the real steel production process, which is used in this study.

## 2. Methodology

**2.1. Hybrid Petri Net.** Petri Nets (PNs), firstly introduced by Petri in 1962 [12], are mathematical modelling tools used to analyze and simulate concurrent systems. Since then, Petri Nets and their concepts have been extended and applied in a variety of areas. Continuous PNs are used for modeling continuous systems. However, this model does not allow logical conditions or discrete behavior modeling (e.g., a valve may be open or closed). For permitting modeling of discrete states, Hybrid PNs were defined and presented [13, 14]. Hybrid Petri nets are made of “continuous part” (continuous places and transitions) and “discrete part” (discrete places and transitions), and included continuous and Hybrid Petri Nets, fluid stochastic petri nets, batch petri nets, hybrid flow nets, and so on [15].

First-order hybrid Petri nets is one of Continuous and Hybrid Petri nets and defined as follows.

**2.1.1. FOHPN Description.** A FOHPN is a bipartite digraph described by the 7-tuples [6]:

$$N = (P, T, \text{Pre}, \text{Post}, D, C, \text{RS}). \quad (1)$$

The parameters are described below.

- (1) Places  $P$ :  $P = P_C \cup P_D$  is partitioned into a set of discrete places  $P_D$  (represented by circles) and a set of continuous places  $P_C$  (represented by double circles). The set of transitions  $T = T_C \cup T_D$  is partitioned into a set of discrete transitions  $T_D$  and a set of continuous transitions  $T_C$  ( $T_C$  represented by double boxes).
- (2) Transitions  $T$ :  $T = T_I \cup T_D \cup T_E$  is further partitioned into a set of immediate transitions  $T_I$  (represented as bars), a set of deterministic timed transitions  $T_D$  (represented as black boxes), and a set of exponentially

distributed timed transitions  $T_E$  (represented as white boxes). We also denote by  $T_t = T_D \cup T_E$  the set of timed transitions. Moreover,  $T_D = T_I \cup T_t$  means the set of distributed timed transitions.

- (3) Pre- and Postincidence functions Pre and Post (represented as arcs):

$$\text{Pre, Post} : \begin{cases} P_C \times T \longrightarrow R_0^+, \\ P_D \times T \longrightarrow N, \end{cases} \quad (2)$$

where all  $t \in T_C$  and for all  $p \in P_D$  (well-formed nets) are required to be satisfied the formula  $\text{Pre}(p, t) = \text{Post}(p, t)$  to ensure that the firing of continuous transitions does not change the marking of discrete places.

- (4) Function  $D: T_t \rightarrow R_0^+$  specifies the timing associated with timed discrete transitions. We associate with a deterministic timed transition  $t_j \in T_D$  its (constant) firing delay  $\delta_j = D(t_j)$  and associate with an exponentially distributed timed transition  $t_j \in T_E$  its average firing rate  $\lambda_j = D(t_j)$ ; that is, the average firing delay is  $1/\lambda_j$ , where  $\lambda_j$  is the parameter of the corresponding exponential distribution.
- (5) The function  $C: T_C \rightarrow R_0^+ \times R_\infty^+$  specifies the *firing speeds* associated with continuous transitions. For any continuous transition  $t_j \in T_C$ , we let  $C(t_j) = (V_{mj}, V_{Mj})$ . Here  $V_{mj}$  represents the *minimum firing speed* (mfs) and  $V_{Mj}$  represents the *maximum firing speed* (MFS).
- (6) Function RS:  $T_D \rightarrow R_0^+$  associates a probability value called random switch to conflicting discrete transitions.

**2.1.2. Marking and Enabling.** Let  $\langle N, m(\tau_0) \rangle$  be an FOHPN with an initial marking  $m(\tau_0)$ , where  $m$  is a function that assigns to each discrete place a nonnegative integer number of tokens, represented by black dots, and assigns to each continuous place a fluid volume.

For a discrete transition  $t$ , it is enabled at  $m$  if, for all  $p_i \in t$ ,  $m_i \geq \text{Pre}(p_i, t)$ . As to continuous transition  $t$ , it is enabled at  $m$  if, for all  $p_i \in {}^{(d)}t$ ,  $m_i \geq \text{Pre}(p_i, t)$ . We say that an enabled transition  $t \in T_C$  is strongly enabled at  $m$  if, for all places  $p_i \in {}^{(c)}t$ ,  $m_i > 0$  and weakly enabled at  $m$  if for all places  $p_i \in {}^{(c)}t$ ,  $m_i = 0$ .

**2.1.3. Optimal Control Law for FOHPNs.** Jinsong and Qiqiang [7] built up a linear algebraic formalism to study the problem of deriving an optimal control law for FOHPNs under the assumption of admissible *instantaneous firing speed* (IFS) vectors.

Let  $\langle N, m(\tau_0) \rangle$  be an FOHPN with  $n_c$  continuous transitions and incidence matrix  $C$ . Let  $T_E(m) \in T_C$  ( $T_N(m) \in T_C$ ) be the subset of continuous transitions enabled (not enabled) at  $m$ . Let  $P_E = \{p \in P_C \mid m_p = 0\}$  be the subset of empty continuous places.

Any admissible IFS vector  $v = [v_1, \dots, v_{n_c}]^T$  at  $m$  is a feasible solution of the following linear set:

$$\begin{aligned}
 & \text{(a) } V_j - v_j \geq 0, \quad \forall t_j \in T_E(m) \\
 & \text{(b) } v_j - V'_j \geq 0, \quad \forall t_j \in T_E(m) \\
 & \text{(c) } v_j = 0, \quad \forall t_j \in T_N(m) \\
 & \text{(d) } \sum_{t_j \in T_E} C(p, t_j) \cdot v_j \geq 0, \quad \forall p \in P_E(m) \\
 & \text{(e) } v_j \geq 0, \quad \forall t_j \in T_C.
 \end{aligned} \tag{3}$$

The set of all feasible solutions is denoted by  $S(N, m)$ . And (3) is the constraint condition aiming at optimizing any given objective functions.

**2.2. Iron and Steel Manufacturing Process.** Currently, there are three main routes in the world for steel production, conventional integrated (pelleting, sintering, and coke plants-blast furnace-BOF route), semi-integrated (pelleting and DRI plant-EAF route), and new integrated with smelt reduction (pelleting plant-COREX-BOF/EAF route) [16]. In addition, the conventional integrated process is the most important steelmaking process (ratio of BOF steel remain about 80% [1]) in China, so we focus on this route only in this paper.

As described in Section 1, the conventional integrated process is extremely difficult to analyze. Therefore, in this paper, we set the boundaries of the iron and steel manufacturing process including pelletizing, sintering, iron making, steelmaking, steel casting, hot rolling, cold rolling, internal energy conversion system, and auxiliary production system.

**2.3. Optimization Model.** Based on the methodology explained in Section 2.1, the defined Hybrid Petri Net turns to be a flexible modeling process that makes sense to model steel manufacturing processes, by allowing places using actual material flow and transitions using actual manufacturing equipment. In order to reflect the actual production of steel process, one closed mass and energy balance model for each process are built to figure out the type and quantity of materials entering and leaving the process system.

In order to deal with multiobjective linear optimization problem, fuzzy linear programming method is a good way to resolve the problem [17], and this method will be adopted in this paper by software Lingo. The specific steps are as follows.

*Step 1.* Separate every objective function  $Z_j$  into its maximum  $Z_{j1}$  and minimum  $Z_{j2}$  value by solving

$$\begin{aligned}
 Z_{i1} &= \max Z_i, & Z_{i2} &= \min Z_i, \\
 Z_{l1} &= \max Z_l, & Z_{l2} &= \min Z_l.
 \end{aligned} \tag{4}$$

And  $Z_{j1}$  and  $Z_{j2}$  are obtained through solving the multiobjective problem as a single objective subject to the constraints equation like (3).

*Step 2.* Obtain the membership functions of the fuzzy objective functions for minimization goals ( $Z_i$ ) and maximization goals ( $Z_l$ ), which are constructed as

$$\begin{aligned}
 \mu_{z_i}(x) &= \begin{cases} 1, & \text{for } Z_i \leq Z_{i2}, \\ \frac{Z_{i1} - Z_i(x)}{Z_{i1} - Z_{i2}}, & \text{for } Z_{i2} \leq Z_i \leq Z_{i1}, \\ 0, & \text{for } Z_{i1} \leq Z_i, \end{cases} \\
 \mu_{z_l}(x) &= \begin{cases} 1, & \text{for } Z_l \geq Z_{l1}, \\ \frac{Z_l(x) - Z_{l2}}{Z_{l1} - Z_{l2}}, & \text{for } Z_{l2} \leq Z_l \leq Z_{l1}, \\ 0, & \text{for } Z_l \leq Z_{l2}. \end{cases}
 \end{aligned} \tag{5}$$

*Step 3.* In order to find optimal solution ( $x^*$ ) in the above fuzzy model, it is equivalent to solving the following crisp model.

Maximize  $\lambda$ : Subject to the constraints equation and  $\lambda \leq \mu_{z_i}(x)$ ,  $\lambda \leq \mu_{z_l}(x)$ .

### 3. Case Study

**3.1. Case Introduction and Data Acquisition.** Chinese steel industry owns its unique characteristics, like large production capacity, ore based process, and coal dominant energy consumption structure. One typical integrated steelmaking plant with an annual ten millions tons steel production capacity, located in Yangtze River delta, is selected in our case study. Coking, sintering, pellet, iron making, steelmaking and rolling are the main processes. The auxiliary production processes are combined with heat and power, limekiln, and dynamical transition system. In order to visualize the material flow, the material flow diagram is drawn based on the real manufacturing shown in Figure 1. Main material inputs of the system are iron ore, scraps, coal, coke, flux, air/oxygen, steam and electricity. The products are mainly steel bar, steel tube, heavy plate, hot rolling steel cold rolling steel, and so on.

In this paper, we collected the data mainly from company-level questionnaire surveys and production statistics. Some data are from the plant's technology acceptance inspection reports, which can fill the rest of the data gaps. With careful verification, we retain valid questionnaires of 2009 as the principal data source. The maximum capacity of each process is the result of all the devices under the best working condition, and the relationship between the material flow of each process is the average of the first quarter of 2009. For this steelmaking processes, 1.52 tons of sinter and 0.17 tons of pellet are required to produce 1 ton crude steel, contain pig iron and scrap, 0.99 tons pig iron is required to produce 1 ton of crude steel, and 1.02 tons of crude steel is required to make 1 ton of hot rolled steel.

**3.2. FOHPN Model Building.** In this section, we obtain the FOHPN model for steel production process by software named Visual Object Net. In addition, the declarations of transitions and the maximum firing speed (MFS), which is the maximum production capacity, for each continuous places, are presented in Table 1. Moreover, the declarations of

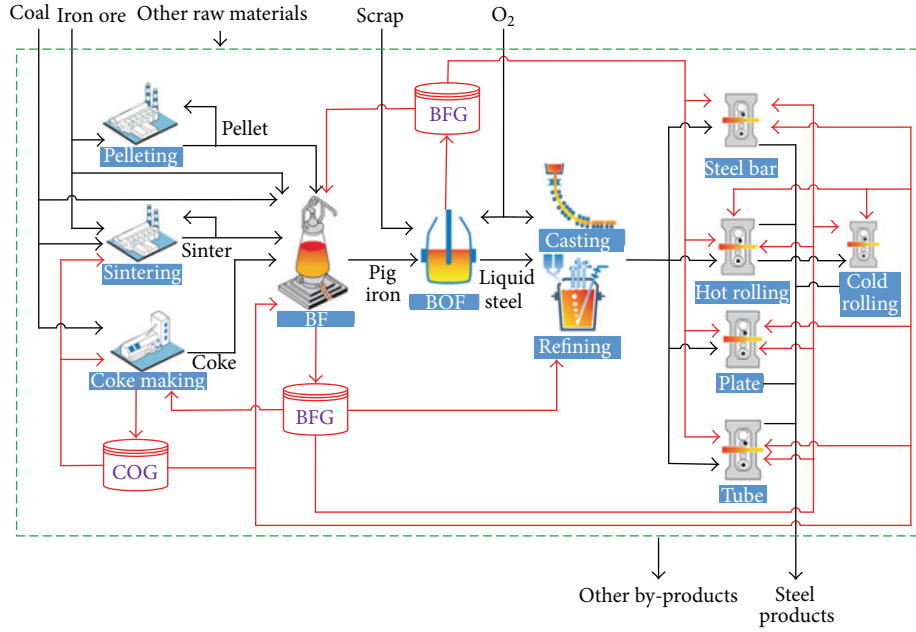


FIGURE 1: Main material flow diagram of iron and steel manufacturing process.

places and the weights of the arcs connected these places are shown as Table 2, and the weights of the arcs are modified by the material flow of each process.

There are several statements that should be noted in our approach.

- (1) The elements in our model are represented as icons, shown as Figure 2.
- (2) We take the material inventory as a continuous place without upper limit.
- (3) We take the main continuous production equipment as a continuous transition, which is controlled by a discrete transition nearby. If the discrete place has a token inside, the continuous production equipment functions properly and vice versa. Obviously, the discrete place's operational status is controlled by discrete transitions  $T_{x1}$  and  $T_{x2}$ , where  $X \in (a, b, c, d, e, \dots, k)$ . At the same time, the production capacity of the continuous production equipment means the fire speed for the corresponding continuous transition.
- (4) The weight of the arcs in front of the continuous transition is obtained by the related input material's mass proportion to the transition production capacity and vice versa.

The FOHPN model network is built after defining the places and transitions in steel production process shown in Figure 3. According to Section 2.1, we can obtain the constraint condition for our model as (6). Based on this constraint condition, the result is obtained from different optimization conditions like maximum mass of different

products, and then analyze the material and energy flow for steel production process in any given conditions:

$$\begin{cases}
 0 \leq V_a \leq 150, 0 \leq V_b \leq 40, 0 \leq V_c \leq 50, \\
 0 \leq V_d \leq 110, 0 \leq V_e \leq 110, 0 \leq V_f \leq 100, \\
 0 \leq V_g \leq 15, 0 \leq V_h \leq 15, 0 \leq V_i \leq 15, \\
 0 \leq V_j \leq 90, 0 \leq V_k \leq 50 \\
 (0.226 - 0.054) V_c \\
 - (0.0062V_a + 0.003V_d \\
 + 0.0017V_f + 0.014697V_g \\
 + 0.0322739V_h + 0.04084V_i \\
 + 0.01735V_j + 0.00846V_k) \geq 0 \\
 V_a - 1.517V_d \geq 0 \\
 V_b - 0.168V_d \geq 0 \\
 \text{St. } (2.7 - 0.558) V_d \\
 - (1.87V_c + 0.10859V_g \\
 + 0.14911V_h + 0.15307V_i \\
 + 0.05922V_j + 0.04648V_k) \geq 0 \\
 V_c - 0.527V_d \geq 0 \\
 0.107V_e - (0.056V_d + 0.00925V_g + 0.01525V_h \\
 + 0.04619V_j + 0.00634V_k) \geq 0 \\
 V_d - 0.99V_e \geq 0 \\
 V_e - 1.241V_f \geq 0 \\
 V_f - (1.02V_g + 1.02V_h \\
 + 1.02V_i + 1.02V_j) \geq 0 \\
 0.6V_j - 1.02V_k \geq 0.
 \end{cases} \quad (6)$$

3.3. *The Baseline Case.* In our research, we take the actual production situation as a benchmark whose data are derived

TABLE 1: The meaning and MFS of transition [unit:  $10^4$  t per month].

Transition	Meaning	MFS
Ta	Sintering	150
Tb	Pelletizing	40
Tc	Coking	50
Td	BF	110
Tf	Refining and continuous casting	100
Te	BOF	110
Tg	Steel bar	15
Th	Steel tube	15
Ti	Heavy plate	15
Tj	Hot rolling	90
Tk	Cold rolling	50

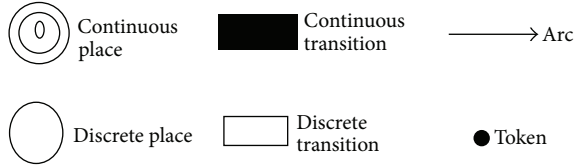


FIGURE 2: Icons for the elements in the FOHPN model.

from survey and statistical on the spot. Figure 4 shows the baseline case visually by e!sankey software, which is based on the average of survey and statistical data. The total of products and by-products was  $85.627 \times 10^4$  tons/m, the energy consumption of the system is  $22.437$  GJ/t, and the self-made gas surplus amount is  $1.42 \times 10^6$  m<sup>3</sup>/m.

**3.4. The Steel Production Case (Case 1).** Because many steel plants only treat the production as their main goal, we considered steel product production as the objective function in this case shown as (7), and the material flow is shown in Figure 5:

$$\text{Max}: p = V_g + V_h + V_i + 0.4 \times V_j + V_k, \quad (7)$$

where  $p$  represents the total steel production of the system, including steel bar, steel tube, heavy plate, hot rolled products and cold rolled products.

**3.5. The Energy Efficiency Case (Cases 2 and 3).** As mentioned above, energy efficiency is a critical issue for steel production nowadays. Therefore, the energy efficiency case is carried out by minimizing the energy efficiency of the process system. Additionally, the self-made gas system is the important part of energy system; reducing gas losses becomes more and more important for steel plants to decrease the demand of natural resources, cut down the discharge of exhaust gas, and diminish their influence to circumstances. The objective functions and results are shown as follows.

**Case 2.** Minimize the energy efficiency of the process system

$$\text{Min}: R = \sum_x \frac{P_x}{E_x}, \quad (8)$$

$$E_x = e_x V_x + \sum_i e_i V_i,$$

where,  $x = g, h, i, j, k$ ,  $i = a, b, c, d, e, f$ ,  $e_x, e_i$  represent the energy intensity of each procedure and  $E_x$  represents the total energy consumption for  $x$  production process, which is obtained by production data from B steel company (Figure 6).

**Case 3.** Minimize self-made gas surplus amount under the steel production maximization condition

$$\text{Max}: p = V_g + V_h + V_i + 0.4 \times V_j + V_k, \quad (9)$$

$$\text{Min}: G = G_{\text{COG}} + G_{\text{BFG}} + G_{\text{LDG}},$$

where  $G_{\text{COG}} + G_{\text{BFG}} + G_{\text{LDG}}$  represent the surplus amount of COG (Pa1), BFG (Pc1), and LDG (Pd1) (Figure 7).

## 4. Results and Discussion

Production and energy utilization for each procedure of four cases are presented in Figures 8(a) and 8(b). In addition, Table 3 shows the total steel production, specific energy consumption, and self-made gas surplus amount of four different cases.

As we can see from Figure 8(a), we can find that almost every procedure's production of Case 2 and Case 3 compared to Case 1 has been reduced by comparing the three optimized cases. In other words, to reduce energy consumption and reduce surplus production gas is bound to cause decline in steel production. Interestingly, however, the coking production in Case 1 has increased by  $14.8 \times 10^4$  t/m compared to Case 2. It is mainly because that arcs weight of generating blast furnace gas is more than the arcs weight of generating coke oven gas, but steel production procedures consume more coke oven gas relatively. Therefore, it is a reasonable choice to minimize self-made gas surplus amount reducing the Blast furnace gas amount and increasing the amount of coke oven gas (shown in Figure 5).

By comparing the optimized cases 2 and 3, we can find that production of every procedure except cold rolling in case 2 is less than that in Case 3, and so is the total energy utilization amount, which fully demonstrates that minimizing surplus self-made gas amount could not achieve the best the overall energy saving status. In addition, the amount of gas in these three conditions is always greater than zero. This indicates that the supply of self-made gas has greatly exceeded demand for the entire steel process. Meanwhile, the steel mills also purchase a large number of external energy media; for example, the purchased natural gas reached  $155$  m<sup>3</sup>/m. Therefore, the process should be arranged for the consumption of gas reasonably, trying to consume self-produced gas and reduce the use of purchased natural gas, to improve this low efficiency and high whole cost situation. Figure 8(b) shows that energy utilization for every procedure from small to large ranked Cases 2, 3, 1. Where, under any circumstances, the energy consumption of the blast furnace is the largest in all procedures.

Another important thing that must be considered in our study is the production capacity of each procedure in the manufacturing process. In the first case (maximum output),

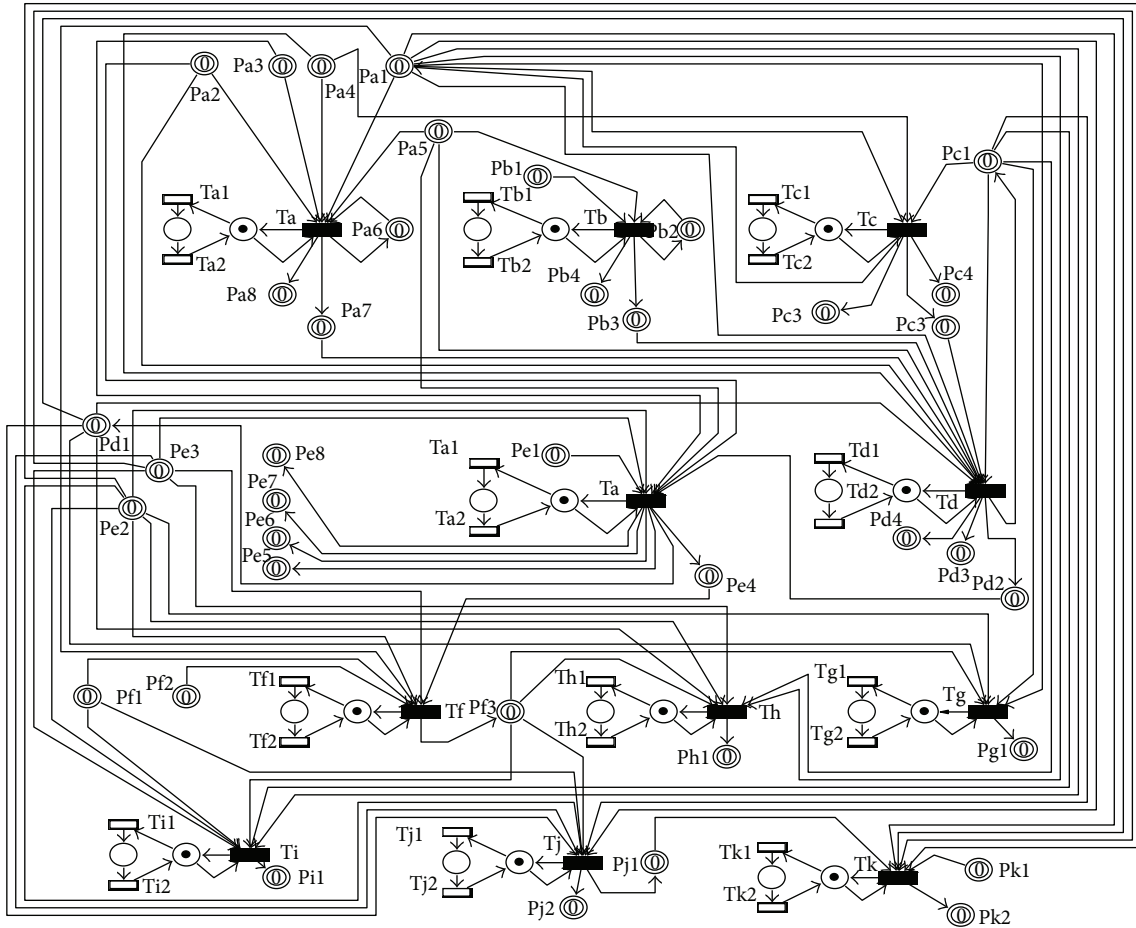


FIGURE 3: FOHPN model of the steel production process network.

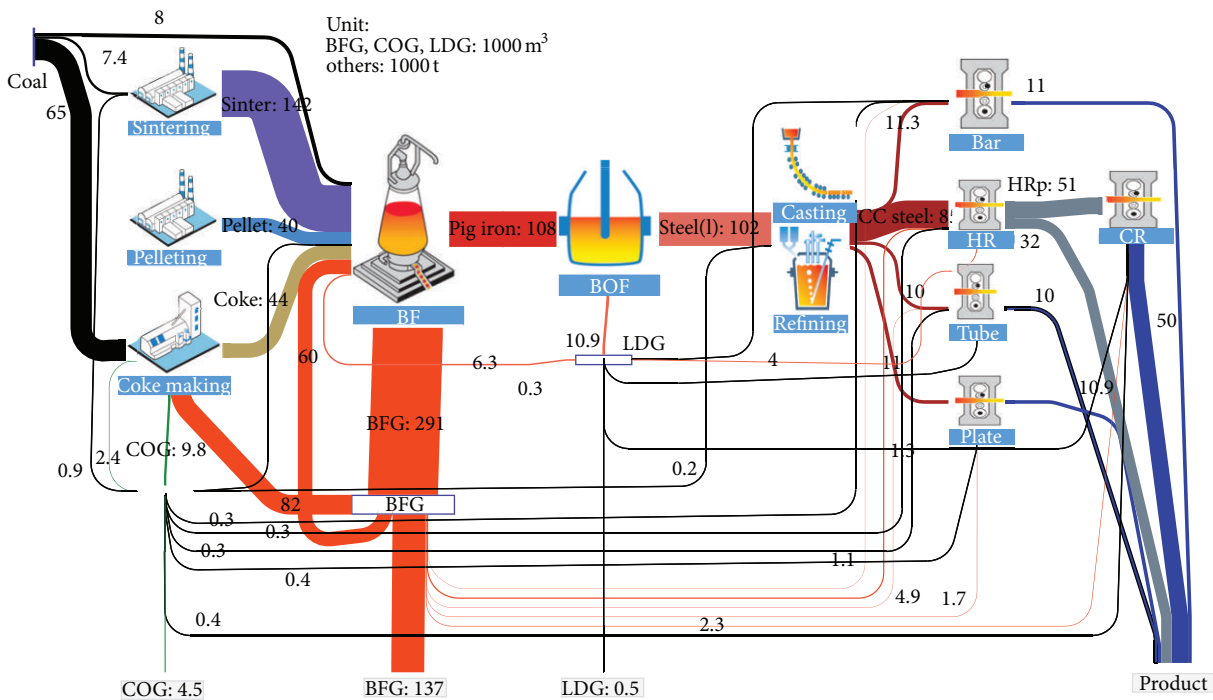


FIGURE 4: The material flow analysis of steel production process in baseline case.

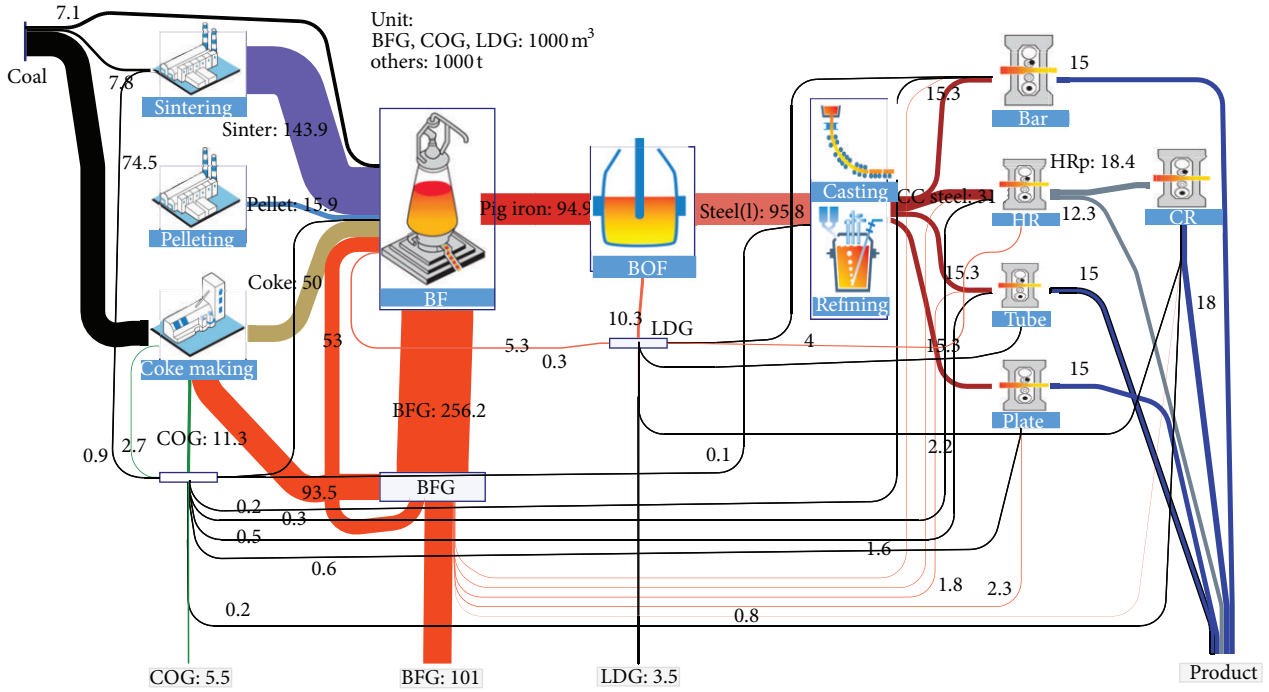


FIGURE 5: The material flow analysis of steel production process in steel production case.

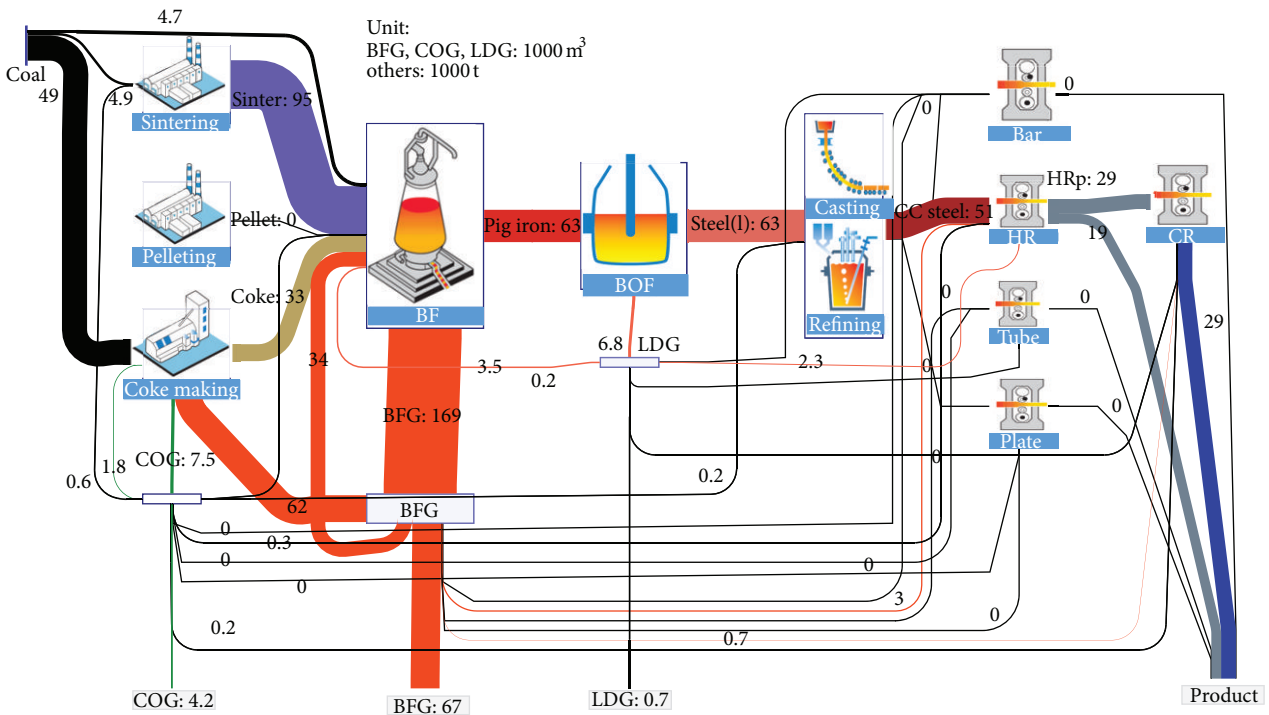


FIGURE 6: The material flow analysis of steel production process in Case 2.

sintering and pelletizing (before steelmaking procedure) work at full capacity production, which illustrate the sintering and pelletizing impose restrictions on iron-making process; coking and blast furnace are enough to spare. Therefore, in this case, a factory should add sintering and pelletizing

equipment to increase their production power to raise the utilization of the facilities. BOF and refining (after steelmaking procedure) are limited by the production of BF, which cannot operate at full ability. However, on product selection, in order to achieve the maximum output, the preference is to choose

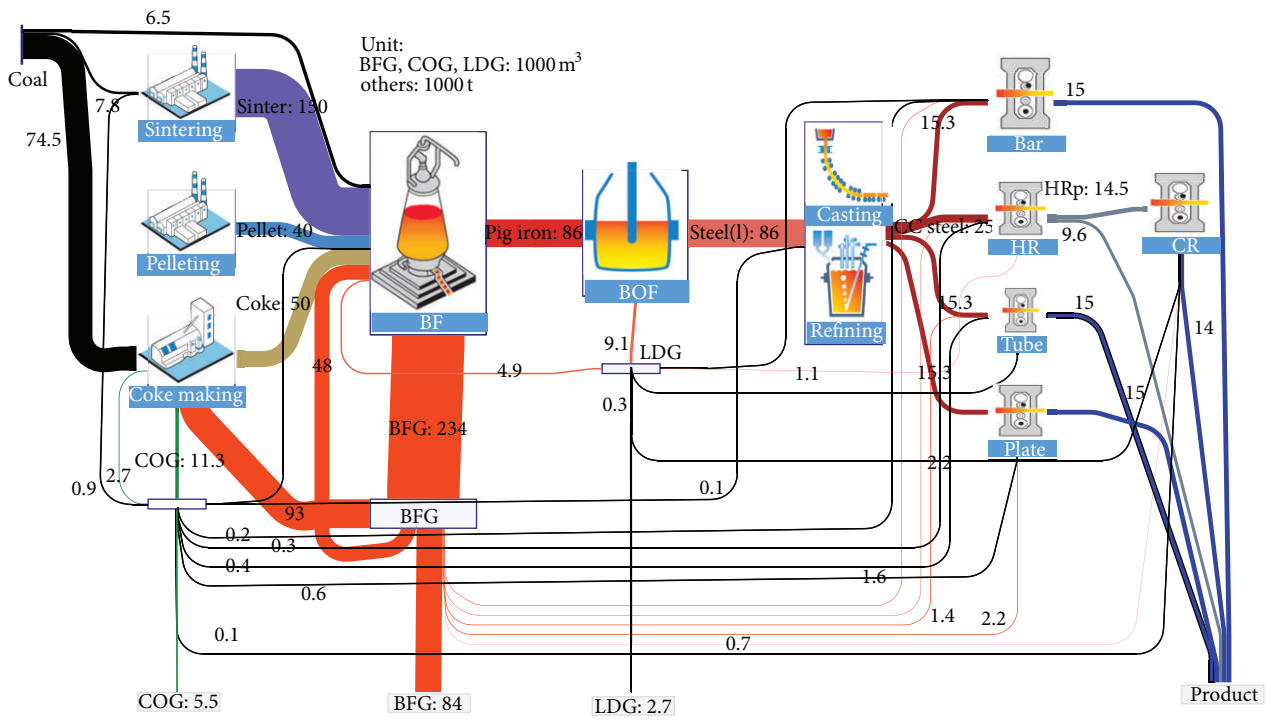


FIGURE 7: The material flow analysis of steel production process in Case 3.

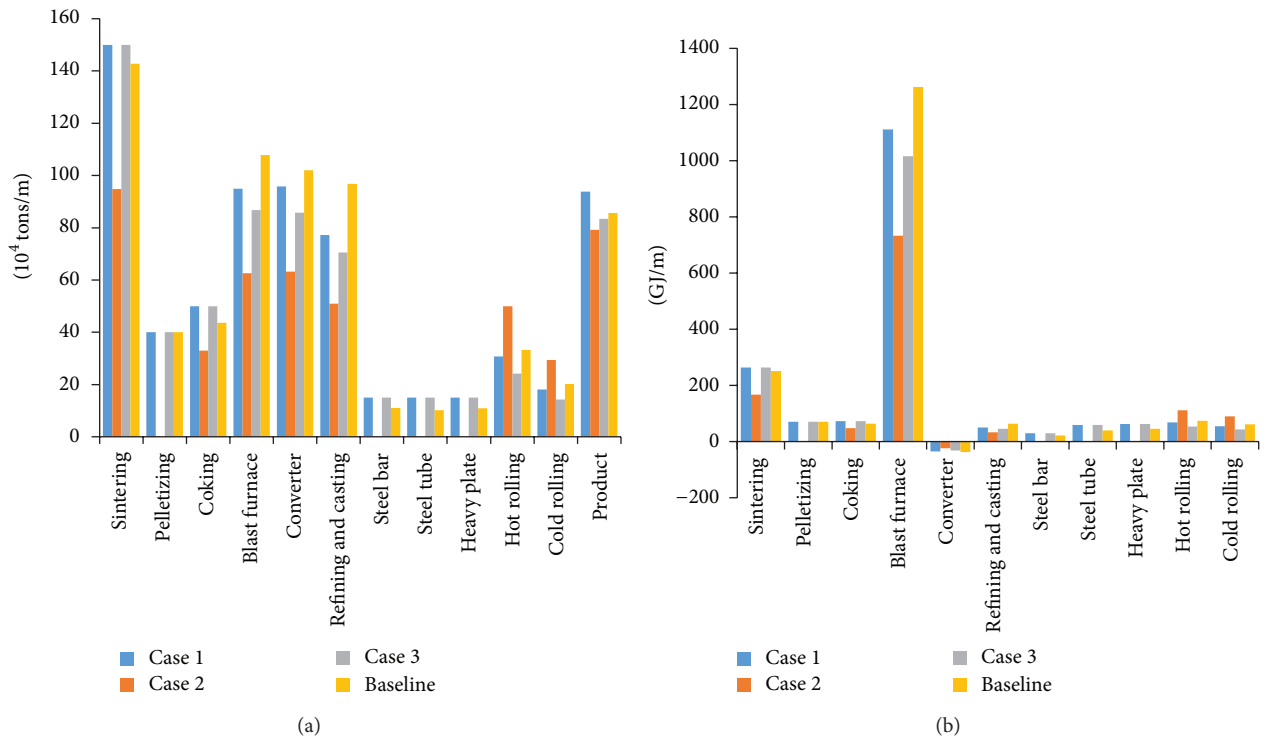


FIGURE 8: Production (unit: 10<sup>4</sup> t/m) and energy consumption amount (unit: GJ/m) for each procedure.

TABLE 2: The meaning of place and the weight of the connected arcs.

Place	Meaning	Direction	Weight
Pa1	COG	a1-a	0.0062
		a1-c	0.054
		a1-d	0.003
		a1-f	0.0017
		a1-g	0.0147
		a1-h	0.0322
		a1-i	0.04084
		a1-j	0.01735
		a1-k	0.00846
		c-a1	0.226
Pa2	Limestone	a2-a	0.104
		a2-d	0.032
		a2-e	0.056
		a2-a	0.104
		a2-d	0.032
Pa3	Dolomite	a3-a	0.052
		a3-e	0.3
Pa4	Coal	a4-a	0.052
		a4-c	1.49
		a4-d	0.075
		a4-a	0.052
Pa5	Mineral powder	a5-a	0.459
		a5-b	1.053
		a5-d	0.187
		a5-e	0.01
Pa6	Return sinter fines	a6-a	0.26
Pa7	Sinter	a-a7	1
		a7-d	1.517
Pa8	Burning loss	a-a8	0.107
Pb1	Bentonite	b1-b	0.0194
Pb2	Pellet fines	b2-b	0.009
Pb3	Pellet	b-b3	1
		b3-d	0.168
Pb4	Burning loss	b-b4	0.0079
		c1-c	1.87
		c1-d	0.558
		d-c1	2.7
		c1-g	0.10859
		c1-h	0.1491
		c1-i	0.1531
		c1-j	0.0592
		c1-k	0.0465
		Pg1	Steel bar
Ph1	Steel tube	h-h1	1
Pi1	Heavy plate	i-i1	1
Pj1	Hot rolling product	j1-k	1.02
Pj2	Hot rolled for sell	j-j2	0.4
Pc2	Coke	c-c2	1
		c2-d	0.527
Pc3	Tar	c-c3	0.0069

TABLE 2: Continued.

Place	Meaning	Direction	Weight
Pc4	Crude benzene	c-c4	0.007
		d1-d	0.056
		e-d1	0.107
Pd1	Converter gas (LDG)	d1-g	0.0093
		d1-h	0.015
		d1-j	0.046
		d1-k	0.0063
		d-d2	1
Pd2	Pig iron	d2-e	0.99
		d-d3	0.549
Pd3	BF slag	d-d4	0.065
Pd4	BF dust	e1-e	0.099
Pe1	Steel scrap	e2-e	0.08
		e2-f	0.0027
		e2-g	0.0027
		e2-h	0.00388
		e2-i	0.00072
Pe2	Oxygen	e2-j	0.000065
		e2-k	0.000000315
		e3-e	0.001
		e3-f	0.0023
		e3-h	0.011916
Pe3	Nitrogen	e3-i	0.0164
		e3-j	0.00044
		e3-k	0.0388
		e-e4	1
		e4-f	1.241
Pe4	Molten steel	e-e5	0.011
		e-e6	0.14
Pe5	Splash	e-e7	0.017
Pe6	Converter slag	e-e8	0.011
Pe7	Converter dust	e-e8	0.011
Pe8	Iron shot	f1-f	0.00016
		f1-i	0.00039
		f1-j	0.00002
Pf1	Natural gas	f1-k	0.00006
		f2-f	0.0019
		f-f3	1
Pf2	Argon	f3-g	1.02
		f3-h	1.02
		f3-i	1.02
Pf3	Casting billet	f3-j	1.02
		k1-k	0.00006
		k-k2	0.4
Pk1	Hydrogen	k-k2	0.4
Pk2	Cold rolled product	j-j1	0.6

iron loss smaller processes, which result in hot rolling and cold rolling equipment utilization rate dropped significantly. The cold rolling product maximized optimization has a big difference compared with the production power; therefore, in the practical production process, the raw material for cold rolling must come from stocking inventory mostly. To achieve the continuity of comprehensive process, it is necessary to design the production capacity of each process.

TABLE 3: Production and energy consumption of four different cases.

Contents	Case 1	Case 2	Case 3	Baseline
Steel production ( $10^4$ t/m)	93.77	79.26	83.41	85.62
Total energy utilization amount (GJ/t)	19.34	14.65	20.598	22.44
Self-made gas surplus amount ( $10^4$ tce/m)	97.48	72.67	75.76	79
Include				
COG	3.008	1.94	3.86	59
BOF	91.45	68.04	68.98	17
LDG	3.02	2.7	2.92	3

## 5. Conclusions and Suggestions

This paper provides a new method based on Hybrid Petri Nets to describe the complex behavior of the steel production process with energy utilization. Moreover, this method is conducted to model and optimize the energy utilization of one China's typical steel plant. The main conclusions and the suggestion to improve the energy utilization and steel production are listed as follows.

- (1) This research describes the HPN model scientifically, including some new definitions of the method and the corresponding optimization principles, especially some analogy methods and definitions about the steel production process.
- (2) The Hybrid Petri Net method is a good way to simulate continuous-discrete production process in this paper, and this method provides reference for the further optimization of steel production structure. In addition, it can largely simplify the research of steel production system.
- (3) We perform the multiobjective optimization by fuzzy linear programming method according to some different optimization conditions and the constraints obtained by the HPN model. The optimizing results go well with the practice. At the same time, the results can give guidance for the process of, such as energy medium distribution design, and allocate some processes' production capacity.
- (4) The adjustment of devices' capacity to reduce the gas surplus can improve the energy efficiency of the completely steel production process, which can reduce the energy consumption indirectly.
- (5) Due to the limitation of each plants' equipment, the steel production and specific energy consumption cannot reach the best situation contemporary. Therefore, it is essential to arrange the capacity of each plant in the integrated steel plant. The model is helpful in device configuration.
- (6) This model can use the computer to realize dynamic simulation and optimization on the spot, so it can guide the production process real-time. On the other hand, the modeling method of this paper can provide reference for other process industries.

## Acknowledgments

This research is financially supported by the National Basic Research Program of China (973 Program) (no. 2012CB720405) and supported by the Fundamental Research Funds for the Central Universities (no. FRF-SD-12-006B). The authors also greatly thank the editors and reviewers for their comments.

## References

- [1] World Steel Association, *Steel Statistical Yearbook 2012*, World Steel Committee on Economic, 2012.
- [2] Y. Ruiyu, "Green manufacturing versus steel industry," *Iron and Steel*, vol. 35, no. 6, pp. 61–65, 2000.
- [3] B. J. Finch and J. F. Cox, "Process-oriented production planning and control: factors that influence system design," *Academy of Management Journal*, vol. 31, no. 1, pp. 123–153, 1988.
- [4] L. Liu, "A multi-objective linear programming some method and Lingo implementation," *Journal of Xiangfan Vocational and Technical College*, vol. 11, no. 6, pp. 20–22, 2011.
- [5] T. Zhongfu, W. Mianbin, Q. Jianxun, H. Jian-chao, and L. Xue, "Time-of-use price optimizing model and fuzzy solving method," *System Engineering Theory and Practice*, vol. 28, no. 9, pp. 145–151, 2008.
- [6] W. Naiqi, B. Liping, and C. Chengbin, "Hybrid petri net modeling for refinery process," in *Proceedings of the IEEE International Conference on Systems, Man and Cybernetics (SMC '04)*, vol. 2, pp. 1734–1739, IEEE, October 2004.
- [7] Z. Jinsong and L. Qiqiang, "Application of hybrid Petri net in modeling of process industry's production logistics," *Journal of System Simulation*, vol. 10, article 005, 2006.
- [8] B. Sharda and B. Amarnath, "Robust manufacturing system design using multi objective genetic algorithms, Petri nets and Bayesian uncertainty representation," *Journal of Manufacturing Systems*, vol. 32, no. 2, pp. 315–324, 2013.
- [9] J. Zhenping, C. Wenming, and Y. Ge, "Hierarchy Coloured Petri Net (HCPN) and application in material flow system simulation modeling for steel making and continuous casting production of Baosteel," *Metallurgical Industry Automation*, vol. 26, no. 2, pp. 6–9, 2002.
- [10] Z. Fei, Z. Jun, Q. Fei, and W. Qidi, "Modeling for work process energy consumption of steel industry and research on its transformation to hybrid Petri network model," *Systems Engineering*, no. 6, pp. 70–75, 2010.
- [11] Z. Jun, Q. Fei, L. Li, and L. Guiqin, "Modeling for gas energy flow network and optimizing for weight functions of steel enterprises based on hybrid Petri net," *Journal of Southeast University*, vol. 42, article z1, 2012.

- [12] C. A. Petri, *Communication with automata [Ph.D. thesis]*, Technische Universitat Darmstadt, Darmstadt, Germany, 1962.
- [13] R. David and H. Alla, *Discrete, Continuous, and Hybrid Petri Nets*, vol. 1, Springer, Berlin, Germany, 2005.
- [14] T. Murata, "Petri nets: properties, analysis and applications," *Proceedings of the IEEE*, vol. 77, no. 4, pp. 541–580, 1989.
- [15] M. Dotoli, M. P. Fanti, A. Giua, and C. Seatzu, "First-order hybrid Petri nets. An application to distributed manufacturing systems," *IEEE Transactions on Nonlinear Analysis: Hybrid Systems*, vol. 2, no. 2, pp. 408–430, 2008.
- [16] M. M. Costa, R. Schaeffer, and E. Worrell, "Exergy accounting of energy and materials flows in steel production systems," *Energy*, vol. 26, no. 4, pp. 363–384, 2001.
- [17] H. J. Zimmermann, *Fuzzy Sets, Decision Making and Expert Systems*, vol. 10, Kluwer Academic, New York, NY, USA, 1987.

## Research Article

# Numerical Simulation of Force Enhancement by Cellular Material under Blast Load

**Chang Qi, Shu Yang, and Renjing Gao**

*School of Automotive Engineering, State Key Laboratory of Structural Analysis for Industrial Equipment, Dalian University of Technology, Dalian 116024, China*

Correspondence should be addressed to Shu Yang; yangshu@dlut.edu.cn

Received 18 June 2013; Accepted 26 August 2013

Academic Editor: Lei Zhang

Copyright © 2013 Chang Qi et al. This is an open access article distributed under the Creative Commons Attribution License, which permits unrestricted use, distribution, and reproduction in any medium, provided the original work is properly cited.

The cause of force enhancement phenomenon when using cellular material, such as metal foam, for blast protection is discussed using both finite element method (FEM) and analytical method. Finite element (FE) models of cellular material under blast load are presented, in which the blast load is modeled by CONWEP blast function and the cellular material is modeled by the homogenized modeling method and the multiunit-cell modeling method. A one-dimensional analytical model is also presented for comparison purpose. Utilizing these models, an aluminum foam bar under blast load is simulated and the mechanism of both force attenuation and enhancement are depicted. The relationship between blast load intensity and the length of the foam bar is analyzed based on the simulation. It is found that the time of momentum transfer between the compacted foam bar and the protected structure is very short compared to the total time of the blast event, which causes force enhancement. Corresponding countermeasures are proposed based on this finding. The study will not only provide new modeling methods for the simulation of cellular material subjected to blast load but will also be beneficial to understand the mechanisms of force attenuation and enhancement, so as to seek for countermeasures.

## 1. Introduction

Cellular materials, such as metal foams, are widely used to attenuate the effects of blast load upon structures due to their high energy absorption capability compared to relatively low density, a characteristic that is very preferable for light-weight applications. The porous nature of the material also helps in heat dissipation as well as provides damping to the shock-wave. Besides all these benefits, an undesired phenomenon observed when using cellular material for blast protection is that, under certain conditions, the peak force transmitted to the protected structure can be even higher than when the cellular material is not used. This unexpected phenomenon, the so-called “force enhancement”, has been mentioned in several publications. The initial framework for investigation of force enhancement phenomenon was established by Monti [1] as early as 1970. Gel'fand et al. [2] first demonstrated pressure amplification by foam material using the experimental method. The stress or force enhancement phenomenon was observed by Reid et al. [3, 4] in wood and packed ring systems, and by Song et al. [5] in plastic foams. Skew et al. [6]

demonstrated a substantial increase in the back wall pressure when a slab of porous polyester and polyether foams was mounted to the back wall of a shock tube. Mazor et al. [7] and Ben-Dor et al. [8] found that the actual blast pressure acting on the structural surface is a function of the response of the surface itself since this influences the states of the gaseous phase. Hanssen et al. [9] conducted full-scale free-field blast-loaded pendulum tests; an increase of the swing angle of the blast-loaded pendulum was observed when a foam panel was attached. Hanssen attributed this angle (energy) increase to the continuous transformation of the shape of the initially planar panel surface into a concave shape during the blast. Ouellet et al. [10] conducted both shock tube experiments and free-field blast trials on three polymeric foams of varying thickness and density and concluded that three different regimes of amplification and attenuation of foam transmitted overpressure can be identified.

Numerical simulation by Olim et al. [11] based on a two-phase flow model (a dust-gas model) supported the experimental results of Skew et al. [6]. This model treats the solid phase as suspension dusts in the gas phase. This is applicable

to foam of low density. Li and Meng [12] attributed the stress or force enhancement of cellular material to the formation of a shock wave when a critical impact velocity is reached for intensive loads. They showed that stress enhancement may occur during its propagation through a cellular material, which was demonstrated using a one-dimensional mass-spring model. Ma and Ye [13, 14] first considered the coupling effects of the foam claddings and the protected main structure using a one-dimensional analytical model.

Despite all the above mentioned efforts, there is little information available in literature that gives a detailed explanation of the force enhancement phenomenon of cellular material under blast load or high-speed impact load; the physical background of this phenomenon still needs to be discovered. Due to the lack of theoretical support, no practical solutions have been proposed to prevent this undesired phenomenon from happening. As a result, application of cellular material for blast protection design is still limited at the present time.

To find the reason of force enhancement when using cellular material, such as aluminum foam, for blast protection, detailed investigation of the physical process is a premise. In this study, finite element method (FEM) is applied for this purpose. Two types of modeling methods are proposed to model the cellular material based on the explicit program LS-Dyna. The effect of using aluminum foam for blast protection is simulated with various blast load intensities. Simulation results of the finite element models are compared with the data from a one-dimensional analytical model originally proposed in the literature, which is then employed to investigate the root cause of force enhancement.

The structure of the paper is as follows: in Section 1, the current situation of researches for cellular material under blast load is surveyed. In Section 2, the basic problem is first described; a one-dimensional analytical model is then briefly introduced; some basic theories of finite element modeling of cellular material under blast load are described, including blast load simulation models and cellular material models, the latter include a homogenized model and a model that consists of multiunit-cells. In Section 3, numerical simulations of a case study are conducted based on the proposed models to demonstrate the phenomena of both force attenuation and enhancement; contrastive analysis between the simulation results of different models is carried out; the analytical model is employed to seek the root cause of the force enhancement effect of cellular materials subject to blast loads. At last, some conclusions are deduced in Section 4.

## 2. Numerical Modeling of Cellular Material under Blast Load

**2.1. Problem Description.** The studied problem is shown in Figure 1; that is, a fixed end cellular material bar is subjected to a blast pressure pulse  $p(t)$ . The length and the cross-section area of the bar are  $L$  and  $A$ , respectively. The transmitted force on the fixed end is monitored to evaluate the effect of the cellular material under blast load.

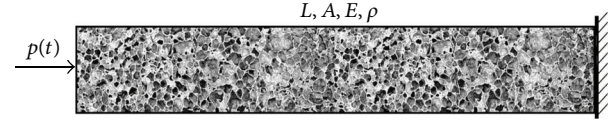


FIGURE 1: Cellular material bar subject to blast pulse load.

**2.2. One-Dimensional Analytical Model.** A one-dimensional analytical model proposed by Li and Meng [12] is shown in Figure 2, which has  $N$  discrete lumped masses connected by  $N$  identical nonlinear springs, where  $m_i = m = \rho AL/N$ ,  $i = 1, 2, \dots, N$ , and  $\rho$  is the density of the cellular material. The elastic property of the spring is determined by  $k_i = k = EAN/L$ . The input blast pressure pulse is applied on the  $N$ th lumped mass. The first spring is connected to a rigid wall.

Neglecting the change of cross-section area, equilibrium equations of the system can be written as

$$\mu \ddot{y}_i = \sigma_{i+1} - \sigma_i \quad \text{for } 1 \leq i \leq N \text{ with } \sigma_{N+1} = p_t, \quad (1)$$

where compressive stress has a positive value.  $\mu = \rho L/N$  and  $y_i$  is the displacement of  $i$ th mass in the given direction in Figure 2. The initial conditions are

$$y_i = 0, \quad \dot{y}_i = 0 \quad \text{at } t = 0. \quad (2)$$

A complete description of the compressive stress-strain relation of the non-linear spring is shown in Figure 3 and is characterized by the compressive modulus,  $E$ , plateau stress,  $\sigma_0$ , lock-up strain,  $\epsilon_l$ , and compressive stress-strain relation  $\sigma = \sigma(\epsilon)$  in the densification range. The non-linear differential equation (1) with the initial condition (2) can be solved numerically to achieve the force transmission in the system.

**2.3. Finite Element Modeling of Blast Load.** For blast impact simulation, the complexity of the problem lies in the following difficulties: the high speed wave front propagation, the flow of various materials, and the large structural deformation. Existent numerical models developed for blast simulations can be roughly divided into two categories: the numerical models based on the Arbitrary Lagrangian Eulerian (ALE) method and the empirical models for blast pressure approximation.

**2.3.1. ALE Model.** The ALE methods combine the advantages of Eulerian and Lagrangian methods and allow for a type of "automatic remapping" in the simulation. The time and space distribution of the blast pressure profile are calculated through the Eulerian mesh by utilizing the equation of state (EOS) for high explosives. The mix of the air and explosive reaction products is modeled using multimaterial capabilities (\*ALE\_MULTIMATERIAL\_GROUP\_OPTION) in LS-Dyna. The blast pressure wave traveling through the air interacts with the structure by means of a gas-structure interfacing algorithm in LS-DYNA (\*CONSTRAINED\_LAGRANGE\_IN\_SOLID). Physical quantities such as stress, displacement, velocities, and accelerations in the structure are computed.

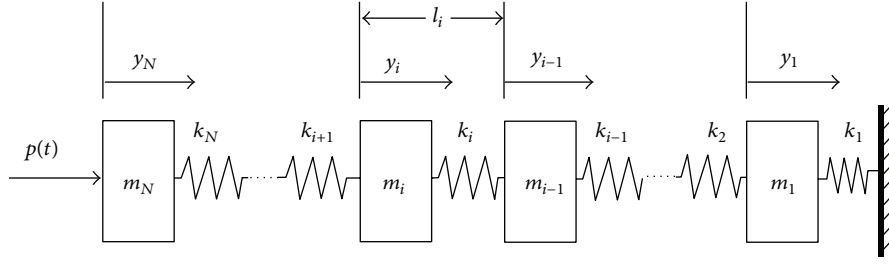


FIGURE 2: One-dimensional analytical model of the cellular bar.

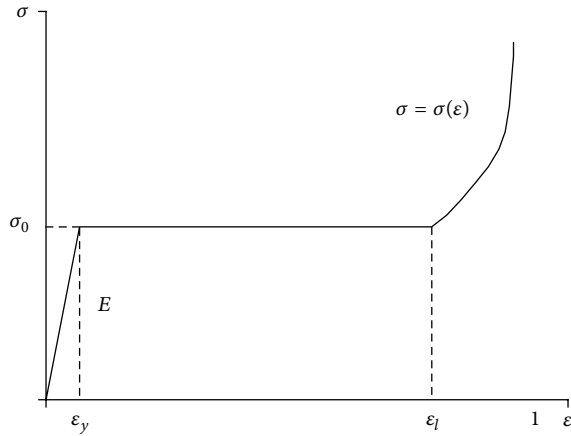


FIGURE 3: Stress-strain curve of nonlinear springs.

At any given time, the pressure in a high explosive element is given by

$$p = F p_{\text{eos}}(V, E), \quad (3)$$

where  $p_{\text{eos}}$  is the pressure from the EOS;  $F$  is called burn fraction, which multiplies the EOS for high explosive, and controls the release of chemical energy for simulating detonations. The Jones-Wilkins-Lee (JWL) EOS model for explosive detonation product is given by

$$p = A \left(1 - \frac{\omega}{R_1 V}\right) e^{-R_1 V} + B \left(1 - \frac{\omega}{R_2 V}\right) e^{-R_2 V} + \frac{\omega E}{V}, \quad (4)$$

where  $p = p(x, y, z, t)$  is the pressure field,  $V$  is the volume of the material at pressure  $p$  divided by the initial volume of the unreacted explosive,  $E$  is the internal energy per unit initial volume, and  $A$ ,  $B$ ,  $R_1$ ,  $R_2$ , and  $\omega$  are adjustable parameters. For TNT,  $A = 3.712$  Mbar,  $B = 0.0323$  Mbar,  $R_1 = 4.15$ ,  $R_2 = 0.95$ , and  $\omega = 0.3$ . The air is usually modeled to represent the medium in which the blast wave propagates. A linear polynomial EOS is usually used to simulate the proper air behavior, and the pressure is given by

$$p = C_0 + C_1 \mu + C_2 \mu^2 + C_3 \mu^3 + (C_4 + C_5 \mu + C_6 \mu^2) E, \quad (5)$$

where  $\mu = \rho/\rho_0 - 1$  with  $\rho/\rho_0$  being the ratio of current density to initial density, and  $C_{(i)}$  being the constants. For gases to which the gamma law EOS applies, including atmospheric

air,  $C_0 = C_1 = C_2 = C_3 = C_6 = 0$  and  $C_4 = C_5 = \gamma - 1$ , with  $\gamma$  as the ratio of specific heats. Therefore, for air, (5) reduces to

$$p = (\gamma - 1) \frac{\rho}{\rho_0} E. \quad (6)$$

The units of  $E$  are the units of pressure.

One drawback of the ALE method is its high computational cost, and it is, therefore, appropriate only for simulating blast events with small standoff distances.

**2.3.2. Empirical Model.** Compared to the ALE method, the empirical models have a much less computational cost, and it is, therefore, appropriate for simulating blast events with large standoff distances. In this study, the blast loads are simulated using one of the empirical models based on the CONWEP air blast function developed by Kingery and Bulmash [15]. This model, which has been implemented as the \*LOAD\_BLAZT loading card in LS-Dyna, can predict the blast overpressure under certain conditions: the free air detonation of a spherical charge and the surface detonation of a hemispherical charge; the surface detonation approximates the conditions of a mine blast. The model takes into consideration the angle of the incidence of the blast,  $\theta$ , the incident pressure,  $p_{\text{in}}$ , and the reflected pressure,  $p_{\text{ref}}$ . The predicted blast overpressure is expressed as

$$p(t) = p_{\text{ref}} \cos^2 \theta + p_{\text{in}} (1 + \cos^2 \theta - 2 \cos \theta) \quad (7)$$

with  $p_{\text{in}}$  and  $p_{\text{ref}}$  given by

$$p_{\text{in}} = p_{i0} \left(1 - \frac{t}{t_0}\right) e^{-bt/t_0}, \quad (8)$$

$$p_{\text{ref}} = p_{r0} \left(1 - \frac{t}{t_0}\right) e^{-at/t_0},$$

where  $p_{i0}$  and  $p_{r0}$  are the peak incident overpressure and the peak reflected overpressure, respectively.  $a$  and  $b$  are decay coefficients and  $t_0$  is the positive phase duration time. The model uses the following inputs to calculate the pressure: equivalent mass of TNT, coordinates of the point of explosion, and the delay time between when the LS-Dyna solution starts and the instant of explosion. The model does not account for shadowing by the intervening objects or the effects of confinement.

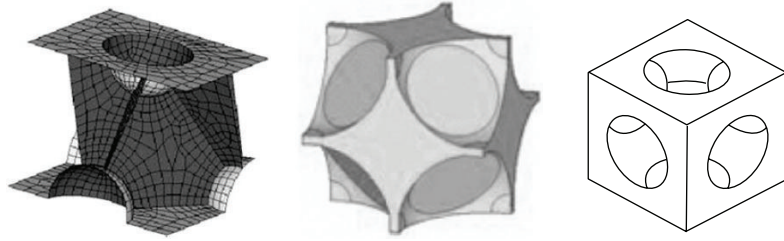


FIGURE 4: Example unit-cell model of cellular material.

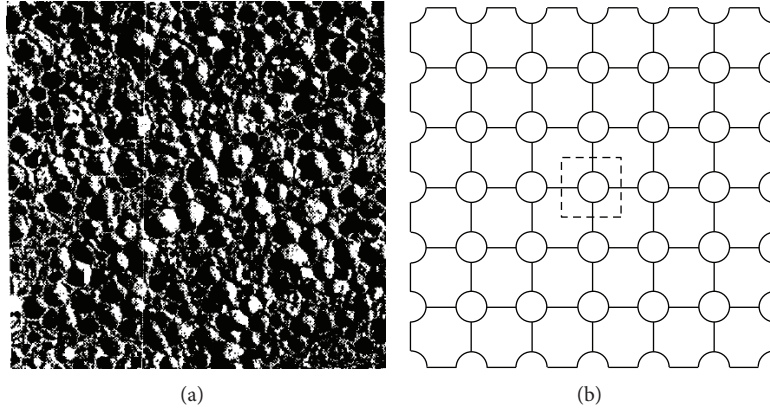


FIGURE 5: Morphology of the hemisphere model: (a) real structure and (b) numerical model.

**2.4. Finite Element Modeling of Cellular Material.** Finite element model of cellular material can be roughly divided into two groups: homogenized model and models that consist of multi-unit-cell.

**2.4.1. Homogenized Model.** Homogenized model neglects the microstructure of a specific cellular material, only the homogenized macroscopic properties are taken into consideration. Homogenized model uses solid elements for space discretization while the properties of cellular material are represented through material models by assigning appropriate parameters and load-deformation curves or stress-strain curves. In LS-Dyna, homogenized models for cellular material include MAT26, MAT57, MAT63, MAT75, and MAT126.

**2.4.2. Multiunit-Cell Model.** Multi-unit-cell model of cellular material accounts for material morphology in which the material is approximated by an assembly of unit-cells. The multi-unit-cell model is capable of reflecting the complex loading conditions of the cellular material. The properties of the cellular material are represented by parameters of the unit-cell. Several representative unit-cell models of cellular material found in the literature [16–18] are shown in Figure 4.

In this study, we employed a unit-cell model of cellular material proposed by Santosa and Wierzbicki [19] and improved by Wang [20] based on the morphology analysis of cellular material microstructure as illustrated in Figure 5. The unit-cell of cellular material is represented by two hollow hemispheres connected through a cruciform section and a web section as shown in Figure 6. Generally, both cell size and

wall thickness of the unit-cell contribute to idealized foam density. We assumed a uniform thickness at every point. Contacts are defined among the unit-cells to represent the internal connections and friction of the cellular material. Denoting the cube width by  $b$ , diameter of the sphere by  $D$ , and thickness by  $t$ , the relative density or solidity ratio  $\rho_f/\rho_s$  of the reference multi-unit-cell foam model with respect to a solid volume of which the foam is made can be expressed as

$$\frac{\rho_f}{\rho_s} = 3\frac{t}{b} + \frac{\pi}{4}\left(\frac{D}{b}\right)^2\frac{t}{b}, \quad (9)$$

and the lock-up strain,  $\varepsilon_l$ , can be obtained as

$$\varepsilon_l = \frac{b - 2h_t}{b}, \quad (10)$$

where

$$h_t = \left(\frac{\pi}{4} - \frac{1}{2}\right)D. \quad (11)$$

### 3. Numerical Simulation Case Study

**3.1. Problem Description.** An aluminum foam bar is attached to a fixed rigid reaction wall; the other end of the foam bar is attached to an aluminum cover plate, which is subject to blast loads with equivalent TNT of 4 kg (Case 1) and 8 kg (Case 2), respectively, as illustrated in Figure 7. It is assumed that the distance from the location of the blast to the loading surface of the cover plate is large enough so that the length of the foam bar and the cover plate can be neglected.

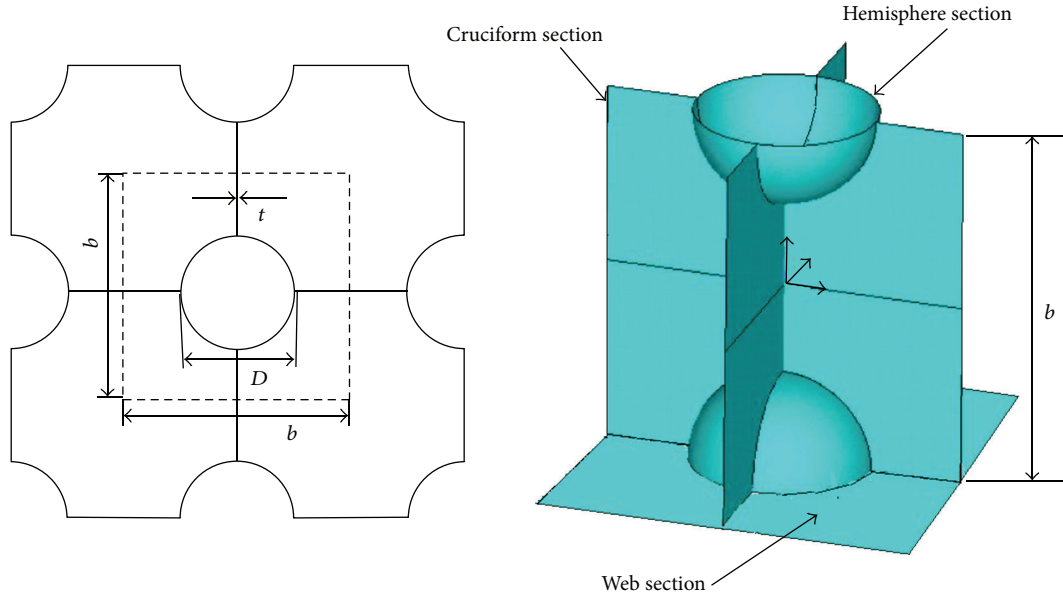


FIGURE 6: Unit-cell of hemisphere model for cellular material.

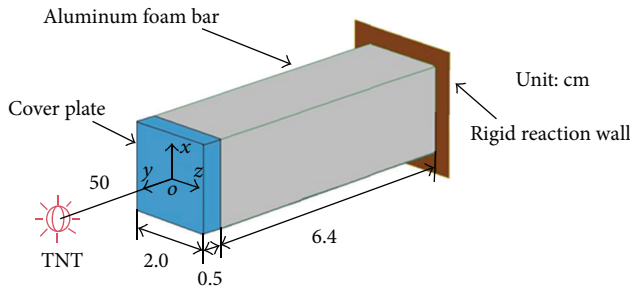


FIGURE 7: Aluminum foam bar under blast load.

3.2. *Modeling Method.* Both analytical method and FEM are used for the simulation. The analytical model comprises 3 nonlinear springs to represent the aluminum foam bar and one nonlinear spring to represent the cover plate.

In finite element modeling, due to the distance between the explosive spot and the foam bar, the empirical model is employed to simulate the blast load on the cover plate. Keyword \*LOAD\_BLAST in LS-Dyna is set to generate the air burst load of the TNT exerted on the cover plate, which is modeled by constant stress 8-nodes brick element. Two methods are used to model the aluminum foam bar: one is the homogenized modeling method using MAT26 in LS-Dyna (model 1), the other one is the multi-unit-cell modeling method with unit-cell shown in Figure 7 (model 2) with  $b = 2$  mm,  $D = 1$  mm, and  $t = 0.075$  mm, respectively. Quarter symmetry is used in both models to reduce the number of elements; all nodes on the plane of symmetry are constrained to stay on the planes of symmetry. The number of elements is 55200 with the nodes of 61302 in model 1, while the number of elements is 348495 with the nodes of 277397 in model 2.

\*CONTACT\_AUTOMATIC\_SINGLE\_SURFACE card is defined in both models to account for the effect of contact

during simulation. Material properties used in the finite element models are listed in Table 1. Strain rate effect of aluminum was accounted for by using the Cowper and Symonds model which scales the yield stress with the factor  $1+(\dot{\epsilon}/C)^{1/P}$ , where  $\dot{\epsilon}$  is the strain rate, and strain rate parameters are set as  $C = 40.4$  and  $P = 5$ , respectively.

### 3.3. Simulation Results and Discussions

3.3.1. *Case 1 (4 kg TNT).* The simulated deformation and pressure distribution in the system at different times are shown in Figure 8 (model 1) and Figure 9 (model 2), respectively. Both finite element models predicted that the aluminum bar deforms from near the blast point to the distal end, layer by layer, in a manner similar to what happens in real tests [9].

The displacement of the front panel is shown in Figure 10. FE model 1 underpredicted the displacement compared to the analytical model, while FE model 2 overpredicted the displacement. The simulation error is less than 5%.

Figure 11 depicts the force attenuation effect of aluminum foam under blast load. Force exerted on the rigid reaction wall is equivalent to the product of the plateau stress  $\sigma_0$  and the contact area, that is, the cross section area of the foam bar, which is less than the blast load peak. Energy from the blast is fully absorbed by the aluminum foam through plastic deformation. It is seen from Figure 11 that the predicted force transmitted on the reaction wall by both FE models is in very good agreement with the data given by the one-dimensional analytical model. Model 2 based on the multi-unit-cell modeling method predicted an early occurrence of force transmission. This means the model is stiffer due to the strain rate effect.

Figure 12 compares the time history of total energy, absorbed energy, and kinetic energy of the system. The total

TABLE 1: Material properties used in the finite element models.

Material	Properties	Value
Aluminum	Young's modulus, $E$ (GPa)	70
	Poisson's ratio, $\nu$	0.3
	Density, $\rho$ ( $\text{kg}/\text{m}^3$ )	2700
Aluminum foam	Young's modulus before compaction $E_u$ (GPa)	0.2
	Density, $\rho_f$ ( $\text{kg}/\text{m}^3$ )	400
	Poisson's ratio of densified foam, $\nu_{\text{densified}}$	0.285
	Yield stress of densified foam, $\sigma_y$ (MPa)	265
	Volume fraction of densified foam, $v_f$	0.25
	Modulus of densified foam, $E_c$ (GPa)	69

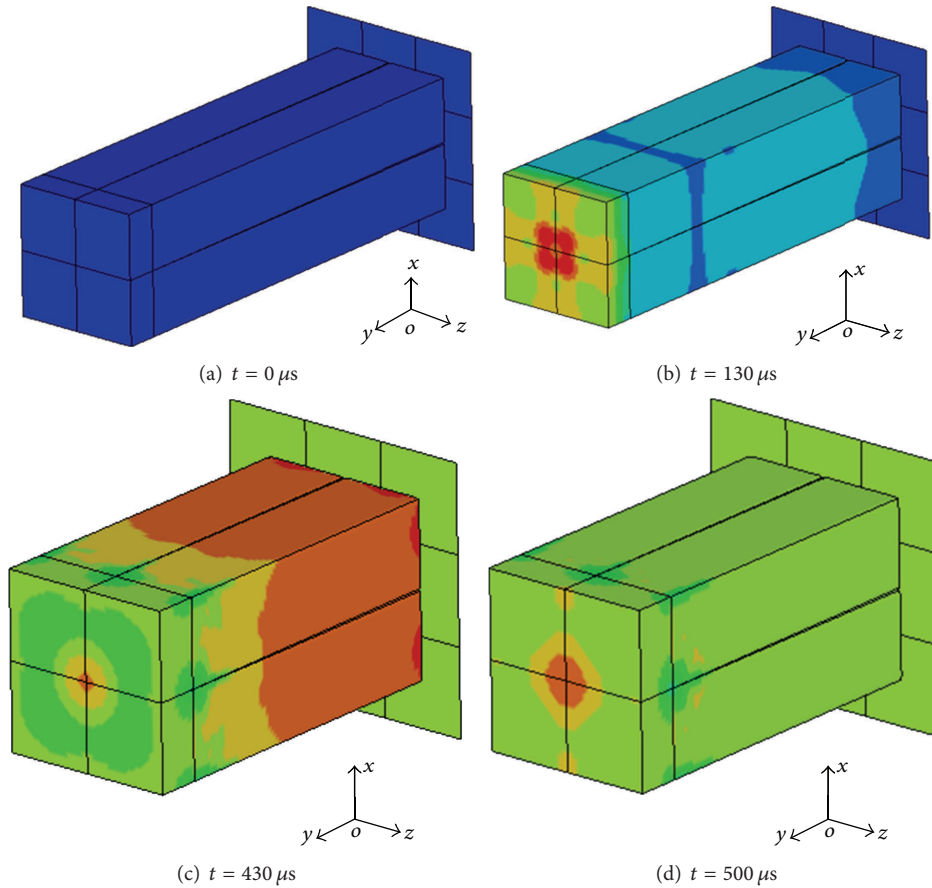


FIGURE 8: Simulation results of load pressure and deformation of aluminum foam bar under blast load at different time in model 1.

energy is equal to the work done on the cover plate by the blast load. It is observed that both FE models give results which are in good agreement with the results predicted by the analytical model. The kinetic energy of the system increases initially due to the blast load, then drops eventually to zero.

**3.3.2. Case 2 (8 kg TNT).** In case that the blast load is above a critical level, as in Case 2, the blast energy cannot be completely absorbed when the foam bar is fully compacted, peak force exerted on the reaction wall is greater than the blast peak load itself, and the so-called force enhancement occurs as shown in Figure 13. Both FE models predicted force enhancement occurrence successfully. It shows that model

1 over-predicted the enhanced force peak as compared with the analytical model while model 2 predicted the enhanced peak force in very good agreement with the analytical model. It also shows that the occurrence time of force enhancement predicted by both FE models is earlier than the one-dimensional analytical model.

**3.3.3. Discussions.** Based on the developed models, for a fixed-end cellular bar of specific configuration (material and cross-section area), a critical length can be identified according to the intensity of the blast load; if the length of the cellular bar is greater than the critical length, blast force can be attenuated; otherwise, force enhancement will occur. On the other

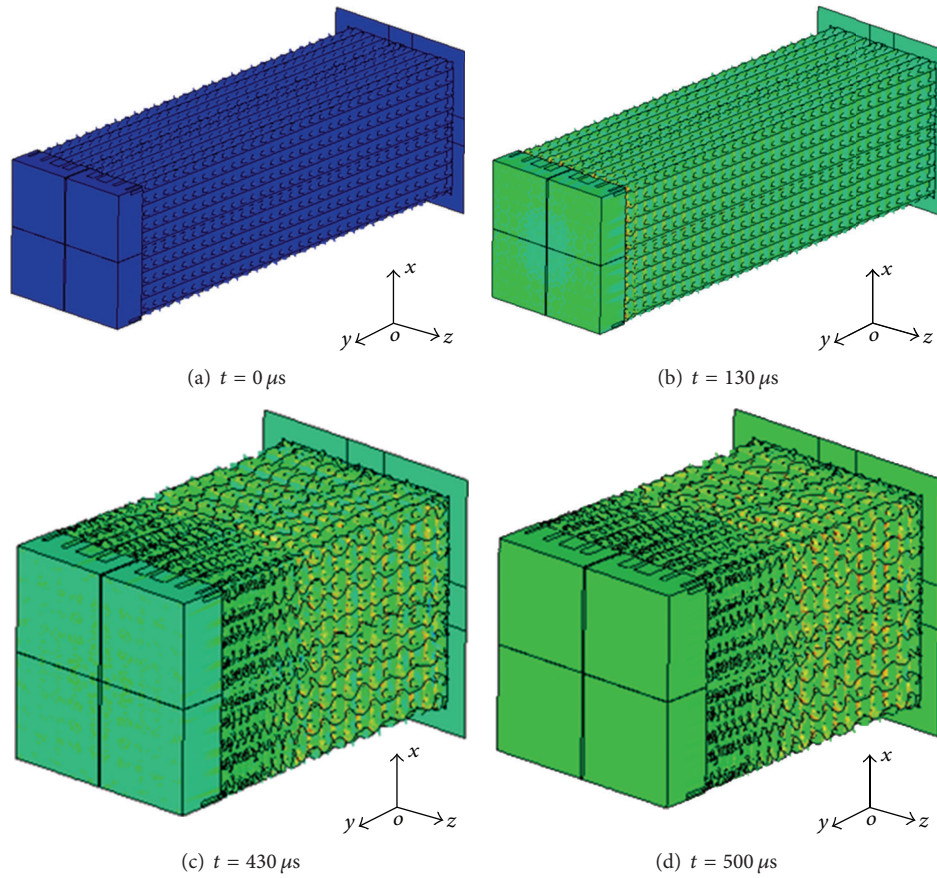


FIGURE 9: Simulation results of load pressure and deformation of aluminum foam bar under blast load at different times in model 2.

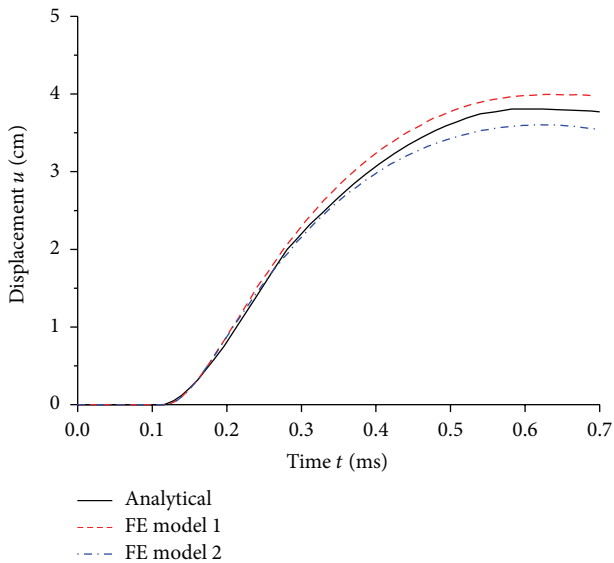


FIGURE 10: Displacement of foam bar predicted by simulation models.

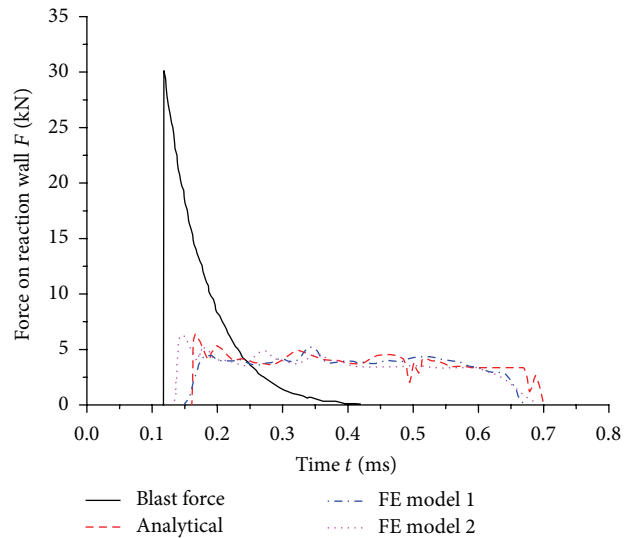


FIGURE 11: Force attenuation by aluminum foam under a blast load.

hand, for a fixed-length cellular bar, a critical value of the blast load intensity can be identified as well, above which force enhancement will occur. Figure 14 shows the relationship between the critical length of the foam bar and the critical blast load level. For blast loads under the critical curve,

the cellular bar will not be fully compacted, and the blast force is attenuated at the fixed end. But, for blast loads above the critical curve, once the cellular bar is fully compacted, force enhancement is expected. This critical curve can be used to determine when “force enhancement” will happen, so as to assist in the appropriate design process.

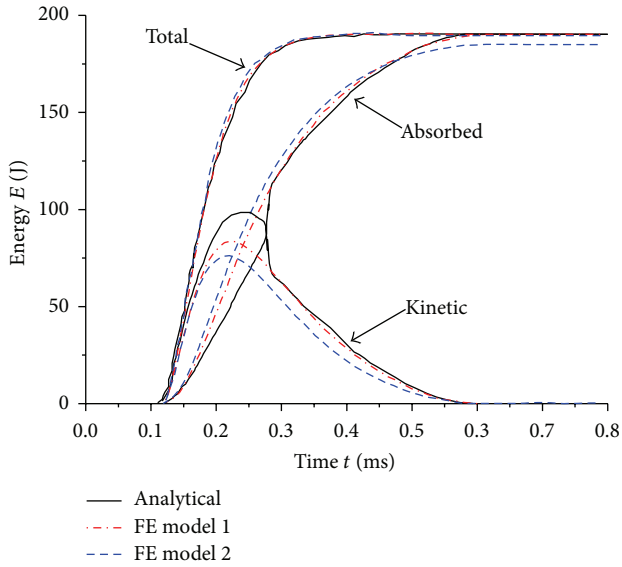


FIGURE 12: Energy history of foam bar under blast load of a 4 kg TNT equivalent.

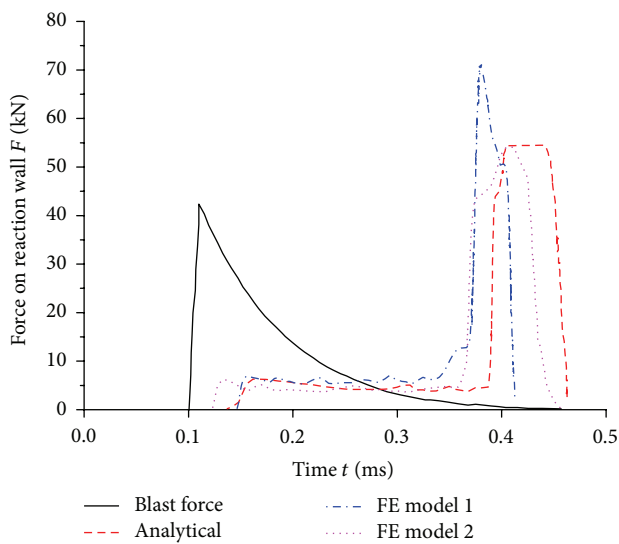


FIGURE 13: Force enhancement of aluminum foam bar under a blast load.

To further investigate the physical process causing force enhancement, momentum transfer in the system was investigated using the one-dimensional analytical model for both load cases. Figure 15 compares the momentum histories in Case 1. Because node 1 and node 2 are connected by the spring element representing the aluminum cover plate, which can be considered as rigid compared to aluminum foam under blast load, node 1 and node 2 have an identical momentum history curve as shown in Figure 16. It also shows that the momentum transfer between nodes 1(2) and node 3 occurred at around 0.3 ms, and no momentum transfer occurred between node

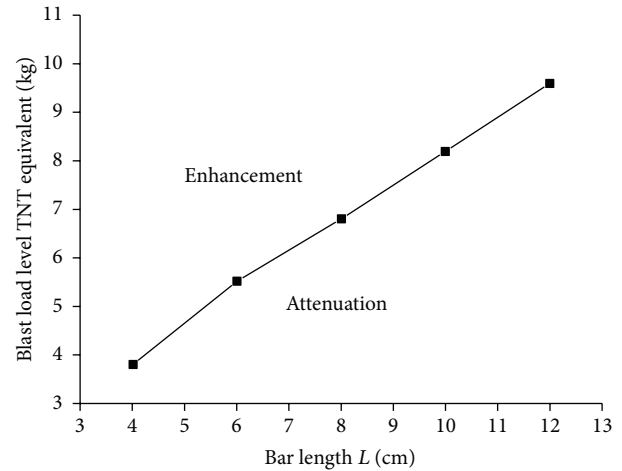


FIGURE 14: Critical curve of a fixed-end cellular bar under blast load.

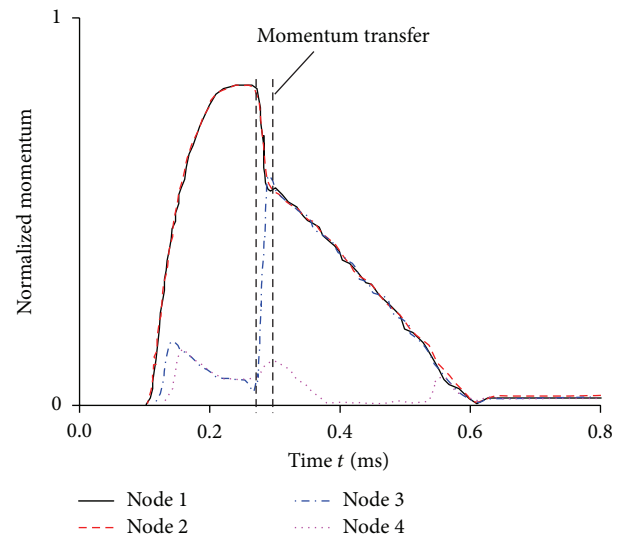


FIGURE 15: Normalized momentum in Case 1.

3 and node 4, which means that momentum was fully dissipated before the foam bar fully compacted in Case 1. In contrast, momentum transfer occurs between all nodes and is finally transmitted to the rigid reaction wall in Case 2. It is also seen that these momentum transfers occur within very short periods of time compared to the total time of the event. Once the propagated momentum transferred through the system reaches the fixed end, a high magnitude force is expected, and this will cause the force enhancement at the fixed end. Countermeasures which can increase the time duration for momentum transfer between the compacted foam bar and the protected structure are needed to eliminate the undesired force enhancement. Adding well-designed interim isolation (I-I) structure between the cellular material and the protected structure was proven to be effective in preventing force enhancement [21].

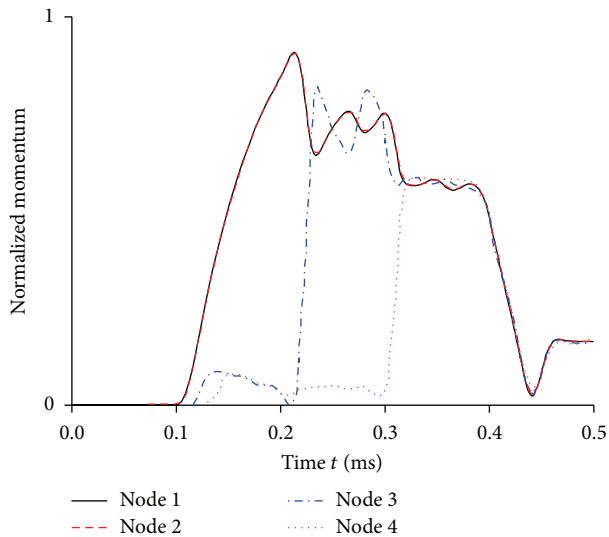


FIGURE 16: Normalized momentum in Case 2.

## 4. Conclusions

Two finite element models are presented to simulate the effect of using cellular materials for blast protection. Both force attenuation and force enhancement phenomena are simulated successfully. Good agreement between the two FE models and the one-dimensional analytical model has confirmed the correctness and credibility of the models. Critical curve of a fixed-end aluminum foam bar under blast load was identified based on the simulation results of the proposed models, which can be employed to assist in the appropriate design process of cellular material for blast protection applications. Based on the one-dimensional analytical model, force enhancement of cellular material under blast load is related to the momentum transfer between the cellular material and the protected structure within short periods of time compared to the total time of the event. Countermeasures which can increase this time duration are needed to eliminate the undesired force enhancement.

## Acknowledgments

This work is funded by the National Natural Science Foundation of China (nos. 50905024, 51105053), Liaoning Provincial Natural Science Foundation of China (no. 20102026), the Research Fund for the Doctoral Program of Higher Education of China (nos. 20090041120032, 20110041120022), and the Fundamental Research Funds for the Central Universities (DUT13Lk47).

## References

- [1] R. Monti, "Normal shock wave reflection on deformable solid walls," *Meccanica*, vol. 5, no. 4, pp. 285–296, 1966.
- [2] B. E. Gelfand, S. A. Gubin, S. M. Kogarko, and O. E. Popov, "Investigation of the special characteristics of the propagation and reflection of pressure waves in a porous medium," *Journal of Applied Mechanics and Technical Physics*, vol. 16, no. 6, pp. 897–900, 1975.
- [3] S. R. Reid, W. W. Bell, and R. A. Barr, "Structural plastic shock model for one-dimensional ring systems," *International Journal of Impact Engineering*, vol. 1, no. 2, pp. 175–191, 1983.
- [4] S. R. Reid, T. Y. Reddy, and C. Peng, "Dynamic compression of cellular structures and materials," in *Structural Crashworthiness and Failure*, pp. 295–340, Elsevier Application Science, London, UK, 1993.
- [5] B. Song, S. S. Hu, and J. F. Liu, "Shock wave in foam plastic," *Journal of Experimental Mechanics*, vol. 14, pp. 273–278, 1999.
- [6] B. W. Skew, M. D. Atkins, and M. W. Seitz, "The impact of a shock wave on porous compressive foams," *Journal of Fluid Mechanics*, vol. 253, pp. 245–265, 1993.
- [7] G. Mazor, G. Ben-Dor, O. Igra, and S. Sorek, "Shock wave interaction with cellular materials. Part I: analytical investigation and governing equations," *Shock Waves*, vol. 3, no. 3, pp. 159–165, 1994.
- [8] G. Ben-Dor, G. Mazor, O. Igra, S. Sorek, and H. Onodera, "Shock wave interaction with cellular materials. Part II: open cell foams; experimental and numerical results," *Shock Waves*, vol. 3, no. 3, pp. 167–179, 1994.
- [9] A. G. Hanssen, L. Enstock, and M. Langseth, "Close-range blast loading of aluminium foam panels," *International Journal of Impact Engineering*, vol. 27, no. 6, pp. 593–618, 2002.
- [10] S. Ouellet, D. Frost, and A. Bouamoul, "Using a shock tube to predict the response of polymeric foam to a blast loading," *Journal de Physique IV*, vol. 134, pp. 783–787, 2006.
- [11] M. Olim, M. E. H. Van Dongen, T. Kitamura, and K. Takayama, "Numerical simulation of the propagation of shock waves in compressible open-cell porous foams," *International Journal of Multiphase Flow*, vol. 20, no. 3, pp. 557–568, 1994.
- [12] Q. M. Li and H. Meng, "Attenuation or enhancement—a one-dimensional analysis on shock transmission in the solid phase of a cellular material," *International Journal of Impact Engineering*, vol. 27, no. 10, pp. 1049–1065, 2002.
- [13] G. W. Ma and Z. Q. Ye, "Analysis of foam claddings for blast alleviation," *International Journal of Impact Engineering*, vol. 34, no. 1, pp. 60–70, 2007.
- [14] G. W. Ma and Z. Q. Ye, "Energy absorption of double-layer foam cladding for blast alleviation," *International Journal of Impact Engineering*, vol. 34, no. 2, pp. 329–347, 2007.
- [15] C. N. Kingery and G. Bulmash, "Air-blast parameters from TNT spherical air blast and hemispherical surface blast," ARBRL-TR-O2555, U.S. Army Ballistic Research Laboratory, Aberdeen Proving Ground, 1984.
- [16] A. Czekanski, M. A. Elbestawi, and S. A. Meguid, "On the FE modeling of closed-cell aluminum foam," *International Journal of Mechanics and Materials in Design*, vol. 2, no. 1-2, pp. 23–34, 2005.
- [17] Y. Q. Tu, L. L. Liu, J. F. Wan, and M. Yang, "Improvement of the tetrakaidecahedral model for closed-cell aluminum foams," *Chinese Journal of Computational Mechanics*, vol. 27, no. 2, pp. 275–279, 2010.
- [18] Y. H. Yu, Z. Yang, and B. Liang, "Finite element simulation of foamed aluminum compression behavior," *Computer Simulations*, vol. 27, no. 7, pp. 317–320, 2010.
- [19] S. Santosa and T. Wierzbicki, "On the modeling of crush behavior of a closed-cell aluminum foam structure," *Journal of*

*the Mechanics and Physics of Solids*, vol. 46, no. 4, pp. 645–669, 1998.

- [20] H. X. Wang, *Study on spherical pore Al alloy foam with fractal theory and FEM method [M.S. thesis]*, Southeast University, Nanjing, China, 2006.
- [21] C. Qi, *A magic cube approach for crashworthiness and blast protection designs of structural and material systems [Ph.D. dissertation]*, University of Michigan, Ann Arbor, Mich, USA, 2008.

## Research Article

# Austenite Grain Growth Behavior of AISI 4140 Alloy Steel

Lin Wang,<sup>1</sup> Dongsheng Qian,<sup>2,3</sup> Jun Guo,<sup>2</sup> and Yan Pan<sup>2</sup>

<sup>1</sup> School of Mechanical and Electronic Engineering, Wuhan University of Technology, Wuhan 430070, China

<sup>2</sup> School of Materials Science and Engineering, Wuhan University of Technology, Wuhan 430070, China

<sup>3</sup> Hubei Key Laboratory of Advanced Technology for Automotive Components, Wuhan 430070, China

Correspondence should be addressed to Dongsheng Qian; bestcx@yahoo.com.cn

Received 4 May 2013; Accepted 26 August 2013

Academic Editor: Gang Wang

Copyright © 2013 Lin Wang et al. This is an open access article distributed under the Creative Commons Attribution License, which permits unrestricted use, distribution, and reproduction in any medium, provided the original work is properly cited.

AISI 4140 alloy steel is widely applied in the manufacture of various parts such as gears, rams, and spindles due to its good performance of strength, toughness, and wear resistance. The former researches most focused on its deformation and recrystallization behaviors under high temperature. However, the evolution laws of austenite grain growth were rarely studied. This behavior also plays an important role in the mechanical properties of parts made of this steel. In this study, samples are heated to a certain temperature of 1073 K, 1173 K, 1273 K, and 1373 K at a heating rate of 5 K per second and hold for different times of 0 s, 120 s, 240 s, 360 s, and 480 s before being quenched with water. The experimental results suggest that the austenite grains enlarge with increasing temperature and holding time. A mathematical model and an application developed in Matlab environment are established on the basis of previous works and experimental results to predict austenite grains size in hot deformation processes. The predicted results are in good agreement with experimental results which indicates that the model and the application are reliable.

## 1. Introduction

During the hot deformation of metal material, there occurs recrystallization including dynamic recrystallization, static recrystallization, and metadynamic recrystallization. When the accumulative fraction of recrystallization is over 95%, considered as the complete recrystallization, the newly formed austenite grains will grow up. Besides, when the metal material is heated before deformation, austenite size will also enlarge. Therefore, in order to gain products with better microstructure, it is necessary to investigate the growth laws of austenite and establish the mathematical model to predict the grain growth behavior under different high temperature and holding time, which also plays an important role in the kinetic metallurgical transformation.

AISI 4140 alloy steel has been widely used in the manufacture of gears, shafts, rams, spindles, and so on due to its good balance of strength, toughness, and wear resistance especially for some large annular parts such as the wind tower flange and bearing ring generator usually produced under high temperature. At present, there are many researches on the deformation behaviors of AISI 4140 steel. Lin et al. [1–3] studied the deformation behaviors of casting AISI 4140 steel at

high temperature and strain rate. Zhou et al. [4, 5] established the flow stress constitutive equations of forging AISI 4140 alloy steel by hot compression tests. Lin et al. [6–8] discussed the effects of different temperatures, deformation degrees, and strain rates on the dynamic and static recrystallization. Hong and Kang [9] investigated the dynamic microstructure change with initial rolling temperature for hot rolling process of AISI 4140 steel using LARSTRAN/SHAPE platform. However, there are few efforts taken to understand the austenite growth laws of this steel. Also, the existed mathematical models for predicting austenite grain size can only be used in isothermal environment instead of nonisothermal forming processes such as heating or hot deformation. Actually, precise prediction of austenite grain size is of great significance to optimize the hot forming processing parameters.

In this study, heat insulation tests of AISI 4140 steel are carried out under different temperatures and holding times, and the grains sizes are measured to deduce the mathematical model of austenite grain growth. And an application based on Matlab is also written to calculate the austenite grain size under variable temperature. The results can be applied in finite element simulation or practical production of various parts made of this material for further study.

TABLE 1: Average diameter values of samples.

1073 K		1173 K		1273 K		1373 K	
Time (s)	Diameter ( $\mu\text{m}$ )						
0	10.43	0	21.54	0	45.02	0	79.93
120	14.11	120	29.27	120	55.97	120	107.75
240	16.11	240	33.73	240	63.68	240	119.48
360	18.07	360	36.68	360	68.56	360	128.25
480	19.78	480	38.93	480	73.15	480	136.17

## 2. Experiments

**2.1. Experimental Preparation.** The cylindrical samples with the diameter of 8 mm, the length of 12 mm, and the end face roughness of  $1.6 \mu\text{m}$  are taken from a continuous casting AISI 4140 steel ingot compositions (mass%) 0.39 C-0.49 Ni-0.24 Si-1.04 Cr-0.69 Mn-0.12 Cu-0.006 P-0.19 Mo-0.002 S and the balance is Fe. Then, they are placed in the Gleeble-3500 thermomechanical simulation machine which can precisely simulate the hot deformation behaviors of various materials under a wide range of conditions by the feedback servomechanism. The thin tantalum sheets smeared with graphite lubricant are put between samples and fixture to maintain good contact for better accuracy of temperature control.

**2.2. Experimental Procedure.** As shown in Figure 1, the samples were heated to a certain temperature (1073 K, 1173 K, 1273 K, and 1373 K) at a heating rate of 5 K/s and held for different times (0 s, 120 s, 240 s, 360 s, and 480 s) before being quenched with water. After the heat insulation tests, the samples were polished using abrasive papers and corundum agent, etched in the mixture of 50 ml supersaturated picric acid, 2 g Sodium dodecyl benzene sulfonate and 10 ml alcohol at 323 K~333 K. Then, the sizes of emerged austenite grains were measured automatically by metallographic observation software using mean value method. The average grain size of the casting ingot is  $21 \mu\text{m}$ .

## 3. Results and Discussion

Figures 2 and 3 show graphs of austenite grains under temperatures of 1273 K and 1373 K. It can be seen that the austenite grains becomes larger as the samples are held for longer time. This is because grains can merge each other under a certain temperature which results in smaller ones combining into bigger ones [10]. The longer the holding time is, the more remarkable this phenomenon will be. From Figures 2(b) and 3(b), we can know that austenite grains enlarge to a great extent with higher temperature when samples are held for the same time. According to [11], we have

$$\mu = K \exp\left(-\frac{Q_m}{RT}\right) \frac{\sigma}{D}, \quad (1)$$

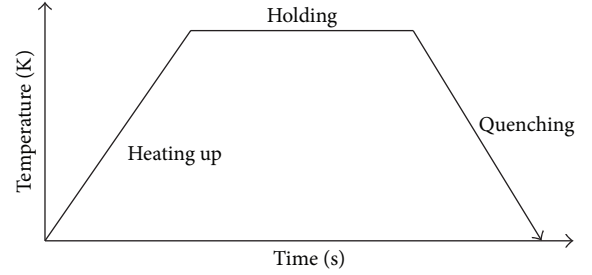


FIGURE 1: Schematic of heat insulation tests.

where

- $\mu$ : growth speed of austenite grains;
- $K$ : constant;
- $Q_m$ : movement activation energy of grain boundaries;
- $R$ : gas constant;
- $T$ : absolute temperature;
- $\sigma$ : specific boundary energy;
- $D$ : austenite grain diameter.

It can be observed that when temperature arises, the growth speed of austenite grains will increase exponentially. Therefore, higher temperature can drive grains to grow faster to larger dimensions.

In detail, the average diameter values of each sample are listed in Table 1 and Figure 4. For 1273 K, increments of average diameters are  $3.68 \mu\text{m}$ ,  $2.00 \mu\text{m}$ ,  $1.96 \mu\text{m}$ , and  $1.71 \mu\text{m}$  with holding time being longer, respectively. That is to say, the growth speed of austenite grain becomes slower, which also occurs at other temperature. From (1), it can be learned that this speed is inversely proportional to the grain diameter. Hence, under a certain temperature, the larger the grains are, the smaller their size increments will be.

**3.1. Model of AISI 4140 Steel Austenite Grain Growth.** From the existing literature, there are two typical mathematical models of austenite grain growth under constant temperature for alloy steel written as follows [12, 13]:

$$d_g^{m_1} = A_1 t^n \exp\left(-\frac{Q'_{gg}}{RT}\right), \quad (2)$$

$$d_g^{m_2} = d_0^{m_2} + A_2 t \exp\left(-\frac{Q''_{gg}}{RT}\right), \quad (3)$$

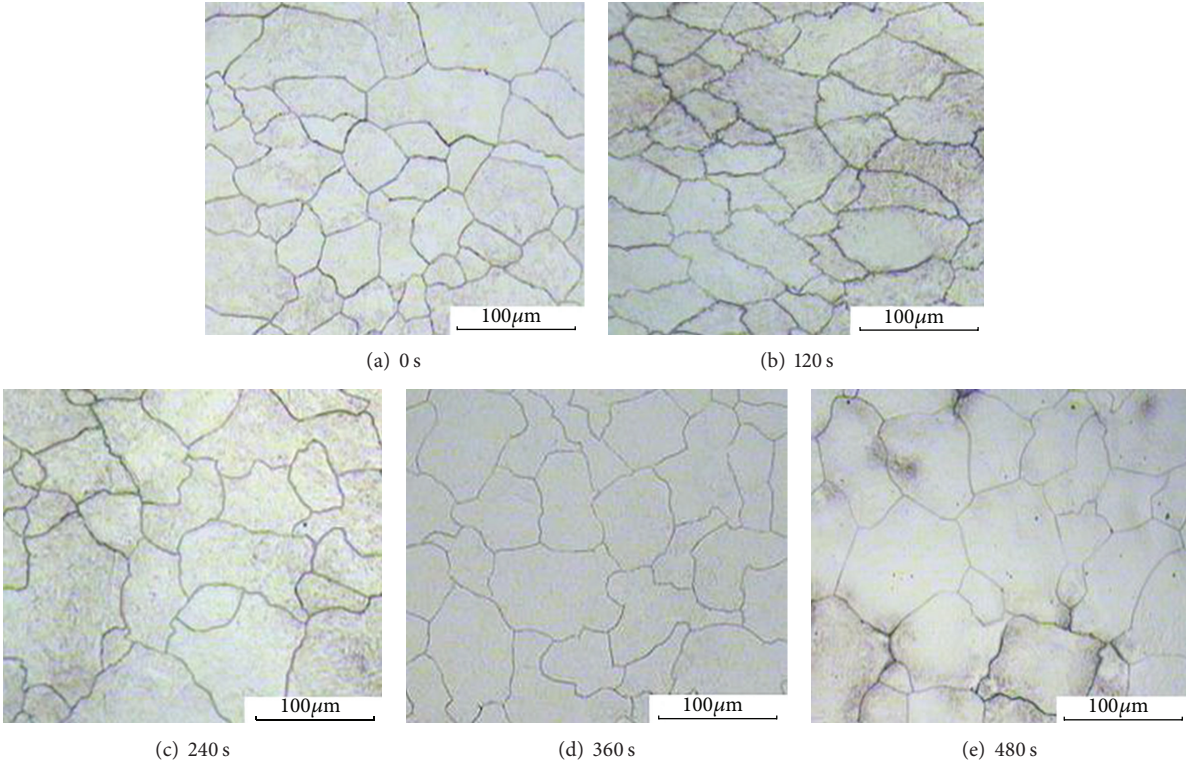


FIGURE 2: Micrographs of austenite grains of 1273 K.

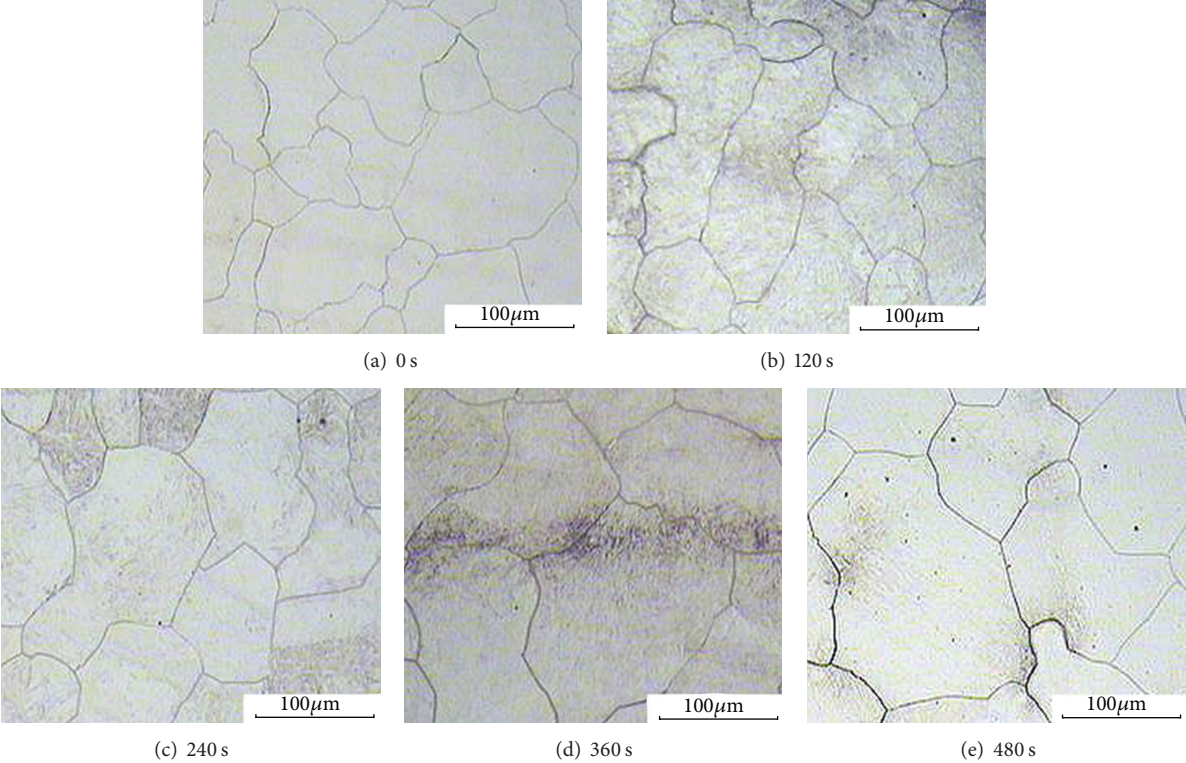


FIGURE 3: Micrographs of austenite grains of 1373 K.

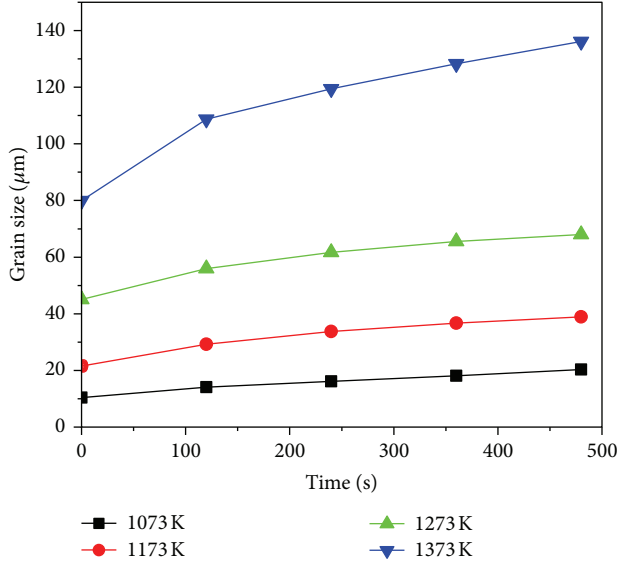


FIGURE 4: Variation of austenite grain sizes.

where

$t$ : time (s);

$d_g, d_0$ : average austenite grain size at time of  $t$  ( $\mu\text{m}$ );

$Q'_{\text{gg}}, Q''_{\text{gg}}$ : activation energy of austenite grain growth ( $\text{J}\cdot\text{mol}^{-1}$ );

$T$ : absolute temperature (K);

$A_1, A_2, m_1, m_2, n$ : constants.

It can be seen from (2) that when the holding time  $t$  is 0 s, the grain size will be 0  $\mu\text{m}$ , which does not conform to actual situation. In (2), the exponent of  $t$  is 1, which usually also does not match experimental results well [14–16]. Therefore, a general model can be derived from these two equations as follows:

$$d_g^m = d_0^m + At^n \exp\left(-\frac{Q_{\text{gg}}}{RT}\right). \quad (4)$$

Calculate the logarithm of both sides of (4), it can get

$$\ln(d_g^m - d_0^m) = \ln A + n \ln t + \left(-\frac{Q_{\text{gg}}}{RT}\right). \quad (5)$$

The constants  $A$ ,  $n$  and activation energy of austenite grain growth  $Q_{\text{gg}}$  can be calculated by linear regression using experimental data listed in Table 1. For the constant  $m$ , its value ranges from 2 to 5 in most cases [17]. Consequently,  $m$  can be supposed to be 2, 2.5, 3, 3.5, 4, 4.5, and 5 at first, and a function used to determine its best value will be figured out.

For example, we can order  $m$  equals 2. Then, take the partial of (5) with respect to  $1/T$  and make some transpositions as follows:

$$\bar{k}_1 = -\frac{Q_{\text{gg}}}{R} = \frac{\partial [\ln(d_g^2 - d_0^2)]}{\partial (1/T)} \Bigg|_t. \quad (6)$$

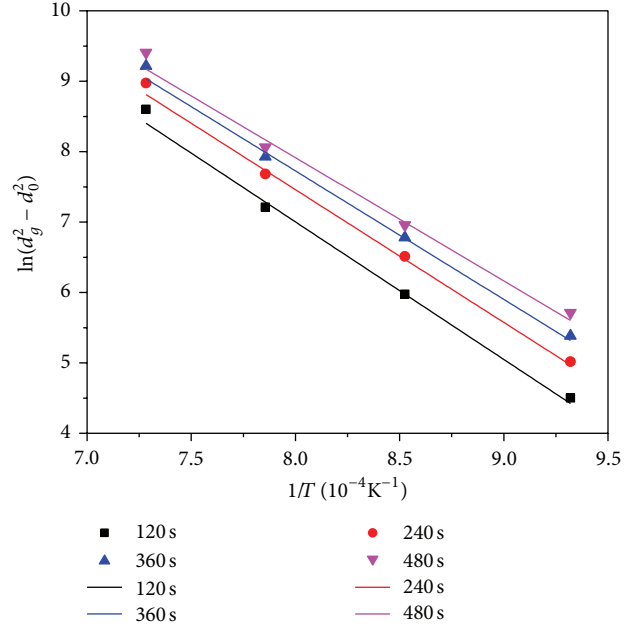


FIGURE 5: The relationship between  $\ln(d_g^m - d_0^m)$  and  $1/T$  at different temperatures when  $m = 2$ .

Substitute the experimental datum with holding time of being 120 s, 240 s, 360 s, and 480 s to the right side of the second equal sign, respectively. In consequence, there obtains four lines through linear fitting which are drawn in Figure 5.  $\bar{k}_1$  is the average value of slopes of these lines and  $Q_{\text{gg}}$  is equal to  $-\bar{k}_1$  multiplies  $R$ .

Similarly, take the partial of (5) with respect to  $\ln t$ , the solution equation of  $n$  can be written as follows:

$$n = \frac{\partial [\ln(d_g^2 - d_0^2)]}{\partial (\ln t)} \Bigg|_T. \quad (7)$$

Substitute the diameter values with same heating temperature to the right side of this equation. As shown in Figure 6,  $n$  is the mean value of slopes of the four linear fitting lines corresponding to 1073 K, 1173 K, 1273 K, and 1373 K.

Plug  $Q_{\text{gg}}$ ,  $n_1$  and grain sizes into (5) to gain the value of  $A$ . Therefore, a mathematic model of austenite grain growth with  $m$  being 2 is described as follows:

$$d_g^2 = d_0^2 + 1.089 \times 10^8 t^{0.693} \exp\left(-\frac{154117.18}{RT}\right). \quad (8)$$

Using the same method, models with  $m$  being other values can be obtained, and then a set of theoretical austenite grain sizes can also be calculated under the same heating condition as experiments for each model. The average standard error (ASE) between all theoretical and experimental datum of each model will be figured out to establish a function of ASE and  $m$  expressed as follows through polynomial fitting:

$$\text{ASE} = 16.03087 - 1.03311m_1 + 0.33248m_1^2 - 0.04524m_1^3 + 0.00239m_1^4. \quad (9)$$

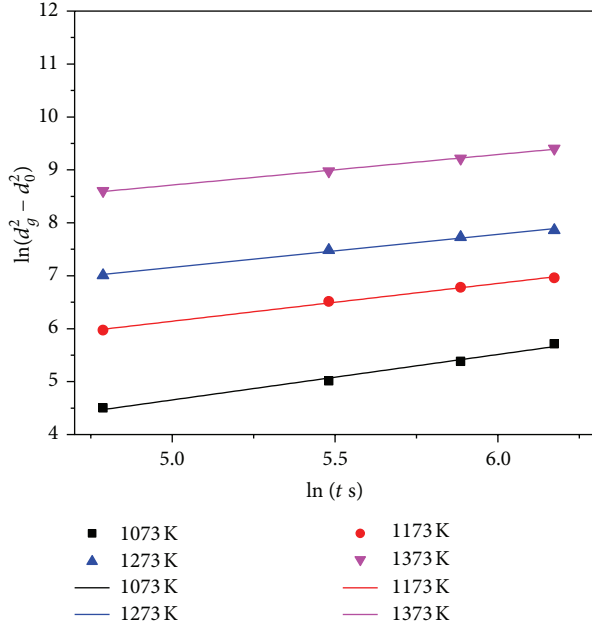


FIGURE 6: The relationship between  $\ln(d_g^m - d_0^m)$  and  $\ln t$  at different temperatures when  $m = 2$ .

It can be known from Figure 7 that, with the increasing value of  $m$ , ASE decreases first and then increases indefinitely. When  $m$  is equal to 3.015, ASE reaches its lowest level, which means that the model with  $m$  being 3.015 is the most accurate. So substitute it to (5) to reobtain values of  $A$ ,  $n$ ,  $Q_{gg}$ , and the mathematical model of austenite grain growth of AISI 4140 steel under constant temperature can be written as

$$d_g^{3.015} = d_0^{3.015} + 1.154 \times 10^{13} t^{0.823} \exp\left(-\frac{236317.26}{RT}\right). \quad (10)$$

Figure 8 shows a comparison between theoretical values predicted by (10) and experimental ones. The maximum relative error is only 5.10%, which suggests that this model is reliable.

However, during the hot forming process, the ambient and dies temperature are not isothermal, which makes the workpiece is not thermostatic. Besides, during the heating process before preservation, the workpiece temperature varies from time to time. That is to say, this model cannot be applied for the previous situation. Therefore, modification is needed to make the model better fit for all hot forming processes.

In the processes of the nonisothermal heating and hot deformation, the temperature of workpiece can seem as constant during a tiny time step  $\Delta t$ , and the whole process can be divided into a number of such steps. So the average size of austenite grains at the end of  $N$ th time step can be expressed as

$$d_N^{3.015} = d_{N-1}^{3.015} + 1.154 \times 10^{13} \Delta t^{0.823} \exp\left(-\frac{236317.26}{RT_N}\right), \quad (11)$$

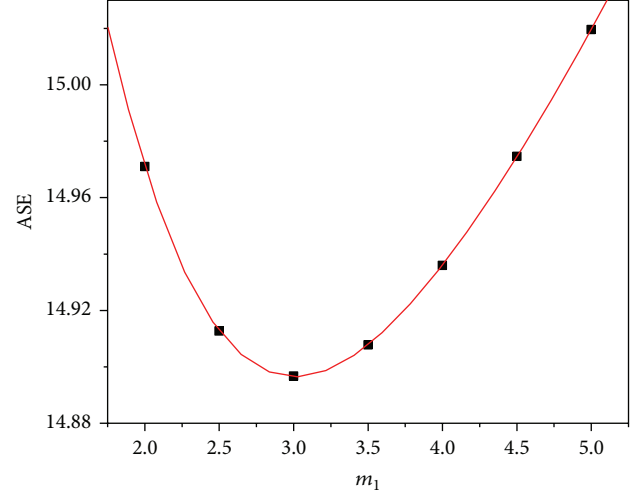


FIGURE 7: Variation of ASE with the value of  $m$ .

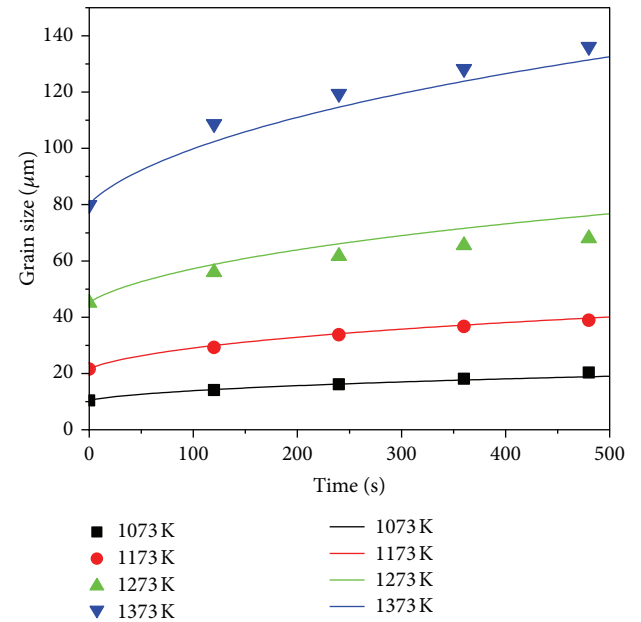


FIGURE 8: Comparison between theoretical and experimental results.

where

$d_{N-1}^{3.015}$ : average size of austenite grains at the end of  $(N - 1)$ th time step;

$T_N$ : temperature of the  $(N - 1)$ th time step.

The shorter the time step is, the more accurate grain size will be calculated by this equation. But it also can be seen that lots of efforts are needed for the computing by manual. The commercial mathematic software Matlab is employed to deal with this complex computation.

As Figure 9 shows, firstly, a temperature-time curve file (.xls) in which temperature being given out at a certain time interval ( $\Delta t$ ) should be input into Matlab, and the number of time step ( $n$ ), the inquiry time ( $t_i$ ), and the initial grain size ( $d_0$ ) should be given. This software will calculate

TABLE 2: Calculated austenite grain size.

N	Grain size ( $\mu\text{m}$ )			Max relative error (%)	Time consumption
	120 s	240 s	360 s		
100	62.3	71.5	78.2	-13.26	About 30 s
1000	65.1	75.2	81.4	-9.66	About 2 mins
10000	67.6	78.5	86.9	-3.09	About 30 mins

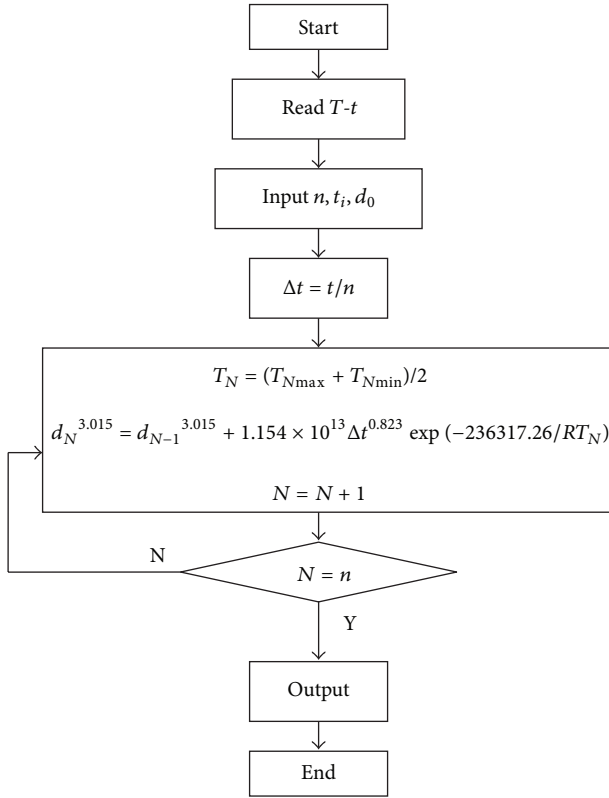


FIGURE 9: Flow chart of austenite grain size calculation in Matlab.

the austenite grain size of each time step by (11) automatically. The temperature of each time step ( $T_N$ ) is the mean value of lowest and highest temperature in this step. The final grain size of the previous step is considered as the initial grain size of the following time step. So, the instantaneous grain size of the inquiry time and the final size after the whole process can be obtained.

A user interface as displayed in Figure 10 is set up using programming language in Matlab. Press the “Read Temperature-time Curve from Files” button to input the variation of temperature, and fill in the blank with appropriate values. After pressing the button “Calculate,” the required grain sizes and variation of grain size with increasing time will be exhibited soon.

For correctness validation of this application, another three heat insulation tests were carried out. The holding temperature is 1323 K and holding times are 120 s, 240 s, and 360 s, respectively. The predicted sizes of austenite grain sizes under same conditions are listed in Table 2. The micrographs of

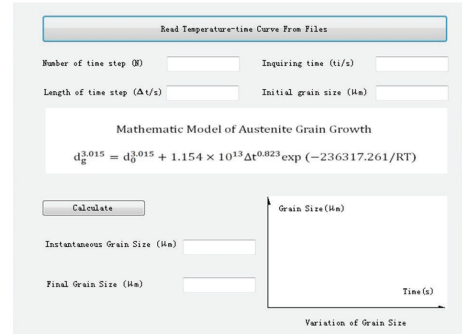


FIGURE 10: The application for austenite grain size calculation.

experimental samples after testing are showed as Figure 11. Their average austenite grain sizes are measured as  $68 \mu\text{m}$ ,  $81 \mu\text{m}$ , and  $89 \mu\text{m}$ , respectively. It can be known that the greater the value of  $N$  is, the more precise the predicted values are and the longer time computation needs. When  $N$  is chosen to a certain value, the maximum relative error is defined as

max relative error

$$= \max \left\{ \frac{\text{calculated size} - \text{experimental size}}{\text{expericmental size}} \times 100\% \right\}_{t_i}, \quad (12)$$

where  $t_i$  mean different holding times.

As a result, the maximum relative error is 3.09% when compared with the predicted results with  $N$  being 10000, which suggests that this application is fit for the calculation of austenite grain size in hot forming processes.

## 4. Conclusion

The growth behavior of austenite grains of AISI 4140 alloy steel was studied through heat insulation tests. On the basis of the experimental results, three main conclusions are stated as follows.

- (1) The austenite grains become larger as the samples being held for longer time; meanwhile, the growth speed of austenite grain becomes slower. Higher temperature will also enlarge austenite grains to a greater extent.
- (2) A reliable mathematical model for predicting average austenite grain size of AISI 4140 alloy steel at constant

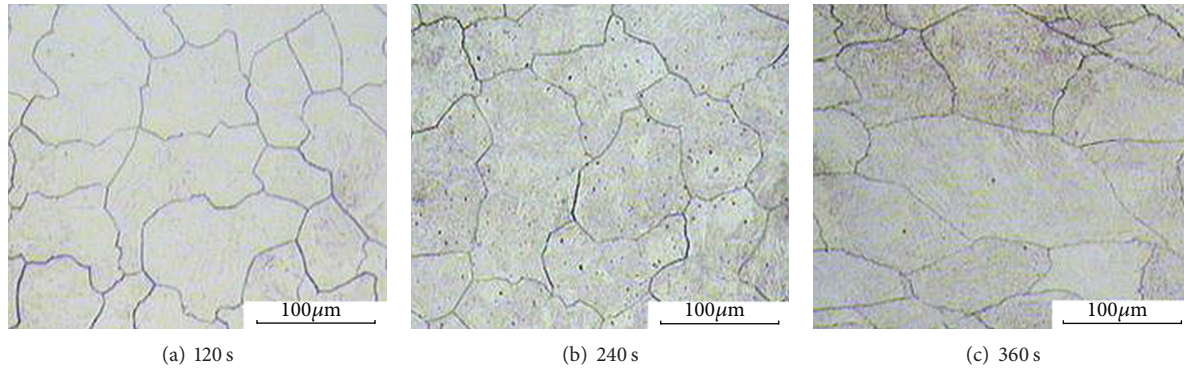


FIGURE II: Micrographs of austenite grains of 1323 K.

temperature was established, and predicted results are in good agreement with experimental ones.

- (3) An application for predicting average austenite grain size of AISI 4140 alloy steel at ever-changed temperature was established, and predicted results match experimental datum well.

## Acknowledgments

This work was supported by the Grant from the State Key Program of National Natural Science Foundation of China (no. 51135007), the National Natural Science Foundation for Young Scientists of China (no. 51005171), the State Key Development Program for Basic Research of China (Grant no. 2011CB706605), and the Grant from the Innovative Research Groups of the National Natural Science Foundation of Hubei province (no. 2011CDA122).

## References

- [1] Y.-C. Lin, M.-S. Chen, and J. Zhang, "Modeling of flow stress of 42CrMo steel under hot compression," *Materials Science and Engineering A*, vol. 499, no. 1-2, pp. 88–92, 2009.
- [2] Y. C. Lin, M.-S. Chen, and J. Zhong, "Prediction of 42CrMo steel flow stress at high temperature and strain rate," *Mechanics Research Communications*, vol. 35, no. 3, pp. 142–150, 2008.
- [3] Y. C. Lin, M.-S. Chen, and J. Zhong, "Constitutive modeling for elevated temperature flow behavior of 42CrMo steel," *Computational Materials Science*, vol. 42, no. 3, pp. 470–477, 2008.
- [4] G. Zhou, L. Hua, J. Lan, and D. S. Qian, "FE analysis of coupled thermo-mechanical behaviors in radial-axial rolling of alloy steel large ring," *Computational Materials Science*, vol. 50, no. 1, pp. 65–76, 2010.
- [5] G. Zhou, L. Hua, and D. S. Qian, "3D coupled thermo-mechanical FE analysis of roll size effects on the radial-axial ring rolling process," *Computational Materials Science*, vol. 50, no. 3, pp. 911–924, 2011.
- [6] Y. C. Lin and M.-S. Chen, "Study of microstructural evolution during static recrystallization in a low alloy steel," *Journal of Materials Science*, vol. 44, no. 3, pp. 835–842, 2009.
- [7] Y. C. Lin, M.-S. Chen, and J. Zhong, "Study of static recrystallization kinetics in a low alloy steel," *Computational Materials Science*, vol. 44, no. 2, pp. 316–321, 2008.
- [8] Y. C. Lin, M.-S. Chen, and J. Zhong, "Effects of deformation temperatures on stress/strain distribution and microstructural evolution of deformed 42CrMo steel," *Materials and Design*, vol. 30, no. 3, pp. 908–913, 2009.
- [9] H. P. Hong and Y. L. Kang, "FEM simulation on dynamic microstructure change during hot rolling of 42CrMo4 alloy steel," in *Proceedings of the 10th International Conference on Steel Rolling*, The Chinese Society for Metals, Beijing, China, 2010.
- [10] Z. C. Liu, H. P. Ren, and H. Y. Wang, *Austenite Formation and Pearlite Transformation*, Metallurgical Industry Press, Beijing, China, 4th edition, 2010.
- [11] W. M. Mao and X. B. Zhao, *Recrystallization and Grain Growth of Metal*, Metallurgical Industry Press, Beijing, China, 2nd edition, 1994.
- [12] E. Anelli, "Application of mathematical modelling to hot rolling and controlled cooling of wire rods and bars," *ISIJ International*, vol. 32, no. 3, pp. 440–449, 1992.
- [13] C. M. Sellars and J. A. Whiteman, "Recrystallization and grain growth in hot rolling," *Metal Science*, vol. 13, no. 3-4, pp. 187–194, 1978.
- [14] L.-N. Duan, J.-M. Wang, Q.-Y. Liu, X.-J. Sun, and J.-C. Cao, "Austenite grain growth behavior of X80 pipeline steel in heating process," *Journal of Iron and Steel Research International*, vol. 17, no. 3, pp. 62–66, 2010.
- [15] W. Li and K. Xia, "Kinetics of the  $\alpha$  grain growth in a binary Ti-44Al alloy and a ternary Ti-44Al-0.15Gd alloy," *Materials Science and Engineering A*, vol. 329-331, pp. 430–434, 2002.
- [16] S. S. Zhang, M. Q. Li, Y. G. Liu, J. Luo, and T. Q. Liu, "The growth behavior of austenite grain in the heating process of 300M steel," *Materials Science and Engineering A*, vol. 528, no. 15, pp. 4967–4972, 2011.
- [17] C. Yue, L. Zhang, S. Liao, and H. Gao, "Kinetic analysis of the austenite grain growth in GCr15 steel," *Journal of Materials Engineering and Performance*, vol. 19, no. 1, pp. 112–115, 2010.

## Research Article

# Gas-Assisted Heating Technology for High Aspect Ratio Microstructure Injection Molding

Shia-Chung Chen,<sup>1,2,3</sup> Chen-Yang Lin,<sup>1</sup> Jen-An Chang,<sup>1,2,3</sup> and Pham Son Minh<sup>1,2,3,4</sup>

<sup>1</sup> Department of Mechanical Engineering, Chung Yuan Christian University, Chung-Li 32023, Taiwan

<sup>2</sup> R&D Center for Membrane Technology, Chung Yuan Christian University, Chung-Li 32023, Taiwan

<sup>3</sup> R&D Center for Mold and Molding Technology, Chung Yuan Christian University, Chung-Li 32023, Taiwan

<sup>4</sup> Faculty of High Quality Training, University of Technical Education, Ho Chi Minh City 70000, Vietnam

Correspondence should be addressed to Shia-Chung Chen; shiachun@cycu.edu.tw

Received 28 June 2013; Accepted 26 August 2013

Academic Editor: Lei Zhang

Copyright © 2013 Shia-Chung Chen et al. This is an open access article distributed under the Creative Commons Attribution License, which permits unrestricted use, distribution, and reproduction in any medium, provided the original work is properly cited.

A hot gas is used for heating the cavity surface of a mold. Different mold gap sizes were designed. The mold surface temperature was heated to above the glass transition temperature of the plastic material, and the mold then closed for melt filling. The cavity surface can be heated to 130°C to assist the melt filling of the microfeatures. Results show that hot gas heating can improve the filling process and achieve 91% of the high aspect ratio microgrooves (about 640.38 μm of the maximum of 700 μm). The mold gap size strongly affects the heating speed and heating uniformity. Without surface preheating, the center rib is the highest. When the heating target temperature is 90°C or 100°C, the three microribs have a good uniformity of height. However, when the target temperature exceeds 100°C, the left side rib is higher than the other ribs.

## 1. Introduction

Nowadays, injection molding is one of the most widely used processing technologies in the manufacture of plastic products. Among typical molding parameters, the mold surface temperature is critical. At higher mold surface temperatures, the surface quality of the part will improve [1, 2]. In the injection molding field, microinjection molding is used to manufacture a variety of polymer components, because of its low cost and potential for high-volume production. Most applications are in the field of microoptics (such as CDs and DVDs) and microfluidic devices. Production of other molded microoptical components including optical gratings, optical switches, and waveguides [3–5] as well as a variety of molded microfluidic devices including pumps, capillary analysis systems, and lab-on-a-chip applications [6, 7] is ongoing.

In general, to improve an injection molding part, it requires higher mold temperatures during injection to minimize part thickness and injection pressure. However, maintaining high mold temperature during the filling process

and lowering the mold temperature to below the deflection temperature during the postfilling process, while avoiding great increases in cycle time and energy consumption, is not easy. To address this problem, a variety of dynamic mold temperature controls (DMTC) have been explored in recent years. Their purpose is to eliminate the frozen layer, ideally producing a hot mold during the filling stage and a cold mold for cooling. The most inexpensive way to achieve high mold temperature is to use cooling water at temperatures as high as 90°C or 100°C [8].

Local mold heating using an electric heater [9] is sometimes used to assist high mold temperature control. However, this requires additional design and tool costs. Further, electrical heating is usually used as auxiliary heating and is limited to increases in mold temperature of roughly several tens of degrees centigrade.

Mold surface heating, such as induction heating [10–12], high-frequency proximity heating [13, 14], and gas-assisted mold temperature control (GMTC) [15, 16], can provide sufficient heating rates without significant increases in cycle time. In recent years, we have conducted systematic study of

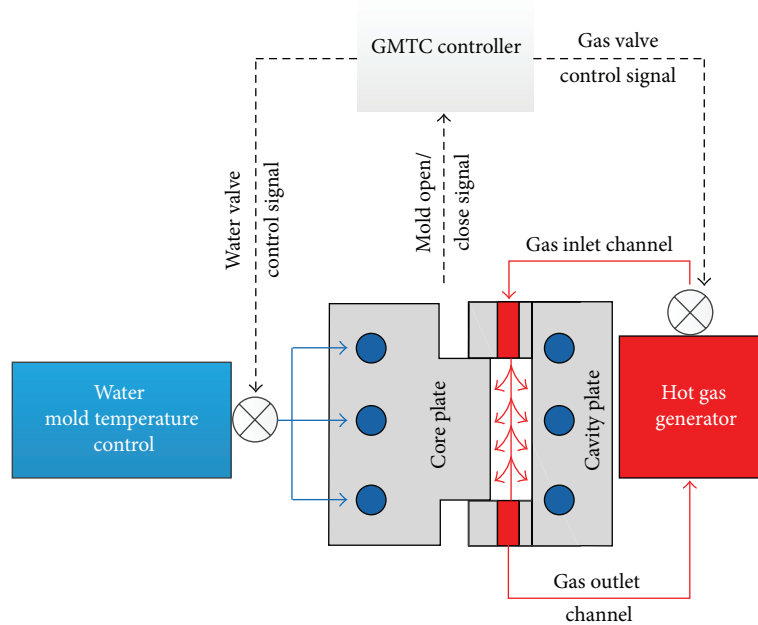


FIGURE 1: Schematic of the GMTC system.

mold surface heating and mold surface localization heating of the processing characteristics.

In this study, gas-assisted mold temperature control (GMTC) combined with water cooling is used with different mold gap sizes (4 mm, 6 mm, and 8 mm) to achieve rapid mold surface temperature control for high aspect ratio microinjection molding. A set of systematic experiments were conducted to correlate the effect of heating conditions, including heating efficiency and temperature distribution uniformity. The feasibility of gas-assisted heating for mold surface temperature control during the injection process to improve the microfeatures was evaluated.

## 2. Experimental Method

Gas-assisted mold temperature control (GMTC) is a new technique in the field of mold temperature control, which can heat and cool the cavity surface rapidly during the injection molding process. In general, the goal of mold temperature control is to increase the mold surface to the target temperature before filling with the melt and then cooling the melt to the ejection temperature. In this research, the GMTC system consists of a GMTC controller, a hot-gas generator system, and a water mold temperature controller, as shown in Figure 1.

The hot gas generator consists of an air compressor, an air dryer, a digital volumetric flow controller, and a high efficiency gas heater. The function of the high power hot gas generator system is to support a heat source, which provides a flow of hot air up to 500°C with a flow rate up to 500 l/min. For the coolant system, a mold temperature control was used to provide water at a defined temperature to cool the mold

after the filling process and to warm the mold to the initial temperature at the beginning of the process. The valve system was used to control the water for the cooling channels and the air for the heating stage. To both control and observe the temperature at the cavity surface, two temperature sensors were used to obtain the real time mold temperature and to provide feedback to the GMTC controller. After achieving the target temperature, the gas valve closes and the mold will then completely close for the melt injection. A Sodick-TR85EH injection molding machine is used for the molding experiments.

In this paper, the hot gas will be used as a heating source to increase the cavity surface temperature of the injection mold. After the filling process is finished, the hot melt is solidified using the cool water. During operation, first, when the mold is closed, the core will move to the heating position (Figure 2—step 1). Next, the hot gas will flow into the cavity, pushing out the cool air and leaving only the hot gas (Figure 2—step 2). Therefore, the heat transfer coefficient will rapidly increase. The energy transferred from the hot gas to the mold wall will heat the cavity surface. This is the heating process of gas-assisted mold surface heating in injection molding. Finally, when the cavity surface is heated to the target temperature for assistance in the filling and packing of the melt, the mold will completely close in preparation for the filling process (Figure 2—step 3).

Figures 3 and 4 show the injection mold with the microstructure blocks inserted into the center of the mold. The heating area is 80 mm × 40 mm which covers the molding area of 60 mm × 25 mm. The structure of the gas flow, gas inlet, and gas outlet channel was built into the mold for ease of operation during the gas heating period to the melt injection.

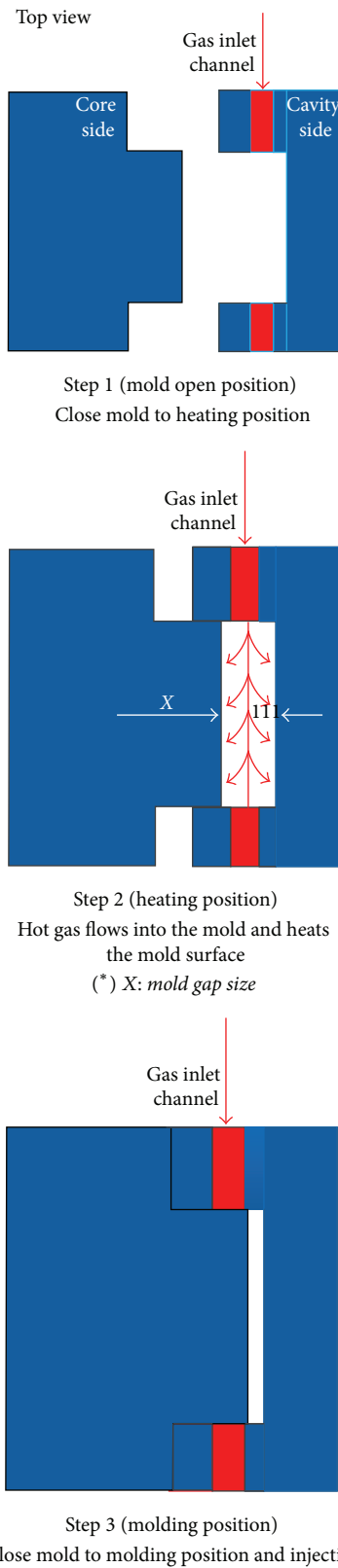


FIGURE 2: Mold position in the heating stage of GMTC process.

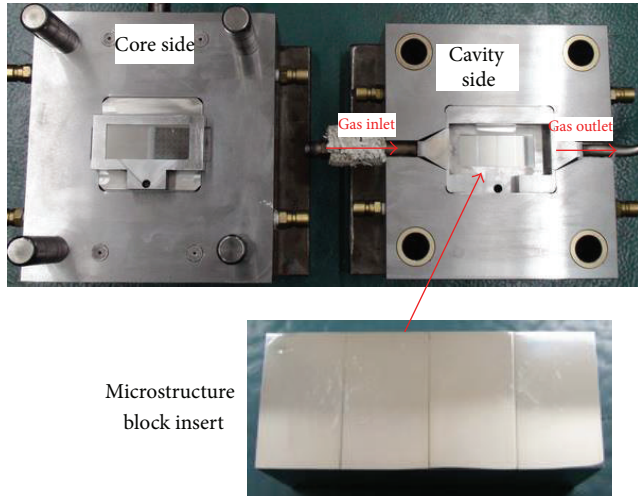


FIGURE 3: Experimental mold design and microstructure block insert.

TABLE 1: Experimental parameters for microinjection molding.

Material	ABS PA758
Glass transition temperature (°C)	105
Melt temperature (°C)	230
Mold temperature (°C)	70
Injection speed (mm/s)	50
Injection pressure (Mpa)	100
Packing time (s)	2.5
Gas heating temperature (°C)	500
Gas flow rate (l/min)	500
Mold gap size (mm)	5
Heating target temperature (°C)	90/100/110/120/130

For observing the heating effect of the microstructure, three types of temperature sensors were used.

Figure 5 shows the sensor positions: one near the cavity surface (Type A), one 0.3 mm beneath the groove (Type B), and one 0.3 mm (Type C) beneath the cavity surface. The temperature measurement was performed at the location of the three microgrooves (gas inlet, center, and gas outlet groove). The ABS PA758 plastic, which has a glass transition temperature of about 105°C, was used as the molding resin. The operating parameters are shown in Table 1.

### 3. Results and Discussions

**3.1. Effect of GMTC on the Heating Process.** The variation in the mold temperature (at the center area—Figure 5) versus time for a heating time of 50 s is described in Figure 6. For an initial mold temperature of 70°C, the GMTC can heat the temperature at the groove bottom to above 130°C. After approximately 2 seconds as the mold closes completely (Step 3 in Figure 2), the groove temperature will cool to about 110°C. This temperature value is higher than the glass transition temperature of ABS PA 758 material.

In our former study, when the GMTC was used for mold surface heating, there is a temperature difference between the inlet and outlet area [2, 15]. Therefore, in this research, to evaluate the uniformity of the heating process for various mold gap sizes, the temperature at the gas inlet area and the gas outlet area was collected. In previous research, the GMTC heated the mold surface very efficiently [2, 11]. However, in this research, because the GMTC is applied to improve the filling of the melt into the microgroove, the temperature at the bottom groove is collected and compared in Figure 7. Based on these results, the mold gap size has a clear impact on the temperature uniformity of the inlet and outlet area. When the mold gap size is larger, the difference in temperature between the inlet and outlet sensor was reduced. Figure 7 shows that the temperature difference is 44.3°C, 11.3°C, and 0.3°C when the mold gap size is 4 mm, 6 mm, and 8 mm, respectively. This result is in good agreement with our previous research [2, 15].

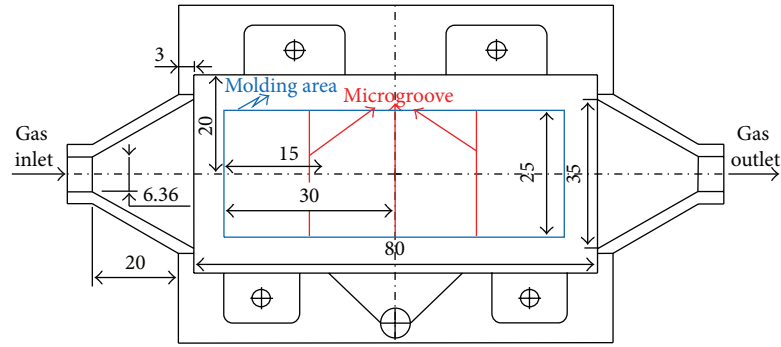
Using an infrared camera, the temperature distribution with the mold gap size of 4 mm, 6 mm, and 8 mm was observed and compared in Figure 8. In the heating process, this result also shows that a higher temperature is concentrated near the gas inlet gate. However, the larger the mold gap size is, the more uniform the temperature becomes. This result is in good agreement with Figure 7.

**3.2. Effect of Gas-Assisted Mold Surface Heating on the Microstructure.** For high aspect ratio microinjection molding, the mold surface temperature was heated from 70°C to the target temperatures of 90, 100, 110, 120, and 130°C. After heating, the mold plates required roughly two seconds to close. The injection molding cycle was then completed. After the molding cycle finished, the molded part was removed for measurement of the microribs. Figure 9 shows the molding product and the microstructure (micro rib).

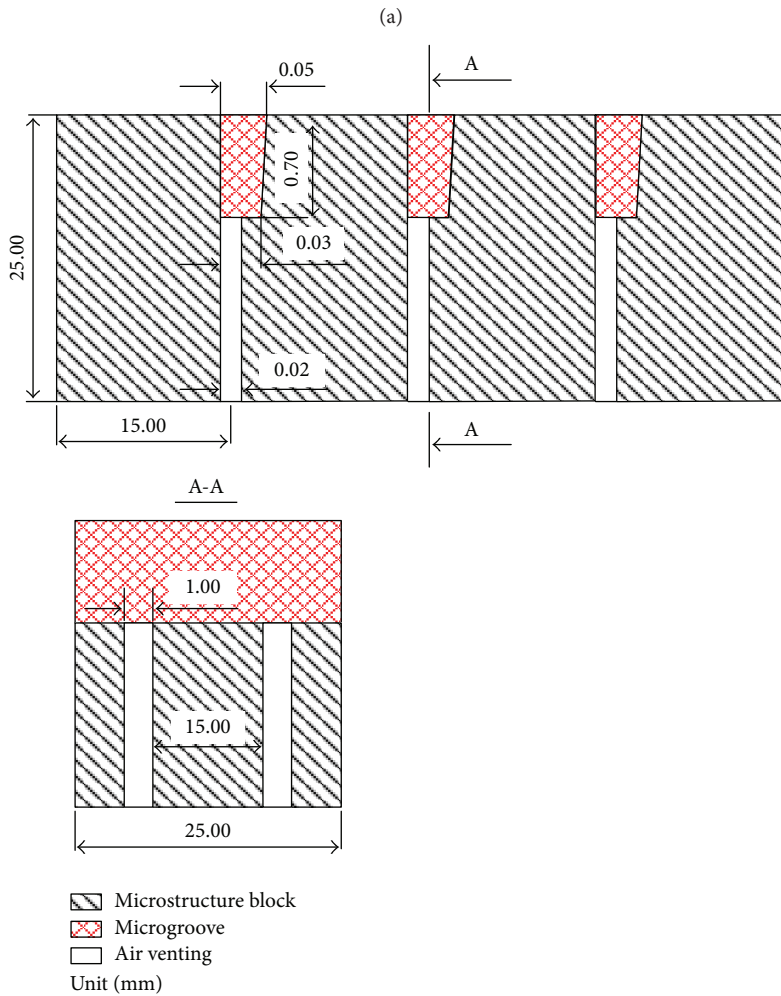
For the application of GMTC on the melt filling into the microgroove, a melt of ABS PA758 was injected into the cavity, with a mold temperature of 70°C. The molding conditions are shown in Table 1, where the part size is 60 mm × 25 mm × 1 mm. After molding, a height comparison of the micro rib was performed. With regular molding operations, the mold temperature is set at 70°C, meaning that the cavity temperature at the filling state remains at 80°C. With GMTC, the mold surface temperature can rise from 70°C to the heating target temperature. The mold then needs 2 s to close completely. The real mold surface temperature during the melt injection is about 230 ± 5°C.

Figure 10 shows a 3D laser microscope image of the center rib under different heating target temperatures. Based on these results, it is clear that without the GMTC, the height of the rib is only 212.37 μm. Using GMTC with its higher heating target temperatures, a higher rib can be reached. The highest rib is 640.38 μm when the heating target temperature is 130°C. This provides clear evidence of the effect of GMTC on high aspect ratio microinjection molding. In this study, the microgroove with a maximum depth of 700 μm can be filled to over 91% of its full height.

To observe the effect of temperature uniformity on the height of the microribs, using the same molding process as in



Unit (mm)

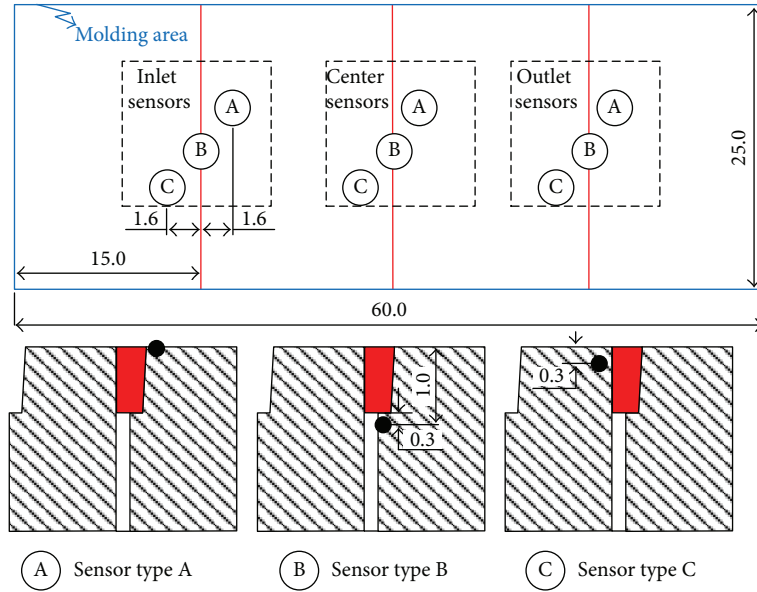


(b)

FIGURE 4: Dimensions of microstructure block insert (a) and microstructure block insert (b).

Table 1, the rib height was measured under different heating target temperatures. The results are shown in Table 2 and compared in Figure 11. At a mold temperature of 70°C, the center rib (at point P2) is the highest (212.37 μm), while the left and right side ribs (Figure 11) are clearly lower. In the next case, when the mold surface was preheated to 90°C, the height

of the center rib increases slightly. However, with the left and right side ribs, the height has a significant improvement (87% higher than without GMTC). This strength is maintained as the heating target temperature rises to 130°C. At this temperature target, all ribs were filled to over 91% of the full height.



Unit (mm)

FIGURE 5: Sensor location.

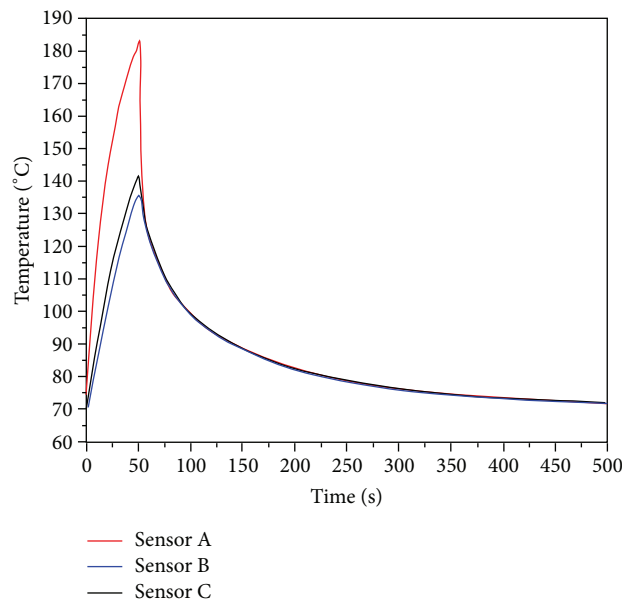


FIGURE 6: Temperature history with gas heating and water cooling of center sensors.

TABLE 2: Experimental results for the microstructure.

Heating target temperature	Height of the microstructure ( $\mu\text{m}$ )		
	P1	P2	P3
70°C	123.75	212.37	98.31
90°C	231.75	245.88	205.47
100°C	324.91	322.27	302.57
110°C	535.58	430.88	424.18
120°C	640.46	615.91	600.31
130°C	668.59	640.38	618.76

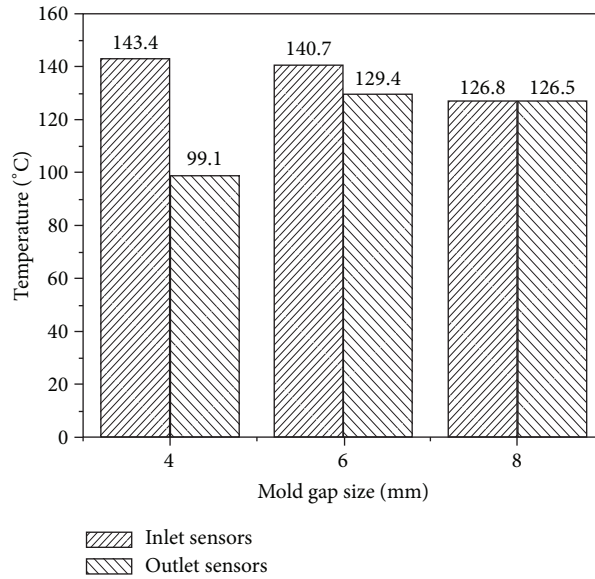


FIGURE 7: Comparisons of heating uniformity results for the various gas inlet designs (initial temperature: 70°C, heating time: 50 seconds, sensor type B).

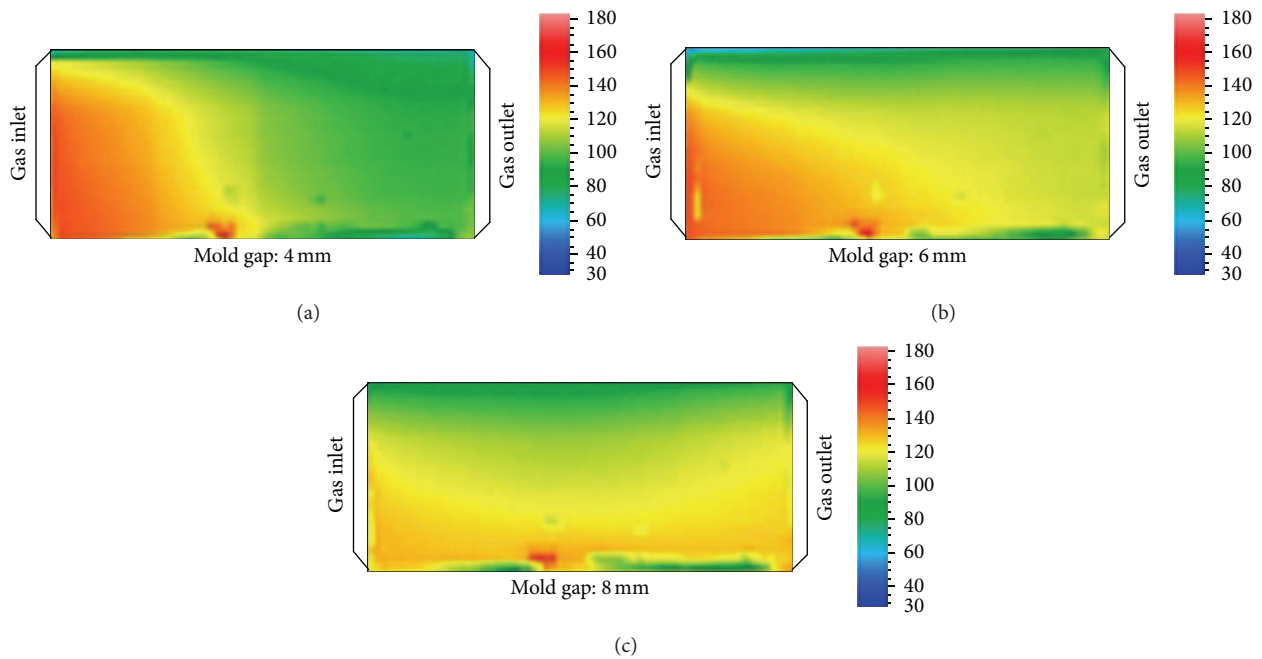


FIGURE 8: Temperature distribution of the molding area with an initial temperature of 70°C, a gas temperature of 500°C, a gas flow rate of 400 l/min, and a heating time of 50 s.

Comparison of the height of the ribs shows that without heating, the center rib is the highest, and the left and right side ribs are much lower. This is because in this part design, the center rib is closest to the injection gate. Therefore, the filling pressure and the packing pressure are much higher than for the other ribs. This difference in height negatively affects product quality. However, this difference was reduced when the GMTC was used at target temperatures of 90°C and 100°C. This result may be explained by the temperature distribution

at the end of the heating step as shown in Figure 8. Using the GMTC, the molding area was heated and the filling step of the molding cycle was assisted. Therefore, melt filled into the groove more easily, resulting in higher ribs with better rib uniformity. When the heating target temperature exceeded 100°C, the height of the three ribs increased continuously. However, the left side rib (at point P1) became the highest. This result is due to the heating effect of the GMTC. In this case, the surface temperature near the gas inlet is higher than

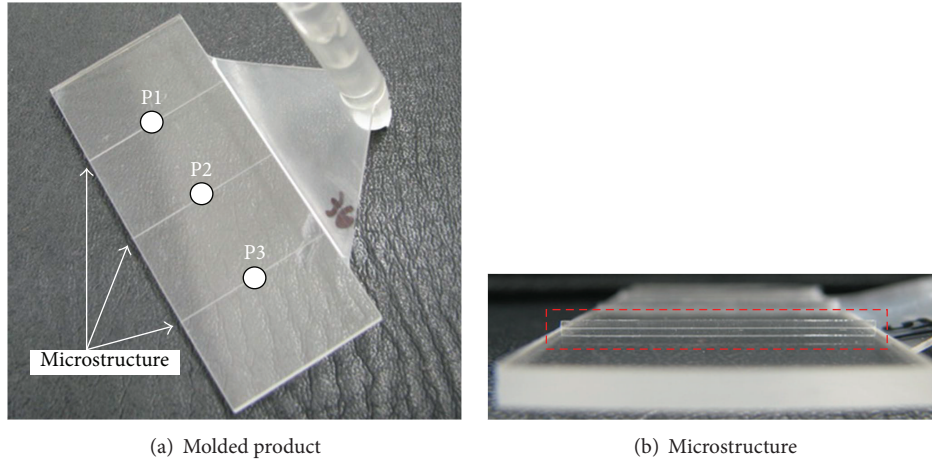


FIGURE 9: Molded product (a) and microstructure (b).

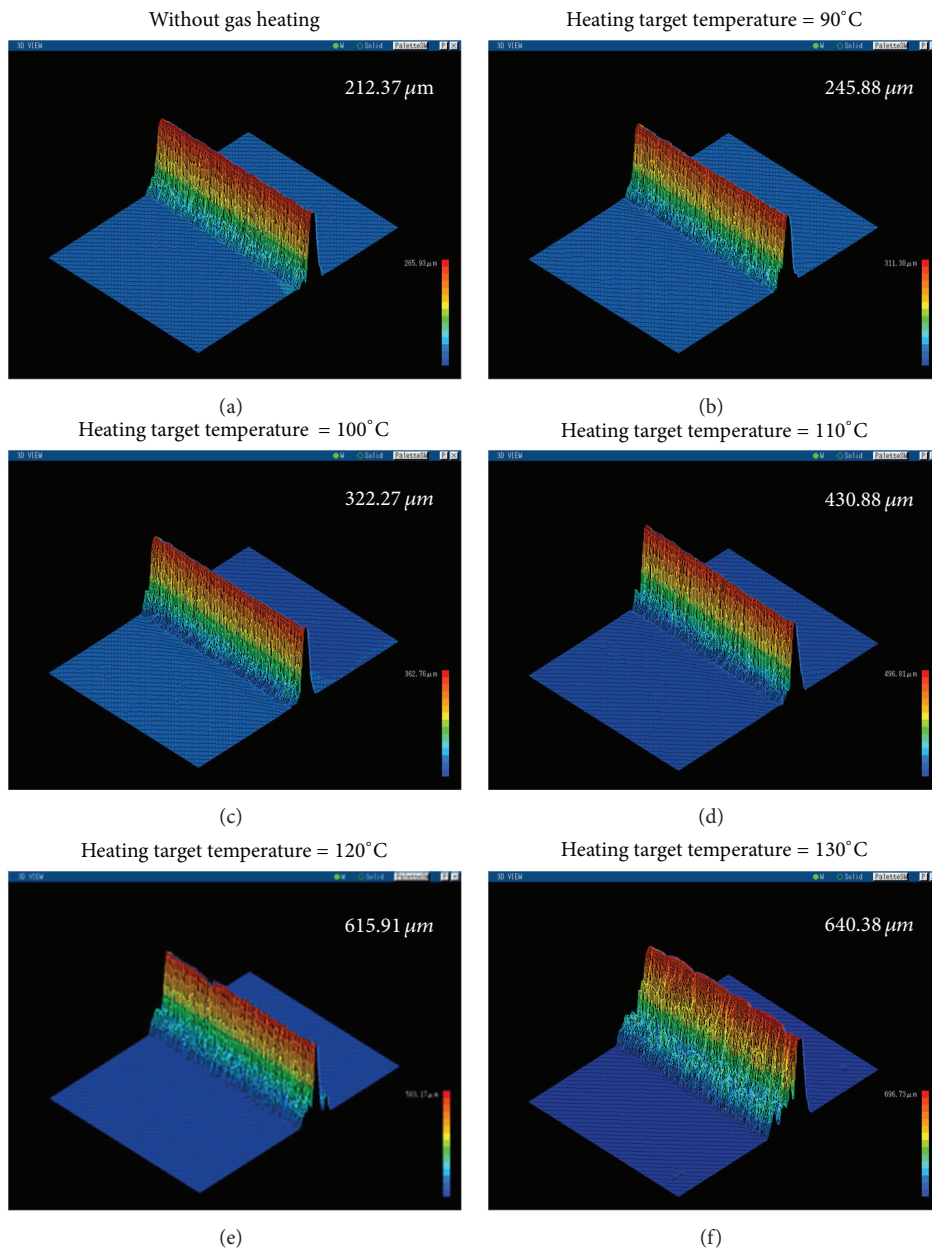


FIGURE 10: 3D laser microscope images of the plastic stamp at the center point.

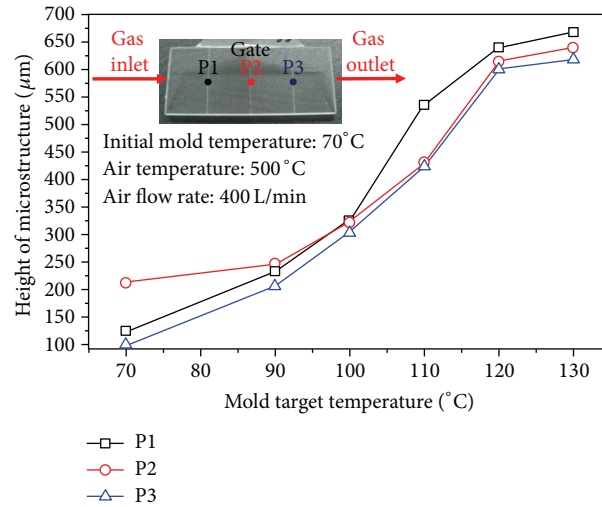


FIGURE 11: Height of micro-structure at different heating target temperatures.

the other areas, meaning that the melt filled into the left side rib more easily than into the other two ribs.

#### 4. Conclusions

In this study, a gas-assisted mold surface heating system combined with water-cooling to achieve rapid mold temperature control for microstructure injection molding was established. The effect of GMTC and the uniformity of the rib height were evaluated. Based on the results, the following conclusions were obtained.

- (i) The mold gap size at the heating position can affect the heating speed and heating uniformity.
- (ii) By using the GMTC for preheating, the temperature of the microgroove can be higher than the glass transition temperature of ABS PA 758.
- (iii) The application of hot gas heating could improve the height of the microrib to 91% of the maximum height of 700  $\mu\text{m}$  (640.38  $\mu\text{m}$ ).
- (iv) At heating target temperatures of 90°C and 100°C, the uniformity of the rib was improved. However, when the heating target temperature exceeded 100°C, the left side rib became higher than the other two ribs.

#### Acknowledgment

This research was supported by the Center-of-Excellence Program on Membrane Technology of the Ministry of Education and the R&D Center for Mold and Molding Technology.

#### References

- [1] K.-Y. Lin, F.-A. Chang, and S.-J. Liu, "Using differential mold temperatures to improve the residual wall thickness uniformity around curved sections of fluid assisted injection molded tubes," *International Communications in Heat and Mass Transfer*, vol. 36, no. 5, pp. 491–497, 2009.
- [2] S.-C. Chen, P. S. Minh, and J.-A. Chang, "Gas-assisted mold temperature control for improving the quality of injection molded parts with fiber additives," *International Communications in Heat and Mass Transfer*, vol. 38, no. 3, pp. 304–312, 2011.
- [3] K.-M. Tsai, C.-Y. Hsieh, and W.-C. Lo, "A study of the effects of process parameters for injection molding on surface quality of optical lenses," *Journal of Materials Processing Technology*, vol. 209, no. 7, pp. 3469–3477, 2009.
- [4] C.-H. Wu and W.-S. Chen, "Injection molding and injection compression molding of three-beam grating of DVD pickup lens," *Sensors and Actuators A*, vol. 125, no. 2, pp. 367–375, 2006.
- [5] V. Kalima, J. Pietarinen, S. Siitonen et al., "Transparent thermoplastics: replication of diffractive optical elements using micro-injection molding," *Optical Materials*, vol. 30, no. 2, pp. 285–291, 2007.
- [6] C. Khan Malek, L. Robert, G. Michel, A. Singh, M. Sahli, and B. G. Manuel, "High resolution thermoplastic rapid manufacturing using injection moulding with SU-8 based silicon tools," *CIRP Journal of Manufacturing Science and Technology*, vol. 4, no. 4, pp. 382–390, 2011.
- [7] M. Vázquez and B. Paull, "Review on recent and advanced applications of monoliths and related porous polymer gels in micro-fluidic devices," *Analytica Chimica Acta*, vol. 668, no. 2, pp. 100–113, 2010.
- [8] G. Lucchetta, M. Fiorotto, and P. F. Bariani, "Influence of rapid mold temperature variation on surface topography replication and appearance of injection-molded parts," *CIRP Annals*, 2012.
- [9] W. Guilong, Z. Guoqun, L. Huiping, and G. Yanjin, "Analysis of thermal cycling efficiency and optimal design of heating/cooling systems for rapid heat cycle injection molding process," *Materials & Design*, vol. 31, no. 7, pp. 3426–3441, 2010.
- [10] M.-S. Huang and Y.-L. Huang, "Effect of multi-layered induction coils on efficiency and uniformity of surface heating," *International Journal of Heat and Mass Transfer*, vol. 53, no. 11–12, pp. 2414–2423, 2010.
- [11] W.-B. Kim and S.-J. Na, "A study of residual stresses in the surface hardening of a blade mould by high frequency induction heating," *Surface and Coatings Technology*, vol. 58, no. 2, pp. 129–136, 1993.

- [12] S.-C. Chen, W.-R. Jong, Y.-J. Chang, J.-A. Chang, and J.-C. Cin, "Rapid mold temperature variation for assisting the micro injection of high aspect ratio micro-feature parts using induction heating technology," *Journal of Micromechanics and Microengineering*, vol. 16, no. 9, pp. 1783–1791, 2006.
- [13] D. Yao, T. E. Kimerling, and B. Kim, "High-frequency proximity heating for injection molding applications," *Polymer Engineering and Science*, vol. 46, no. 7, pp. 938–945, 2006.
- [14] S.-C. Chen, P. S. Minh, J.-A. Chang, S.-W. Huang, and C.-H. Huang, "Mold temperature control using high-frequency proximity effect induced heating," *International Communications in Heat and Mass Transfer*, vol. 39, no. 2, pp. 216–223, 2012.
- [15] S.-C. Chen, R.-D. Chien, S.-H. Lin, M.-C. Lin, and J.-A. Chang, "Feasibility evaluation of gas-assisted heating for mold surface temperature control during injection molding process," *International Communications in Heat and Mass Transfer*, vol. 36, no. 8, pp. 806–812, 2009.
- [16] J. A. Chang, *Investigation on the establishment and analyses of rapid mold surface temperature control using gas-assisted heating [Ph.D. thesis]*, 2008.

## Research Article

# An Experimental Investigation of Residual Stresses in High-Speed End Milling 7050-T7451 Aluminum Alloy

Xiaoming Huang,<sup>1</sup> Jie Sun,<sup>1</sup> Jianfeng Li,<sup>1</sup> Xiong Han,<sup>2</sup> and Qingchun Xiong<sup>2</sup>

<sup>1</sup> School of Mechanical Engineering, Shandong University, Jinan 250061, China

<sup>2</sup> Chengdu Aircraft Industrial Group (CAC) Co. Ltd., Chengdu 610092, China

Correspondence should be addressed to Jie Sun; sunjie@sdu.edu.cn

Received 29 May 2013; Revised 3 August 2013; Accepted 19 August 2013

Academic Editor: Feng Jiang

Copyright © 2013 Xiaoming Huang et al. This is an open access article distributed under the Creative Commons Attribution License, which permits unrestricted use, distribution, and reproduction in any medium, provided the original work is properly cited.

A high-speed milling experiment by means of orthogonal method with four factors was conducted for aluminum alloy 7050-T7451. The residual stresses (RS) on the surface and subsurface of the work piece were measured using X-ray diffraction technique and electropolishing technology. The exponent's mathematical model for milling residual stress of 7050-T7451 aluminum alloy was established related to machining parameters. The predicted values were compared with the data from experiments. The effect of cutting speed, feed rate, and width and depth of cut on residual stress was investigated using the ANOVA techniques. The affecting degree of milling parameters are shown as  $v > f_z > a_p > a_e$  in order. The influence trend of milling factors on residual stresses was also studied; the machine-induced residual compressive stresses tend to decline with the increase of cutting speed and decrease of the feed rate.

## 1. Introduction

7050-T7451 aluminium alloy has been widely used in aircraft structures due to their perfect strength, fracture toughness, and high stress/density ratio after supersaturated solid solution and prestretching treatment [1, 2]. High-speed milling is one of the most common processes to produce structural parts out of aluminum in the aerospace industry, where removing huge volume of material is essential. It is known that machining process creates residual stress on the surface of machined components, and the residual stress state can significantly extend or shorten the work pieces' lifetime by influencing fatigue strength, creep, and stress-corrosion-cracking resistance. In addition, machining-induced RS has, especially, important effects on part distortion for thin monolithic aerospace components [3].

Residual stresses can be attributed to mechanical and thermal loads, which occur in an interdependent manner during machining processes. Their combination determines the final residual stress state of the workpiece. Different researchers have carried out experimental investigations in order to study the influence of the machining parameters, tool

geometry, cutting edge geometry, tool wear, and cutting tool material on the residual stresses.

In order to analyze and control the residual stress, finite element methods [4, 5], numerical methods [6, 7], and experimental methods [8] are used to predict and evaluate the residual stress distribution. Since the pioneering works in 1950s, a substantial amount of experimental work has accumulated regarding the development of residual stresses as a function of the machining process [9, 10]. Jang et al. [11] studied the effects of different machining parameters on surface residual stress when turning AISI 304 stainless steel, and tool-edge radius was found to have the most significant effect on residual stress. M'Saoubi et al. [12] analyzed the residual stress in orthogonal machining of standard and resulfurized AISI 316L steels, and that high tensile residual stress values of around 800 MPa are found in the workpiece surface. Yang et al. [13] investigated the machined residual stress of Ti-6Al-4V and found that residual stress on the ground surfaces had a larger scatter than that of the face turned ones in a statistical sense. Sharman et al. [14] studied the influence of coated and uncoated WC tools on the residual stresses, and the results showed that the surface produced

with the coated tool had higher tensile stress (up to 747 MPa) than the corresponding surface cut with the uncoated tool. Devillez et al. [15] compared the residual stress profile with dry and wet machining conditions for three different cutting speeds.

There is limited study on the effect of machining processes on residual stresses in aluminum alloys. Fuh and Wu [16] proposed the tool nose radius, cutting speed, and flank wear had the most significant effects on the residual stresses of aluminum alloy 2014-T6. Tang et al. [17] studied the influence of tool flank wear on residual stress of aluminum alloy 7050-T7451, the results revealed that the small flank wear produced lower compressive stresses on the surface and the stresses shifted to tensile state with an increase in the flank wear. Denkena et al. [18] analyzed the influence of the cutting edge geometry on residual stress of a forged aluminum alloy 7449-T7651.

Most researchers focus on the effect of tool wear and cutting edge geometry on the residual stresses in turning and grinding. It is very critical to find a fast and precise solution to predict residual stresses in a high-speed milled component given the process parameters and material properties. Therefore, a comprehensive study of the influence of machining conditions on residual stresses in high strength aluminum alloys is necessary in the manufacture of large and thin monolithic aerospace components. The objective of this research is to study the relation of machined-induced residual stresses and the end milling parameters of 7050-T7451 aluminum alloy. In this study, the experimental setup is described in Section 2, in Section 3, a mathematical model for milling residual stress was established and the effect of machining parameters on RS was discussed, finally conclusions are given in Section 4.

## 2. Experimental Setup and Procedure

**2.1. Work Material.** The block used in this experiment was manufactured by Kaiser Aluminum and Chemical Corp., USA. The mechanical properties of the material are given in Table 1.

**2.2. Experimental Design.** Experiments based on orthogonal methods were performed to reduce variations in the output response. Factorial design was applied with 4 factors and 4 levels ( $4^4$  designs), factors consist of cutting speed ( $v$ ), feed rate ( $f_z$ ), width of cut ( $a_e$ ), and depth of cut ( $a_p$ ). The details are shown in Table 2. Values of cutting speed above 300 m/min were chosen so that it falls in the range of high-speed machining. The values of the feed rate, width of cut, and depth of cut were selected based on the available information of the factory manufacture and cutting tool manufacturer's catalogue.

**2.3. Cutting Tools and Machine Tool.** Milling test was performed on a DECKEL MAHO DMU 70V 5-axis universal machining center, and the tool was end mill without coating. The detailed values of the experiment conditions were presented in Table 3. The experiment setup is shown in Figure 1,

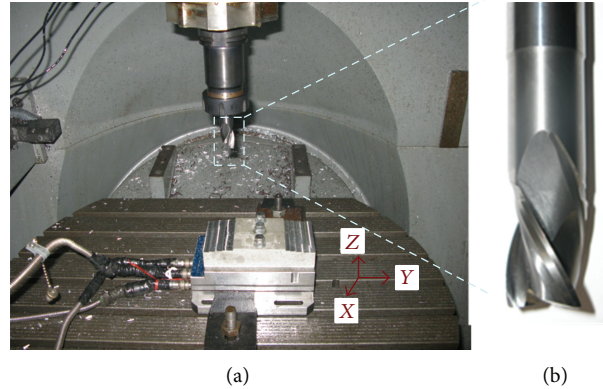


FIGURE 1: Experimental setup: (a) DECKEL MAHO DMU 70V. (b) Cutting tool.

X and Y denote the feed direction and perpendicular to the feed direction, respectively.

**2.4. Residual Stress Measurement.** The residual stress state in machined surfaces was analyzed by X-Ray diffraction technique (XRD) as shown in Figure 2. An approach based on the combination of psi-oscillation and phi-oscillation was adopted to obtain more accurate measurement results, for the results are usually invalid when measuring aluminum alloy materials due to its grains' apparent preferred orientation [19]. The parameters used in the Stresstech Group's XSTRESS 3000 analyzer are listed in Table 4. Under these conditions, the maximal penetration depth of the radiation amounts to  $z = 11 \mu\text{m}$ .

In order to determine the in-depth residual stresses, the surface material was removed layer by layer using an electropolishing method. The removed layer thickness can be determined using electronic digital micron indicator (about  $8 \mu\text{m}$  for each measurement). There were 4 points with the equal distance of 15 mm in the middle of each machined surface, which are the residual stresses testing points and they take the average value as analysis data to ensure the accuracy of the measurement.

## 3. Results and Discussion

**3.1. Machine-Induced Residual Stresses.** The profile of the residual stresses below the surface was obtained by electropolishing layer removals up to  $100 \mu\text{m}$ . Compressive residual stresses were found on the machined surface in each case. The residual stresses in feed direction were generally greater than that in cutting direction, with values around 20 MPa. The level of compressive stresses increased continuously with depth up to a maximum value in depth of about  $25 \mu\text{m}$  and then stabilized at a level corresponding to the state of the material before machining, this being true for both the feed and the cutting directions. Figure 3 represents a typical residual stress distribution obtained for a cutting speed of 628 m/min, feed rate of 0.06 mm/z, and depth of cut and width of cut were 5 mm and 12 mm.

TABLE 1: Mechanical properties of 7050-T7451.

Modulus of elasticity	Tensile yield strength	Shear strength	Hardness	Thermal conductivity	Specific heat capacity	Density
71.7 GPa	469 MPa	303 MPa	140 HB	157 W/m°C	0.86 J/g°C	2.83 g/mm <sup>3</sup>

TABLE 2: Orthogonal experiment parameters.

Level	$v$ (m/min)	$f_z$ (mm/z)	$a_p$ (mm)	$a_e$ (mm)
1	314	0.06	3	6
2	502	0.10	4	8
3	628	0.14	5	10
4	942	0.18	6	12

TABLE 3: The experiment conditions.

Machine tool	DECKEL MAHO DMU 70V 5-axis universal machining center	
	Max power	15 KW
	Max spindle speed	18000 rpm
Machining state	Dry, down milling	
Tool	Tool material	Solid cemented carbide
	Number of teeth	3
	Rake angle	14°
	Diameter	20 mm
	Relief angle	12°
	Helix angle	30°
	Corner radius	1 mm
		4 mm

TABLE 4: Residual stress measurement parameters.

Measurement method	$\sin^2\psi$
Radiation	$CrK\alpha$
Spot size	3 mm
$\psi$	0°, ±24.1°, ±35.3, ±45°
$\phi$	0°, ±5°, ±10°
Lattice plane	{311}
Bragg angle $2\theta$	139.3°

Because of the high stress gradient, the arithmetic mean stress ( $\bar{\sigma}$ ) in the residual stress affected zone was obtained to characterize the machine-induced RS according to the following calculation:

$$\bar{\sigma} = \frac{\int_0^{L_z} \sigma dz}{L_z}, \quad (1)$$

where  $L_z$  is the thickness of the machine-induced stress below the surface. The results were calculated using commercial software Origin 8.0 and listed in Table 5.

**3.2. Regression Equation and ANOVA Significance Testing.** Table 5 shows the orthogonal experiment schemes and experiment results, it can be found that there is a complex

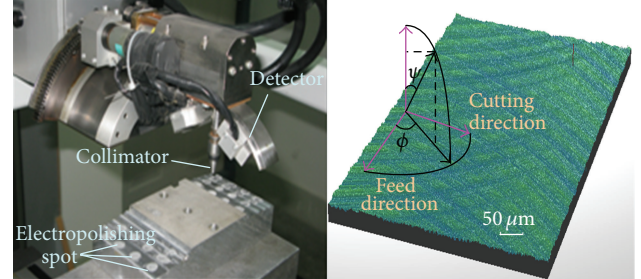


FIGURE 2: Residual stress measurement setup and schematic of diffraction planes.

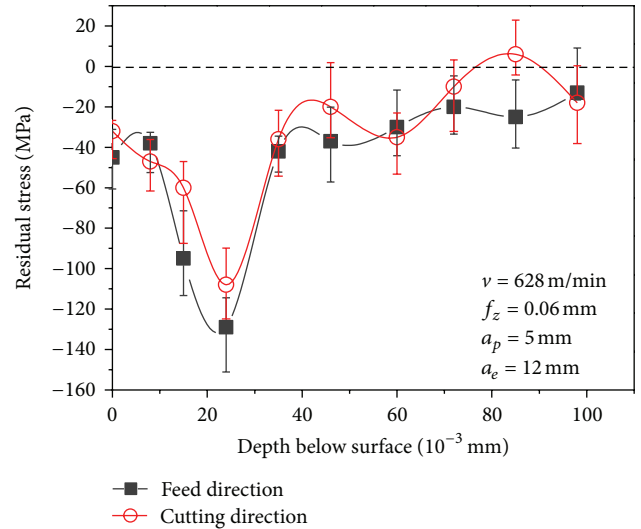


FIGURE 3: Residual stresses depth profiles in machining 7050-T7451.

relationship between cutting parameters and residual stress in the milling process. It is important to put the relation between residual stresses and the machining parameters in a mathematical form by obtaining the results. Therefore, a mathematical model between machining parameters and the residual stresses was as follows:

$$\bar{\sigma} = C v^{b_1} f_z^{b_2} a_p^{b_3} a_e^{b_4}, \quad (2)$$

where  $\bar{\sigma}$  is the arithmetic mean stress;  $C$  is stress coefficient depending on workpiece material, machine tool, and cutting tool geometry parameter;  $b_1$ ,  $b_2$ ,  $b_3$ , and  $b_4$  are exponents of  $v$ ,  $f_z$ ,  $a_p$  and  $a_e$ , respectively. The empirical equations of residual stress could be achieved based on multiple linear regression analysis, as shown (3) and (4).

TABLE 5: Orthogonal experiment schemes and experiment results.

No.	$\nu$ (m/min)	$f_z$ (mm/z)	$a_p$ (mm)	$a_e$ (mm)	$\bar{\sigma}_x$ (MPa)	$\bar{\sigma}_y$ (MPa)
1	314	0.06	3	6	-64.83	-55.37
2	314	0.18	6	12	-112.02	-83.41
3	314	0.1	4	8	-86.42	-69.02
4	314	0.14	5	10	-91.79	-85.68
5	502	0.06	4	10	-63.56	-45.49
6	502	0.1	3	12	-78.40	-57.50
7	502	0.14	6	6	-74.52	-66.32
8	502	0.18	5	8	-83.60	-78.53
9	628	0.06	5	12	-59.18	-44.83
10	628	0.1	6	10	-70.35	-52.45
11	628	0.14	3	8	-62.38	-45.57
12	628	0.18	4	6	-75.93	-59.24
13	942	0.06	6	8	-57.57	-30.85
14	942	0.1	5	6	-54.38	-37.59
15	942	0.14	4	12	-70.17	-48.25
16	942	0.18	3	10	-67.72	-47.69

Consider

$$\bar{\sigma}_x = -907.2451\nu^{-0.3950} f_z^{0.2193} a_p^{0.1524} a_e^{0.1027}, \quad (3)$$

$$\bar{\sigma}_y = -1873.5618\nu^{-0.4835} f_z^{0.3813} a_p^{0.1246} a_e^{0.0877}. \quad (4)$$

The residual stresses in the feed direction were evaluated using (3). Rank in order of the experimental measured RS and compared with the predicted RS of the samples. The scatterplot between them in Figure 4 indicated that the experimental and calculated values were matched reasonably with minimal errors.

An analysis of variance (ANOVA) for residual stresses was shown in Table 6. The ANOVA results indicated that the most significant factor affected by RS was cutting speed as shown  $F$  value of 40.6 and 29.27 for  $\bar{\sigma}_x$  and  $\bar{\sigma}_y$  at the level of 0.05. The affecting degree of the parameters was described as  $\nu > f_z > a_p > a_e$  in order.  $F$  value of the cutting direction is less than feed direction, this is because RS in cutting direction is less than feed direction and is affected by the noise signal more seriously.

**3.3. Influence of the Machining Parameters on Residual Stress.** Figure 5 shows the influence of the machining parameters on the arithmetic mean RS values by the range analysis taking into account the four parameters reported above, it is possible to describe how the RS are affected both for the feed and cutting directions.

Figure 5(a) shows that at an increase of the cutting speed from  $\nu = 314$  m/min to  $\nu = 628$  m/min causes a linear reduction of the compressive residual stresses, beyond this cutting speed, the reduced rate slows down. The observed effect may be explained from understanding of the quantum of heat dissipation that determines the nature of plastic deformation in the machining. At the lowest cutting speed of 314 m/min, the chips stay in the machining zone for a relatively longer duration than at the cutting speed of

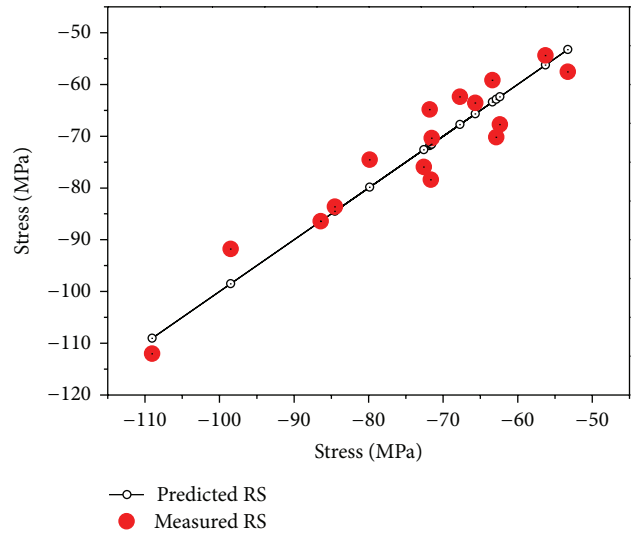


FIGURE 4: Scatter plots of the measured RS and the predicted RS of the multiple regression prediction model of  $\bar{\sigma}_x$ .

628 m/min. The heat accumulation in the chips is more, so less heat dissipates into the machined surface. It leads to increase of compressive residual stresses in the machined surface. The trends depicted in Figure 5 are similar to those obtained during the high-speed face milling of Ti-6Al-4V alloy [20].

An increase of the feed rate  $f_z$  from 0.06 mm/tooth to 0.1 mm/tooth leads to a pronounced effect on the residual stress, see Figure 5(b). But, further increase in the feed rate to 0.18 mm/tooth shows a small increase in the compressive residual stresses, and residual stress values remain nearly constant of 70 MPa for feed direction. An explanation for these observations can be found in the analysis of the cutting forces, due to the increase of the feed higher machining forces can be observed [18]. The increased cutting force and more

TABLE 6: Significance testing of the machining parameters on RS.

Factors	Sum of squares		DF	Mean of squares		F		Major-minor order of factors
	$\bar{\sigma}_x$	$\bar{\sigma}_y$		$\bar{\sigma}_x$	$\bar{\sigma}_y$	$\bar{\sigma}_x$	$\bar{\sigma}_y$	
$v$	1599.3	2348.9	3	533.1	782.9	40.60	29.27	$v > f_z > a_p > a_e$
$f_z$	1119.4	1190.6	3	373.1	396.9	28.42	14.84	
$a_p$	218.29	220.6	3	72.8	73.5	5.54	2.75	
$a_e$	117.6	371	3	39.2	12.4	2.98	0.46	
Error	39.4	80.3	3	13.1	26.7			
Total	3294.0	3877.5	15					

Notes:  $F_{0.05}(3, 3) = 9.28$ .

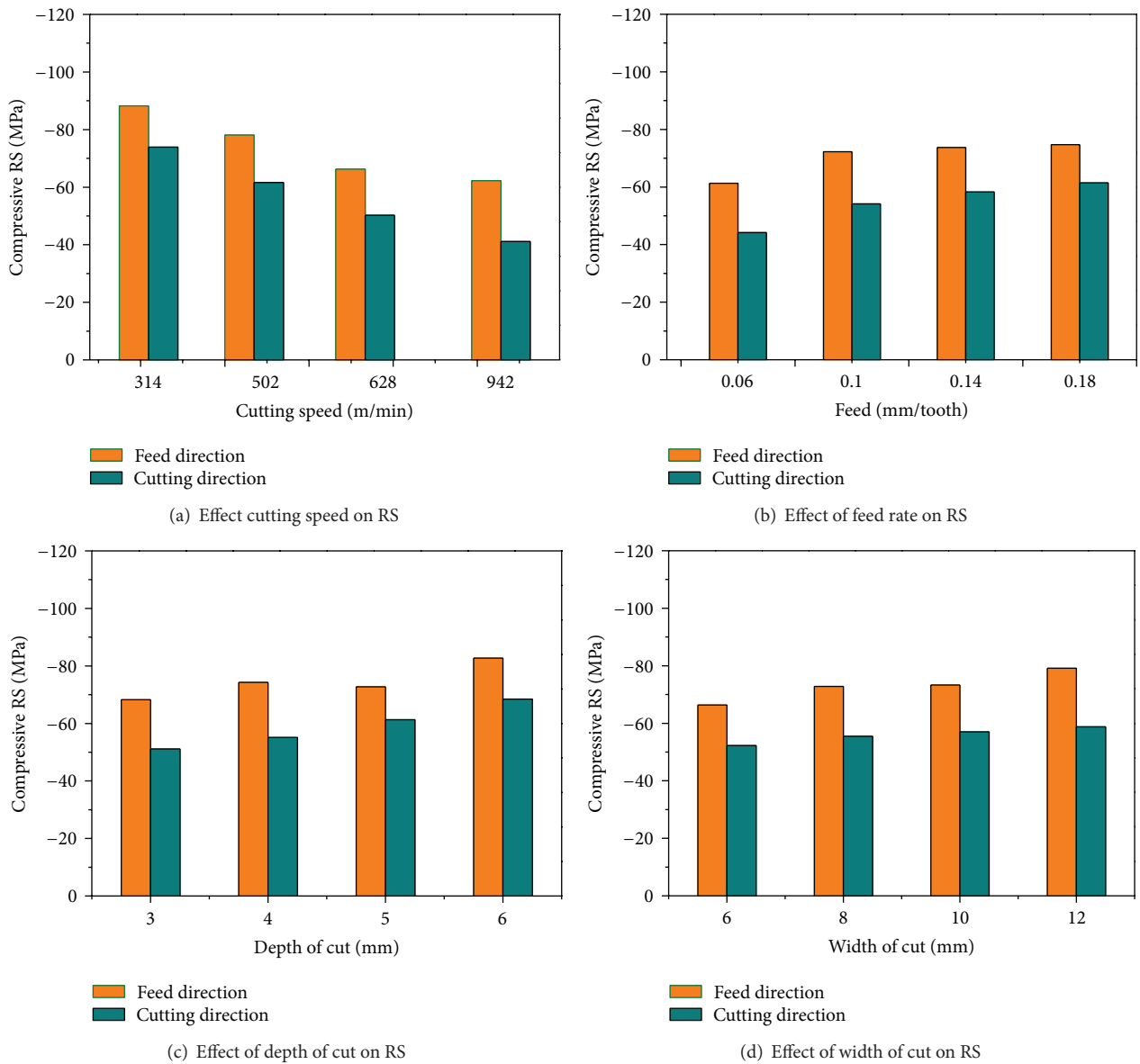


FIGURE 5: Range analysis of residual stress.

plastic deformation were generated with the increasing of feed rate.

Figure 5(c) shows that a fluctuating variation of the compressive residual stresses in the surface and subsurface is the consequence of an increase of the depth of cut from  $a_p = 3$  mm to  $a_p = 6$  mm. A variation of the cutting depth causes a direct proportional increase of the forces. At the same time, cutting temperature increases with more cutting heat, it is envisaged that the effect of cutting force goes hand-in-hand with the cutting temperature change in the RS. Further, the chart of Figure 5(d) shows that the width of cut does not present obvious influence on the arithmetic mean compressive residual stress.

#### 4. Conclusions

The influence of machining parameters on the final residual stress within the subsurface zone of 7050-T7451 aluminum alloy was investigated by orthogonal experiment. The important conclusion drawn from the present research was summarized as follows.

- (1) The solid carbide end mill cutting tool induces compressive residual stresses on material when they were used in high-speed milling manufacture. The residual stresses in feed direction were higher than that in cutting direction.
- (2) The surface stresses could be predicted effectively by applying cutting speed, feed rate, depth of cut, width of cut, and their interactions in the multiple regression exponent models. Their affecting degree diminishes in order, described as  $v > f_z > a_p > a_e$  based on the ANOVA analysis of orthogonal experiment.
- (3) It has been shown that decrease of the cutting speed and increase of the feed rate lead to significant increase of compressive residual stresses on 7050-T7451 finished surface. To some extent, the analysis of the machining forces and thermal effects provides explanations for the observed residual stress transformation trends.

#### Acknowledgments

The authors acknowledge the support from the National Natural Science Foundation of China (Grant no. 51275277) and the school-enterprise collaboration project (Grant no. (11)-018).

#### References

- [1] A. Heinz, A. Haszler, C. Keidel, S. Moldenhauer, R. Benedictus, and W. S. Miller, "Recent development in aluminium alloys for aerospace applications," *Materials Science and Engineering A*, vol. 280, no. 1, pp. 102–107, 2000.
- [2] R. Bao and X. Zhang, "Fatigue crack growth behaviour and life prediction for 2324-T39 and 7050-T7451 aluminium alloys under truncated load spectra," *International Journal of Fatigue*, vol. 32, no. 7, pp. 1180–1189, 2010.
- [3] J.-F. Chatelain, J.-F. Lalonde, and A. S. Tahan, "A comparison of the distortion of machined parts resulting from residual stresses within workpieces," in *Proceedings of the 4th International Conference on Manufacturing Engineering, Quality and Production Systems (MEQAPS '11)*, pp. 79–84, Barcelona, Spain, September 2011.
- [4] W. J. Zong, D. Li, K. Cheng, T. Sun, and Y. C. Liang, "Finite element optimization of diamond tool geometry and cutting-process parameters based on surface residual stresses," *International Journal of Advanced Manufacturing Technology*, vol. 32, no. 7-8, pp. 666–674, 2007.
- [5] T. Özel and E. Zeren, "Finite element modeling the influence of edge roundness on the stress and temperature fields induced by high-speed machining," *International Journal of Advanced Manufacturing Technology*, vol. 35, no. 3-4, pp. 255–267, 2007.
- [6] M. H. El-Axir, "A method of modeling residual stress distribution in turning for different materials," *International Journal of Machine Tools and Manufacture*, vol. 42, no. 9, pp. 1055–1063, 2002.
- [7] D. Ulutan, B. E. Alaca, and I. Lazoglu, "Analytical modelling of residual stresses in machining," *Journal of Materials Processing Technology*, vol. 183, no. 1, pp. 77–87, 2007.
- [8] B. Coto, V. G. Navas, O. Gonzalo, A. Aranzabe, and C. Sanz, "Influences of turning parameters in surface residual stresses in AISI 4340 steel," *International Journal of Advanced Manufacturing Technology*, vol. 53, no. 9–12, pp. 911–919, 2011.
- [9] E. K. Henriksen, "Residual stresses in machined surfaces," *Transactions of the American Society of Mechanical Engineers*, vol. 73, pp. 265–278, 1951.
- [10] E. Brinksmeier, J. T. Cammett, W. König, P. Leskovic, J. Peters, and H. K. Tönshoff, "Residual stresses-measurement and causes in machining processes," *CIRP Annals*, vol. 31, no. 2, pp. 491–510, 1982.
- [11] D. Y. Jang, T. R. Watkins, K. J. Kozaczek, C. R. Hubbard, and O. B. Cavin, "Surface residual stresses in machined austenitic stainless steel," *Wear*, vol. 194, no. 1-2, pp. 168–173, 1996.
- [12] R. M'Saoubi, J. C. Outeiro, B. Changeux, J. L. Lebrun, and A. Morão Dias, "Residual stress analysis in orthogonal machining of standard and resulfurized AISI 316L steels," *Journal of Materials Processing Technology*, vol. 96, no. 1-3, pp. 225–233, 1999.
- [13] X. Yang, C. R. Liu, and A. F. Grandt, "An experimental study on fatigue life variance, residual stress variance, and their correlation of face-turned and ground Ti 6Al-4V samples," *Journal of Manufacturing Science and Engineering, Transactions of the ASME*, vol. 124, no. 4, pp. 809–819, 2002.
- [14] A. R. C. Sharman, J. I. Hughes, and K. Ridgway, "An analysis of the residual stresses generated in Inconel 718 when turning," *Journal of Materials Processing Technology*, vol. 173, no. 3, pp. 359–367, 2006.
- [15] A. Devillez, G. Le Coz, S. Dominiak, and D. Dudzinski, "Dry machining of Inconel 718, workpiece surface integrity," *Journal of Materials Processing Technology*, vol. 211, no. 10, pp. 1590–1598, 2011.
- [16] K.-H. Fuh and C.-F. Wu, "A residual-stress model for the milling of aluminum alloy (2014-T6)," *Journal of Materials Processing Technology*, vol. 51, no. 1-4, pp. 87–105, 1995.
- [17] Z. T. Tang, Z. Q. Liu, Y. Z. Pan, Y. Wan, and X. Ai, "The influence of tool flank wear on residual stresses induced by milling aluminum alloy," *Journal of Materials Processing Technology*, vol. 209, no. 9, pp. 4502–4508, 2009.

- [18] B. Denkena, D. Boehnke, and L. de León, "Machining induced residual stress in structural aluminum parts," *Production Engineering Research and Development*, vol. 2, no. 3, pp. 247–253, 2008.
- [19] Z. Tang, Z. Liu, and X. Ai, "Experimentation on the superficial residual stresses generated by high-speed milling aluminum alloy," *China Mechanical Engineering*, vol. 19, no. 6, pp. 699–703, 2008.
- [20] B. Rao, C. R. Dandekar, and Y. C. Shin, "An experimental and numerical Study on the face milling of Ti-6Al-4V alloy: tool performance and surface integrity," *Journal of Materials Processing Technology*, vol. 211, no. 2, pp. 294–304, 2011.

## Research Article

# Mesh Regeneration Method for Jig-Shape Optimization Design of the High-Aspect-Ratio Wing

S. H. Huo,<sup>1,2</sup> F. S. Wang,<sup>1</sup> Z. Yuan,<sup>1</sup> and Z. F. Yue<sup>1</sup>

<sup>1</sup> School of Mechanics Civil Engineering and Architecture, Northwestern Polytechnical University, Xi'an 710129, China

<sup>2</sup> The 11th Institute of the Six Academy of CASC, Xi'an 710100, China

Correspondence should be addressed to S. H. Huo; hshxin1985@163.com

Received 2 June 2013; Revised 5 August 2013; Accepted 9 August 2013

Academic Editor: Lei Zhang

Copyright © 2013 S. H. Huo et al. This is an open access article distributed under the Creative Commons Attribution License, which permits unrestricted use, distribution, and reproduction in any medium, provided the original work is properly cited.

A mesh regeneration method was put forward, and its application on the jig-shape optimization design of a high-aspect-ratio wing was carried out in the present study. In the mesh regeneration method, some control lines were selected based on configuration characters of the wing structure firstly. And then a new aerodynamic model was built according to the new control lines distribution which always keeps the same outline. Finally, mesh generation and quality optimization were carried out. Three different jig-shape optimizations based on mesh regeneration method were carried out on a high-aspect-ratio wing. All of them can obtain the designed jig-shapes which have excellent agreement with the expectant one under the impact of static aeroelasticity. Lift coefficients of all the three jig-shape optimization were larger than that of the original flat wing. The results of integrated jig-shape optimization which considered both flexure and torsion were not as well as those in their own independent optimization. An appropriate jig-shape optimization method needs to be selected according to the practical high-aspect-ratio wing design.

## 1. Introduction

Transonic range cruise capability needs to be considered in the design of large transport airplane, high-speed bomber, and civil aircraft. The high-aspect-ratio wing structures are always adopted in these aircrafts. Stiffness of the high-aspect-ratio wing structure is generally low, which seriously affects aeroelasticity characters. Flying quality will decline due to elastic deformation of the aircraft. So jig-shape optimization design, which is used to eliminating the influence of aeroelasticity on load distribution and configuration of the wing structure, is necessary in the preliminary aircraft design, especially for the high-aspect-ratio wing.

Many scholars dedicated to research in the field of aeroelasticity analysis and optimization design. A lot of design methods and basic theories were put forward. As early as in 1990s, Sherift et al. [1] had begun to research aircraft static aeroelasticity and jig-shape optimization design based on N-S equation. Hansen and Horst [2] regarded the choice of an appropriate design as an optimization problem and solved

by the application of a multilevel optimization procedures based on detailed Finite Element models of certain structural parts. T.-L. Ma and D.-L. Ma [3] expatiated on the relationship between multidisciplinary design optimization for aircrafts and the large-scale system theory. Alonso et al. [4] described briefly a set of procedure for the optimization design of full mission aerospace systems which involves multiphysics simulations at various fidelity levels, surrogates, distributed computing, and multiobjective optimization. Chintapalli et al. [5] presented a methodology for the design optimization of a skin-stringer panel of an aircraft wing box. Oktay et al. [6] presented a set of structural optimization tools for topology optimization of aircraft wing structures coupled with Computational Fluid Dynamics analyses. At the same time, a series of configuration design tools was introduced, such as Generic Parameterized Aircraft Surface [7], RAGE [8] and RDS-Professional [9].

In solving Computational Fluid Dynamics (CFD)/Computational Structural Dynamics (CSD) coupling problem, computational zone changes over time and the corresponding

regional grids need to be changed. There are two methods to change the mesh, they are mesh regeneration and dynamic mesh. Several methods in dynamic mesh were put forward and applied in the field of aeroelasticity analysis, such as Spring Analogy Method [10–12], Elastic Solid Method [13, 14], and Layered Elastic Solid Method [15]. A rather large deformation will be caused by the flexibility of high-aspect-ratio wing, which gives dynamic mesh a great challenge. Mesh regeneration method which rebuilds the mesh in computational zone is superior in dealing with the large deformation problem. A serious aeroelasticity problem will be caused due to the state of high-aspect-ratio design. It needs to be considered carefully in the preliminary aircraft design.

In the present study, mesh regeneration method and its application on aeroelasticity analysis of high-aspect-ratio wing were present. And then, three different jig-shape optimization methods, which consider flexure, torsion and both of them, respectively, were studied based on mesh regeneration method.

## 2. Mesh Regeneration Method

**2.1. Mesh Regeneration.** Usually, chordwise cross-section can be assumed to be rigid in aeroelasticity analysis of high-aspect-ratio wing. Flexure and torsion are the main influencing factors of aeroelasticity characteristics. So, geometric model, especially for some regular structures such as wing and blade, can be generated based on some special control lines of exterior surface. The selection of control lines has a direct influence on geometric model. So, control lines selected must have the capability of representing the geometric characteristics. A point-curve-surface order is used to build geometric model through stepwise, and the mesh is generated based on batch process automatically. Figure 1 shows the detailed mesh regeneration process. Structural nodes are adopted as the points used in control lines regeneration. The location of point is the sum of initial position and its displacement. So, structural deformation does not need to be transferred to aerodynamic analysis mesh as usual, which eliminates the error generated through conventional deformation information transfer.

In the model regeneration of deformed wing structure, flexure and torsion of chordwise cross-section can be obtained through structural analysis. A new series of control lines is generated based on the new node coordinates, where the outlines remain unchanged. Computational zone selection and mesh regeneration are carried out on the deformed model automatically according to a certain process. It can be conveniently used in coupled solving problems which need mesh to be regenerated many times.

**2.2. Mesh Quality Optimization.** Batch processing treatment on mesh regeneration greatly facilitates the solving of some multistep coupling problems. But the batch processing mesh regeneration method cannot deal with local special parts well, especially for some sharp changed parts. Decline in mesh

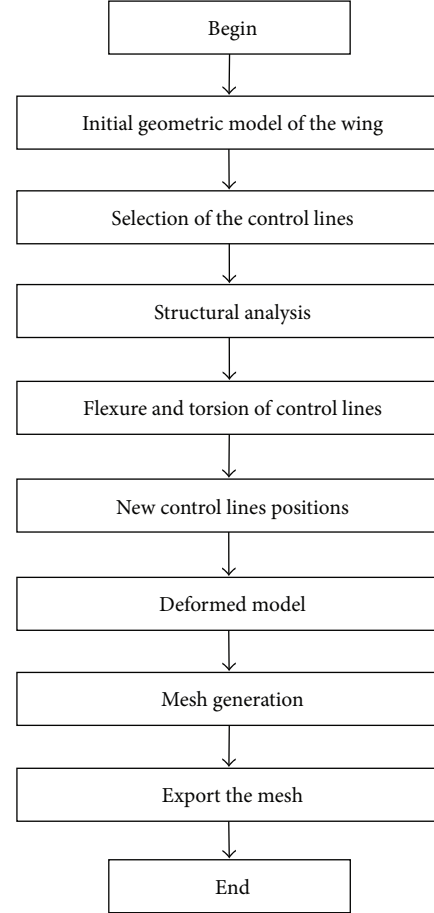


FIGURE 1: Mesh regeneration process.

quality has a direct impact on computational precision. So, a mesh quality optimization treatment is necessary for the regenerated mesh.

Spring analogy method (SAM) can be well used in mesh quality optimization [16]. In SAM, the whole computational zone is regarded as a system composed of springs. Internal grids reach a new equilibrium according to the local condition when the boundary movement occurs. Vertex springs analogy method, in which the equilibrium length of spring is assumed to be zero, is one description of SAM. It can be better used in mesh quality optimization. In vertex spring analogy method, spring tension between internal grids of  $i$  and  $j$  can be expressed as

$$\mathbf{F}_{ij} = K_{ij}(\mathbf{r}_j - \mathbf{r}_i), \quad (1)$$

where  $K_{ij}$  is the stiffness of spring between internal grids of  $i$  and  $j$ ,  $\mathbf{r}_i$  and  $\mathbf{r}_j$  are the position vectors of internal grids of  $i$  and  $j$ , respectively. For the internal grid  $i$ , its resultant force can be written as

$$\mathbf{F}_i = \sum_{j=1}^N K_{ij}(\mathbf{r}_j - \mathbf{r}_i), \quad (2)$$

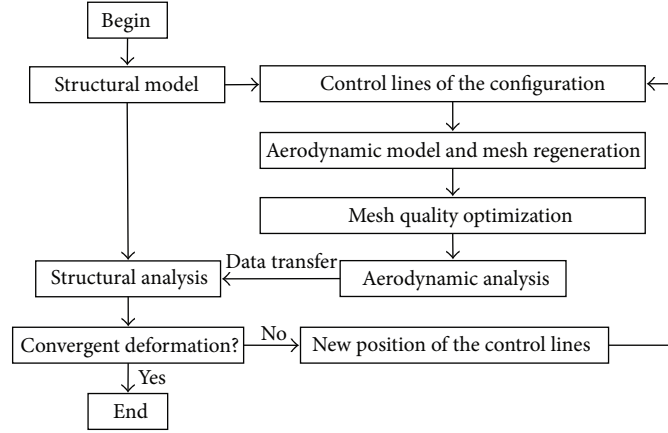


FIGURE 2: Computational process of coupled method.

where  $N$  is the number of internal grids connected with  $i$ . The initial state of whole computational zone can be written as

$$\begin{bmatrix} -\sum_{j=1}^N K_{1j} & \cdots & K_{1j} & \cdots & K_{1N} \\ \vdots & \ddots & \cdots & \cdots & \vdots \\ K_{i1} & \cdots & -\sum_{j=1}^N K_{ij} & \cdots & K_{iN} \\ \vdots & \cdots & \cdots & \ddots & \vdots \\ K_{m1} & \cdots & K_{mj} & \cdots & -\sum_{j=1}^N K_{mj} \end{bmatrix} \begin{bmatrix} \mathbf{r}_1 \\ \vdots \\ \mathbf{r}_i \\ \vdots \\ \mathbf{r}_N \end{bmatrix} = \begin{bmatrix} \mathbf{F}_1 \\ \vdots \\ \mathbf{F}_i \\ \vdots \\ \mathbf{F}_m \end{bmatrix}. \quad (3)$$

Some boundary constraints are added to (3), such as outer boundary maintains the initial position and inter-boundary changes to the new position. The iterative equation to be solved reads

$$\mathbf{r}_i^{(k+1)} = \frac{1}{K_{ii}} \left( \mathbf{F}_i - \sum_{j=1}^{i-1} K_{ij} \mathbf{r}_j^{(k+1)} - \sum_{j=i+1}^N K_{ij} \mathbf{r}_j^{(k)} \right), \quad (4)$$

$$i = 1, 2, \dots, N; \quad k = 0, 1, 2, \dots$$

Spring stiffness has an obvious influence on SAM [17]. The conventional spring stiffness can be expressed as

$$K_{ij} = l_{ij}^{-1}, \quad (5)$$

where  $l_{ij}$  is the distance between internal grids of  $i$  and  $j$ . Collision between different internal grids can be well avoided through introducing  $l_{ij}$  into the spring stiffness. However, the decline of mesh quality is still obvious when a large deformation occurs. Mesh quality control parameters, such as skewness and aspect ratio, are added to the conventional spring stiffness for optimizing some bad meshes. It can be found as

$$K_{ij} = q_s q_a \frac{1}{l_{ij}}, \quad (6)$$

where  $q_s = 1 - 3\alpha_{\min}/\pi$  and  $q_a = 1 - (2/\sqrt{3})(h_{\min}/l_{\max})$  are skewness and aspect ratio, respectively.  $\alpha_{\min}$  is the minimal angle and  $h_{\min}$  is the minimal height, while  $l_{\max}$  is the maximal side of the mesh.  $q_s$  and  $q_a$  are two common used mesh quality evaluation parameters. Their values tend to be zero when the mesh has a high quality, while increase with the decline of mesh quality. A very bad mesh will be generated when one of the values tend to be one. In the mesh quality optimization, the mesh which has a lower quality will tend to change to a favorable status until achieving mesh quality demand.

**2.3. Application on Aeroelasticity Analysis.** Static aeroelasticity analysis is an iterative solving process. First of all, aerodynamic calculation of the initial wing model is carried out. The deformation under the function of aerodynamic load above is obtained through structural analysis. Then the mesh regeneration and optimization are adopted to build the new mesh for the next aerodynamic calculation. Under the function of message transfer, structural analysis is carried out again until both aerodynamic load distribution and deformation are convergent. Then static aeroelasticity parameters including aerodynamic and structural characteristics are obtained. Figure 2 shows computational process of coupled method based on mesh regeneration method. Flexure and torsion of the cross-section which is selected as one of the control lines can be obtained through structural analysis. The next aerodynamic model is regenerated based on the control lines after flexure and torsion processing.

Figure 3 shows finite element model of the high-aspect-ratio wing structure. The wing structure is mainly composed of skin, lengthwise and transverse components. Lengthwise components include spar and stringer while transverse components include rib and thin-walled jointed structure. All the components are made of aluminium alloy of LY12. Its Young's modulus is 66 GPa and Poisson's ratio is 0.33. The structural analysis is carried out through the software of NASTRAN which can consider the geometrical nonlinear well.

Figure 4 shows the aerodynamic model generated based on the control lines. As can be viewed from Figure 4, eleven

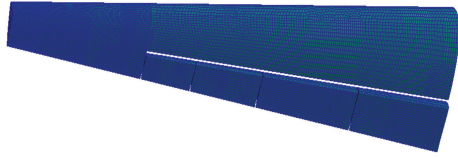


FIGURE 3: Finite element model of the high-aspect-ratio wing.

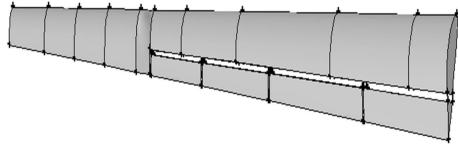


FIGURE 4: Aerodynamic model generated based on the control lines.

cross-sections are selected to control the deformation of main wing structure, while five cross-sections are selected for the aileron. Control lines of the cross-section are adjusted based on the deformation of wing structure, and a new wing model is built based on them.

CFD software FLUENT is adopted for aerodynamic analysis while FEM software NASTRAN for structural analysis. Pressure distribution on the coupled surface can be obtained through aerodynamic analysis, but load for structural analysis often needs to be applied directly on structural nodes or elements. So load interpolation transfer is necessary. For every CFD node, three CSD nodes which can enclose it and have a minimal area are selected firstly. Load information of the CFD node is transferred to these three CSD nodes. It can be expressed as

$$\begin{bmatrix} F_{x,i} \\ F_{y,i} \\ F_{z,i} \end{bmatrix} = \begin{bmatrix} \frac{A_i}{A} & 0 & 0 \\ 0 & \frac{A_i}{A} & 0 \\ 0 & 0 & \frac{A_i}{A} \end{bmatrix} \begin{bmatrix} G_x \\ G_y \\ G_z \end{bmatrix}, \quad (7)$$

where  $G_x$ ,  $G_y$ , and  $G_z$  are the three directions compression force obtained through CFD software FLUENT,  $F_{x,i}$ ,  $F_{y,i}$  and  $F_{z,i}$  are load applied on structure.  $A_i$  and  $A$  are area of two triangles, the former one is formed by one CFD node and two CSD nodes, while the latter one is formed by three CSD nodes. After the load interpolation transfer of all CFD nodes, the new load format for structural analysis can be obtained.

Static aeroelasticity is analyzed under the flight attitude of 15 Km altitude, Ma 0.5, and attack angle of  $2^\circ$ . After iterated twelve times, lift coefficient and deformation are convergent. Figures 5 and 6 show the iterative processes of lift coefficient and flexure, respectively. It can be seen that lift coefficient converges at 0.16 while flexure converges at 1700 mm. Both lift coefficient and flexure decreased under the impact of static aeroelasticity.

Figures 7 and 8 present the flexure and torsion distribution of the cross-sections, respectively. As can be viewed from Figure 7, flexure of wing root which is restrained is 0 mm while wing tip has the maximum flexure of 1700 mm. Intermediate cross-sections deformed glossily. From Figure 8,

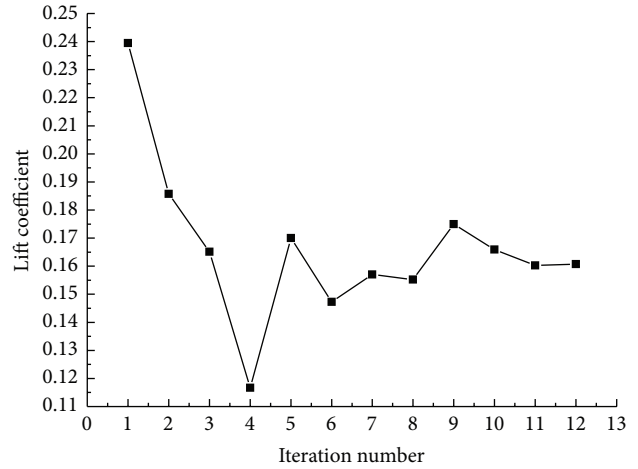


FIGURE 5: Iterative process of lift coefficient.

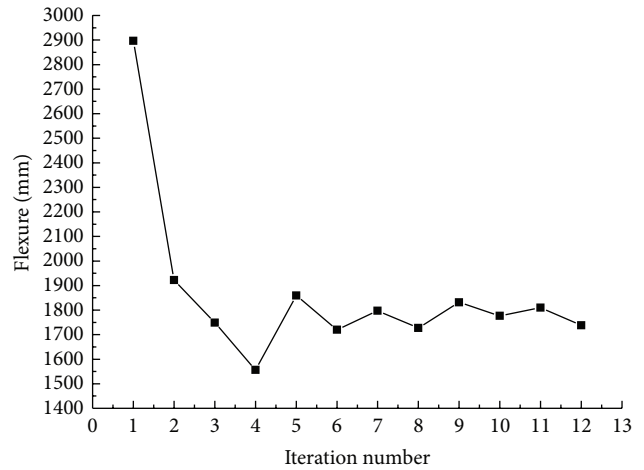


FIGURE 6: Iterative process of deformation.

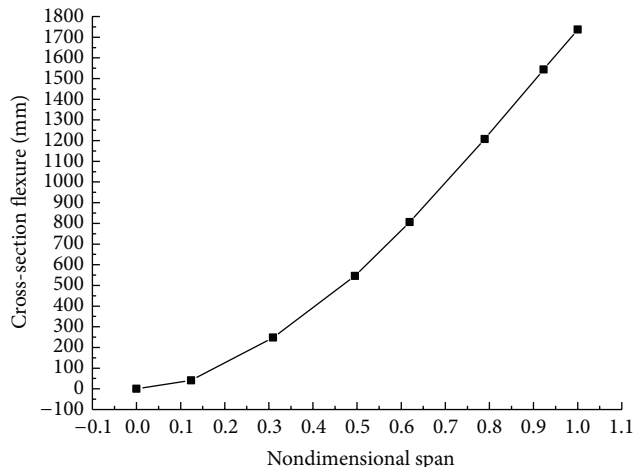


FIGURE 7: Deformation distribution of the cross-section.

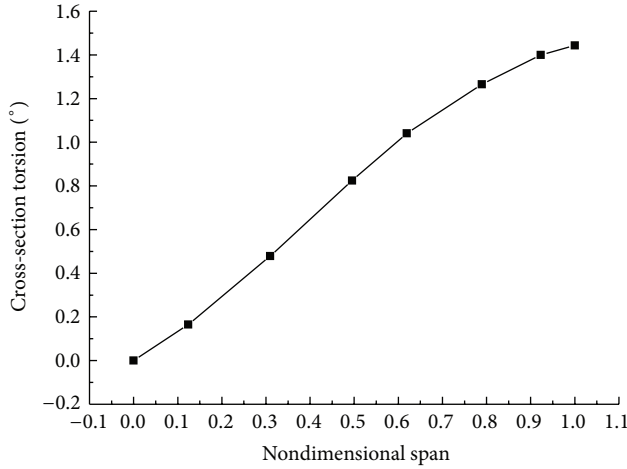


FIGURE 8: Torsion distribution of the cross-section.

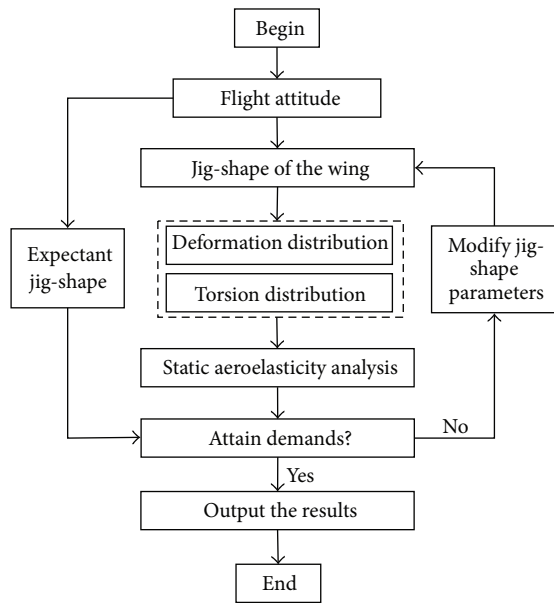


FIGURE 9: Jig-shape optimization process.

it can be seen that torsion distribution of the cross-sections has the same trend, and the maximum torsion angle is  $1.4^\circ$ . Torsion of the cross-sections reduce practical attack angle, which leads to the decrease of lift.

### 3. Jig-Shape Optimization

Aerodynamic distribution and deformation are changed under the impact of static aeroelasticity. Along with them, jig-shape of the wing structure cannot keep its initial form. Jig shape optimization is a pre-design. Its target is to obtain a designed jig-shape which will converge to the expectant one under the impact of static aeroelasticity. Figure 9 shows the jig-shape optimization process. As can be viewed from Figure 9, deformation of the wing structure can be divided into flexure and torsion distribution of the cross-sections.

For one of the cross-sections of the high-aspect-ratio wing, which is denoted as the  $r$ th cross-section here, iterative deformation in jig-shape optimization can be expressed as

$$X_r^{n+1} = X_r^n + \xi (X_r^n + X_{e,r}^n - X_{e,r}), \quad (8)$$

where  $X_r^n$  means the flexure or torsion of the  $r$ th cross-section before the  $n$  time iteration,  $X_{e,r}^n$  expresses the change of flexure or torsion of the  $r$ th cross-section at the  $n$  time iteration,  $X_{e,r}$  is the expectant flexure or torsion of the  $r$ th cross-section, and  $\xi$  is a relaxation parameter placed between 0 and 1.0. After  $N$  times iteration, when the flexure or torsion meets (9), a jig-shape optimization result will be obtained.

Consider

$$\frac{(X_r^n + X_{e,r}^n - X_{e,r})}{l} < \varepsilon, \quad (9)$$

where  $l$  is wingspan of the high-aspect-ratio wing  $\varepsilon$  is used to judge the convergence of the iteration and is 0.5% here.

The control lines always keep the same outline in the whole jig-shape optimization process, which is the basic assumption for every cross-section. According to the new flexure and torsion distribution, control line state of every cross-section is adjusted. And the new aerodynamic model is generated based on the new control lines. In the mesh regeneration method, the deformation of wing structure is seen as the control line state distribution. It is conducive to have an independent control of every cross-section in the whole jig-shape optimization process.

Three different optimization parameters are considered in the present study, they are flexure, torsion, and both of them. Static aeroelasticity results of the original wing, which can be seen in Figures 7 and 8, are set to initial values after a negative treatment.

**3.1. Independent Flexure Optimization.** In the independent flexure optimization, torsion of cross-section keeps the initial value during the whole optimization process. Figure 10 shows the results of independent flexure optimization. Only flexure distribution of cross-section is considered, and a flat wing is assumed to be the expectant jig-shape in the present study. Three different flexure distributions of the cross-section are present in Figure 10. They are expectant, designed, and convergent jig-shape, respectively. As can be viewed from Figure 10, excellent agreement between the convergent jig-shape and the expectant one is observed. The independent flexure optimization based on mesh regeneration method can be well used in jig-shape optimization when just flexure is considered. As can be viewed from designed jig-shape in Figure 10, a smoothly downward flexure distribution design can be convergent to a flat wing under the impact of static aeroelasticity.

**3.2. Independent Torsion Optimization.** In the independent torsion optimization, flexure of cross-section keeps the initial value during the whole optimization process. Figure 11 shows the results of independent torsion optimization. Only torsion distribution of cross-section is considered here,

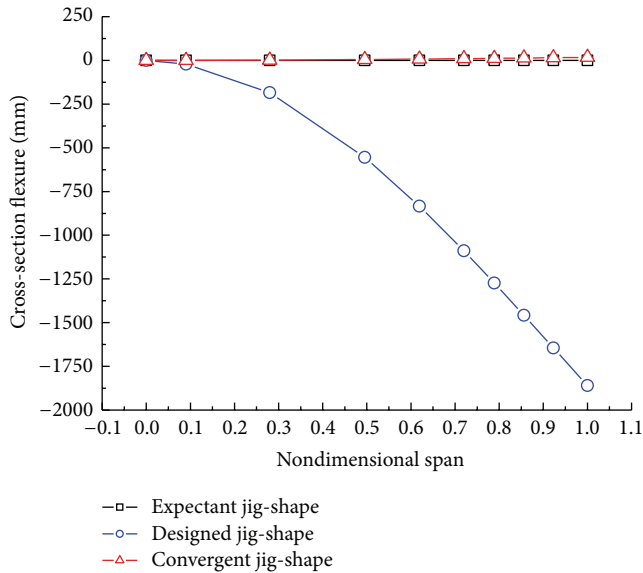


FIGURE 10: Independent flexure optimization results.

and the expectant jig-shape is assumed to be an attack angle of  $2^\circ$  in all of the cross-sections. Three different torsion distributions of the cross-section are present in Figure 11. They are expectant, designed, and convergent jig-shape, respectively. As can be viewed from Figure 11, excellent agreement between the convergent jig-shape and the expectant one is observed. The independent torsion optimization based on mesh regeneration method can be well used in jig-shape optimization when just torsion is considered. As can be viewed from designed jig-shape in Figure 11, a smoothly increased torsion distribution design can be convergent to the expectant jig-shape under the impact of static aeroelasticity.

**3.3. The Integrated Jig-Shape Optimization.** Both flexure and torsion distribution are considered in the integrated jig-shape optimization. Its expectant flexure and torsion distribution are assumed to be the same values as those in their own independent optimization above. Figures 12 and 13 show the integrated jig-shape optimization results, they are flexure and torsion distribution, respectively. Comparing the results in Figures 12 and 13 with those in Figures 10 and 11, it can be seen that both optimization results in integrated jig-shape optimization are similar with their own independent results. The slight difference is that the error between convergent jig-shape and expectant one are larger than those in their own independent optimization. But the errors are still in an acceptable range for a wing structure design. The integrated jig-shape optimization based on mesh regeneration method can be well used in jig-shape optimization when both flexure and torsion are considered.

**3.4. Comparison of Different Optimization Methods.** Figure 14 shows lift coefficient iterative processes of different jig-shape wings in static aeroelasticity analysis. It can be seen that the convergent lift coefficients of torsion and integrated

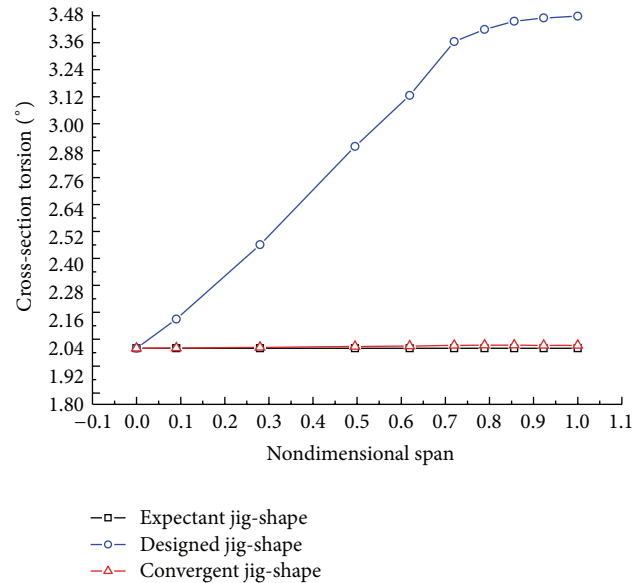


FIGURE 11: Independent torsion optimization results.

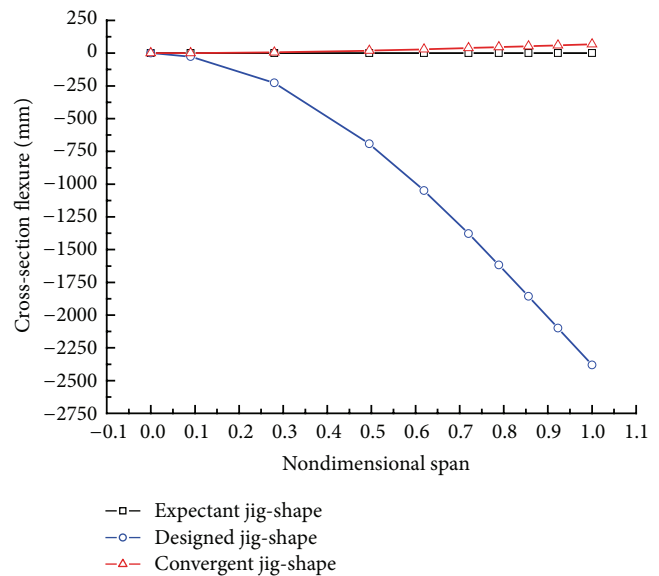


FIGURE 12: Flexure results of the integrated jig-shape optimization.

jig-shape optimization have the similar value and are larger than those of flexure jig-shape optimization and the original flat wing. Lift coefficient of the wing structure after flexure jig-shape optimization is larger than that of original flat wing too, but the incremental value is less than those of other two optimization methods. In the high-aspect-ratio wing design, the effect of torsion, which has an obvious influence on attack angle, on lift coefficient is still dominant. Flexure along with span also affects the lift coefficient, but it is not as obvious as torsion.

All the three jig-shape optimization methods can obtain the expectant jig-shape wing structure and their convergent lift coefficients are larger than that of original flat wing. The results of integrated jig-shape optimization method are not

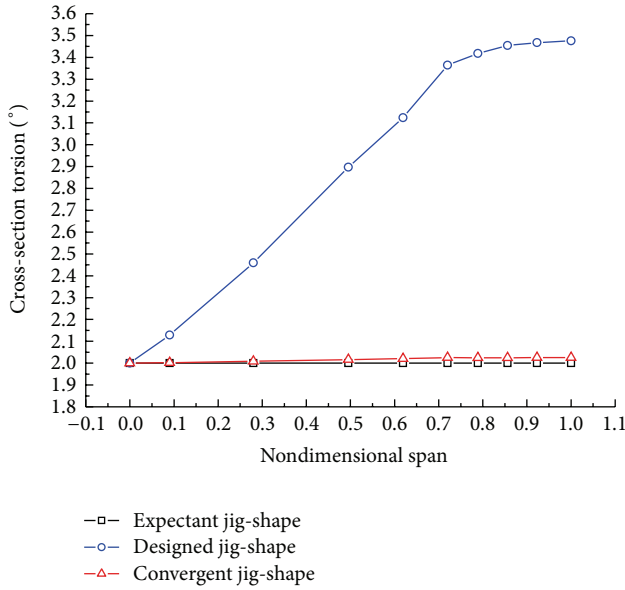


FIGURE 13: Torsion results of the integrated jig-shape optimization.

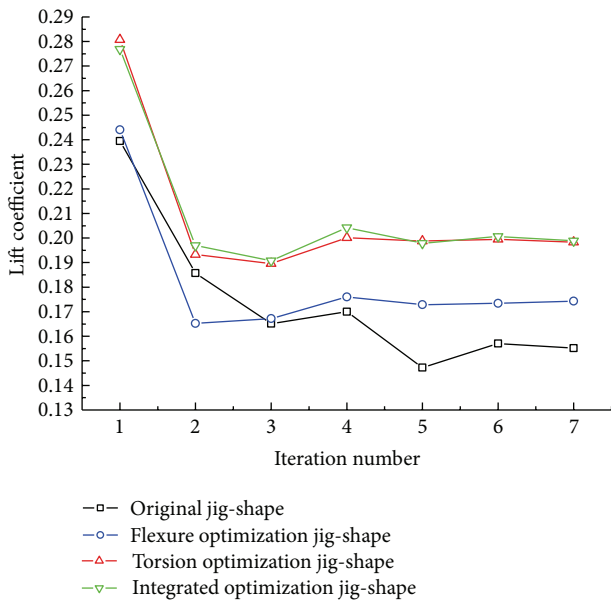


FIGURE 14: Lifts coefficient iterative processes of different jig-shape wings.

as well as those in their own independent optimization. But both flexure and torsion are considered and its convergent lift coefficient can obtain a larger value. So, it is needed to select one of the jig-shape optimization methods based on practical high-aspect-ratio wing design.

#### 4. Conclusions

A mesh regeneration method and its application on static aeroelasticity analysis and jig-shape optimization design were

put forward in the present study. Some useful conclusions can be drawn.

- (1) A mesh regeneration method which contains mesh regeneration and mesh quality optimization was put forward in the present study. An automatic mesh regeneration and mesh quality optimization based on control lines was carried out on a high-aspect-ratio wing.
- (2) Static aeroelasticity of a high-aspect-ratio wing was analyzed based on mesh regeneration method. It can be well used in dynamic mesh application, especially for a large deformation.
- (3) Three different jig-shape optimizations based on mesh regeneration method were carried out on a high-aspect-ratio wing. All of them can obtain the designed jig-shapes which have excellent agreement with the expectant ones under the impact of static aeroelasticity.
- (4) Lift coefficients of all the three jig-shape optimization were larger than that of original flat wing. The results of integrated jig-shape optimization which considered both flexure and torsion were not as well as those in their own independent optimization. An appropriate jig-shape optimization method needs to be selected according to the practical high-aspect-ratio wing design.

#### Acknowledgments

This study is supported by the National Natural Science Foundation of China (no. 51175424) and Shaanxi Provincial Natural Science Foundation (no. 2009JQ1006).

#### References

- [1] A. Sherif, O. Madara, B. Richard, and S. Michael, "A decoupled stochastic approach to the jig-shape aeroelastic wing design problem," *AIAA Paper*, AIAA 1998-0906, 1998.
- [2] L. U. Hansen and P. Horst, "Multilevel optimization in aircraft structural design evaluation," *Computers and Structures*, vol. 86, no. 1-2, pp. 104-118, 2008.
- [3] T.-L. Ma and D.-L. Ma, "Multidisciplinary design optimization methods for aircrafts under large-scale system theory," *System Engineering Theory and Practice*, vol. 29, no. 9, pp. 186-192, 2009.
- [4] J. J. Alonso, P. LeGresley, and V. Pereyra, "Aircraft design optimization," *Mathematics and Computers in Simulation*, vol. 79, no. 6, pp. 1948-1958, 2009.
- [5] S. Chintapalli, M. S. A. Elsayed, R. Sedaghati, and M. Abdo, "The development of a preliminary structural design optimization method of an aircraft wing-box skin-stringer panels," *Aerospace Science and Technology*, vol. 14, no. 3, pp. 188-198, 2010.
- [6] E. Oktay, H. U. Akay, and O. Merttopcuoglu, "Parallelized structural topology optimization and CFD coupling for design of aircraft wing structures," *Computers and Fluids*, vol. 49, no. 1, pp. 141-145, 2011.
- [7] S. S. Sarakinos, I. M. Valakos, and I. K. Nikolos, "A software tool for generic parameterized aircraft design," *Advances in Engineering Software*, vol. 38, no. 1, pp. 39-49, 2007.

- [8] D. L. Rodriguez and P. Sturdza, "A rapid geometry engine for preliminary aircraft design," *AIAA Paper*, AIAA-2006-0929, 2006.
- [9] D. Raymer, "RDS-professional in action: aircraft design on a personal computer," SAM/AIAA Paper 965567, 1996.
- [10] T. J. Blom, "Considerations on the spring analogy," *Journal of Aircraft*, vol. 32, pp. 647–668, 2000.
- [11] K. Matsushima, M. Murayama, and K. Nakahash, "Unstructured dynamic mesh for large movement and deformation," AIAA 2002-0122, 2002.
- [12] S. J. Zhang, J. Liu, and Y. S. Chen, "A dynamic mesh method for unstructured flow solvers," in *Proceedings of the AIAA Computational Fluid Dynamics Conference*, pp. 2003–3843, 2003.
- [13] K. Stein, T. Tezduyar, and R. Benney, "Mesh moving techniques for fluid-structure interactions with large displacements," *Journal of Applied Mechanics, Transactions ASME*, vol. 70, no. 1, pp. 58–63, 2003.
- [14] K. Stein, T. E. Tezduyar, and R. Benney, "Automatic mesh update with the solid-extension mesh moving technique," *Computer Methods in Applied Mechanics and Engineering*, vol. 193, no. 21–22, pp. 2019–2032, 2004.
- [15] S. H. Huo, F. S. Wang, W. Z. Yan, and Z. F. Yue, "Layered elastic solid method for the generation of unstructured dynamic mesh," *Finite Elements in Analysis and Design*, vol. 46, no. 10, pp. 949–955, 2010.
- [16] S.-H. Huo, F.-S. Wang, and Z.-F. Yue, "Spring analogy method for generating of 2D unstructured dynamic meshes," *Journal of Vibration and Shock*, vol. 30, no. 10, pp. 177–182, 2011.
- [17] J. B. Frederic, "Considerations on the spring analogy," *International Journal For Numerical Methods in Fluids*, vol. 32, pp. 647–668, 2000.

## Research Article

# Melt Pressure Signature Tracking Using an Adaptive Kalman Filter in Microinjection Molding

Hang Liu,<sup>1</sup> Hong Hu,<sup>1</sup> Kai Leung Yung,<sup>2</sup> Yan Xu,<sup>2</sup> and Xing Wei Zhang<sup>3</sup>

<sup>1</sup> Harbin Institute of Technology Shenzhen Graduate School, Shenzhen 518055, China

<sup>2</sup> Department of Industrial & Systems Engineering, The Hong Kong Polytechnic University, Hung Hom, Kowloon, Hong Kong

<sup>3</sup> College of Engineering Shantou University, Shantou University, Shantou 515063, China

Correspondence should be addressed to Hong Hu; honghu@hit.edu.cn

Received 13 May 2013; Accepted 23 July 2013

Academic Editor: Lei Zhang

Copyright © 2013 Hang Liu et al. This is an open access article distributed under the Creative Commons Attribution License, which permits unrestricted use, distribution, and reproduction in any medium, provided the original work is properly cited.

In order to manufacture high quality microproducts, the precision control of injected plastic melt in the injection chamber during a microinjection process requires real-time tracking of the melt pressure when the melt passes through the nozzle. A novel type of adaptive Kalman filter algorithm based on  $F$ -distribution is proposed in this paper. This adaptive Kalman filter can switch the system between the steady state and transient state by comparing the differences of input data in  $F$ -distribution. By resetting the Kalman gain and other relevant parameters, the adaptive function guarantees the convergence of the filtered signal during the tracking process and tracks the moments which sudden changes occur in the pressure signature. The simulation experiment results show that the method can reduce the effect of measurement noise more quickly and effectively. The method is proven to be effective for microinjection molding applications.

## 1. Introduction

Target tracking, which is considered to be a problem caused by the uncertainty of the target's acceleration, has been studied in the field of state estimation for decades. In micro injection molding, the tracking of the target's acceleration is very important for shot volume control. The micro injection molding process heats plastic granules to melting point and then injects a precise amount at high pressure through a nozzle into a mold. Micro injection has many merits and is one of the most cost effective methods in the mass production of components. It has a stable quality and good dimensional accuracy down to a micrometer. Due to the high sensitivity of the microstructures, a very precise volume of plastic melt is required. In order to achieve high precision volume control, a micro injection machine has been developed in our lab, a sketch of which is shown in Figure 1. The injection unit has a nozzle at its end that connects to the mold, and the plunger can push the molten plastic which passes through the nozzle into the mold. A pressure sensor is mounted in the injection

unit for monitoring the micro injection process and promoting the precision of the volume control.

Since the electromagnetic noise severely hinders recognition of the pressure (sharp increment) signature in the micro injection process, a pressure signal process is required. The Kalman filter has been widely used as a tracking filter to estimate the position, the velocity, and the acceleration of a target. Most digital tracking filters are based on the Kalman filter equations, where the process noise and the measurement noise are presumed white. In the most simple models, target accelerations or acceleration increments are regarded as white noise, as is done to obtain the well-known  $\alpha$ - $\beta$  ( $-\gamma$ ) filters. These basic discrete-time filters have properties suitable for many applications [1]. The least-mean-square (LMS) algorithm and the recursive least-squares (RLS) algorithms have established themselves as the principal tools for linear adaptive filtering. Lopes and Gerald used the LMS algorithm to get the faster convergence and a much higher noise immunity when the reference signal vector norm takes on a low value [2], while Barnawi et al. used RLS algorithm

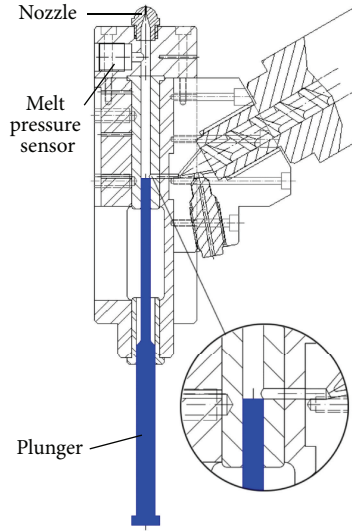


FIGURE 1: Sketch of injection unit.

to get much less convergence time [3]. Rosendo Macías and Expósito presented a method for self-tuning of the model error covariance to overcome the sudden changes of the input signal, so that they could properly track signal fluctuations in digital protection applications [4]. In the similar field, Hu et al. [5] developed the new adaptive Kalman algorithm which has a good robustness and can handle the sudden changes of vehicle motion and measurement errors. Lee et al. [6] proposed the interacting multiple model algorithm using intelligent input estimation for maneuvering target tracking. Anilkumar et al. utilized the constant Kalman gains for an efficient online prediction of the reentry time of space objects [7]. J.-Y. Kim and T.-Y. Kim proposed the dynamic Kalman filter which robustly tracks a ball in the dynamic condition by controlling the velocity of the state vector [8]. Based on the ARMA innovation model and Lyapunov equations, Deng et al. [9] presented an approach to handle the information fusion filtering, prediction, and smoothing problems for the state and signal. Ding et al. [10] and Geng and Wang [11] proposed the adaptive Kalman methods to tune the Q matrix to the optimal magnitude automatically. Geng and Wang [11] used the statistical method of Chi-square test to evaluate the filter residuals.

Concluding the above methods, the recursive algorithm based on analysis, as given by the Kalman filter, is a good way to detect abrupt changes (transients) of harmonic parameters. Micro injection molding is a fast procedure, but it needs a real-time tracking filter to deal with the abrupt changes during the procedure. From the above methods, in order to deal with the abrupt changes, we consider that developing an adaptive Kalman filter to track the micro injection molding procedure is suitable. The method is easy and robust.

This research proposes a novel adaptive Kalman filter that tracks the pressure signature's sudden change around the nozzle during the micro injection molding process. Simulation results show that this new method accurately tracks the pressure signal profile in high and low speed injection and

that its processed pressure signature is consistent with design standards.

## 2. Methods of Signature Filtering

**2.1. Problems.** During the micro injection procedure, the injection volume control is of great importance. The control method needs correct and real-time signals. The signals are always acquired by a pressure sensor and processed by a tracking filter. The micro injection procedure is divided into two stages: uniform injection and deceleration injection. Before the plastic melt reaches the nozzle position, the ascending plunger pushes the molten melt at a uniform speed. This is the preinjection stage. When the plastic melt front passes the nozzle, the pressure sensor will catch the melt arrival signal. Then the signal should be transferred to the computer and processed by the real filter. Based on the filtered signal, the melt's arrival instant should be ascertained. The shooting controller will then adjust the shooting parameters and feedback to the linear motor. The plunger first maintains its travelling speed for a finite instant, then gradually slows down to zero. That is the injection stage.

During the micro injection procedure, the signal generated by the plastic melt passing through the nozzle is called the pressure signature. If a tracking filter is not used to deal with the pressure signature, the electromagnetic noise in the pressure signature may cause an error of judgment on the micro injection control unit, which means that the injection volume may be less or more than the volume needed. This may cause insufficient and excessive shootings. Figure 2 and Figure 3 show insufficient and excessive shootings during the micro injection molding procedure, without a real-time tracking filter.

**2.2. Kalman Filter Process.** The Kalman filter is a set of mathematical equations that provide an efficient computational (recursive) solution to the discrete data linear filtering problem [12]. The Kalman filter addresses the general problem of trying to estimate the state  $x \in R^n$  of a discrete-time controlled process that is governed by the linear stochastic difference equation:

$$x_k = Ax_{k-1} + Bu_{k-1} + w_{k-1}, \quad (1)$$

with a measurement  $z \in R^m$ ; that is,

$$z_k = Hx_k + v_k, \quad (2)$$

where  $u$  is the control input.  $A$  is the  $n \times n$  matrix that relates the state at the previous time step to the current step.  $B$  is the  $n \times 1$  matrix that relates the control input.  $H$  is the  $m \times n$  matrix that relates the state. The random variables  $w_k$  and  $v_k$  represent the process and measurement noise, respectively.

The final estimation algorithm is the predictor corrector for solving numerical problems. The discrete Kalman filter time update equations are the following.

(1) Project the state ahead:

$$\hat{x}_k^- = A_k \hat{x}_{k-1} + B_k u_k, \quad (3)$$



FIGURE 2: Insufficient shooting.

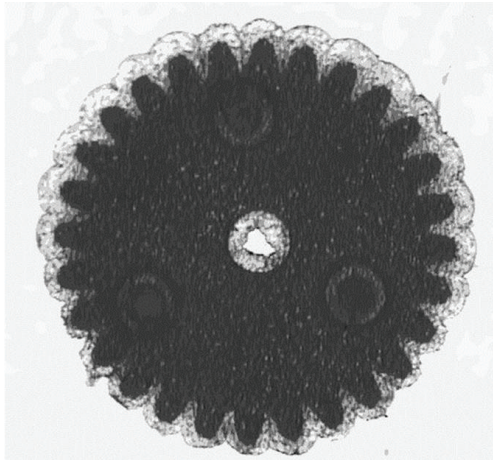


FIGURE 3: Excessive shooting.

(2) project the error covariance ahead:

$$P_k^- = A_k P_{k-1} A_k^T + Q. \quad (4)$$

The discrete Kalman filter measurement updates equations:

(1) compute the Kalman gain:

$$K_k = P_k^- H^T (H P_k^- H^T + R)^{-1}, \quad (5)$$

(2) update estimate with measurement:

$$\hat{x}_k = \hat{x}_k^- + K_k (z_k - H \hat{x}_k^-), \quad (6)$$

(3) update the error covariance:

$$P_k = (I - K_k H) P_k^-, \quad (7)$$

where  $Q$  is the process noise covariance and the elementary matrix,  $R$  is the measurement noise covariance,  $\hat{x}_k^-$  is the

a priori state estimate,  $\hat{x}_k$  is the a posteriori state estimate,  $P_k^-$  is the a priori estimate error covariance,  $P_k$  is the a posteriori estimate error covariance,  $K_k$  is the Kalman gain,  $R$  is the measurement error covariance, and  $H$  is the  $m \times n$  matrix that relates the state to the measurement.

After each time and measurement update, the process is repeated with the previous a posteriori estimates used to project or predict the new a priori estimates. This recursive nature will timely adjust itself and track the varying signature acquired. It is also easy to use mathematical induction to prove the correctness of the algorithm [13].

**2.3. Adaptive Kalman Filter Based on  $F$ -Distribution.** Although the Kalman filter provides a dynamic and precise parameter estimation of the injection process, it often suffers from a problem known as “filter dropping off.” That is, if the parameters to be estimated have not been changed for a long time, the filter parameters (Kalman gain  $K$ , internal error covariance matrix  $P$ ) have a very small stationary value, and the filter becomes insensitive to abrupt changes of state variables. Thus, in the case of the estimation of dynamic variations of signature components, the standard Kalman filter loses the ability to match these changes quickly. A previous study [14] of the adaptive Kalman filter focused on the  $t$ -distribution to distinguish the two different models for steady-state and transient-state estimations. However, due to its poor robustness, the Kalman filter based on the  $t$ -distribution can be only used in low speed and low noise injection molding environments because it is not able to track the pressure signature and causes mistakes at higher injection velocities. For a wider application of injection molding requirements, the adaptive Kalman filter based on  $F$ -distribution is proposed. A hypothesis-testing procedure for the equality of two variances is based on the following procedure. Let  $\{X_{11}, X_{12}, \dots, X_{1x}\}$  be a random sample from a normal population with variance  $\sigma_1^2$ , and then let  $\{X_{21}, X_{22}, \dots, X_{2y}\}$  be a random sample from a second normal population with variance  $\sigma_2^2$ . Assume that both normal populations are independent. Let  $S_1^2$  and  $S_2^2$  be the sample variances. Then the ratio is

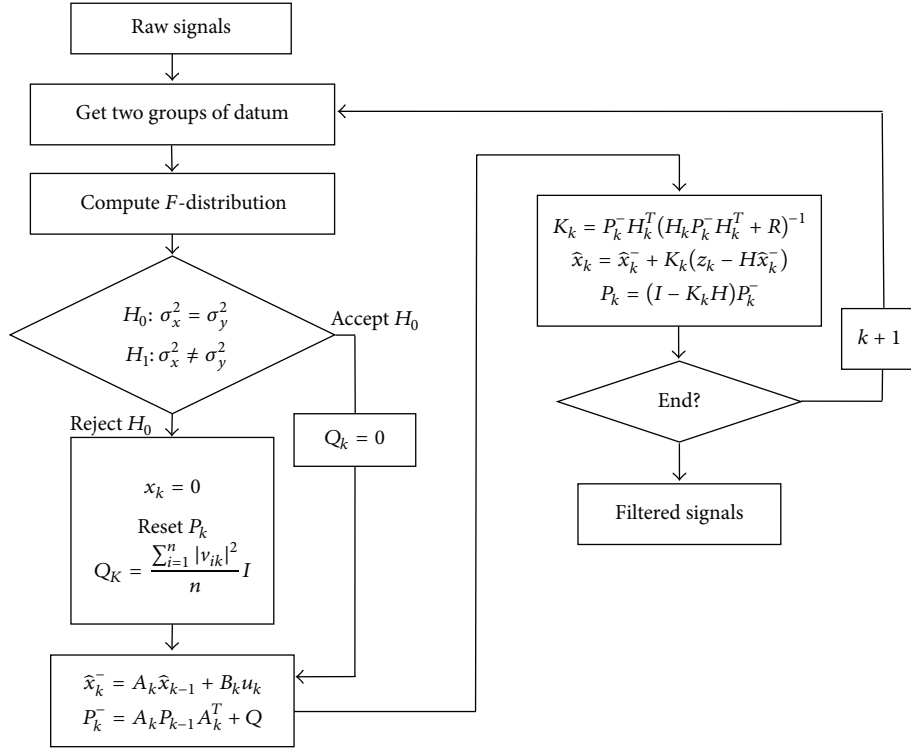
$$F = \frac{S_1^2}{S_2^2}, \quad (8)$$

where the  $F$ -distribution has  $x - 1$  degrees of freedom at the numerator and  $y - 1$  degrees of freedom at the denominator.

The steps are as follows.

Firstly get  $n$  pressure data from the recent pressure signature, assuming the data group as  $\{X_1, X_2, \dots, X_n\}$  and the variance of the data group is  $\sigma_x$ . Secondly, erase the first data  $X_1$  and add the current data  $X_{n+1}$  at the next sample time, so the current data group becomes  $\{X_2, X_3, \dots, X_{n+1}\}$  and the variance of the data group is  $\sigma_y$ .

The null hypothesis  $H_0 : \sigma_x^2 = \sigma_y^2$ , alternative hypothesis  $H_1 : \sigma_x^2 \neq \sigma_y^2$ , and rejection criterion is  $F_0 > F_{\alpha/2, x-1, y-1}$  or  $F_0 < F_{1-\alpha/2, x-1, y-1}$ . Assume  $\alpha = 0.05$  (the value of  $\alpha$  is decided by analyzing the data and is changeable); if the value of  $F$  is within the significance of  $\alpha = 5\%$ , it means that

FIGURE 4: Adaptive Kalman filter based on  $F$ -distribution flow chart.

the current pressure signature is in the steady state, and the traditional Kalman process from (3) to (7) can be used to filter the pressure signals. If the value of  $F$  is out of the significance of  $\alpha = 5\%$ , it means that the current pressure signature is in the transient state; then from (2) we get

$$v_k = z_k - H_k x_k, \quad (9)$$

where  $v_k$  is the filter error and the input  $x_k$  resets as zero; thus,  $v_k$  is equal to  $z_k$ . At this time, the value of  $P_k$  in (7) is becoming smaller because of the long time steady-state estimation, so a larger value of  $P_k$  is required to increase the Kalman gain  $K_k$  for transient-state estimation. The new  $\hat{x}_k$  in (6) from the changed  $K_k$  is best fit for the transient-state estimation. Meanwhile, as the value of the noise  $Q_k$  in (4) is becoming smaller and will not fit the transient situation, the model sets a lower value for it. When the transient estimation is coming, the  $Q_k$  will be reset as

$$Q_k = \frac{\sum_{i=1}^n |v_{ik}|^2}{n} I, \quad (10)$$

where  $n$  is the order for the model and  $I$  is the identity matrix [4]. So the adaptive Kalman filter consists of steady and transient estimations by using the  $F$ -distribution judgment, where the steady estimation performs the traditional Kalman filter, and the transient estimation performs parameter resets and the traditional Kalman filter. The computational sequence for the adaptive Kalman filter is shown in Figure 4.

For an adaptive Kalman filter, when  $k \rightarrow \infty$  and  $K_k \rightarrow 0$ , the filter is divergent with an increasing  $k$  value. We can

prove that  $K_k$  is always greater than zero and the stability of the adaptive Kalman filter. During micro injection, if the null hypothesis is accepted, it means that the melt front has not yet reached the nozzle and the system is assumed to be in a steady state ensuring  $Q_k$  to be 0. Likewise, if the null hypothesis is rejected, it means that the plastic melt front reaches the nozzle and the system is assumed to be in a transient state and resets to a set of initial conditions. Suppose when  $k \rightarrow \infty$ ,  $K_k \rightarrow 0$ , from (2), we can get

$$K_k = P_k^- H_k^T (H_k P_k^- H_k^T + R_k)^{-1}. \quad (11)$$

Because  $H_k$  and  $R_k$  are not zero,  $P_k = 0$ :

$$\begin{aligned} P_{k+1}^- &= A_k P_k A_k^T + Q_k = Q_k > 0, \\ P_k &= (I - K_k H_k) P_k^- = P_k^- > 0. \end{aligned} \quad (12)$$

This clearly contradicts the conclusion of  $P_k = 0$ . So  $K_k > 0$ , and the filter is not divergent. The adaptive Kalman filter based on  $F$ -distribution can track real-time signal and perfectly overcome the “filter dropping off” problem. Compared with the Kalman filter, the robustness of the adaptive Kalman filter based on  $F$ -distribution makes it suitable for many more injection molding purposes. In view of the above, this adaptive Kalman filter based on  $F$ -distribution uses the statistical methods to adjust the system’s state. The  $Q$  model will be replaced if the system’s state is changed from steady to transient. It avoids the search time of the optimal  $Q$  in original Kalman filter, so it meets the real time needs in micro injection molding procedure.

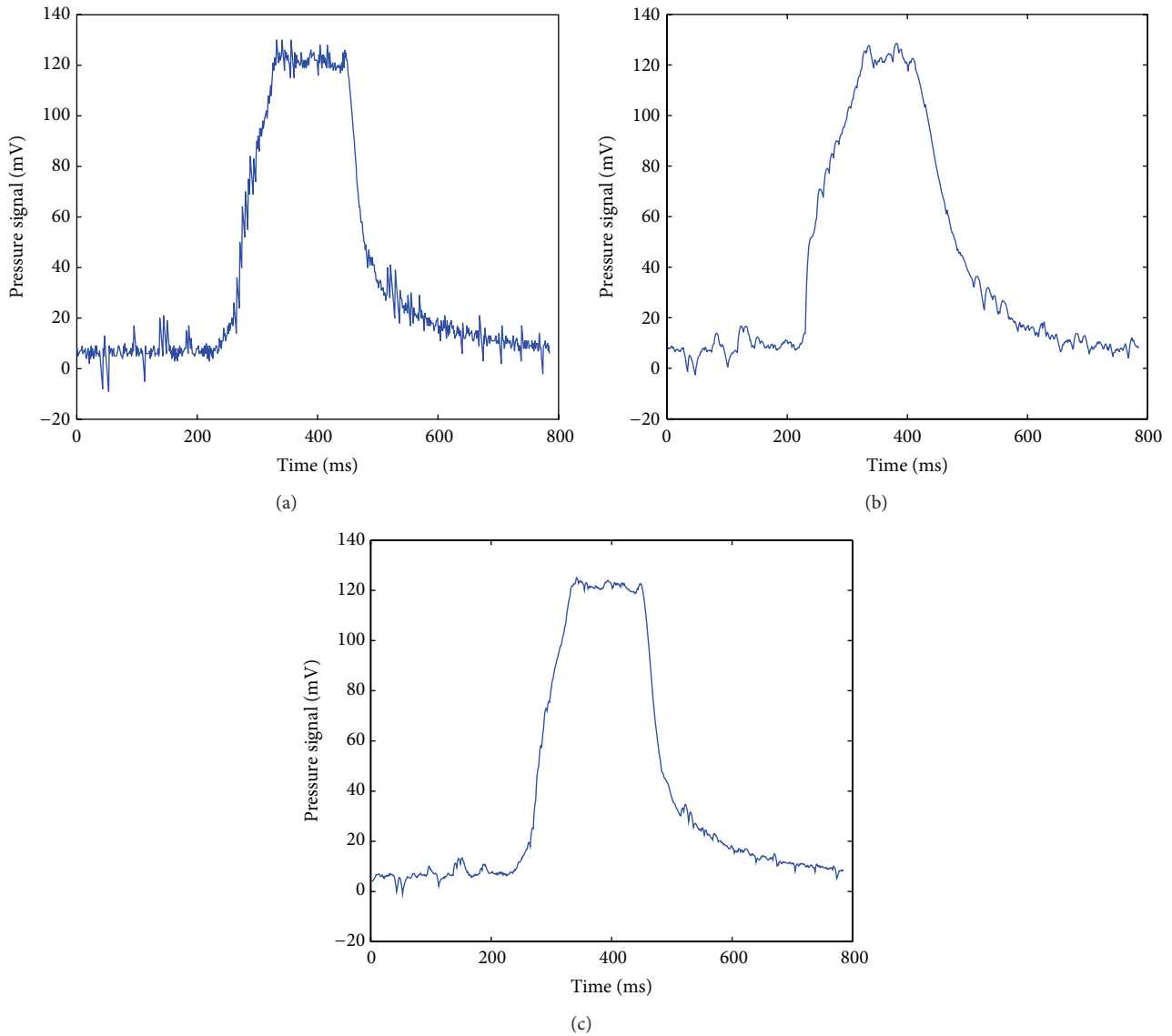


FIGURE 5: Injection velocity 50 mm/s. Signature width 340 ms. Signature peak height 125 mV. Injection volume 0.12 cc. (a) Experimental pressure signature without filter. (b) Experimental pressure signature processed by traditional Kalman filter. (c) Experimental pressure signature processed by adaptive Kalman filter based on  $F$ -distribution.

### 3. Simulation Comparison

To realize accurate injection volume control of plastic melt during micro injection, the effective detection of the moment for the arrival of the plastic melt front at the injection nozzle is necessary. The plastic PMMA (MF-001) is selected for the pressure signature tracking in our micro injection experiments. The temperature of the injection part is 240°C. The diameter of the nozzle is 2.0 mm and made of stainless steel. Due to the high injection velocity associated with the micro injection machine, the pressure sensor responsible for monitoring the nozzle pressure requires a high sensitivity and frequency response. A piezoelectric melt pressure sensor manufactured by Kistler is employed and is mounted beneath

the nozzle (Kistler 6171BA, range = 0 to 2000 bar). The plastic melt generates the pressure signature during its passage through the nozzle (Figure 1). Before the plastic melt reaches the tapered nozzle, the pressure change recorded by the pressure sensor would be minor. Yet, when the plastic melt flows through the narrowed opening at a constant volume flow rate (depends on the traveling speed of the plunger), the developed pressure causes the signal to undergo a sudden rise and maintains its maximum level for a finite instant; then the signature performs a rapid decline as the plunger stops at its end position. The purpose of the current study is to investigate the role of the difference in filtering the pressure signatures between the traditional Kalman filter and adaptive Kalman filter based on  $F$ -distribution. Different injection

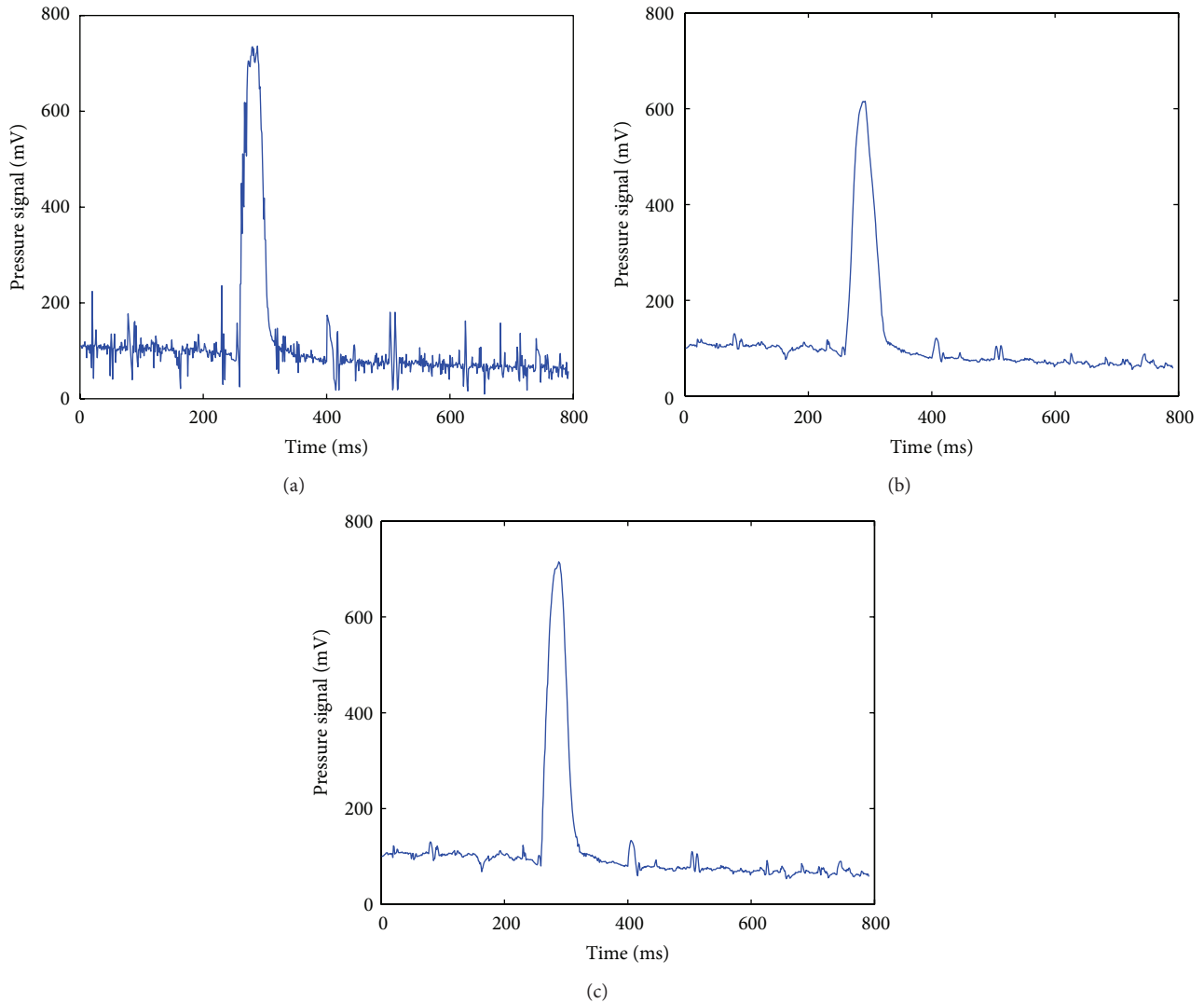


FIGURE 6: Injection velocity 475 mm/s. Original signature width 60 ms. Signature peak height 624 mV. Injection volume 0.12 cc. (a) Experimental pressure signature without filter. (b) Experimental pressure signature processed by traditional Kalman filter. (c) Experimental pressure signature processed by adaptive Kalman filter based on  $F$ -distribution.

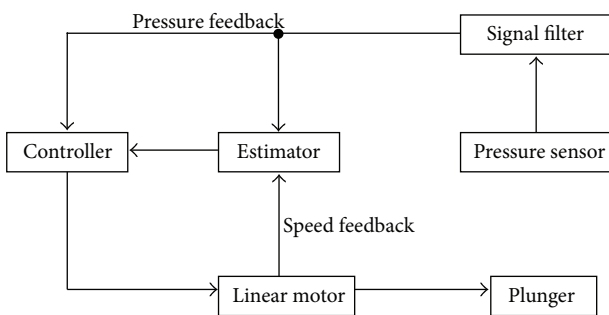


FIGURE 7: Signal process flow chart.

velocities are selected to compare the pressure signatures filtered by the traditional Kalman filter and the adaptive Kalman filter based on  $F$ -distribution.

The pressure signatures under different injection velocities are obtained by a pressure sensor (Kistler 6171BA, range = 0 to 2000 bar) and plotted by MATLAB 7; then the signatures are processed by MATLAB 7 using the traditional Kalman filter and adaptive Kalman filter based on  $F$ -distribution, respectively. The simulation results are shown in Figures 5 and 6. The simulation computer's CPU is Intel Core i7-2620M Dual-Core Processor. The memory is 8 GB DDR3 1333 MHz. In Figure 5 the injection velocity is 50 mm/s, the signature width is 342 ms, the signature peak height is 125 mV, and the injection volume is 0.12 cc. In Figure 6 the injection velocity is 475 mm/s, the original signature width is 60 ms, the signature peak height is 624 mV, and the injection volume is also 0.12 cc. Figures 5(a) and 6(a) show the experimental pressure signatures without filter. We can see the signatures have severe electromagnetic noise; this may affect the judgment of the start and end points during the micro injection procedure.

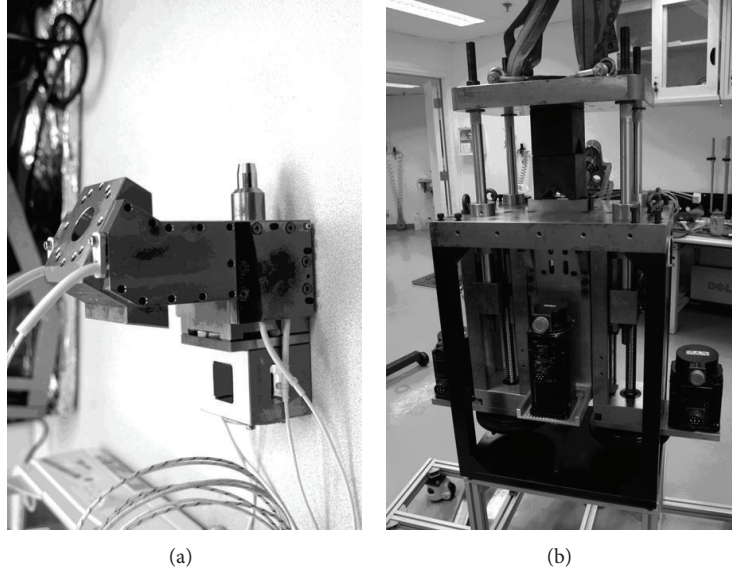


FIGURE 8: (a) Injection part. (b) Micro injection molding machine.

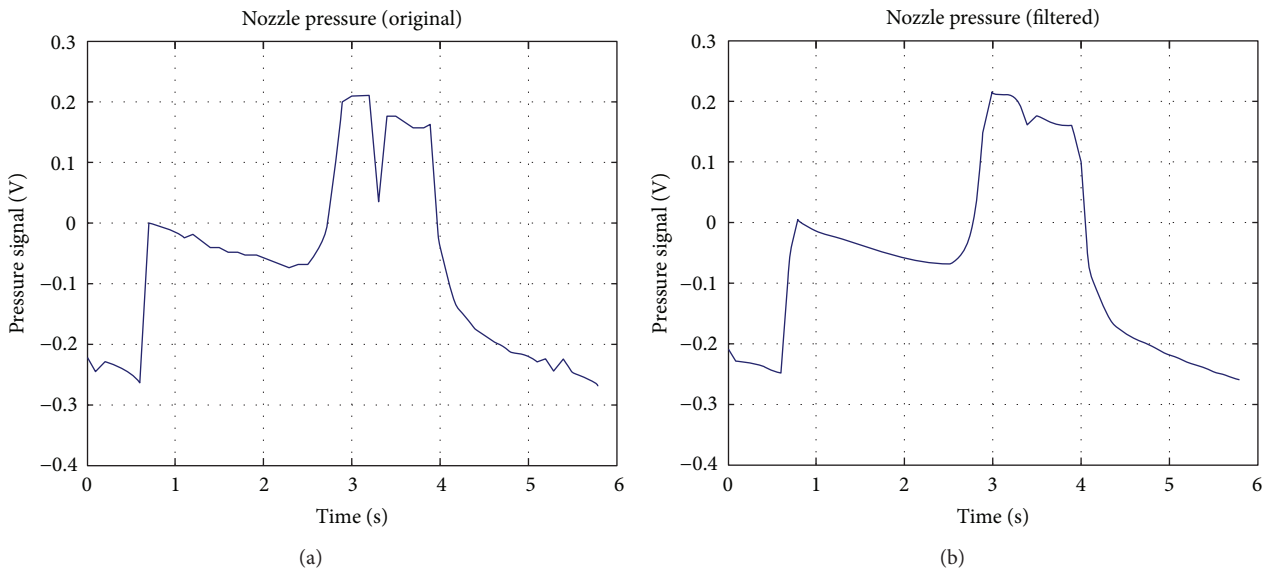


FIGURE 9: Experiment plastic POM. Injection velocity 15 mm/s. Injection volume 0.32 cc. (a) Original signature: signature width 3350 ms, signature peak height 445 mV. (b) Filtered signature: signature width 3356 ms, signature peak height 443 mV.

Figures 5(b) and 6(b) show the experimental pressure signatures processed by traditional Kalman filter. In Figure 6(b), the peak height of pressure signature is lower than that in Figure 6 (a), which only has got 530 mV, while in Figures 5(b) and 6(b), the pressure signatures have longer rising edges and falling edges because of the “filter dropping off,” so the signature widths of Figures 5(b) and 6(b) are 450 ms and 84 ms, respectively. They are longer than the signature widths in Figures 5(a) and 6(a), which may cause excessive shooting (Figure 3). From Figures 5(c) and 6(c), we can see the pressure signatures processed by adaptive Kalman filter based on *F*-distribution do not have the shortcoming of the traditional Kalman filter. Compared with Figures 5(a) and 6(a), the electromagnetic noise in Figures 5(c) and 6(c) is reduced

significantly. The signature widths in Figures 5(c) and 6(c) are 346 ms and 62 ms, and the signature peak heights are still the same as the original signatures. From the simulation results we can see the adaptive Kalman filter based on *F*-distribution performs better in the micro injection molding procedure.

#### 4. Experiments

The injection volume control needs to get the precise signature width to confirm when the injection process starts and finishes. From the former simulation results, the adaptive Kalman filter based on *F*-distribution meets this demand. Then the experiments should be carried out to verify if the adaptive Kalman filter based on *F*-distribution is suitable

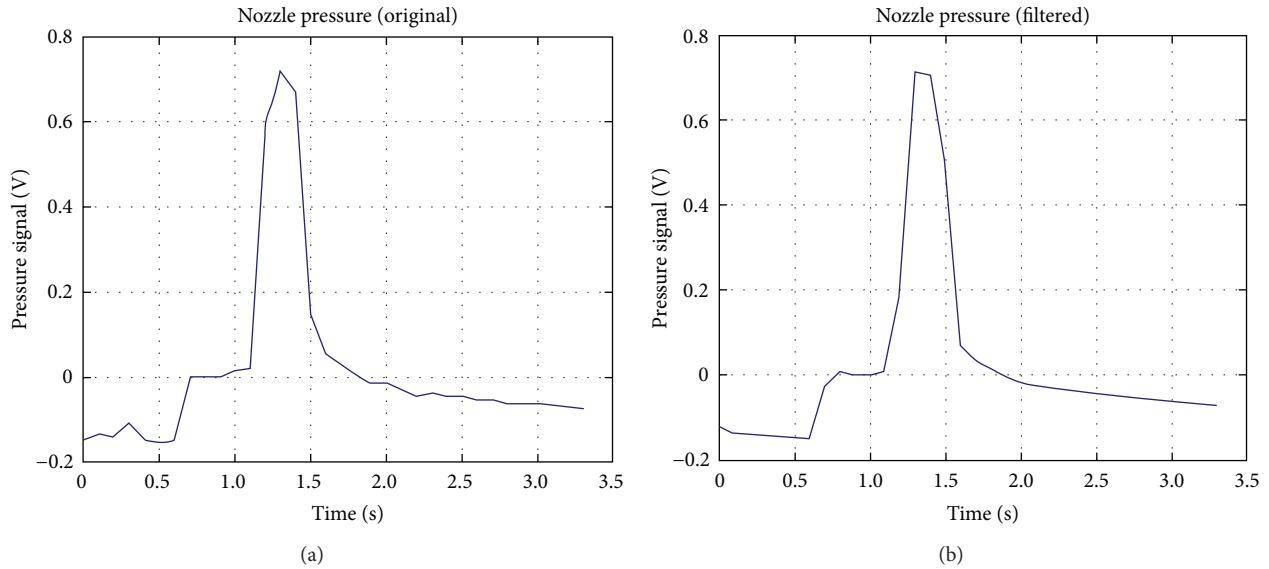


FIGURE 10: Experiment plastic POM. Injection velocity 150 mm/s. Injection volume 0.45 cc. (a) Original signature: signature width 486 ms, signature peak height 710 mV. (b) Filtered signature: signature width 488 ms, signature peak height 708 mV.

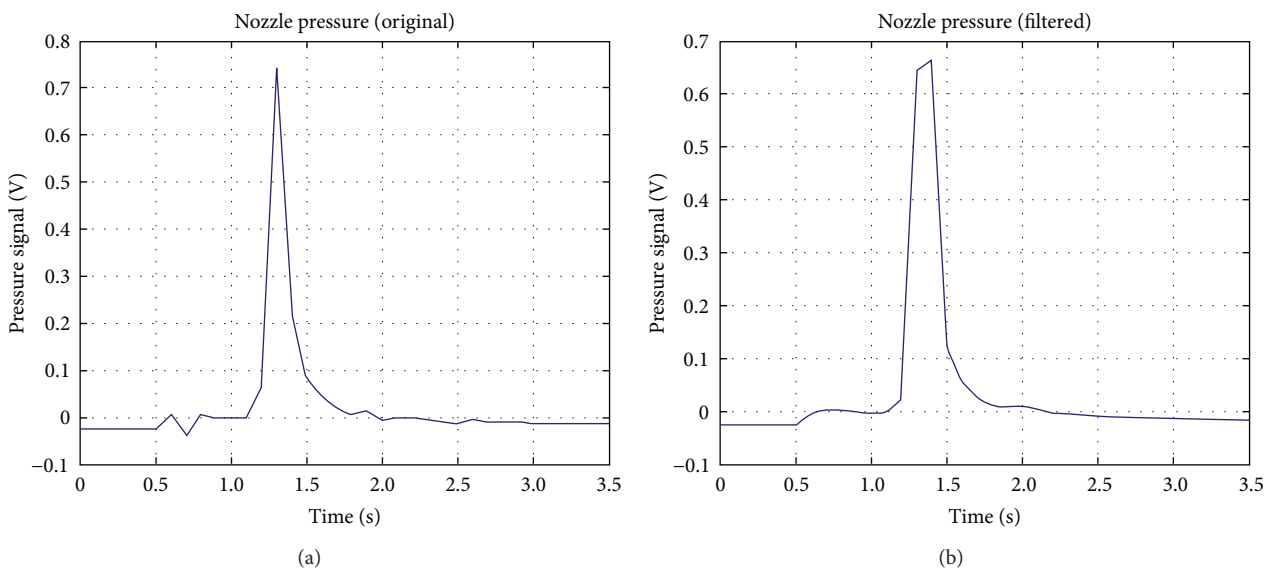


FIGURE 11: Experiment plastic PMMA. Injection velocity 150 mm/s. Injection volume 0.45 cc. (a) Original signature: signature width 477 ms, signature peak height 753 mV. (b) Filtered signature: signature width 480 ms, signature peak height 768 mV.

for tracking the pressure signature during micro injection molding process.

Figure 7 shows the signal process flow chart for the micro injection molding procedure. The controller and the estimator are called the control part. The pressure signal filter is called the pressure feedback. The control part uses the pressure feedback and the speed feedback to adjust the travelling speed of the plunger. So it is very important to get the correct and real-time pressure signatures from the digital filter.

A series of experiments is conducted to study the effects of plastic material when using the adaptive Kalman filter based on  $F$ -distribution. The rejection criterion  $\alpha$  is chosen as 5%

by analyzing the experiments' results. The injection assembly and the assembly of the micro injection molding machine are shown in Figures 8(a) and 8(b). The pressure sensor is the Kistler 6171BA (range = 0 to 2000 bar). The sensor is in turn connected to a charge amplifier (Kistler 5039A, range = 0 to 20,000 pC), which converts the charge generated by the sensor to a voltage that represents the measured pressure. The oscilloscope is Tektronix TDS 3014B and the control theory is proportional-integral-derivative (PID) control.

In the injection experiments we have recorded the original and the filtered pressure signatures. Figures 9, 10, and 11 depict the injection process with different shot volumes at

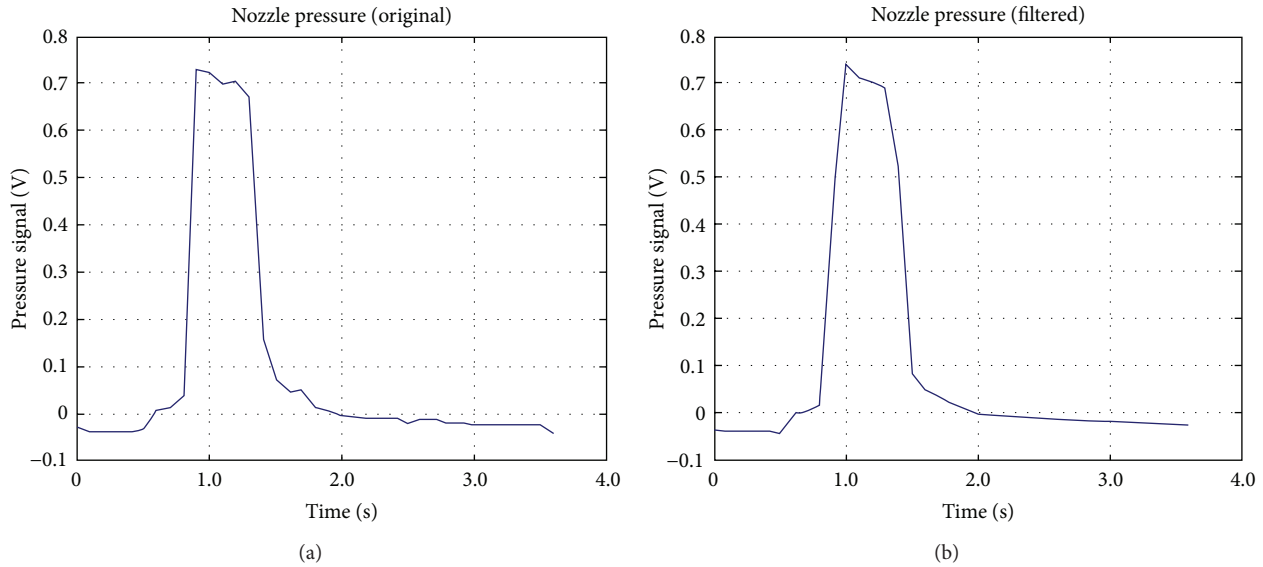


FIGURE 12: Microgear trial production. Experiment plastic POM. Injection velocity 150 mm/s. Injection volume 0.86 cc. (a) Original signature: signature width 989 ms, signature peak height 696 mV. (b) Filtered signature: signature width 993 ms, Signature peak height 695 mV.

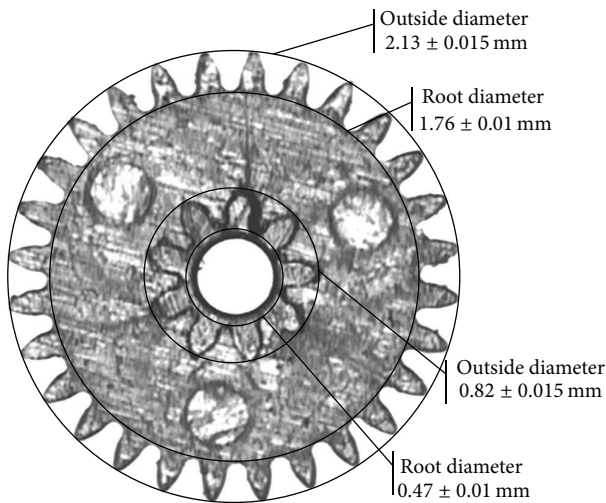


FIGURE 13: Micro gear profile and some of the dimension demands.

different injection velocities by using different plastics. The plastic POM (Delrin 900P) is used in Figures 9 and 10. The plastic PMMA (MF-001) is used in Figure 11. In Figure 9, the injection velocity is 15 mm/s, and the injection volume is 0.32 cc. Figure 9(a) shows that the original signature width is 3350 ms and the signature peak height is 445 mV. Figure 9(b) shows the filtered signature width as being 3356 ms with a signature peak height of 443 mV. In Figure 10, the injection velocity is 150 mm/s and the injection volume is 0.45 cc. Figure 10(a) depicts the original signature width as 486 ms and the signature peak height as 710 mV. Figure 10(b) shows that the filtered signature width is 488 ms and the signature peak height is 708 mV. In Figure 11, the injection velocity is 150 mm/s and the injection volume is 0.45 cc. Figure 11(a)

depicts the original signature width as 477 ms and the signature peak height as 753 mV. Figure 11(b) shows that the filtered signature width is 480 ms and the signature peak height is 768 mV. From the datum it can be seen that the rising edges of the pressure signatures are captured perfectly and the delay times are very short. The changes of peak height between the original and filtered signatures are tiny in Figures 9 and 10, but the change is larger in Figure 11. However, the signature width change between Figures 11(a) and 11(b) is still tiny. So it will not affect the injection volume control. In view of the above, the experimental and simulation results are consistent; no matter how the injection velocity changes, the filtered pressure signatures are always stable and reliable. It is good for the accuracy control of the micro injection molding process. Also, the filter can effectively eliminate the high frequency electromagnetic noise in the pressure transducer signal.

To further test the accuracy and micro injection performance of the new filter, a microgear is produced by the micro injection molding machine. The plastic material used in the experiment is POM (Delrin 900P). As there are 16 microcavities in the mold, 16 microgears can be accessed during the micro injection molding procedure. The pressure signature of the micro gear trial production is shown in Figure 12. The injection velocity is 150 mm/s, and the injection volume is 0.86 cc. Figure 12(a) shows that the original signature width is 989 ms and that the signature peak height is 696 mV. Figure 12(b) shows that the filtered signature width is 993 ms and that the signature peak height is 695 mV. Figure 13 shows the profile of the microgear product used in the experiment and some of its dimension demands. The profile is taken by the Leica DM300 microscope. The microgear has two layers in Figure 13. The outer gear has 28 teeth; the outside diameter is  $2.13 \pm 0.015$  mm, and the root diameter is  $1.76 \pm 0.01$  mm. The inner gear has 9 teeth; the outside diameter is  $0.82 \pm 0.03$  mm, and the root diameter is  $0.47 \pm 0.03$  mm. It

TABLE 1: Measurement result of outer gear (diameter).

Number	Outside diameter (mm)	Root diameter (mm)
1	2.125	1.752
2	2.126	1.763
3	2.139	1.766
4	2.122	1.769
5	2.132	1.764
6	2.137	1.755
7	2.137	1.753
8	2.131	1.752
9	2.135	1.759
10	2.128	1.752
11	2.125	1.763
12	2.136	1.754
13	2.138	1.754
14	2.131	1.760

TABLE 2: Measurement result of inner gear (radius).

Number	Outside radius (mm)	Root radius (mm)
1	0.406	0.233
2	0.407	0.234
3	0.407	0.232
4	0.411	0.231
5	0.413	0.237
6	0.410	0.238
7	0.406	0.238
8	0.409	0.231
9	0.417	0.230

has very subtle teeth and a delicate tooth profile. It validates the effectiveness of the filter.

The measurement tool is the Leica DM300 microscope. As the outer gear has an even number of teeth, the opposite two vertexes are measured to determine the diameters; the results are shown in Table 1. The inner gear has an odd number of teeth, so the center of the micro gear is first fixed by two intersecting diameters of the outer gear, and then the radius of the inner gear is measured; the results are shown in Table 2. The dimension demands for radius of the inner gear are adjusted as the outside diameter is  $0.41 \pm 0.015$  mm and the root diameter is  $0.235 \pm 0.015$  mm. From Tables 1 and 2, we can see the measurement data of the micro gear produced satisfies the dimension demands proposed.

## 5. Conclusion

This paper derives an adaptive Kalman filter based on  $F$ -distribution to track the pressure signature generated by an ascending plunger that pushes plastic melt through a nozzle into a micro injection mold. The filter switches the system between a transient and steady state in real time, effectively eliminating electromagnetic noise and precisely capturing the rising and falling edges of the pressure signature. According to the simulation results, the adaptive Kalman filter avoids the shortcoming of the original Kalman filter at high and low injection velocities, and the pressure signatures meet

control requirements. The experimental filter satisfies dimension demands and is proven suitable for use in the mass production of micro injection moldings.

## Acknowledgments

This work is supported in part by the Hong Kong Innovation & Technology Foundation (ITF/025/03), the Natural Science Foundation of China (NSFC) under Grant 60974069, and Shenzhen Government Foundation under JC200903120188A.

## References

- [1] B. Ekstrand, "Poles and zeros of  $\alpha$ - $\beta$  and  $\alpha$ - $\beta$ - $\gamma$  tracking filters," *IEE Proceedings on Control Theory and Applications*, vol. 148, no. 5, pp. 370–376, 2001.
- [2] P. A. C. Lopes and J. B. Gerald, "New normalized LMS algorithms based on the Kalman filter," in *Proceedings of the IEEE International Symposium on Circuits and Systems (ISCAS '07)*, pp. 117–120, May 2007.
- [3] A. Barnawi, A. Albakkar, and O. P. Malik, "RLS and Kalman Filter identifiers based adaptive SVC controller," in *Proceedings of the 39th North American Power Symposium (NAPS '07)*, pp. 615–622, October 2007.
- [4] J. A. Rosendo Macías and A. G. Expósito, "Self-tuning of Kalman filters for harmonic computation," *IEEE Transactions on Power Delivery*, vol. 21, no. 1, pp. 501–503, 2006.
- [5] C. Hu, W. Chen, Y. Chen, and D. Liu, "Adaptive Kalman filtering for vehicle navigation," *Journal of Global Positioning Systems*, vol. 2, pp. 42–47, 2003.
- [6] B.-J. Lee, J.-B. Park, and Y.-H. Joo, "IMM algorithm using intelligent input estimation for maneuvering target tracking," *IEICE Transactions on Fundamentals of Electronics, Communications and Computer Sciences*, vol. E88-A, no. 5, pp. 1320–1327, 2005.
- [7] A. K. Anilkumar, M. R. Ananthasayanam, and P. V. Subba Rao, "A constant gain Kalman filter approach for the prediction of re-entry of risk objects," *Acta Astronautica*, vol. 61, no. 10, pp. 831–839, 2007.
- [8] J.-Y. Kim and T.-Y. Kim, "Soccer ball tracking using dynamic kalman filter with velocity control," in *Proceedings of the 6th International Conference on Computer Graphics, Imaging and Visualization (CGIV '09)*, pp. 367–374, August 2009.
- [9] Z.-L. Deng, Y. Gao, L. Mao, Y. Li, and G. Hao, "New approach to information fusion steady-state Kalman filtering," *Automatica*, vol. 41, no. 10, pp. 1695–1707, 2005.
- [10] W. Ding, J. Wang, C. Rizos, and D. Kinlyside, "Improving adaptive kalman estimation in GPS/INS integration," *Journal of Navigation*, vol. 60, no. 3, pp. 517–529, 2007.
- [11] Y. Geng and J. Wang, "Adaptive estimation of multiple fading factors in Kalman filter for navigation applications," *GPS Solutions*, vol. 12, no. 4, pp. 273–279, 2008.
- [12] G. Welch and G. Bishop, *An Introduction To the Kalman Filter*, Department of Computer Science, University of North Carolina at Chapel Hill, 1997.
- [13] W. W. Hines and D. C. Montgomery, *Probability and Statistics in Engineering and Management Science*, John Wiley and Sons, New York, NY, USA, 1990.
- [14] K. L. Yung, H. Liu, Y. Xu et al., "Target tracking in micro injection molding," *Key Engineering Materials*, vol. 364–366, pp. 1292–1295, 2008.